CONCEPTUAL DESIGN OF HIGH-LIFT PROPELLER SYSTEMS FOR SMALL ELECTRIC AIRCRAFT

A Dissertation
Presented to
The Academic Faculty

by

Michael D. Patterson

In Partial Fulfillment
of the Requirements for the Degree
Doctor of Philosophy in the
School of Aerospace Engineering

Georgia Institute of Technology
August 2016

CONCEPTUAL DESIGN OF HIGH-LIFT PROPELLER SYSTEMS FOR SMALL ELECTRIC AIRCRAFT

Approved by:

Professor Brian J. German, Advisor
School of Aerospace Engineering
Georgia Institute of Technology

Professor Marilyn J. Smith
School of Aerospace Engineering
Georgia Institute of Technology

Professor Lakshmi N. Sankar
School of Aerospace Engineering
Georgia Institute of Technology

Dr. Nicholas K. Borer
Aeronautics Systems Analysis Branch
NASA Langley Research Center

Dr. Erik D. Olson
Aeronautics Systems Analysis Branch
NASA Langley Research Center

Date Approved: 27 April 2016

To the One "who is able to do immeasurably more than all we ask or imagine"[1] *and to my son Isaac who is living proof of His immeasurable power*

[1] *Ephesians 3:20 (NIV)*

ACKNOWLEDGEMENTS

This work would not have been completed without the help and encouragement of many people. There is simply not sufficient time or space to acknowledge everyone who has helped me make it through graduate school and finish this document.

First and foremost, my wife, Laura, has helped keep me sane throughout the many stressful times and transitions that have occurred in my life since beginning grad school. From providing me encouragement when things were getting overwhelming, to picking up the slack around our home when I was slammed with work, to being an awesome mother to our kids, she has helped me more than any other person to complete this work.

All the other members of my family have also provided love, support, encouragement, and much-needed diversions from work throughout grad school. My boys, William and Isaac, have helped me keep perspective on what's really important in life (particularly recently). The rest of my extended family, not least of which are my parents and parents-in-law, have also been great sources of support throughout my life and in particular through this last year.

Perhaps the single most influential person in helping to guide the general direction of my research has been Mark Moore of NASA Langley. I would certainly not be where I am today physically or professionally if Mark had not taken a chance in funding my advisor and one of his young grad students to help with the Zip Aviation study back nearly five years ago. Mark has also been instrumental in promoting electric aircraft and on-demand mobility research at NASA, and the SCEPTOR project (among many others) simply would not have happened without his tireless efforts.

I would also like to thank my entire thesis committee for their guidance, feedback,

and inspiration. I am very thankful for Dr. German's decision to bring me into his research group and for the many conversations and meetings we had together throughout my time in grad school. He has been a great advisor, and I am certainly a better researcher, engineer, and writer because of him. Dr. Borer has been an awesome mentor at NASA. Virtually every aspect of this dissertation has come either directly or indirectly from conversations I've had with him. Without his encouragement and pragmatic advice, I would not have completed this document. It was in Dr. Sankar's class where I first learned about rotor design, and many elements of this document would likely not have come about without his teaching. Dr. Smith's teaching and technical excellence have pushed me to perform as high-quality work as possible. I have been inspired by Dr. Olson's work in applying corrections to lower-order tools to obtain more accurate results, and I emulate some of his general techniques in this document.

Big thanks are also due to all the members of the "German Research Group" (formal and honorary) for their friendship, doubt raising, humor, and all-around awesomeness throughout grad school. Y'all made life in asbestos-laden ESM and the dungeon of Weber much more enjoyable than it could have been. David Pate deserves special thanks, as I'm not sure if I would have made it through qualifying exams without him.

The OVERFLOW CFD results presented in Chapter III would not have been possible without Dr. Joe Derlaga of NASA Langley. He was quite patient with me in helping get me set up to run cases for which I am very thankful. His practical aerodynamic knowledge has been a huge asset to me and the broader SCEPTOR project team. Joe has been a great colleague, and I look forward to continuing to work along side him into the future.

I would also like to thank the entire SCEPTOR project team including everyone at Joby Aviation, Empirical Systems Aerospace (ESAero), and across NASA. In terms

of technical content in this document, the FUN3D CFD results from the LEAPTech configuration discussed in Chapter III were performed by Karen Deere, Salley Viken, and Steve Bauer of NASA Langley, and the STAR-CCM+ CFD results for the same configuration were run by Alex Stoll of Joby Aviation. I'm also grateful for Alex's help in tracking down and discussing various simplified methods of estimating lift increases due to propeller blowing. Brandon Litherland of NASA Langley performed the parasite drag estimation of the SCEPTOR aircraft without flaps and helped me get up and running in VSPAero.

I would also like to acknowledge the funding that has made this work possible. First, the NASA Aeronautics Scholarship Program provided funding for my final years on campus. Second, much of this work has been performed while I have been working at NASA Langley Research Center on the Convergent Aeronautics Solutions (CAS) and Transformational Tools and Technologies (TTT) Projects, which are both part of the NASA Aeronautics Research Mission Directorate's Transformative Aeronautics Concepts Program.

TABLE OF CONTENTS

LIST OF TABLES

LIST OF FIGURES

LIST OF SYMBOLS OR ABBREVIATIONS

Abbreviations

CFD	computational fluid dynamics
DEP	distributed electric propulsion
FAA	Federal Aviation Administration
FAR	Federal Aviation Regulation
GA	general aviation
HEIST	Hybrid-Electric Integrated Systems Tested
HLP	high-lift propeller
HLPA	an aircraft equipped with a high-lift propeller system
LEAPTech	leading edge asynchronous propellers technology
MIL	minimum induced loss
NASA	National Aeronautics and Space Administration
RPM	revolutions per minute
SCEPTOR	Scalable Convergent Electric Propulsion Technology Operations Research
UAV	unmanned aerial vehicle
V/STOL	vertical or short takeoff and landing

Greek Symbols

α	angle of attack
β	velocity multiplier or twist angle of local blade element
Γ	circulation
κ	circulation multiplier
Ω	angular velocity of the propeller
ω	local angular velocity of blade element
ϕ	local inflow angle of a blade element

ρ	density
θ_{swirl}	swirl angle
φ	propeller installation angle

Symbols

$(\Delta\alpha)_{\text{approach}}$	angle of attack margin in approach
$(\Delta C_L)_{\text{approach}}$	total lift coefficient margin in approach
$(\Delta C_{L_\alpha})_{\text{approach}}$	lift coefficient margin in approach due to angle of attack
$\left(\Delta C_{L_{\text{blowing}}}\right)_{\text{approach}}$	lift coefficient margin in approach due to blowing
A	propeller disk area
a	axial induction factor
a'	tangential induction factor
a_0	lift curve slope
AR	aspect ratio
B	number of blades
b	span
c	chord length
C_D	drag coefficient
c_d	section drag coefficient
C_{D0}	parasite drag coefficient
C_L	lift coefficient
c_l	section lift coefficient
$\bar{C}_L$	adjusted lift coefficient
$\bar{C}_L^*$	adjusted lift coefficient in a uniform freestream
C_{L_α}	lift coefficient generated by angle of attack
$C_{L_{\text{blowing}}}$	lift coefficient generated by the slipstreams of high-lift propellers
D	drag
d	parameter defining width of Joukowski velocity profile

e_0	Oswald efficiency factor
F	Prandtl tip loss factor
i_p	propeller slipstream inclination angle
K	induced drag factor
K_i	coefficient row vector for β surrogate model
K_L	lift multiplier (i.e., ratio of blown to unblown lift)
K_{a_0}	lift curve slope multiplier
$k_{i,j}$	scalar coefficient value for β surrogate model
L	lift
L'	lift per unit span
$\dot{m}$	mass flow rate
P	power
p	static pressure
Q	torque
q	dynamic pressure
R	radius
r	radial location
R'	radius for use in determining the tip loss factor
S	wing reference area
T	thrust
u	distance of disk upstream of wing leading edge
V	velocity
V_{stall}	stall speed
V_{app}	approach speed
V_{REF}	reference landing approach speed
V_{S0}	stall speed in the landing configuration
V_{S1}	stall speed in a specific configuration

v_i	induced axial velocity
W	weight or local velocity at a blade element
w	induced velocity
W/S	wing loading
X	column vector for β surrogate model, $\begin{bmatrix}1 & u/c & (u/c)^2 & (u/c)(V_j/V_\infty) & (V_j/V_\infty) & (V_j/V_\infty)^2\end{bmatrix}^T$
z	vertical coordinate relative to airfoil chord

Subscripts

∞	freestream
a	axial or absolute
c	center
ep	effective value aft of the propeller
j	jet
$L=0$	zero-lift
p	propeller
T	tip
t	tangential
0	original value
avg	average
max	maximum

SUMMARY

The maturation of electric propulsion technologies presents intriguing new degrees of freedom for aircraft designers because the characteristics of electric motors are distinctly different from those of conventional internal combustion engines. Because electric motors are compact and have high specific power, they can be integrated in the aircraft configuration design in ways that are not possible with conventional engines in order to achieve synergistic aerodynamic, propulsive, acoustic, or other benefits. One particularly promising integration concept is to distribute many small propulsors in advantageous locations along the wing or fuselage. This concept has been termed "distributed electric propulsion" and is the focus of a growing field of research.

One proposed distributed electric propulsion concept involves placing many smaller propellers upstream of the wing's leading edge. The function of these propellers is to augment the lift produced by increasing the dynamic pressure and/or circulation experienced by the downstream wing at low speed conditions. This increased lift capability allows smaller wings to provide sufficient low-speed performance, enabling higher wing loading and increasing aerodynamic efficiency at nominal cruise speeds. The propellers can be folded for higher speed flight, with main propulsion provided by additional cruise-optimal propulsors. Although other aircraft have installed propellers to augment lift, these same propellers are also required to provide primary propulsive thrust for the aircraft; in the proposed concept, the smaller, distributed propellers are decoupled from cruise thrust generation and installed solely to augment lift. Consequently, these distributed propellers act collectively as a form of high-lift device for the wing and have therefore been termed "high-lift propellers."

This dissertation focuses on how high-lift propellers should be designed and how the design of high-lift propeller systems can be incorporated into the wing design process. One contribution is a novel method for quickly assessing wing lift augmentation based on changes in the dynamic pressure and circulation due to the propeller's influence. The method predicts lift augmentation performance based on the propeller loading, diameter, installation angle, and upstream distance from the wing. The analysis method is based on consideration of momentum theory and thin wing theory, with semi-empirical corrections abstracted from higher-order computational fluid dynamics (CFD) simulations. The CFD corrections are implemented in a surrogate model that executes rapidly and can be practically implemented into a conceptual design process. The overall approach provides not only lift augmentation predictions but also practical and transparent insights into effective design strategies. A second contribution is a high-lift propeller design method based on blade element momentum theory that is capable of generating blades that produce the specified lift augmentation performance while requiring on the order of 15% lower power than conventional minimum induced loss propeller designs. These design tools are applied to estimate the performance of high-lift propeller design strategies for novel aircraft configurations employing the technology. Additionally, existing Federal Aviation Administration stall and reference approach speed regulations are examined, and guidance for developing regulations appropriate for aircraft with high-lift propellers is presented. Finally, example trade studies are performed for the upcoming flight demonstrator aircraft being developed as a part of NASA's Scalable Convergent Electric Propulsion Technology Operations Research (SCEPTOR) project.

CHAPTER I

INTRODUCTION

1.1 Motivation

The rising costs of fossil fuels and growing environmental concerns are leading to changes in the world's transportation systems. Alternative energy sources including biofuels and hybrid/fully electric systems are being explored to power land-based forms of transportation. The automotive industry is largely leading the way in the development of both fully electric and hybrid electric vehicles, as well as flexible fuel engines. Hybrid and fully electric automobiles are increasing in popularity, and biofuels such as E85 gasoline are entering the market as well. The push for more environmentally friendly transportation extends also to aviation. Much work has been undertaken in recent years to find technologies that can reduce aircraft fuel consumption. Some of this work has focused on evolutionary aerodynamic and propulsive improvements such as incorporating winglets or developing higher bypass ratio engines while other work has investigated more revolutionary changes in aircraft configuration design [5, 6].

In an effort to foster the advancement of environmentally friendly aircraft technologies, NASA and the CAFE Foundation sponsored the 2011 Green Flight Challenge, which featured the largest monetary prize to date in aviation history. The main goal of this competition was to "push technology and make passenger aircraft more efficient" [7], specifically targeting aircraft that could travel over 200 miles in less than two hours while achieving over 200 passenger-miles per gallon (equivalent) with reduced noise. The competition included entries powered by biofuels as well as electric and hybrid electric systems. Of the aircraft in the competition, only two were

able to meet the lofty 200 passenger-miles per gallon requirement; both of these aircraft utilized fully electric propulsion systems and achieved over 375 passenger miles per gallon equivalent. The winning aircraft, the Pipistrel Taurus G4 [8, 9], averaged 403.5 passenger-miles per gallon equivalent [10]. The successful flights of these two fully electric aircraft lead NASA's chief technologist Joe Parrish to remark, "Today we've shown that electric aircraft have moved beyond science fiction and are now in the realm of practice" [11].

1.1.1 Electric Aircraft Propulsion

Apart from the potential to achieve incredibly high effective fuel efficiency and very low emissions, electric motors have many other advantages over conventional engines. These advantageous characteristics include [12]:

- high power-to-weight ratios (i.e., lower weights than conventional reciprocating engines),
- very high efficiencies (above 90%) over a wide range of operating conditions,
- "scale-invariant" efficiency and power-to-weight ratio (i.e., the ability to maintain similar efficiencies and power-to-weight ratios regardless of size),
- few moving parts, high reliability, and simple maintainability,
- low vibration levels and low noise,
- no shaft power lapse with altitude or flight speed,
- digital control signal that can easily be controlled via an autopilot,
- redundancy with little or no penalty through utilizing multiple motors or multiple coils within a single motor to spin the same shaft,
- compactness (i.e., reduced volume required for a given power than a conventional engine),
- synergy with many renewable energy technologies to virtually eliminate full system-level emissions, and

- the ability to operate at powers above the maximum continuous rated power for short periods of time (on the order of half a minute to two minutes depending on the motor cooling).

To help illustrate some of the potential opportunities that electric motors may provide aircraft designers and operators, a notional electric motor map showing contours of the efficiency of the motor at various operating torques and rotational speeds is shown in Figure 1. This figure was generated using a parametric electric motor model presented by McDonald [13], and the characteristics of the motor were proposed by McDonald as being similar to the UQM PowerPhase 125 electric motor [14]—an existing production electric motor.[1]

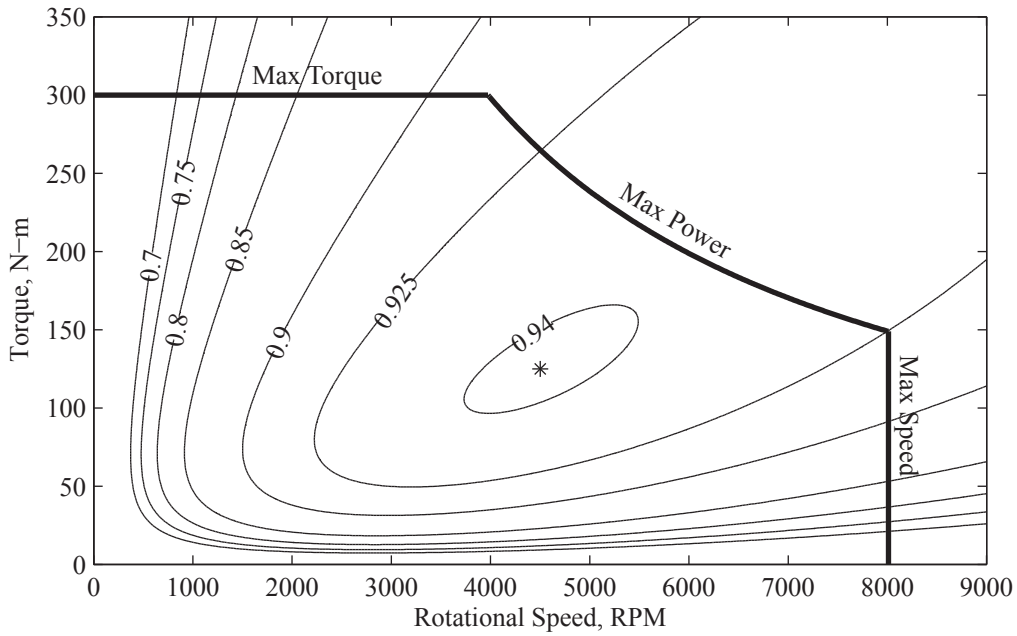

Figure 1: A notional electric motor efficiency map generated by a parametric electric motor model

The motor represented by Figure 1 has a peak efficiency of 94.1% that occurs at a rotational speed of 4500 RPM and a torque of 125 N-m; this maximum efficiency

[1]Although Figure 1 is a notional representation of a single electric motor, the general characteristics of the figure hold true for most electric motors.

point is denoted by an asterisk in the figure. The horizontal thick, solid black line represents the rated torque limit (of 300 N-m); the vertical thick, solid black line represents the rotational speed limit (of 8000 RPM); the curved line connecting the rated torque and speed limits is the maximum rated power limit (of 125 kW). One of the major observations that can be made from Figure 1 is that the motor can operate at many different rotational speeds and torques (or powers) and still maintain a very high efficiency. Efficiencies of over 90% are possible from torques of 35 N-m to 300 N-m; additionally, 90% or better efficiencies can be realized at RPMs from 1600 to 8000. These wide "islands" of high efficiency can enable variable propeller rotational speed (i.e., RPM) operation[2] with minimal motor efficiency losses; such operation is akin to employing gears on a conventional engine, but electric motors can provide the same functionality without any weight penalty. The high torques and efficiencies that can be achieved over a wide range of rotational speeds provide flexibility in the design and operation of the aircraft. For example, propellers can be designed for a wide range of tip speeds, which may aid in reducing the propeller's acoustic signature.

The wide efficiency range of electric motors and the impact it may have on the rotational speeds of propellers has been discussed here only as an example of how electric motors may fundamentally change the way aircraft are designed and operated. The other advantages of electric motors have many other implications for the design and operation of aircraft [12], some of which will be discussed below. However, there is also one major disadvantage of utilizing electric propulsion on aircraft, which has, until recently, limited electric propulsion research and applications: the high weight of energy storage mechanisms.

Despite the success of the all-electric Green Flight Challenge aircraft, many people still dismiss the concept of fully-electric aircraft due to the high weights of energy

[2]It is technically more correct to specify that variable propeller advance ratio operation is possible with electric motors, but rotational speed has been specified here for those unfamiliar with the concept of advance ratio to better follow the discussion.

storage devices such as batteries. Although it is true that the specific energy (i.e., energy per unit mass) of batteries is currently considerably less than conventional aviation fuels, past work by the author indicates that with only moderate increases in battery technologies, fully-electric, small, propeller-driven aircraft can be sized for practical mission performance over short ranges [15].

One of the main results from this past study [15] of short-range electric aircraft is shown in Figure 2. This figure illustrates the aircraft gross weight required to fly three different missions for various levels of battery specific energy. The three curves correspond to three different sets of mission requirements and technology assumptions, which were based on anticipated levels of technologies at the three given epochs. The markers on these curves represent the baseline technology assumptions for that year. The aircraft were sized to missions of 200 (statute) miles for 2015, 300 miles for 2035, and 500 miles for 2050 (each with a 45 minute reserve) using an "electric Breguet range"-based sizing logic [15]. Although these ranges are shorter than those of most conventional aircraft, they represent reasonable ranges for aircraft used in on-demand missions as part of a fleet. For example, the average stage length for the air taxi DayJet, one of the more successful air taxi services to operate, was less than 200 miles [16]. Technology assumptions for generating the data in Figure 2 include a lift-to-drag ratio of 18.75 (for all epochs), a propeller efficiency of 0.85 (for all epochs), and electrical system efficiencies of 0.89 for 2015, 0.92 for 2035, and 0.95 for 2050.

The most prominent feature of each of the curves in this figure is the very distinct "knee." At lower pack-level specific energies, the required vehicle weight increases drastically with small reductions in specific energy, and at higher specific energies, the change in vehicle weight with battery specific energy is very small. For the shorter-range mission with the 2015 technology assumptions, the inflection point in the curve occurs at a specific energy of approximately 450 W-hr/kg. If this level of specific energy can be achieved, practical aircraft for on-demand missions can be produced

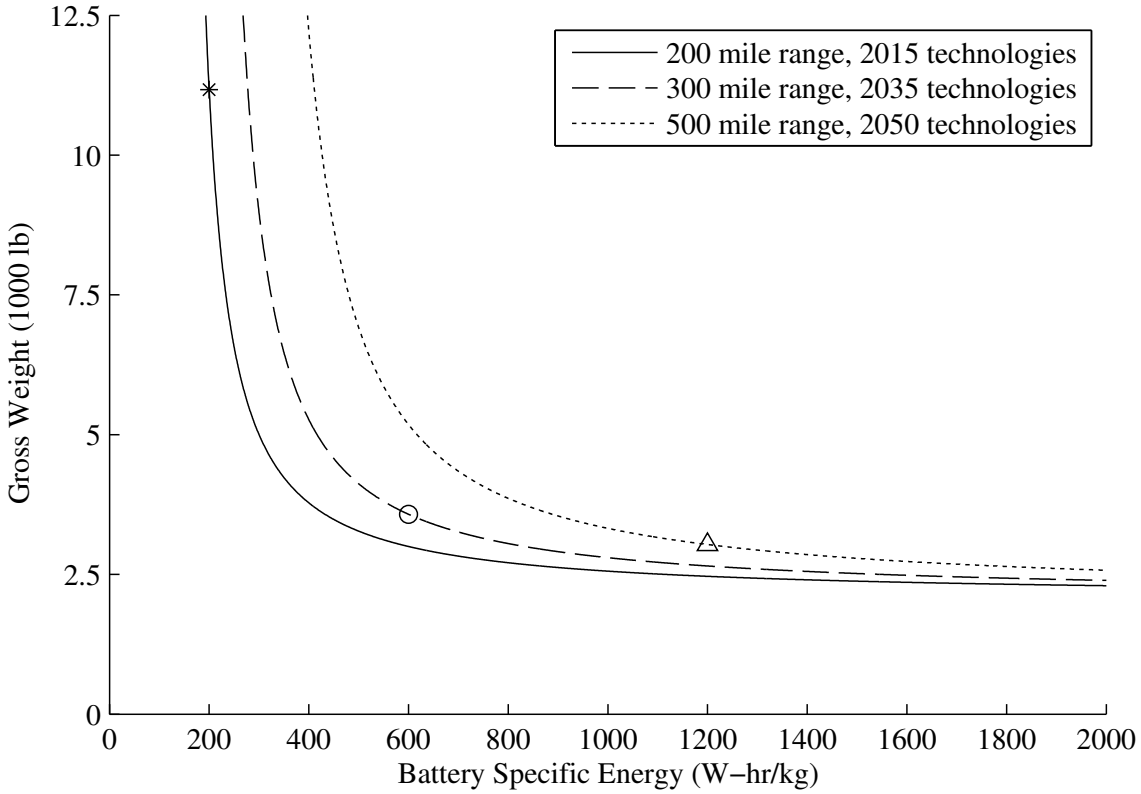

Figure 2: Sizing sensitivity to battery specific energy for three missions and sets of technology assumptions

without further advances in other technologies.

Although current battery technologies achieve less than 200 W-hr/kg, batteries with specific energies up to 400 W-hr/kg have been produced in laboratory settings [17]. It is likely that battery technology will progress to the point of practicality for small aircraft in the not-too-distant future because of the extensive amount of ongoing battery research. For example, the Advanced Research Projects Agency-Energy (ARPA-E) has awarded several multi-million dollar projects to study various battery chemistries including lithium-air, lithium-sulfur, and magnesium as a part of its Batteries for Electrical Energy Storage in Transportation (BEEST) program [18].

As electric motor and battery technologies are maturing, the possibility of applying these technologies in small aircraft is beginning to be explored. Efforts such as that

undertaken by Beyond Aviation [19] are underway to simply replace the traditional internal combustion engine of a small aircraft with an electric motor. Although this approach could potentially save costs by leveraging existing airframe technologies, previous work by the author has indicated that such attempts are likely to produce aircraft with an impractically short range capability in the near term [15].

In order to achieve practical ranges in the near-term, advances in other aspects of the aircraft design will be required. Perhaps the most promising approach is to focus efforts on more efficient aerodynamic design. The effects of aerodynamic improvements are demonstrated in Figure 3 [15], which is based upon the same missions and technology assumptions as Figure 2. Specifically, the specific energy of the batteries is assumed to be 200, 600, and 1200 W-hr/kg for the 2015, 2035, and 2050 epochs, respectively.

Figure 3 demonstrates the vehicle size required to fly three different on-demand missions for various levels of lift-to-drag ratio (L/D). For the 2015 mission and technologies, there is a strong relationship between the required vehicle weight and the lift-to-drag ratio. Current general aviation airframes typically have cruise lift-to-drag ratios of less than 15, which Figure 3 indicates would result in an impractically high gross weight. However, if aircraft can be designed with high lift-to-drag ratios of 20–25 or greater that are more typical of sailplane configurations, Figure 3 indicates that practical aircraft can be developed even without great advances in battery technology.

Several companies such as Yuneec International [20], Pipistrel [21], and Lange Aviation [22] have designed and built electric aircraft aimed at the sport pilot and glider markets. These aircraft, as well as the aircraft in the Green Flight Challenge, all exhibit higher lift-to-drag ratios than typical general aviation aircraft, which allows them to achieve practical performance for short range missions with today's battery technology. Although these aircraft do achieve high L/D values, they are based on more conventional glider-like designs that fly slowly. Even greater improvements in

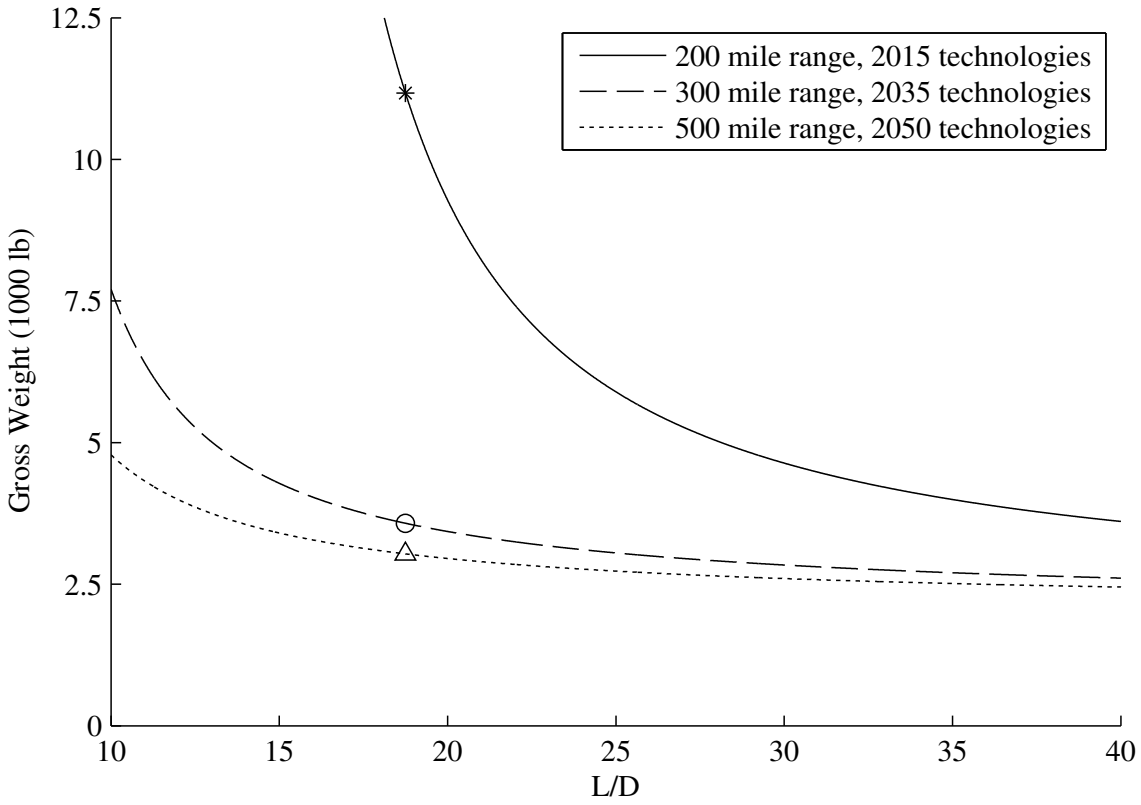

Figure 3: Sizing sensitivity to lift-to-drag ratio for three missions and sets of technology assumptions

aerodynamic efficiency with faster aircraft may be possible through new designs.

1.1.1.1 Potential Near-Term Applications for All-Electric Aircraft

Unless there is a major breakthrough in energy storage technologies, fully-electric aircraft will be highly energy-constrained systems for at least the next decade. Fundamentally, this implies that electric aircraft will only be practical for short-range missions in the near-term. Critics will dismiss these short missions as simply impractical, but such statements lack not only vision for the future but also an understanding of how many aircraft are actually operated today. I will provide a brief summary of the following four potential missions that could benefit greatly from all-electric aircraft:

1. conventional general aviation,

2. essential air services,
3. delivery of goods, and
4. on-demand air transportation.

This list of missions is not exhaustive, but is provided as an example to indicate that short-range aircraft can be practical.

Perhaps the most obvious application for a short-range mission that fully-electric aircraft could practically perform in the very near term is conventional general aviation (GA). In particular, flight schools or flying clubs that need aircraft primarily for operations in the immediate vicinity of an airport are perhaps the most clear early adopter market. In fact, Pipistrel and Airbus are both building all-electric aircraft—the Alpha Electro and E-Fan 2.0, respectively—specifically for the flight training market [23, 24]. Additionally, many private pilots would be able to reduce the operating costs for the typical missions that they fly without losing the ability to perform the vast majority of missions they actually conduct if they were to utilize all-electric aircraft. Electric aircraft have the potentially to completely revolutionize and revitalize the GA industry.

Many short-range missions are currently flown as a part of the U.S. Essential Air Services (EAS) program. The EAS program, which was originally established by Congress as part of the Airline Deregulation Act of 1978 and continues today [25], was initiated to ensure that small communities would continue to be served by air carriers after the deregulation of the airline industry [26]. Many EAS flights are short-range and are currently performed with small aircraft such as the Cessna 208 Caravan, Pilatus PC-12, Piper Navajo, de Havilland Beaver, or Cessna 402. As of October 2015, the program provides over $260 million in subsidies to air carriers to perform EAS flights [27, 28].[3] These subsidies are required largely due to the high

[3]Although a large number of flights occur in Alaska, only approximately $15 million of the subsidies go to air carriers in Alaska.

operating costs per seat of the aircraft flown. Short-range electric aircraft may reduce operating costs sufficiently so that many of these subsidies are no longer required.

There are two potential elements to cargo delivery: replacement of existing cargo feeder aircraft and new unmanned aircraft for delivering packages to customers. As an example of utilizing electric cargo feeder aircraft, FedEx may be able to replace some or all of its existing fleet of Cessna 208 Caravan aircraft with a short-range electric aircraft. Data compiled by McDonald show that as of 2010, FedEx Cessna 208 aircraft flew missions less than 300 nmi 99.5% of the time; furthermore, 91% of the time these aircraft flew missions less than 200 nmi [29]. A compelling business case could be made for FedEx to replace their Cessna 208 aircraft with all-electric aircraft that are less expensive to operate.

Additionally, there has been an explosion in the number of unmanned aerial vehicles (UAVs) in recent years in part due to advances in electric propulsion. Although these UAVs have in the past been flown only as a hobby, several large, well-financed companies such as Amazon, Google, and DHL are all currently researching the possibility of delivering goods directly to customers with UAVs. The distinctly different characteristics of electric motors compared to conventional engines, provides new opportunities for these aircraft to be effectively designed for short and/or vertical takeoff and landing capabilities. Faster point-to-point speeds than current ground-based technologies and the low energy costs of electricity may enable a market for this new means of transporting goods. If existing storefronts and distribution centers are utilized as launching points for these aircraft, an incredibly large number of potential customers can be reached by vehicles with ranges of only tens of miles.

The final example mission for electric aircraft discussed here arguably offers the largest potential market for shorter-range aircraft. Efficient, all-electric aircraft may enable a new mode of *on-demand aircraft* transportation described by Moore [30, 16]. This on-demand transportation model would offer travelers an alternative mode of

transportation that is most ideally suited for trips between approximately 75 and 400 miles in length. Trips of these lengths represent longer car trips that are too short for typical commercial airline travel to be very practical. Moore asserts that this new transportation mode may increase an individual's "mobility reach"—the "area of land that is accessible with a daily travel allowance"—allowing individuals to live and work further away than is currently practical with modern transportation modes [16].

This on-demand air transportation system is similar to air taxi operations. Both current and past air taxi operations have indicated that there is customer demand for more direct air transportation than is currently possible with the hub and spoke airline operations model, particularly for transportation between city pairs that are each reasonably far from a major airport. Furthermore, initial demand modeling of a full on-demand system indicates that considerable demand could result if operating costs are low enough—comparable to automobile travel costs [31]. Growth in air taxi operations has been slowed by high operating costs that stem in part from the high cost of fuel and the use of aircraft that are not designed for typical air taxi missions, which are substantially shorter than range capabilities of modern general aviation aircraft. One of the keys to increasing growth in current air taxi operations or in enabling a new on-demand air transportation system is to develop small aircraft that can fly efficiently at speeds of 150 mph or greater, which may be enabled by utilizing distributed, electric propulsion.

1.1.2 Integrated, Distributed Propulsion and Distributed Electric Propulsion

It has long been known that close integration of the propulsion system and airframe could bring beneficial effects such as aerodynamic/propulsion efficiency increases [32] or reduced landing or takeoff field lengths [33]. Due the potential benefits of propulsion system-airframe integration, a NASA Langley Aeronautics Technical Committee

in 1998 recommended that "all future systems studies in aeronautics consider the application of [synergistic airframe-propulsion interaction and integration] technologies" [34]. The concept of propulsion-airframe integration to reduce aircraft fuel burn and noise and to achieve shorter takeoffs and landings has gained popularity in recent years; many studies have shown significant benefits of synergistic airframe-propulsion design [35, 36, 37, 38, 39, 40]. The aircraft concepts in these studies achieve this synergy through distributed propulsion, which Kim defines as "the spanwise distribution of the propulsive thrust stream such that overall vehicle benefits in terms of aerodynamic, propulsive, structural, and/or other efficiencies are mutually maximized to enhance the vehicle mission" [6].

Despite the fact that Kim's definition of distributed propulsion is restricted to a spanwise distribution of thrust, full synergistic airframe-propulsion integration can be accomplished from distribution of thrust all over the aircraft including the spanwise, longitudinal, and vertical directions. This full distribution of thrust can also enable completely new vehicle capabilities. For example, the NASA Greased Lightning concept distributes propellers spanwise and longitudinally by placing propellers along the leading edges of the wing and horizontal tail. Coupled with a tilting-wing and tilting-tail, this concept can achieve vertical takeoff and landing (VTOL) capability [41]. One could also employ distributed propulsion to either directly or indirectly provide control. Much larger control forces than are possible with conventional control surfaces at low speeds can be created through vectored thrust and/or the blowing of conventional control surfaces [12]. These examples are provided not as an exhaustive list, but as an indication that distributed propulsion can encompass more than simply a spanwise distribution of thrust.

Although the idea of distributed propulsion is far from new—Gohardani et al. cite distributed propulsion concepts dating back to the 1920s [42]—very few aircraft have

incorporated distributed propulsion with synergistic airframe-propulsion system integration. The lack of many aircraft flying today with distributed propulsion is at least in part due to the complexity of analyzing, testing, and designing systems where the propulsion system is tightly coupled with the airframe. It is much simpler to design systems where the performance can be cleanly divided into separate disciplines (e.g., aerodynamics, propulsion, control, and so forth). Furthermore, there are substantial weight, efficiency, maintainability, and cost penalties involved in distributing many smaller conventional engines or distributing power from one or a small number of larger engines.

Many of the more recent distributed propulsion concepts such as NASA's N3-X [40] are exploring the use of electric motors to achieve distributed propulsion to circumvent the weight, efficiency, and complexity issues that arise in systems based on distributing multiple smaller engines. Such concepts utilize what has been termed distributed electric propulsion (DEP) because the propulsion system distribution is enabled through the use of electric motors. In addition to enabling the distribution of propulsion, the scale-invariant nature and other beneficial characteristics of electric motors described above provide entirely new degrees of freedom to aircraft designers.

Because many of the DEP concepts proposed recently have been related to transport category aircraft, superconducting electric generator, motor, and transmission technologies or other high-power electric distribution and motor technologies must still be developed for concepts of this type to become feasible. In contrast, electric transmission, storage, and motor technologies for use on smaller aircraft and UAVs currently exist or are likely to be produced in the near term, as was demonstrated at the 2011 Green Flight Challenge. Furthermore, many important lessons can be learned by first employing distributed propulsion technologies on small aircraft. These aircraft can be utilized as test beds where operational data of distributed propulsion technologies can be gathered to form a basis for certifying these technologies on larger,

transport category aircraft in the future.[4]

1.1.3 Past NASA Distributed Electric Propulsion Research

NASA has been investigating the potential benefits of incorporating electric motors onto small aircraft for the past several years. One of the first NASA concepts to employ a pure-electric propulsion system was the Puffin, which was designed for personal, on-demand transportation [43]. The Puffin was inspired by the Vought V-173 (also known as the "Zimmer Skimmer" or the "Flying Pancake") and its follow-on the Vought XF5U-1 [44, 45]. Electric motors were included in the Puffin to overcome some of the complex mechanical linkages (including a gearbox and long propeller shafts) in the original Vought designs. Additionally, electric motors enabled full propulsion system redundancy, variable RPM operation with minimal efficiency losses, phase synchronization between propellers, and a solid-state cyclic control solution [46].[5]

Another later NASA study focused on how electric motors may enable highly efficient VTOL vehicles [41]. At least five different concepts were evaluated, and each of these concepts relied on distributing the propulsion over the aircraft. Of particular importance for VTOL aircraft is a propulsive distribution in the longitudinal direction. Work has continued on one of these concepts, the Greased Lightning, and a sub-scale prototype of the aircraft, the GL-10, has had successful test flights [47]. The GL-10 test flights help demonstrate the advantages of having propellers placed in

[4] Airbus is utilizing this strategy with its all-electric E-Fan concept, which they are using as a testbed to learn about integrating electric aircraft components onto aircraft that will aid them in producing larger electric or hybrid-electric airliners in the future [24].

[5] Although one could argue that the Puffin did not utilize true distributed electric propulsion since it placed propellers at only two locations, it could be argued that Kim's definition of distributed propulsion (quoted above) holds because there was a (limited) "spanwise distribution of the propulsive thrust stream" to counteract wing tip vortex drag. Furthermore, the Puffin had multiple separate electric motors driving each propeller shaft, which is a distribution of power if not a distribution of thrust. Regardless, the Puffin was one of the first all-electric NASA concepts, and it provided a foundation upon which Moore et al. would build to develop other indisputably *distributed* electric propulsion concepts.

front of the leading edge of the wing; specifically, during flight at low forward speeds and transition from hover to forward flight, the propellers induce a velocity over the wing, which noticeably augments lift, reduces buffeting, and helps maintain control surface effectiveness [48].

Other electric aircraft concepts were developed as a part of a study into a specific potential on-demand transportation system called "Zip Aviation" [16, 49]. Three separate concepts—the e-SWIFT, eV-Twin, and e-ATLIT—were developed as a part of this study [49]. The eV-Twin and e-SWIFT concepts were variants of other existing concepts and the lessons learned from these two concepts along with other technologies were applied to the e-ATLIT. The e-ATLIT, which derives its name from a 1970s concept testing full-span Fowler flaps known as the Advanced Technology Light Twin-Engine (ATLIT) aircraft [50, 51], utilized two propellers at the wingtips and 12 other propellers distributed over the entire wingspan upstream of the wing. By coupling these propellers in front of the wing with full-span flaps, the induced velocities from the propellers would increase wing lift so that at low speeds lift coefficients on the order of five could be achieved. This high-lift system would enable the wing loading of the four-passenger aircraft to be increased by a factor of approximately three to levels equivalent to a regional jet while still maintaining adequate lift at low speeds. The e-ATLIT concept also utilized propeller disks that overlapped in the spanwise direction with phase synchronization and slight longitudinal offset to enable the propellers to blow as much span as possible while helping avoid blade strikes and undesirable acoustic interactions [49].

A revised version of the e-ATLIT was proposed approximately a year later by Moore and Fredericks termed the Leading Edge Asynchronous Propellers Technology (LEAPTech) aircraft [12]. This DEP concept consisted of ten propellers distributed upstream of the wing and two wingtip propellers downstream of the wing. Like the e-ATLIT, this concept utilizes the upstream propellers to increase the dynamic

pressure over the wing. However, borrowing from the Greased Lightning concept, the LEAPTech design also included a variable incidence wing to achieve both high lift and high drag for short landing distances.

Perhaps the most novel aspect of the LEAPTech design relates to the operation of the propellers. Moore and Fredericks proposed that if these propellers were operated at slightly different rotational speeds (i.e., asynchronous RPMs), the acoustics of the aircraft could be improved. By having the blades pass in front of the wing with different frequencies, the strong harmonics associated with blade passage frequency could be reduced by a factor of 12, which offers the potential to greatly reduce the annoyance of the noise generated from such a concept. Another notable change from the e-ATLIT concept related to acoustics is that the propellers in the LEAPTech concept do not overlap. Although this will leave sections of the wing unblown as the slipstream aft of the propellers contract, the inflow to the propellers will be cleaner and there is a lower probability of direct interaction of the tip vortices of adjacent propellers, which should help reduce the noise [12]. Auralizations—i.e., simulations of the anticipated sounds—of the propellers from a DEP concept with LEAPTech have been performed by NASA researchers [52]. Their work indicates that through the asynchronous propeller operation of a LEAPTech concept, the peak sound level can be reduced relative to a single, conventional GA propeller at the same power setting by approximately 11 decibels.

1.1.4 Potential Benefits of Distributed Electric Propulsion for Small Aircraft

The studies cited above all indicate that the potential exists to greatly increase the efficiency and/or utility of aircraft by employing DEP. However, one must understand the major problems that currently limit the efficiency of small aircraft before the impacts of DEP can be appreciated. In this section the major impediments to increasing the cruise efficiency of small aircraft are described. Then, several potential

DEP integration schemes are discussed that can help overcome the current limitations and improve small aircraft cruise efficiency.

1.1.4.1 Primary Causes of Small Aircraft Cruise Inefficiency

The potential efficiency of small aircraft is currently reduced by the requirement to attain acceptably low stall and approach speeds. These stall and approach speed requirements have traditionally led to aircraft with lower than optimal wing loadings for cruise flight at "moderate" to "high" speeds, which negatively impacts vehicle aerodynamics and ride quality. This result is demonstrated in Figure 4, which shows the sensitivity of an aircraft's stall speed and cruise lift-to-drag ratio to wing loading.

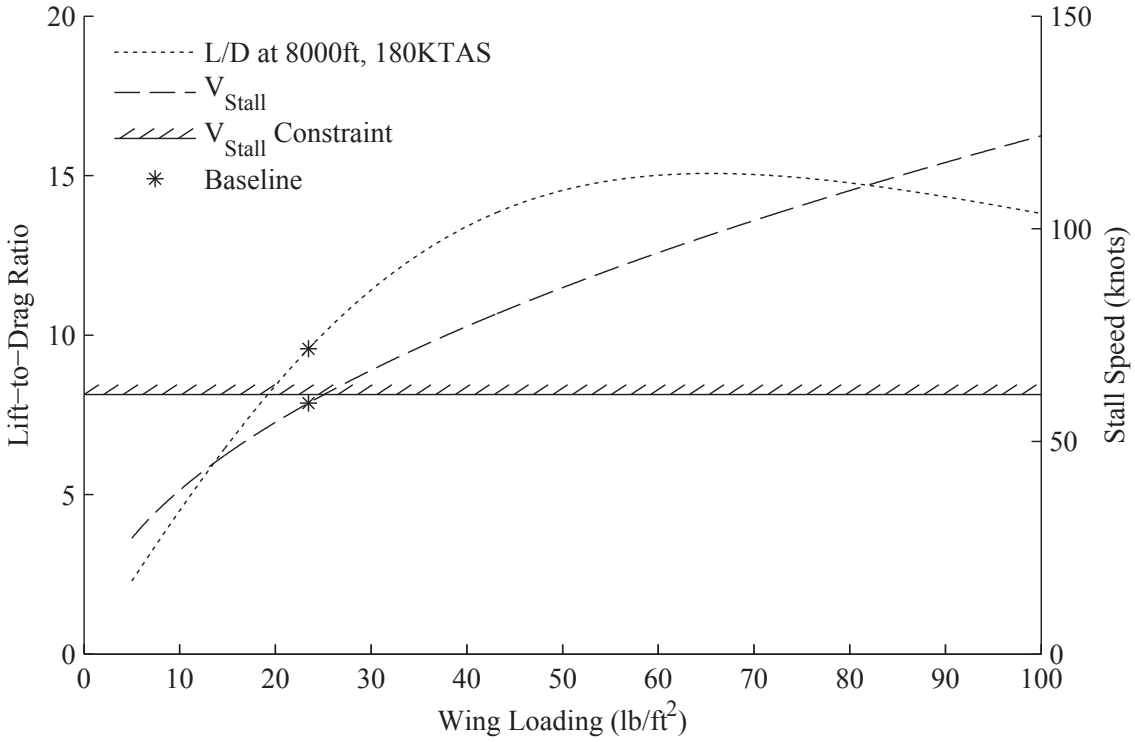

Figure 4: Sensitivity of stall speed and lift-to-drag ratio to wing loading for a fixed $C_{L_{\max}}$

Figure 4 was generated assuming a constant maximum lift coefficient of 2, cruise

flight at lift equals weight at 8000 ft with a 180 knot speed, and a constant, two-parameter drag polar of the form $C_D = C_{D0} + C_L^2/(\pi e_0 AR)$ with $C_{D0} = 0.0252$, $AR = 10.26$, and $e_0 = 0.71$.[6] The drag polar and maximum lift coefficient were selected to be similar to that of the Cirrus SR-22, which is representative of current GA aircraft technologies; furthermore, the 180 knot, 8000 ft cruise condition is often quoted by Cirrus in marketing the SR-22 and represents a typical cruise condition for GA aircraft. Movement along the L/D curve in the figure represents changing the C_L at a fixed altitude and velocity. The asterisks in the figure mark the baseline stall speed and "high-speed" cruise (180 knots at 8,000 ft) L/D for the SR-22. The hatched line represents the 61 knot stall speed requirement set forth in part 23 of the Federal Aviation Regulations (FARs) for small, single-engine aircraft [53].

As can be seen in Figure 4, the stall speed continually increases with wing loading while the lift-to-drag ratio initially increases, but then begins to decrease after reaching a maximum. Ideally the aircraft would cruise at or near the point of maximum L/D, which would be possible if the wing loading were 65 lb/ft^2. However, in order to satisfy the FAR stall speed constraint, the wing loading must be less than 25 lb/ft^2. At this wing loading, the L/D at the high speed cruise condition is 10.1, which is 33% lower than the L/D attainable at a wing loading of 65 lb/ft^2. The actual SR-22 has a stall speed 2 knots slower than required by regulation, which results in a cruise

[6] In reality the drag polar will vary with wing loading for an aircraft with a fixed fuselage wetted area. Although one may assume that these changes would increase the lift-to-drag ratio, there are many competing effects that occur. As the wing loading increases the skin friction drag of the wing will decrease (since the wing size will decrease), but the profile drag of the wing will likely increase due to the need to operate a higher lift-coefficients. The sizes of the vertical and horizontal tails may also change with changing wing sizes. (If constant tail volume coefficients are maintained, the tail sizes will also decrease. These decreased sizes will have the same general effects of reduced wing size. However, tail volume coefficients are often inadequate for capturing the true effects that size tails.) Furthermore, if the same wing aspect ratio is maintained as the wing loading increases, the wing weight may have to increase to provide sufficient structural strength. To avoid increases in weight, the span may need to be decreased, which will generally act to increase the induced drag. The precise impacts of all of these conditions are very application specific; consequently, these effects are neglected here in order to demonstrate the general trends that will occur with variations in wing loading.

L/D 36% lower than the maximum L/D.

To view the problem in another manner, the maximum lift coefficient of an aircraft effectively determines the cruise lift-to-drag ratio. If a drag polar is assumed, the lift-to-drag ratio over a range of speeds at a desired cruise altitude can be determined directly from the wing loading (because the lift coefficient for level flight is set by the vehicle speed and the wing loading). Furthermore, the wing loading can be determined from a desired stall speed and the maximum lift coefficient of the aircraft as shown in Eq. 1, where the density, ρ, should correspond to the altitude at which the desired stall speed, V_{stall}, is defined. (Typically stall speeds are specified for sea level conditions.)

$$(W/S)_{\text{required}} = \frac{1}{2}\rho V_{\text{stall}}^2 C_{L_{\max}} \tag{1}$$

For the example SR-22-like aircraft drag polar presented above and a 61-knot sea level stall speed, the variation of the lift-to-drag ratio with velocity at 8000 ft for four values of the maximum lift coefficient ranging from 1.5 to 5 is shown in Figure 5.[7]

There are two major observations that can be made from Figure 5. First, as the maximum lift coefficient is increased, the velocity at which the maximum lift-to-drag ratio occurs also increases. If higher-speed cruise flight is desired, then higher maximum lift coefficients are advantageous. Second, as the maximum lift coefficient increases there is a wider range of velocities at which the aircraft can operate with high L/D, which increases the flexibility of the aircraft. Said differently, there is a smaller efficiency penalty to be paid when operating at speeds relatively near, but not equal to the speed for maximum L/D if the $C_{L_{\max}}$ is higher.

Since many small aircraft typically have maximum lift coefficients of approximately 2 or less, their maximum aerodynamic efficiency occurs at relatively low speeds; however, these aircraft are very often operated at higher speeds in practice

[7]As mentioned above, this analysis neglects the effects in the variation of the drag polar with wing loading. Also, the assumption of a constant two-parameter drag polar causes the maximum lift-to-drag ratio to be the same regardless of the maximum lift coefficient.

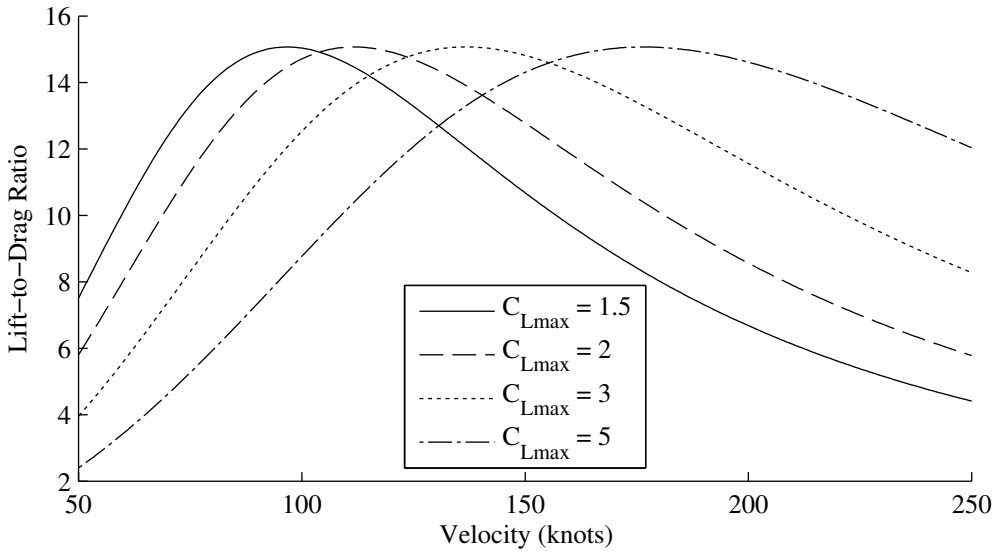

Figure 5: Variation of cruise lift-to-drag ratio with velocity for a 61-knot sea level stall speed and four $C_{L_{\max}}$ values

so the efficiency of the aircraft is not maximized. For the aircraft with a maximum lift coefficient of 2 in Figure 5 (which is similar to the SR-22), the peak L/D occurs at approximately 112 knots, and there is a reduction in L/D of approximately 33% when operating at the high-speed cruise point of 180 knots. If the maximum lift coefficient of this aircraft could be increased to near 5, then maximum efficiency could be obtained at the desired operating point. Additionally, for the aircraft with a $C_{L_{\max}}$ of 2, there is a drop in L/D of approximately 17% when operating 40 knots faster than the speed for maximum L/D; for the same 40 knot increase in speed over maximum L/D for the aircraft with $C_{L_{\max}}$ of 5, there is only a decrease of approximately 8% in L/D. It is clearly advantageous from a high-speed cruise efficiency standpoint to achieve very high maximum lift coefficients. Not only is speed for maximum L/D better matched to desired cruise speeds, but there is also a wider speed range where the aircraft can fly more efficiently.

1.1.4.2 *Potential Applications of Distributed Electric Propulsion to Increase Cruise Efficiency*

There are many potential mechanisms through which DEP can help increase the cruise efficiency of small aircraft. Although the possibilities are likely only limited by the imagination of designers, there are four main means through which the previously-cited concepts seek to improve efficiency:

- increasing the dynamic pressure over the wing above freestream during approach to allow for increased design wing loading,
- offsetting vehicle weight with propeller thrust,
- placing propulsors in the wake of aircraft components, and
- installing propellers at the wingtips to reduce induced drag or increase propulsive efficiency.

Each of these techniques will be briefly described in this section.

The primary mechanism through which the e-ATLIT [49] and LEAPTech [12] concepts achieve high maximum lift coefficients is through increasing the dynamic pressure over a wing compared to the freestream during takeoff and landing. The distributed propellers upstream of the wing each increase the flow velocity aft of the propeller. Because the wing sections in the propeller slipstreams experience an increase in flow velocity, the lift on these sections increases, which makes the wing more effective at low speeds. If the amount of propeller blowing can be tailored, then a "cruise-sized" wing that achieves its maximum efficiency at the desired cruise point can be designed. (For example, in Figure 4, the wing loading could be set to 65 lb/ft^2, which maximizes L/D for the desired cruise condition.) However, even if a true cruise-sized wing is not feasible, the wing loading can still be increased compared to the case with no propeller blowing so that the cruise aerodynamic efficiency is still increased. (For example, in Figure 4, if the wing loading can only be increased from 25 lb/ft^2 to 50 lb/ft^2, the L/D can still be increased.)

Utilizing propellers upstream of the wing to increase lift is not a new concept. There was interest in utilizing propeller blowing to help enable vertical or short takeoff and landing (V/STOL) aircraft in the 1950s, and wind tunnel testing of wing-propeller combinations for use in V/STOL aircraft were performed [54, 55, 56]. Generally, these studies indicated that the propeller slipstream could increase the maximum lift coefficient, increase the angle of attack where $C_{L_{\max}}$ occurred, and diminish the loss of lift at angles of attack above stall. For a specific configuration (i.e., a semi-span wing model with no flaps and two large diameter propellers that overlapped slightly while covering most of the wingspan), lift coefficients of over 14 were obtained at freestream speeds of approximately 26 knots. At speeds of approximately 35 knots, C_L values of more than 4.5 were observed [56]. This wind tunnel testing did not bound the potential lift that could be augmented via upstream propellers; rather, it indicates that significant increases in lift—much greater than possible from conventional high-lift devices—can be obtained by blowing the wing with propeller slipstreams.[8]

Other of the concepts discussed above including the Greased Lightning [41] and the LEAPTech [12] rely on thrust from propellers to directly offset some or all of the weight of the aircraft. For a conventional takeoff and landing aircraft with vertical thrust, the wing loading can be increased because the wing is no longer required to lift the full weight of the vehicle. In this case, the stall speed can be expressed as Eq. 2 (assuming no interaction of the propeller slipstream with the wing), where T_v represents the vertical component of the total thrust and level flight is assumed.

$$V_{\text{stall}} = \sqrt{\frac{2\left(W/S - T_v/S\right)}{\rho C_{L_{\max}}}} \tag{2}$$

[8]Specifically for these tests, Kuhn and Draper maintained a nearly constant dynamic pressure in the propeller slipstream regardless of freestream speed [56]. If even greater slipstream velocities were generated, lift could be increased. Similarly, utilizing high-lift devices on the wing could further increase the maximum C_L.

This equation can be rearranged into the form of Eq. 3, which indicates the required wing loading for a specified stall speed.

$$W/S = 0.5\rho V_{\text{stall}}^2 C_{L_{\max}} + T_v/S \tag{3}$$

As Eq. 3 indicates, the wing loading for a set stall speed can be increased directly by increasing the vertical component of thrust. With electric propulsion, this vertical thrust could be created using dedicated vertical rotors, a variable incidence or tilting wing, or by installing electric motors on tilting installations that can be adjusted to provide different levels of vertical thrust.

The compact size of electric motors also provides the potential to locate propulsors in the wake of a body (e.g., the fuselage) where they can ingest flow with decreased momentum compared to the freestream. This lower-speed flow can then be accelerated by a propulsor to create thrust at a higher efficiency than if the propulsor were ingesting and accelerating the freestream flow. Smith has shown that efficiency improvements on the order of 20% are possible for such propulsion systems [32]. Many of the more novel recent distributed propulsion concepts cited above [35, 36, 37, 39, 40] have utilized wake ingestion to increase the efficiency of the configuration. Additionally, wake ingested propulsion can even provide noticeable improvements on conventional configurations as indicated by a recent NASA study that showed a 7-12% reduction in fuel burn (depending on the mission) for a 737-like configuration utilizing an electric fan mounted at the rear of the fuselage [57].

Another method by which distributed propeller-wing systems may increase the efficiency of small aircraft concepts is by placing propellers at the wing tips. Previous wind tunnel testing [58, 59, 60] as well as analytical and computational modeling [61] have indicated that substantial performance benefits may result from using wingtip mounted propellers. By placing the propellers in front of the wings at the tips, the rotation of the propellers can be used to counteract the effects of the wingtip vorticies to effectively push these vortices farther outboard, which can reduce the induced drag

of the configuration [58]. Alternatively, if the propeller is placed aft of the wingtip, the propeller can recover some of the tangential velocity (i.e., swirl) induced by the wingtip vortex and thus operate with an increased efficiency [60]. Although placing propellers at the wingtips does not directly counteract the low wing loadings required for meeting stall speed constraints, it nonetheless has the potential to increase the cruise efficiency of the configuration.

The potential also exists to use propellers and electric motors at the wingtips as turbines to extract energy from the tip vortices. Flight testing has demonstrated that it is possible at certain flight conditions to extract this energy using tip turbines [62]. Furthermore, since electric motors can also be operated in "reverse" as generators to extract power, no additional mass would be required to enable some battery recharge capability. If variable pitch propellers were installed, it may be possible to extract energy when descending with the propeller operating as a turbine and gain cruise efficiency benefits when operating the propeller to generate thrust.

One may object that if these four techniques (i.e., increasing the dynamic pressure over wing, offsetting vehicle weight with propeller thrust, ingesting the wake of aircraft components for propulsion, and installing wingtip propellers) can enable large performance benefits then current aircraft would employ such strategies. The reasons for not utilizing such systems stems largely from the characteristics of conventional engines—i.e., it is simply impractical to distribute many conventional engines due to their size and weight. Miranda and Brennan note that there are design considerations such as asymmetric thrust or structural implications that may preclude the practical use of wingtip mounted systems in particular [61]. However, by utilizing distributed electric motors, many of these practical design considerations may no longer be barriers to implementing wingtip mounted propellers or any of the other techniques.

If any or all of these techniques can be implemented in practice, practical electric aircraft may become feasible in the near-term even without great advances in energy

storage (e.g., battery) technologies. If energy storage technologies are also improved, even more missions than those discussed above in Section 1.1.1.1 could be flown. Ultimately, research is still required to determine if DEP does truly enable these new integration schemes and to quantify the full system-level benefits.

1.2 NASA's SCEPTOR Project

NASA is currently investigating the application of DEP technologies to small aircraft including the full aircraft system-level impacts of DEP in a project called Scalable Convergent Electric Propulsion Technology Operations Research (SCEPTOR). This project builds upon past NASA research discussed above in Section 1.1.3, and it developed out of a team seedling project to test the high-lift capability of the leading edge propellers and large-span flaps of the LEAPTech concept [63]. The main goal of the SCEPTOR project is to demonstrate a decrease in cruise energy consumption of 5.0 times (with a minimum threshold of at least 3.5 times) compared to a conventional aircraft with a full-scale, manned, flight demonstrator aircraft. The SCEPTOR project will serve as an example throughout this document.

1.2.1 Project Background

The SCEPTOR project evolved from the e-ATLIT and LEAPTech concepts proposed by Moore and Fredericks [49, 12]. Due to the promise of the LEAPTech concept, a team seedling project was awarded to test the high-lift capability of the distributed small diameter propellers [63]. For this testing, a new wing with a span of 31 ft and featuring 18 small diameter propellers upstream of the leading edge was designed. With the aid of two small companies, Empirical Systems Aerospace (ESAero) and Joby Aviation, NASA tested the wing on the Hybrid-Electric Integrated Systems Test (HEIST) truck-mounted rig [64]. These ground tests showed that the system could generate large amounts of lift at low speeds due to the induced velocities from the

propellers [63].

With the basic principle that small diameter propellers could provide high lift capability verified, the SCEPTOR project was formally launched to demonstrate that the same sort of DEP integration scheme could be installed on a functional, full-scale aircraft. This three-year, relatively small project is part of NASA Aeronautics Research Mission Directorate's new Transformative Aeronautics Concepts Program, which seeks to develop revolutionary concepts that may transform the aviation system [65]. Specifically, SCEPTOR is funded under the Convergent Aeronautics Solution Project, which funds projects to rapidly determine the feasibility of novel concepts. The project formally began in October of 2014 and continues through the time of publication of this document.

The SCEPTOR team selected the Tecnam P2006T aircraft [66] as a baseline, and will retrofit an existing P2006T with a new, smaller wing equipped with wingtip propellers and several propellers distributed upstream of the wing leading edge. The cruise efficiency goal will be assessed relative to the baseline Tecnam aircraft. Although the P2006T has a maximum speed of 155 knots and typically cruises at speeds between 130 and 140 knots [66, 67], the SCEPTOR team plans to demonstrate that a cruise efficiency of at least 3.5 times the baseline P2006T is possible even at a higher cruise speed of 150 knots.

1.2.2 Distributed Electric Propulsion System

The particular DEP integration scheme selected for the SCEPTOR aircraft is based on the LEAPTech concept, and includes two different types of propellers: wingtip propellers and propellers distributed upstream of the wing leading edge.

The purpose of the propellers distributed upstream of the wing is to increase the dynamic pressure over the wing at low speeds to augment lift. At higher speeds, these propellers will be passively folded and stowed flush to the nacelles. Since the purpose

of these propellers is the same as conventional high-lift devices such as flaps, Borer has termed these upstream propellers "high-lift propellers" [68, 69]. This nomenclature is adopted in this thesis.

It should be noted that the function of these high-lift propellers—i.e., increasing the flow velocity over the entire wing—differs from upper-surface blowing where only the upper surface of the wing is blown. To effectively only blow a large portion of the upper surface, a larger number of overlapping propellers would be required to avoid large "dead zones" between the props. Overlapping propellers are likely to increase the acoustic signature of the configuration since the trailing vortex systems from upstream propellers would be intersecting with the blades and vortex systems of downstream props. Additionally, upper-surface blowing effects are often very configuration-dependent and are most effective when there is a very large mass flow rate and velocity in the "jet" [70]. Large jet velocities also lead to undesirable increases in noise. Upper-surface blowing also generally creates increased aft-loading over a wing, which can reduce the aircraft's stability. This aft-loading can also effectively mandate larger horizontal tails be installed, which increases the drag of the configuration. Finally, the effects of upper-surface blowing are less robust to changes in vehicle operating conditions (e.g., angle of attack). It will be shown later in Chapter III that at some angles of attack the lift can be dramatically increased via upper-surface blowing, but in other situations the flow departs from the airfoil's surface and lift benefits are lost.

The wingtip propellers will provide all the thrust required for the aircraft at cruise and all other phases of flight where the high-lift propellers are not required for lift augmentation. By placing these "cruise propellers" at the wingtips and rotating them counter to the wingtip vortices, these propellers will decrease the induced drag of the configuration [58, 59, 61].

A notional layout for the flight demonstrator aircraft with a wing based on the

article used in ground tests of the LEAPTech configuration on the HEIST rig is shown in Figure 6. Figure 6(a) shows the configuration at a low speed when all 18 of the high-lift propellers and both wingtip propellers are operating, and Figure 6(b) shows the configuration in higher-speed flight when the high-lift propellers are stowed and only the tip propellers are operating. It is important to note that the number and design of the propellers for the final flight demonstrator are still not finalized; Figure 6 is provided only to help the reader visualize the general operational concept. The tools and methods developed as a part of this thesis will contribute to the actual layout of the final SCEPTOR configuration.

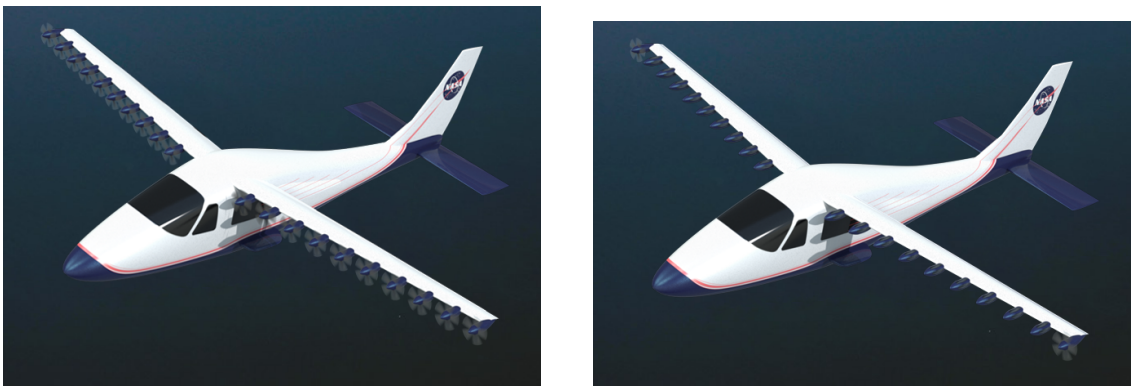

(a) Low-speed propeller configuration (b) Higher-speed propeller configuration

Figure 6: Early notional layout for the NASA SCEPTOR flight demonstrator

All the propellers will be driven by electric motors, and energy will be stored in batteries. Since the SCEPTOR aircraft is a retrofit of an existing airframe, it will not be sized for a particular mission. Instead, the aircraft will be filled with as many batteries as possible to maintain an acceptable takeoff weight. This approach will lead to an aircraft with a shorter range than possible with a new "clean-sheet" design; however, it will enable the team to directly compare the energy consumption of both the baseline Tecnam P2006T aircraft and the SCEPTOR flight demonstrator to determine if the five times reduction in cruise energy consumption goal can be met.

1.2.3 Research Challenges

Despite reducing the risk in the project by retrofitting an existing aircraft as opposed to creating a full clean-sheet design, there are many challenges in designing, manufacturing, and testing of the SCEPTOR aircraft. These challenges include (but are not limited to):

- Designing a new wing (including airfoils, planform shape, and twist) while considering the impacts of wingtip and high-lift propellers
- High-lift propeller system design including the number and placement of the propellers relative to the wing as well as the designs of the propeller blades
- Wingtip (cruise) propeller design including considerations of interactions with the wingtip vortices
- Stability and control, including single wingtip motor out situations in which large yawing moments will be created
- Structural design including how the new wing can be mounted to an existing fuselage with set attach points for a different, larger wing
- Aeroelastic concerns associated with many distributed masses along the wingspan that may be cantilevered ahead of the wing and the unsteady loadings the high-lift propeller slipstreams create over the wing
- Power system architecture for powering many distributed propellers along the entire span of the wing while avoiding issues with electromagnetic interference and limiting/eliminating single points of failure
- Electric motor design and the design of the required cooling systems for the cruise (wingtip) propellers and the high-lift propellers as well as the associated controllers
- Packaging the desired instrumentation for research measurements and safety systems into a new, smaller wing

The SCEPTOR team is addressing each of these challenges (and others) in the project as they progress toward flight testing of the flight demonstrator.

1.3 Scope and Organization of this Thesis

Although there are many potential benefits of distributed electric propulsion, this thesis will focus only on how high-lift propeller systems can be designed, how the presence of a high-lift propeller system impacts the performance of the aircraft, and how the high-lift propeller system fits into and influences the wing design process. The author is unaware of any concepts outside of the SCEPTOR configuration (and its predecessors) equipped with high-lift propellers. Although propellers have certainly been studied as a means of augmenting lift in the past, previous studies have focused on the propellers primarily as a thrust-producing device with a secondary purpose of augmenting lift (e.g., the work of Kuhn and Draper [56] or Gentry et al. [71]). The work in this thesis breaks from this conventional mode of thinking and explores the implications of propellers acting primarily as a form of high-lift device. Novel problems such as landing with high thrust arise with this new viewpoint, and these problems impact the wing design and aircraft operation.

1.3.1 Contributions

The primary contributions of this thesis are as follows:

1. Development of a model that estimates the lift augmentation from high-lift propellers. The model was developed from considerations of thin wing theory and the impacts of propeller slipstreams on dynamic pressure and circulation and was calibrated with computational fluid dynamics results. This model is capable of providing intuition to a designer about the impacts of various propeller installation angles, diameters, and installation locations relative to the wing.

2. Development of a novel method to design high-lift propellers based on blade element momentum theory with a systematic procedure to specify induction factor distributions. This design method was shown to reduce the required propeller power by approximately 15% relative to conventional minimum induced loss design methods in addition to providing other performance benefits.
3. Identification of implied requirements and potential regulatory changes required for aircraft with high-lift propellers. In particular, multiple plausible operating schedules (i.e., propeller torque and aircraft angle of attack) for approach and landing were proposed and evaluated with respect to current FAA requirements for landing reference speed margin.
4. Identification of the appropriate sizing conditions for high-lift propeller systems based on the desired low-speed operation of the aircraft.
5. Demonstration of how the models and methods developed in this dissertation enable the exploration of the vast design space and many tradeoffs that exists in designing high-lift propeller systems.

1.3.2 Outline

Each of the following chapters in this document begins with one or multiple motivation questions that are addressed throughout the chapter. The general content of the remaining chapters and their associated motivating questions are as follows:

- Chapter II addresses the motivating questions:

  How do high-lift propellers increase the lift over downstream wings?

  and

  What methods exist to model high-lift propellers and their interaction with downstream wings?

  This chapter provides an overview of existing analysis and design methods for

wings and propellers and discusses the general aerodynamic interaction of propellers and downstream wings.

- Chapter III explores the motivating question:

  How can the lift augmentation from high-lift propellers be rapidly assessed to facilitate conceptual design?

  This chapter describes a simple theory for predicting the lift augmentation of high-lift propellers that will be used in the design studies performed in subsequent chapters.

- Chapter IV is motivated by the question:

  Since the purpose of high-lift propellers differs from traditional propellers, should high-lift propellers be designed differently, and if so, how?

  This chapter presents a novel method to design effective high-lift propellers.

- Chapter V begins by asking:

  What is the appropriate design point for high-lift propellers?

  This chapter discusses the interdependence of the design point selection with regulations and vehicle operation. The implications of the desired vehicle operation are also explored.

- Chapter VI addresses the motivating question:

  How can the appropriate number of high-lift propellers be determined?

  This chapter describes trade studies that can be performed to select the appropriate number of high-lift propellers for a given wing design and discusses how the design of high-lift propeller systems can be tied into a wing design process.

- Chapter VII presents conclusions, summarizes the contributions of this thesis, and discusses possible avenues for future work.

CHAPTER II

TRADITIONAL PROPELLER ANALYSIS AND DESIGN METHODS AND PROPELLER-WING INTERACTION

The discussion in this chapter seeks to answer the following questions:

How do high-lift propellers increase the lift over downstream wings?

and

What methods exist to model high-lift propellers and their interaction with downstream wings?

To help answer these questions, an overview of aerodynamic analysis methods for wings and propellers is presented in this chapter. The general characteristics of flow in propeller slipstreams as well as the physical principles involved in propeller-wing interaction are discussed. Modeling techniques to account for the interaction of wings and propellers are reviewed with particular attention focused to those methods suitable for early-phase design.

2.1 A Brief Overview of General Aerodynamic Modeling Techniques for Lifting Surfaces

Aerodynamic analysis methods including lifting line methods, lifting surface methods (e.g., the vortex lattice method), and computational fluid dynamics (CFD)[1] are well-established and have been used extensively in wing and propeller design and analysis.

[1]When referring to CFD in this document, a narrow definition of the term is implied. CFD is used here to refer to computational algorithms that solve either the Euler or Navier-Stokes equations.

Different methods are applicable to different stages of the design process, with lower-order methods generally being preferred for early phases when only limited geometric detail is available and fast analysis times are required to analyze many potential designs, and higher-order methods such as CFD preferred for later design phases when fewer configurations are of interest and greater geometric fidelity is available.[2]

Lifting line methods, pioneered by Prandtl [72], are potential flow-based methods that model a wing by placing a series of bound horseshoe vortices along a "lifting line." The horseshoe vortices define a vortex sheet that trails downstream of the lifting line. Variants of this class of methods (e.g., the Weissinger model [73]) enable the modeling of swept wings, but the approach is typically limited to higher aspect ratio wings. These low-order methods are typically lower fidelity, but can be executed very rapidly, which makes them suitable for conceptual design.

Lifting surface methods are an extension of lifting line methods that place a series of vortex lines in both the chordwise and spanwise directions. As with lifting line methods, these techniques are inviscid methods based on potential flow theory. Various implementations of lifting surface methods employ different singularity solutions to the potential equation [74]. The vortex lattice method, one of the most popular lifting surface techniques, places many horseshoe vortices on panels on the wing [75]. Traditional vortex lattice implementations neglect thickness and place the grid of horseshoe vortices over the mean camber line or chord line. Although these methods require more geometric information than lifting line methods, they are often still suitable for conceptual design studies.

CFD methods numerically solve the Euler or Navier-Stokes equations to determine the airflow around a body in a specified condition. If the full Navier-Stokes equations

[2]CFD or other higher-order methods may still be preferred in early-phase design if lower-order methods are known to provide inaccurate results or if new technologies are being studied for which no lower-order methods can adequately capture the physics.

are solved, CFD predicts viscous effects; if viscous effects are neglected, the complexity of the equations is reduced and the resulting equations are known as the Euler equations. For the purposes of conceptual design, including the studies that are the focus of the present work, the requirements for detailed geometric information and the high computational cost of CFD often preclude it from being a useful method.

2.2 Propeller Analysis and Design Methods

All of the previously mentioned methods can be applied to predict propeller aerodynamics because a propeller can be viewed as a rotating, twisted wing. However, certain additional analysis methods including momentum (or actuator disk) theory, blade element theory and blade element momentum theory (BEMT), and vortex theory are relevant for early-phase modeling of propeller performance. Most propeller analysis and design techniques are based on these theories, which are described below.

2.2.1 Momentum Theory

Momentum theory, also called actuator disk theory, is one of the oldest and most simple propeller analysis techniques. It was pioneered by Rankine [76] and Froude [77] in the late 1800s and is still widely used today for its simplicity and depth of insight. There are many sources that describe the theory, but the reader is referred to McCormick [78]. An overview will be presented here since the basic principles of the theory will be referenced later in this dissertation. The theory has been extended and applied in many ways, but "classical" momentum theory is sufficient for the purposes of the present discussion.

Consider a propeller disk of area A shown in the center of Figure 7 producing a thrust, T. The discussion here assumes that the thrust is distributed uniformly over the entire disk, which implies that the prop has an infinite number of blades. It is also assumed that the disk only accelerates the flow in the axial direction (i.e., there

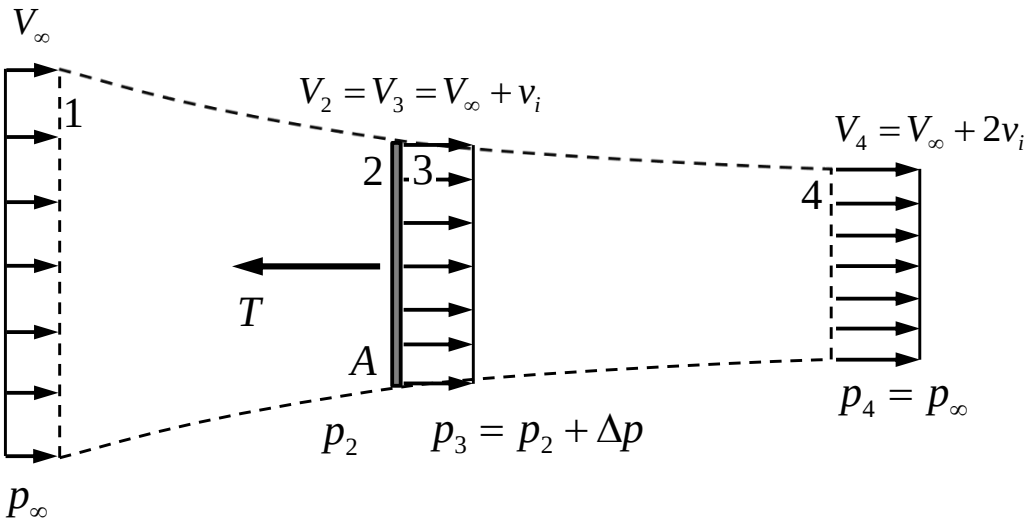

Figure 7: Streamtube passing through a propeller

is no swirl added to the flow).

For analysis, the flow is separated into four discrete stations: 1) infinitely far upstream, 2) just upstream of the propeller, 3) just aft of the disk, and 4) infinitely far downstream. The flow is accelerated by the propeller gradually from the freestream far upstream to a maximum velocity infinitely far downstream by imparting a discontinuous static and total pressure jump of Δp across the disk. The static pressure at the first and last stations is constant, which implies that the static pressure decreases from station 1 to 2, experiences a step increase from stations 2 to 3, and then decreases in moving from station 3 to 4.

If incompressible flow is assumed, Bernoulli's equation can be applied to a streamline in the streamtube upstream of the disk as shown in Eq. 4 as well as downstream of the disk as shown in Eq. 5. Three substitutions have been made in Eq. 5: 1) the static pressure aft of the disk, p_3, has been written in terms of the pressure jump and static pressure upstream of the disk; 2) the velocity just aft of the disk, V_3, has been expressed as V_2 since the velocity is continually increasing from far upstream to far downstream (i.e., there is no discontinuous jump in velocity across the disk); and

3) the downstream static pressure, p_4, has been expressed as the freestream static pressure.

$$p_\infty + \frac{1}{2}\rho V_\infty^2 = p_2 + \frac{1}{2}\rho V_2^2 \tag{4}$$

$$p_\infty + \frac{1}{2}\rho V_4^2 = p_2 + \Delta p + \frac{1}{2}\rho V_2^2 \tag{5}$$

If a cylindrical control surface is drawn around the outside of the streamtube with its ends located at stations 1 and 4, the equations of continuity can be applied to determine the thrust on the propeller. Since the first and last stations are infinitely far upstream and downstream, the direction of the flow is parallel to the axis at these stations. Additionally, if the edges of the control surface are sufficiently far outside of the streamtube shown in Figure 7, then the streamlines at the edges are effectively parallel to the propeller axis and the flow has a velocity of V_∞ there. Because the velocity is increased inside the streamtube at station 4 and the static pressure is equivalent along the ends of the control surface, there must be an inflow through the side walls of the control surface to satisfy the continuity equations. The force on the control volume, which is produced by the propeller, can be determined as the momentum of the flow moving out of the control surface less the momentum flux into the surface. The resulting thrust can be expressed as Eq. 6, where R_4 is the radius of the streamtube at station 4 (infinitely far downstream).

$$T = \rho\pi R_4^2 V_4 \left(V_4 - V_\infty\right) \tag{6}$$

Note that the terms $\rho\pi R_4^2 V_4$ in Eq. 6 represent the mass flow rate through the streamtube at station 4. Because the mass flow rate through the entire streamtube is constant (by definition), Eq. 6 can also be written in terms of the mass flow rate passing through stations 2 and 3, as shown in Eq. 7.

$$T = \rho A V_2 \left(V_4 - V_\infty\right) \tag{7}$$

Eq. 7 states that the thrust on the propeller is equal to the mass flow rate through the propeller ($\dot{m} = \rho A V_2$) times the change in velocity of the flow (from far upstream to far downstream) imparted by the disk ($\Delta V = (V_4 - V_\infty)$), which can also be expressed as Eq. 8. This principle is incredibly helpful in building an intuition about how propellers produce thrust, and it will be referenced later in this document.

$$T = \dot{m}\Delta V \tag{8}$$

The thrust can also be expressed in terms of the static pressure acting on both sides of the propeller disk. Since there is a discontinuous jump in static pressure from one side of the disk to the other, the thrust can be written in terms of this pressure jump as Eq. 9.

$$T = A\Delta p \tag{9}$$

By combining Eqs. 4, 5, 7, and 9 the velocity at the disk can be found in terms of the far upstream and far downstream velocities as $V_2 = (V_\infty + V_4)/2$. Commonly, the velocity at the disk (i.e., V_2 or V_3) is expressed as $V_\infty + v_i$ where v_i is termed the "induced velocity." With this notation, the velocity far downstream can be written as $V_4 = V_\infty + 2v_i$, and the thrust of the disk can be expressed as Eq. 10.

$$T = \rho A (V + v_i)(2v_i) \tag{10}$$

The power required by the propeller can also be predicted from momentum theory, but this calculation will be lower than expected in practice because it does not include losses from profile drag or the trailing vortices. The power is calculated as the difference in the flux of kinetic energy of the fluid from upstream to downstream (i.e., the change in the mass flow rate times the velocity squared from upstream to downstream).

$$\begin{aligned} P &= \frac{1}{2}\rho A (V + v_i)\left[(V_\infty + 2v_i)^2 - V_\infty^2\right] \\ &= T(V + v_i) \end{aligned} \tag{11}$$

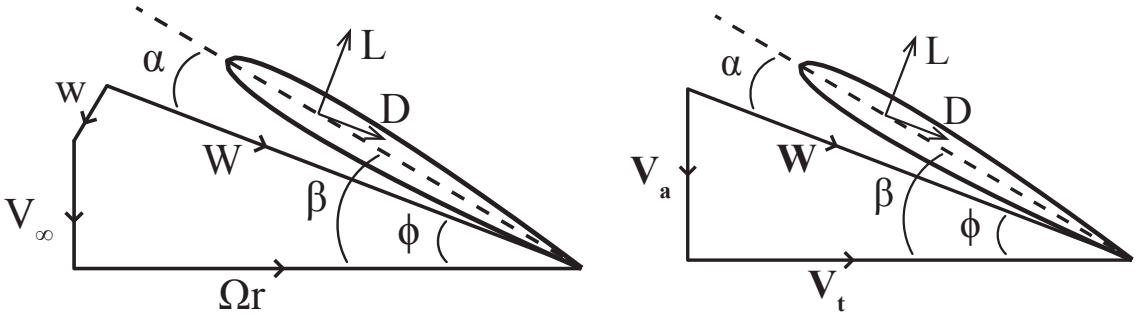

(a) Local velocities presented as rotational, translational, and induced velocities

(b) Local velocities resolved into axial and tangential components

Figure 8: Geometry of a local blade element showing the local forces

From this expression for the power, an efficiency can be found as the ratio of the flight power (i.e., useful power), TV_∞, to the power imparted to the flow by the propeller

$$\eta = \frac{TV_\infty}{P} = \frac{1}{1 + v_i/V_\infty} \tag{12}$$

One of the biggest limitations of momentum theory is that is does not consider the design of individual propeller blades. For some calculations, particularly in very early-phase design it is advantageous to develop performance estimates without needing to know details of a propeller blade design. However, if the propeller design is of interest, then momentum theory is inadequate.

2.2.2 Blade Element Momentum Theory

Blade element theory is commonly used to help overcome the limitation of momentum theory being unable to describe the detailed blade shapes of propellers. Much of the work in developing blade element theory was performed by Drzewiecki [79].[3] In blade element theory [78] the propeller blade is divided along its radial direction into an infinite number of differential "blade elements," which are effectively airfoils of infinitesimal span. A representation of a blade element is shown in Figure 8(a).

[3]Glauert [80] has an excellent overview of the historical background of this and all the classic propeller analysis theories.

The forces on each blade element can be determined from the airfoil section properties (i.e., c_l and c_d) taken at the local flow velocity, W, which includes components from the propeller's rotation, Ωr, and translation, V_∞, as well as those induced by the propeller and its wake, w, as shown in Figure 8(a). Specifically, the thrust from each blade section of width dr can be found as the component of the lift and drag parallel to V_∞ from the geometry in Figure 8(a) as Eq. 13, where B is the number of blades and c is the local chord length.

$$dT = Bc\frac{1}{2}\rho W^2 \left(c_l \cos\phi - c_d \sin\phi\right) \mathrm{d}r \tag{13}$$

Similarly, the torque—the moments of the forces along the direction of Ωr—on the blade element is found from Eq. 14.

$$dQ = Bc\frac{1}{2}\rho W^2 \left(c_l \sin\phi + c_d \cos\phi\right) r\mathrm{d}r \tag{14}$$

The performance of the propeller is estimated by integrating the forces acting on each blade element (i.e., those calculated from Eqs. 13 and 14). In practice, a finite number of blade sections (of finite span) are analyzed and the local forces over each section are summed to build up the performance.

Although the translational and rotational velocities are known a priori when analyzing the propeller performance (i.e., the flight speed and RPM of the propeller are specified), the induced velocity at each blade element will depend on the forces generated by all the various blade elements so the full local velocity, W, is unknown. To determine the local velocity, the induced velocity at each blade element is often calculated with momentum theory principles [80].

Note that the theory presented above in Section 2.2.1 is sometimes termed axial momentum theory and ignores rotation in the slipstream. Typical blade element momentum theory accounts not only for the axial velocity in the propeller slipstream but also the rotational motion. As such a brief introduction to a more general momentum theory is described here based on the work of Glauert [80].

A true propeller will induce velocity not only in the axial direction, but also in the tangential direction. This rotational motion is caused by the reaction of the air to the torque of the propeller. The local tangential velocity is given by ωr where ω is the local angular velocity just aft of the propeller and r is the radial location. This tangential velocity is often expressed in terms of the tangential induction factor, a', which is defined in Eq. 15 where Ω is the angular velocity of the propeller.

$$a' = \frac{\omega}{2\Omega} \tag{15}$$

A similar notation is introduced for the axial velocity increase just aft of the propeller. The axial induction factor, a, is defined as ratio of the induced axial velocity immediately aft of the propeller to the freestream velocity as shown in Eq. 16.

$$a = \frac{v_i}{V_\infty} \tag{16}$$

With these definitions, the total induced velocity at a blade element, w, can be resolved into an axial component and tangential component as shown in Figure 8(b). The local axial velocity can be expressed as Eq. 17 and the local tangential velocity can be expressed as Eq. 18.

$$V_a = V_\infty (1 + a) \tag{17}$$

$$V_t = \Omega r (1 - a') \tag{18}$$

If the propeller disk is divided into many annular rings of thickness dr (equivalent to the dr selected for the blade element width), the thrust and torque of each annular ring can be found from momentum theory. The thrust of an annulus will be the mass flow rate through that annulus times the change in velocity induced by the annulus, which can be expressed in terms of the axial induction factor as shown in Eq. 19.

$$dT = 4\pi r \rho V_\infty^2 (1 + a)\, a \mathrm{d}r \tag{19}$$

The torque on the annulus will be angular momentum per unit time imparted to the slipstream, which is be equal to the mass flow rate through the annulus times the

radial distance times the change in angular velocity induced by the disk. From this, the torque can be calculated as Eq. 20.

$$dQ = 4\pi r^3 \rho V_\infty \Omega \left(1 + a\right) a' \mathrm{d}r \tag{20}$$

By equating Eq. 13 with Eq. 19 and Eq. 14 with Eq. 20, the local induced velocity, w, can be determined with an iterative scheme in solving the resulting system of two equations for a an a'. With this information, the total local velocity, W, can be found and the performance of the propeller estimated.

2.2.3 Vortex Theory and Minimum Induced Loss Design Methods

Vortex theory for propellers is an extension of Prandtl's lifting line theory for wings. Since the propeller blade can be viewed as a rotating, twisted wing, the same principles of the blade possessing a bound vortex and shedding a trailing vortex sheet can be applied. The original instantiation of this theory was developed by Betz [81] and a more complete treatment was later performed by Goldstein [82].

In vortex theory, the propeller blades are treated as lifting lines (i.e., there is a single bound vortex on each blade) where the circulation strength at any point is taken as Γ, and the circulation at both the blade root and tip must be zero. The propeller blade will shed trailing vortices along the entire blade of strength $\mathrm{d}\Gamma/\mathrm{d}r$. The resulting trailing vortex system will be shaped similarly to a helix, which is caused by the combination of the propeller's rotational and translational motion. The trailing vortex system would exactly form a helical shape if the vortex elements did not induce forces on one another.[4]

Betz [81] established a theory for minimum energy loss from the trailing vortex system assuming a rigid helical wake aft of a lightly loaded, frictionless propeller with a large number of blades. This theory, while only valid for an infinite number of

[4]In the words of Goldstein the helical shape occurs when there is no "interference flow" [82]. This is also equivalent to assuming there is no slipstream contraction, which makes the solutions valid for relatively low thrust coefficients.

blades, is profound because it directly specifies the required circulation distribution over the blade radius that will result in "minimum induced loss"—i.e., a propeller whose trailing vortex system would cause as few losses as possible in producing a specified thrust (to the accuracy of the assumptions made). Betz's theory can be applied so that the local loading on propeller blade elements—i.e., $c_l c$—is specified for a desired thrust from the propeller. Various distributions of chord length and blade twist angle can then be found that satisfy this relationship and thus provide an "optimum" minimum induced loss propeller.[5]

Prandtl [83] developed a modification to Betz's solution that could approximately correct it for a finite number of blades. He modeled the trailing vortex sheet as a series of parallel lines with a constant gap that mirrored the typical distance between the trailing vortex sheets. The system moves in a direction perpendicular to the lines, which is representative of the axial velocity of the slipstream. The flow around the edges of these parallel lines approximates the flow around the edges of the propeller slipstream. With this approximation, the circulation for minimum vortex energy loss at a given radial station is represented in terms of what has been termed the "Prandtl tip loss factor," F, which is shown in Eq. 21.

$$F = \frac{2}{\pi} \cos^{-1} \left(e^{\frac{-B}{2} \frac{R-r}{R \sin(\phi_T)}} \right) \tag{21}$$

In Eq. 21, B is the number of blades, R is the propeller radius, r is the local radial location (where $0 \leq r \leq R$), and ϕ_T is the helix angle at the tip. Although Prandtl's solution enables the application to a finite number of blades, it is most accurate with a high number of blades and large ratios of the propeller tip speed to freestream speed (i.e., as the pitch of the helical vortex sheet is reduced [78]).[6]

Ultimately, Prandtl's tip loss factor provides insight into the vortex losses that

[5] Glauert [80] and Veldhuis [1] provide good discussions of this topic.

[6] This can be explained by the fact that the helix angle at the tip is zero for Prandtl's system of parallel lines.

result in propeller blade systems as it represents an effective reduction in the velocity induced on the air as a function of the radial distance, r. In addition to aiding in making Betz's theory applicable to more realistic situations (i.e., a finite number of blades), it is often coupled with blade element momentum approaches to approximate the vortex losses from propellers. Specifically, this involves modifying Eqs. 19 and 20 above by multiplying the right hand side of both equations by F. This approach is followed in Chapter IV of this dissertation.

The most accurate treatment of the trailing vortex system described by Betz was performed by Goldstein [82]. He developed a solution to the potential equations for a helical vortex sheet immersed in a uniform stream with a finite number of blades at a wide range of tip speed to freestream speed ratios. His work results in the specification of the circulation distribution for minimum energy loss of a lightly loaded, frictionless propeller that produces a desired thrust. However, Goldstein's solution is rather cumbersome as it is formulated in terms of a semi-infinite series of Bessel functions, so in practice Prandtl's approximate solution is often applied.

Although the prior solutions (those of Betz, Prandtl, and Goldstein) neglected the impacts of friction, their results can be modified to incorporate blade profile drag losses as well. Glauert [80] demonstrates a simple modification to the distribution of circulation that involves the radial location (i.e., r/R location) and the blade drag-to-lift ratio of the blade section.

There are also more modern treatments of the minimum induced loss theory. Larrabee [84, 85] re-presented the main equations and provided a procedure to practically apply them to design propellers. Adkins and Liebeck [86] provide extensions to the original theories, removing small angle assumptions, adding in viscous effects, and enabling design of more highly-loaded propellers. These methods rely on accurate airfoil section data. For conventional propeller design, the work of Adkins and Liebeck is widely cited and generally accepted as the prime method to date.

2.3 Propeller-Wing Interaction

2.3.1 Propeller Slipstream Flow Characteristics

The helical vortex system produced by propeller blades creates induced velocity fields that produce a complicated, non-uniform flowfield aft of the propeller. Generally speaking, the velocity varies along the propeller radius and around the circumference of the swept disk with time. The velocity at any point aft of the propeller can be in any arbitrary direction, but it is primarily directed along the axis of the propeller and tangent to that axis.

The contraction of the slipstream (such as that shown in Figure 7) represents the largest radial component of velocity, but this is typically small at most points (except those near the slipstream boundaries) when compared to the other directions of motion. Additionally, for lightly loaded propellers the contraction in the wake is often small—Theodorsen shows contractions on the order of 1% [87]—so errors in calculations are small if the contraction is neglected. Consequently, propeller slipstreams are often described only in terms of the axial and tangential velocities.

The axial velocity induced by the propeller (i.e., that directed along the propeller axis) is often the largest induced velocity component. Per momentum theory principles, this is the only velocity component that is actually desirable since the thrust is proportional to the axial velocity increase. The propeller begins to accelerate flow in the axial direction upstream of the disk and this acceleration continues as the flow moves downstream of the disk.

Typically the induced axial velocity from a propeller for small aircraft has a profile similar to that shown by the solid line in Figure 9: near-zero at the tip, increasing to a peak between the mid-radial station and the tip, then decreasing to near-zero at the hub. The velocities in the figure have been normalized to the maximum induced axial velocity value, and it should be noted that the axial velocity value is taken as

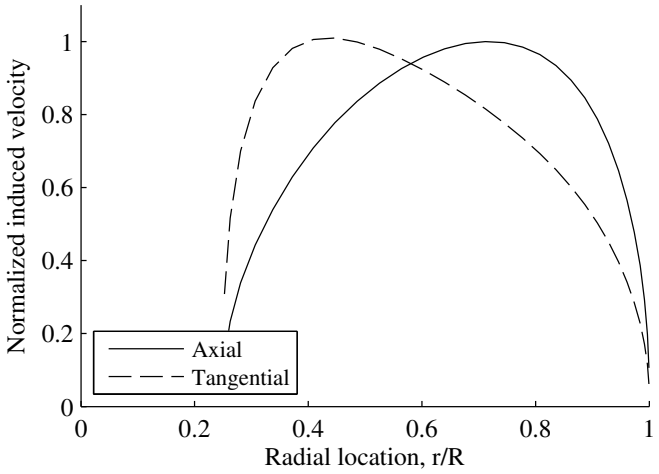

Figure 9: Representative induced axial and tangential velocity distributions immediately aft of a minimum induced loss propeller as predicted by a computational model

that immediately aft of the propeller (which is reduced by approximately two times what it would be far downstream). Although the exact velocity profiles vary with operating conditions and between propellers, the distributions shown in the figure are representative.

The tangential component of velocity, which is often called swirl, is caused by a combination of the trailing vortex system and the viscous drag of the blades. Unlike the axial velocity, the propeller will induce no swirl upstream of the prop; rather, the tangential velocity is first generated at the propeller disk and remains approximately constant moving aft in the slipstream (if viscous dissipation effects are ignored). Since this velocity is not useful for producing thrust, it is generally desired to reduce the swirl imparted to the flow.

A typical distribution of the tangential velocity aft of a propeller is shown in Figure 9 by the dashed line. Typically, the most swirl is located near the blade root, and the tangential velocity diminishes when moving outboard to the propeller tip. The swirl distribution can vary considerably as the propeller operating conditions are changed, though the variation is typically most pronounced near the root [1]. If

the tangential velocity induced is thought of as wasted energy (i.e., an ideal thrust-producing propeller would not swirl the flow at all, so the energy required to add the swirl is effectively wasted), then there will be more energy wasted at certain operating conditions where the propeller is less efficient and, consequently, produces more swirl.

The swirl angle, θ_{swirl}, can be determined from Eq. 22 for any location in the slipstream.

$$\theta_{\text{swirl}} = \tan^{-1}\left(\frac{V_t}{V_\infty + V_a}\right) \tag{22}$$

This angle is useful in appreciating the degree to which the local flow direction deviates from the desired purely axial direction. Because both the tangential and axial velocities will vary along the blade radius, the swirl angle also varies along the blade. Additionally, because the axial velocity changes as the slipstream contracts moving downstream, the swirl angle will vary with axial distance from the propeller (i.e., generally reducing with downstream distance as the axial velocity increases).

It should also be noted that the pressure distribution varies throughout the propeller slipstream as well. The propeller acts to increase both the total and static pressure of the flow. Although basic momentum theory indicates that the static pressure jump is equivalent to the total pressure increase, this is not the case in reality because not all the flow is accelerated in the axial direction. The components of flow in the radial and tangential directions cause the static pressure to be slightly reduced from the rise in total pressure. This difference for the case where there is no slipstream contraction is shown by Veldhuis to be equivalent to $\frac{1}{2}\rho V_t^2$ [1]. Because the axial and tangential velocities vary along the radial direction, the static and total pressures also vary.

2.3.2 General Impacts of Tractor Propellers on Downstream Wings

The primary impacts of a tractor propeller on a downstream wing are related to the characteristics of the flow in the propeller slipstream that were discussed above. The

wing sections will react to the flow in the slipstream much (though not exactly) like they would to a freestream flow of equal velocity and effective angle of attack.

One of the primary impacts of the propeller slipstream on a wing is to increase the apparent velocity over the wing, which generally increases the lift. This is, in fact, the very purpose of high-lift propellers. If the propeller axis is aligned or closely aligned with the freestream (as is typically the case), the axial velocity in the slipstream will effectively work to directly increase the local freestream velocity. In addition to increasing lift, the increased velocity can lead to delayed stall through increases in the local section Reynolds numbers.

The swirl induced by the propeller tends to increase the angle of attack of wing sections aft of the upward moving half of the propeller plane and decrease the angle of attack of those wing sections downstream of the downward moving side. Similarly, there may be spanwise induced flow near the top and bottom of the propeller related to the swirl velocities in the slipstream. Due largely to the presence of swirl, but also to the increased axial velocity, the ideal lift distribution of a wing aft of a propeller is modified considerably from a clean wing as has been demonstrated by Kroo [88]. Consequently, wings designed without consideration of the swirl velocity profile are likely to have reduced efficiency.

The swirl distribution aft of the propeller and its interaction with the wing does not only lead to unfavorable impacts, however. The presence of the wing acts as a sort of stator vane, which tends to reduce the effective swirl of the downstream flow. When the combined wing and propeller system are considered together, this reduction in swirled flow will result in an effective increase in propeller efficiency and/or induced drag [88]. This phenomenon is typically referred to as "swirl recovery" and the favorable impacts on propeller efficiency have been demonstrated in experiments [89, 90].

Swirl recovery can also be explained by considering an uncambered, untwisted

wing at a zero degree angle of attack with a propeller placed upstream so that in the absence of the propeller, the wing would produce no lift. Because the local lift force on an airfoil section is perpendicular to the oncoming net flow velocity, wing sections aft of the upward moving half of the propeller disk will experience a resultant force that is oriented upward and forward. The resultant "lift" force effectively generates positive lift and negative drag.[7] Wing sections aft of the downward moving half of the propeller disk experience a net negative angle of attack. The resultant force in this case will be oriented downward and forward, which effectively produces negative lift and *negative* drag. Therefore, the presence of the wing effectively increases the propeller thrust, which can be viewed as an increase in propeller efficiency or reduction in swirl required to generate a set (net) thrust [1].

A representative figure showing the general impacts of propeller slipstreams is shown in Figure 10, which is reproduced from Reference [1].[8] As shown in the figure, the lift of the wing sections downstream of the upward moving side of the propeller disk is markedly increased due to both the swirl and axial velocity increases in the slipstream. The lift aft of the downward moving side of the propeller disk is reduced from the baseline distribution due to the swirl, but it is not decreased as much as the opposite side is increased due to the axial velocity increase in the flow there.

Another important observation that can be made from Figure 10 is that the propeller impacts on the wing lift are not limited to the width of where the propeller slipstream impacts the wing. The circulation distribution over the wing must be continuous moving spanwise from within to outside the propeller slipstream, so there cannot be a sudden, drastic change in the lift. The modification of the shed vorticity and resulting induced velocity cause additional lift to be carried at spans outside the direct region of influence on the upward moving half of the propeller and a decrease

[7]No consideration is made here for increased friction drag or induced drag. This discussion only considers the direction of the resultant "lift" vector.

[8]Note that there is no fuselage present in this figure.

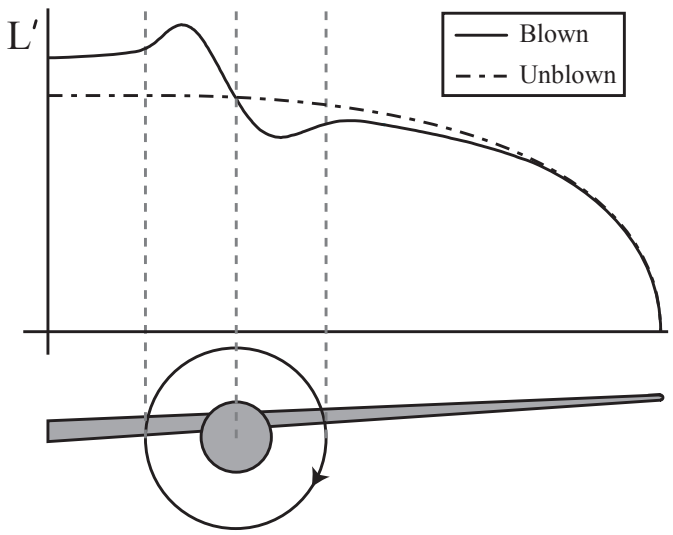

Figure 10: Generic lift distribution of a blown and unblown wing showing the general impacts of the propeller slipstream velocities [reproduced from Reference [1]]

in the lift in regions beyond the slipstream impact on the downward rotating side.[9]

The propeller's spanwise placement and direction of rotation can have noticeable impacts on the change in lift experienced over a downstream wing. Because a greater amount of lift is generally carried closer to the wing root than tip, the propellers placed closer to the root generally will impart greater changes in lift than those towards the tips. Similarly, if the propeller rotates upward on the inboard portion of the wing, greater lift is likely to be obtained than if it rotates downward inboard (so long as stall does not occur). The increased angles of attack from the swirl on the inboard portion of the wing create more lift when the propeller is rotated upward inboard, and greater swirl recovery typically occurs [1]. For extreme propeller placements at or near the wing tip, the propeller can act to reduce the induced drag of the configuration [61, 91, 58]. The swirl from the propeller can work to effectively reduce the downwash from the tip vortex so long as the propeller is rotated down outboard.

The propeller also influences the boundary layer over the wing. It has been shown

[9]It is the author's opinion that the increase in lift relative to the unblown wing inboard of the propeller and outside of the slipstream is likely higher than would occur in practice.

that the slipstream will cause the boundary layer to cycle between laminar, a "turbulent transitional state," and back to laminar at a rate equivalent to the blade passage frequency [92]. The unsteady and transitioning nature of the boundary layer can be explained by considering the helical nature of the wake from the propeller blades. The transitions are initiated when the wake from a blade impacts the wing, but after this wake passes, the boundary layer can re-laminarize. The semi-turbulent nature of the boundary layer will generally increase the friction drag of the wing, though this increase will likely not be as high as if the boundary layer were completely turbulent.

It should also be noted that the wing will influence the propeller. The primary mechanism through which this impact is noticed is in the distortion of the upstream flowfield experienced by the propeller. Since the wing circulation tends to generate upwash upstream of the wing, the propeller disk is likely to encounter non-uniform flow fields that will generally act to decrease the propeller performance. The magnitude of the upwash varies with the location relative to the wing with the largest perturbations occurring closer to the wing.

2.3.3 Modeling Propeller-Wing Interaction

There is a wide volume of work related to the modeling of the interaction between propellers and wings. Early modeling of the propeller-wing interaction problem represented the wing with lifting line theory [93, 94, 95, 3, 96], slender body theory [97], or lifting surface methods [98, 99, 100] where the freestream velocity was modified at spanwise locations behind the propeller disk to account for the propeller slipstream. Typically these works have modeled the slipstream as a "jet" with constant axial velocity, though certain works looked at varying the velocity profile in the slipstreams.

Ultimately, the seminal work of Koning [93] provided a basis from which the other works built. He developed a modified lifting line theory to represent the influence of a propeller on a wing in an inviscid, incompressible flow. The main assumptions

in his work are that the slipstream consists only of a single, averaged axial velocity component, a linear variation of the radial velocity component with the radial station (which accounts for slipstream contraction), and the tangential velocity is negligible. One result of importance from Koning's work is that the influence of the propeller on the wing's circulation can be represented simply as an angle of attack change of the wing in the freestream.[10] Another major finding is that the change in lift from the propeller slipstream consists of two parts: one from the change in the circulation, which is primarily a function of the axial velocity of the slipstream, and a second directly from the axial velocity increase over the wing. Like many of the works to follow, Koning develops solutions for the entire lifting wing in terms of Fourier coefficients.

Later, the influence of the propeller on the wing was modeled in greater detail using helical vortex sheets emanating from the propellers and a flat wake sheet emanating from the wing to model the impact of the propeller on the quasi-steady wing performance [89]. As more detailed free wake models were developed, the interactions of a free propeller wake with a wing have been investigated with various methods including lifting line analysis [101] and a boundary element method [102]. Studies have typically only included the "one-way" interaction of the propeller on the wing, neglecting the influence of the wing on the propeller, but more recent lifting surface-based modeling [103] has considered the mutual interference of wings and propellers each with freely deforming wakes.

CFD has also been applied to the study of propeller-wing interactions. Initially, CFD was coupled with simplified propeller performance models [104], but more recently CFD has been applied to model both the wing and propeller directly by including detailed propeller geometry and wake interaction predictions [105]. Although

[10]To quote Koning: "[T]he change in circulation caused by the action of the propeller is identical with that which would result from a certain change in the angle of attack for the wing located in the undisturbed flow" [93].

the accuracy of results from CFD is appealing, the computational expense and the requirement for detailed geometric knowledge makes CFD impractical for use in the conceptual design studies of interest in this dissertation.

Other branches of research have focused on quantifying the unsteady loadings associated with the propeller blade passage [106, 107, 108]. Although these unsteady effects may have significant influence over the aeroelastic stability of the structure, such analyses are not the focus of this dissertation. For the early-phase configuration design application of interest here, the unsteady loading of the propellers is less important to capture than the time-averaged performance.

Overall, the general trends in the research have focused on adding additional complexity and detail to computational modeling. Although the resulting methods have increased in accuracy, the intuitive insight that can be gained from such models leaves something to be desired. Basic modeling has been essentially unadvanced for many years with the simple models being those developed by Smelt and Davies [2] and Jameson [109]. These techniques are described in more detail below.

2.3.3.1 Smelt and Davies

Smelt and Davies [2] developed a simple method of obtaining the lift augmentation from upstream propellers on a downstream wing in the 1930s. Their theory relies on the same principles as momentum theory for analyzing the propellers and their slipstreams; ignores any influence of the wing on the propeller; and is only applicable to relatively lightly-loaded propellers and wings without flaps. Their work is widely cited and appears to still be generally accepted as a reasonable first-order estimate of propeller lift augmentation (within the limits of the assumptions).

Smelt and Davies noticed that previously developed theories could provide reasonable results for wings with chord lengths relatively small in comparison to the

propeller slipstream diameter, but these theories would break down when considering wings with larger chords. Based on their observations of experimental results and their understanding of the physics, Smelt and Davies postulated maximum and minimum values for the increase in lift from a wing in a propeller slipstream and developed a relationship based on the aspect ratio of the wing in the slipstream that dictated where between these two extremes a particular configuration would fall.

The maximum increase in lift is theorized to occur when the chord is small in comparison to the slipstream diameter, and the resulting maximum lift increase is proportional to the change in the dynamic pressure in the slipstream. They represent this lift change as Eq. 23 where C_{L_0} is the lift coefficient without propeller blowing, D_1 is the contracted slipstream diameter and s is such that the local flow velocity at a given distance aft of the disk is $V_\infty(1+s)$.

$$\Delta C_L = C_{L_0}\frac{D_1 c}{S}\left((1+s)^2-1\right) \approx C_{L_0}\frac{D_1 c}{S}2s \tag{23}$$

The approximate relationship holds for lightly loaded propellers (i.e., relatively small values of s).

The minimum increase in lift would occur when the slipstream diameter is small in comparison to the wing chord. This minimum lift increase would be proportional to the velocity increase in the slipstream, which can be represented mathematically as Eq. 24 and is equivalent to assuming that the circulation around the wing is unchanged from the case without blowing.[11]

$$\Delta C_L = C_{L_0}\frac{D_1 c}{S}s \tag{24}$$

They justify the assumption of an unchanged wing circulation through consideration of the shed vorticies from the wing. Near the edges of the slipstream boundary, the

[11] Although they acknowledge that the circulation is not actually constant over the wing sections in these situations, they observed that the lift increases for smaller diameter propellers was such that the resulting effect was similar to assuming a constant circulation.

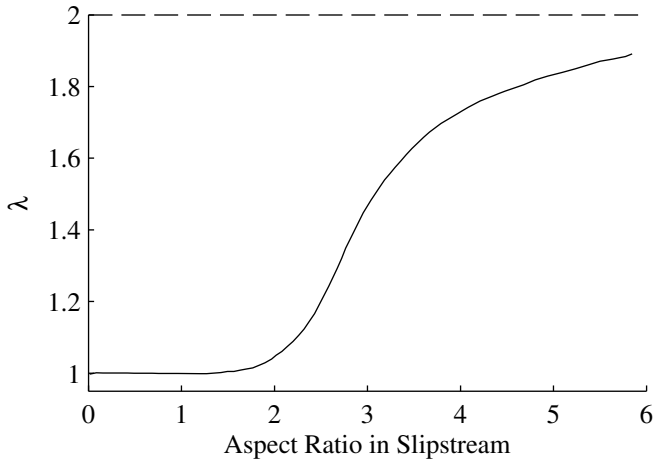

Figure 11: Empirical factor describing the amount of lift augmentation from propellers between two extremes (adapted from Reference [2])

wing will shed stronger vorticies than near the center of the blown portion. These vortices will induce downwash that reduces the effective angle of attack of wing sections near them. As the slipstream width decreases, these stronger vortices move closer to the propeller centerline and have a larger impact on the slipstream in the wing.

The form of Eq. 24 and the approximation in Eq. 23 are such that they can be represented as Eq. 25, where the λ parameter will vary from a minimum value of 1 to a maximum of 2 to represent these equations.

$$\Delta C_L = C_{L_0} \frac{D_1 c}{S} \lambda s \tag{25}$$

To determine an appropriate value for λ based on a given geometry, Smelt and Davies developed an empirical relationship between λ and the aspect ratio of the wing immersed in the slipstream, which is shown in Figure 11. There is no discussion of precisely how this relationship was obtained, but it shows good agreement with the experimental data presented in their paper.

As can be seen from Figure 11, there is a sigmoid-like variation of λ with the aspect ratio in the slipstream. The value of λ is effectively 1 from aspect ratios of zero to

approximately 2. There is a sharp rise in λ from aspect ratios of 2 to approximately 4, and then the rate of increase in λ begins to decrease. Smelt and Davies only show the relationship between λ and aspect ratio in the slipstream for aspect ratios of up to 6, but it can be assumed that the value of $\lambda = 2$ is only achieved in the limit as the aspect ratio becomes infinitely large.

Smelt and Davies also present a relationship that describes how the lift varies as the angle the propeller slipstream makes with the freestream, θ_0, changes. First, they recognize that the angle that the slipstream initially makes with the propeller, θ_0, will be reduced by some amount due to viscous forces by the time it encounters the wing. They present Eq. 26 to calculate the effective reduction of this angle from θ_0 to θ as a function of the distance aft of the propeller, x, and the propeller diameter, D.

$$\frac{1}{\theta^{0.8}} = 0.016\frac{x}{D} + \frac{1}{\theta_0^{0.8}} \tag{26}$$

Practically, this results in a very small reduction in the angle unless both the initial angle and the distance are relatively large.[12] With the value of θ in hand, they estimate the total increase in lift from an inclined slipstream with Eq. 27, where a_0 is the lift curve slope of the wing section airfoil and λ' is an empirical constant.

$$\Delta C_L = C_{L_0}\frac{D_1 c}{S} s\left[\lambda C_{L_0} - \lambda' a_0 \theta\right] \tag{27}$$

They determined from their experiments that a value of $\lambda' = 0.6$ provided reasonable results. Unfortunately, there is no discussion of how the empirical constant λ' should be selected in general, though they imply that the value of 0.6 should be sufficient so long as propeller inclinations within the ranges of their experiments (i.e., where the propeller makes no more than a 10° angle with the freestream) are analyzed. [13]

[12] Changes in angle of more than approximately 1° are not observed until $\theta_0 \gtrsim 10°$ and $x/D \gtrsim 0.5$.

[13] It seems to the author that λ' is simply a "fudge factor" that had to be applied to make their model fit their results.

2.3.3.2 Jameson

Jameson [109] was interested in studying STOL aircraft concepts with multiple propellers. He considered the situation where the propeller slipstreams would effectively merge to form a single, wide slipstream. In his analysis Jameson assumes that the velocity in the propeller slipstreams is uniform with a velocity of V_j purely in the axial direction. The swirl from the propellers is neglected, and the slipstream extends aft parallel to the free stream direction (i.e., it is not deflected by the wing). Furthermore, the flow is assumed inviscid and incompressible, and the height of the slipstream must be greater than half the wing's chord length.

Although Jameson studies the coupling of his method with both lifting line theory and slender body theory to predict wing lift, these solutions include Fourier series, which require computation to practically resolve into a solution due to their infinite summations. However, Jameson was able to determine an analytic solution to the potential equations for a case where the slipstreams from the propellers merged to form a large elliptic slipstream that extended beyond the wing tips so that the tips are located at the foci of the ellipse and the wing downwash was constant. Although this case is not likely to occur in practice, the method is sufficiently simple that it may help build insight into the general trades present in aircraft with many propellers.

To present the equations, Jameson defines μ as the ratio of the freestream velocity to slipstream velocity (i.e., $\mu = V_\infty/V_j$), and Λ represents the ratio of the slipstream width to height.[14] Ultimately, the effect of the slipstream can be approximated as an effective reduction in the aspect ratio from the baseline value, AR, to AR_μ, which can be calculated from Eq. 28.

$$AR_\mu = AR\frac{1+\Lambda\mu^2}{\Lambda+\mu^2} \tag{28}$$

If the wing has a large aspect ratio, then lifting line theory will provide reasonable

[14] Jameson uses a λ instead of Λ to represent the slipstream width-to-height ratio. This notation is changed here to avoid confusion with the λ parameter presented by Smelt and Davies.

results for aggregate wing lift and drag. Furthermore, if the lift and drag coefficients are non-dimensionalized by the velocity in the jet rather than the freestream, the equations take the same form as with conventional lifting line theory. The lift coefficient can be found from Eq. 29, where α is the angle of attack as measured from the zero-lift line. This equation effectively models the jet as a modification to the lift curve slope of the airfoil.

$$C_{L_j} = \left(\frac{a_0}{1 + \frac{a_0}{\pi A R_\mu}} \right) \alpha = C_L \mu^2 \tag{29}$$

The induced angle of attack can be found from Eq. 30.

$$\alpha_i = \frac{C_{L_j}}{\pi A R_\mu} \tag{30}$$

Finally, the induced drag can be determined by Eq. 31.

$$C_{Di_j} = \alpha_i C_{L_j} = \frac{C_{L_j}^2}{\pi A R_\mu} = \mu^2 C_{Di} \tag{31}$$

2.3.4 Desire for New Theory

What is desired for the sake of this dissertation is a theory that is simple and can provide a designer intuition about the lift changes that will result from various high-lift propeller designs as well as installation locations and angles relative to the wing. Although existing theories are adequate to provide sufficiently accurate results, many of these theories involve lengthy calculations and/or utilize semi-empirical data that has been gathered with assumptions of conventional propellers that may not apply well to the envisioned high-lift propellers. Additionally, many theories were developed to be applied to lifting line or lifting surface theory that often require the use of Fourier series to define the solutions, which precludes their usefulness for building a designer's intuition.

Furthermore, from a practical standpoint, the SCEPTOR project team's initial conceptual estimates of the lift augmentation from the high-lift propellers were found

to be far from the lift predicted by CFD tools. The desire to improve the conceptual understanding of the project team serves as one of the largest motivations for the work contained in this dissertation.

2.4 Chapter Summary

This chapter was begun with the desire to answer the following questions:

How do high-lift propellers increase the lift over downstream wings?

and

What methods exist to model high-lift propellers and their interaction with downstream wings?

The answers to these questions are not incredibly simple, but can be summarized with the following points:

1. High-lift propellers will influence the lift of downstream wings primarily through the velocities that they induce in their slipstreams.
2. The velocity in propeller slipstreams is complex, but is often abstracted to two components: an axial velocity, which is directed along the propeller's rotational axis, and a tangential component often called swirl, which perpendicular to the axial velocity.
3. The induced axial velocity tends to increase lift on downstream wings (primarily through the increase in velocity) while the swirl velocity increases lift aft of the upward moving half of the propeller disk and decreases lift on the downward moving half (primarily through angle of attack changes).
4. There is a wide volume of literature studying the impacts of propellers on downstream wings and modeling this interaction. Over time, modeling techniques have generally increased in sophistication by removing assumptions and/or moving to higher-order modeling. However, simple, intuition-building modeling has been unadvanced for many years.

CHAPTER III

A SIMPLE HIGH-LIFT PROPELLER LIFT AUGMENTATION THEORY

The information in this chapter is motivated by the question:

How can the lift augmentation from high-lift propellers be rapidly assessed to facilitate conceptual design?

Although methods were described in the previous chapter that may be able to address portions of this question, the simple models often show significant deviations from experiments and rely on assumptions or semi-empirical data that may be invalid for many high-lift propeller systems as will be discussed below. Consequently, a novel method is developed here to quickly estimate the lift augmentation from configurations in which multiple propellers are distributed upstream of a wing. This method is built on simple, two-dimensional aerodynamic models that incorporate the effects of the propeller installation angle, location relative to the wing, and diameter. The angle of the slipstream relative to the airfoil and the height of the slipstream are both shown to have significant impacts on the lift augmentation. The methods presented below are intentionally simple and can be used to help build a designer's intuition about the effects of distributed leading edge propellers employed as high-lift devices.

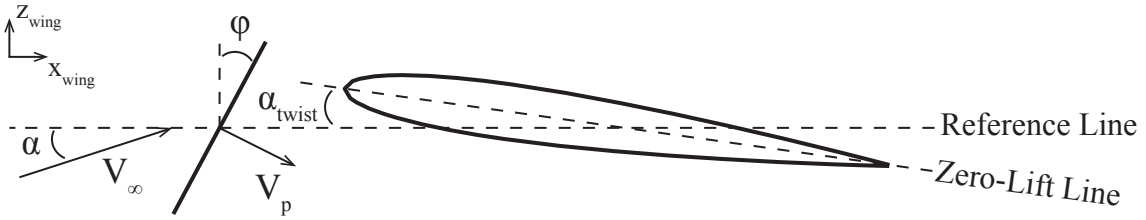

Figure 12: A two-dimensional cross section of the geometry under consideration relative to the wing reference frame.

3.1 A Two-Dimensional Model for Predicting Wing Lift Augmentation from High-Lift Propellers

3.1.1 Geometry

The two-dimensional geometry under consideration in this chapter is shown in Figure 12, where a propeller is placed upstream of a wing. The figure shows the orientation of the freestream velocity vector ($\boldsymbol{V_\infty}$), the propeller disk plane, the slipstream velocity from the propeller ($\boldsymbol{V_p}$), and the local wing section zero-lift line relative to a reference chord line of the wing (i.e., the horizontal line in the figure). The term "zero-lift line" refers to the line drawn through the trailing edge of the airfoil that is parallel to the freestream velocity when the lift generated by the airfoil is zero [110]. The local wing section's zero-lift line is equivalent to the chord line for a symmetric airfoil; therefore, the figures in this section are all drawn with a symmetric airfoil for simplicity.

The airfoil's zero-lift line at any given wing section may be twisted from the wing reference chord line by an angle α_{twist}, and positive twist is shown in Figure 12.[1] The propeller is located forward of the wing and is inclined at an angle of φ relative to the

[1]If it is preferred to separate the effects of the physical twist of the local chord line and zero-lift angle of attack, the angle α_{twist} can be thought of as the local chord line's physical twist angle minus the zero-lift angle of attack (i.e., $\alpha_{\text{twist}} = \alpha_g - \alpha_{L=0}$ where α_g is the angle of attack of the local airfoil section relative to its chord line). Since positively cambered airfoils have negative zero-lift angles of attack, the result of positive camber is to effectively increase the local twist angle over the geometric twist of the chord line.

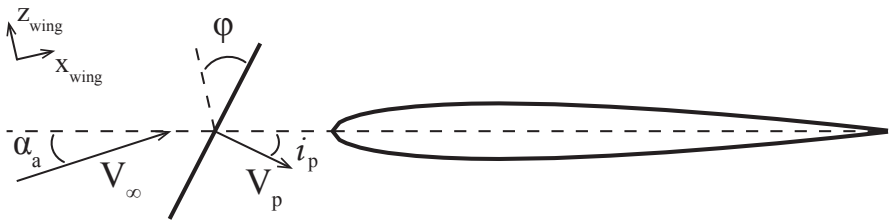

Figure 13: Orientation of freestream velocity and propeller disk with respect to a local airfoil section

wing frame's vertical; a positive φ is shown in the figure and indicates an upward tilt of the resultant thrust vector from the propeller relative to the wing reference chord line.

The geometry in Figure 12 can be formulated instead relative to the local airfoil's zero-lift line as shown in Figure 13 for a symmetric airfoil. In the local reference frame of the airfoil sections, only two angles, α_a and i_p, describe the direction of the incoming velocity vectors $\boldsymbol{V_\infty}$ and $\boldsymbol{V_p}$, respectively. The local absolute angle of attack, α_a, is the angle of attack of the local airfoil section's zero-lift line as shown in Figure 13. This local absolute angle of attack can be written in terms of the local twist angle and the wing angle of attack as Eq. 32.

$$\alpha_a = \alpha + \alpha_{\text{twist}} \tag{32}$$

Consistent with momentum theory [76, 77, 78], the propeller slipstream can be modeled as a uniform velocity oriented in the direction of the axis of rotation.[2] With the assumption that $\boldsymbol{V_p}$ is perpendicular to the propeller disk, the incoming angle of the slipstream, i_p, can be written in terms of the local zero-lift line twist and the propeller installation angle as Eq. 33.

$$i_p = \varphi - \alpha_{\text{twist}} \tag{33}$$

Because two-dimensional geometry will be the focus throughout this chapter, the

[2]That is, there is a uniform induced axial velocity and no swirl.

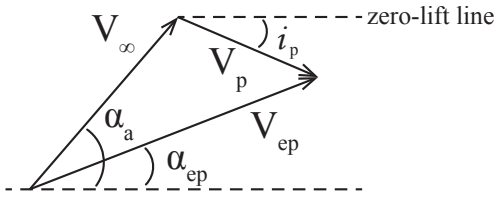

Figure 14: Vector diagram showing the effective angle of attack behind the prop resulting from the axial component of the propwash over the wing

geometry will be referred to in terms of the local variables i_p and α_a as opposed to the variables φ and α.[3]

The slipstream from the propeller causes a change in the effective angle of attack of the airfoil as illustrated in Figure 14. The effective angle of attack behind the propeller, α_{ep}, is defined between the zero-lift line and the effective velocity behind the prop, V_{ep}, which is a vector sum of the freestream and slipstream velocities (i.e., $\boldsymbol{V_{ep}} = \boldsymbol{V_\infty} + \boldsymbol{V_p}$).

An expression for the effective angle of attack of the airfoil section behind the propeller in terms of the absolute angle of attack, the freestream velocity, the velocity of the slipstream, and the local slipstream inclination angle is given in Eq. 34. This relationship is derived from the geometry presented in Figure 14.

$$\tan(\alpha_{ep}) = \frac{V_\infty \sin(\alpha_a) - V_p \sin(i_p)}{V_\infty \cos(\alpha_a) + V_p \cos(i_p)} \tag{34}$$

For small angles of attack and small inclination angles, Eq. 34 can be reduced to Eq. 35.

$$\alpha_{ep} \approx \frac{V_\infty \alpha_a - V_p i_p}{V_\infty + V_p} = \frac{\alpha_a - (V_p/V_\infty)\, i_p}{1 + (V_p/V_\infty)} \tag{35}$$

Finally, the magnitude of the effective local velocity behind the propeller can also be

[3]The assumption that $\boldsymbol{V_p}$ is perpendicular to the propeller disk does not have to be made. The relationships derived below in terms of the local variable i_p hold regardless of if Eq. 33 is true or not. Consequently, the following equations can be thought of as containing the entire slipstream velocity (i.e., both the axial and tangential velocities) oriented at the angle i_p relative to the zero-lift line at any cross section. This will be discussed further in Section 3.1.4.

determined from the geometry in Figure 14 as Eq. 36.

$$V_{ep} = \sqrt{V_\infty^2 + 2V_\infty V_p \cos\left(\alpha_a + i_p\right) + V_p^2} \tag{36}$$

3.1.2 General Model

In this section a simple model that captures the main effects of the propeller slipstream on wing lift is developed. The model is intended to provide design insights and enable "back of the envelope" calculations that may provide a starting point for more detailed studies with higher-order models. The model involves several simplifying assumptions and consequently should be used with caution.

Perhaps the simplest estimation of the wing lift increase in the presence of a propeller slipstream can be made by assuming that the lift is proportional to the dynamic pressure. In this case the fractional increase in the lift per unit span of an airfoil section is simply the fractional increase in the dynamic pressure as shown in Eq. 37, where L'_0 is the lift per unit span in the presence of only the freestream velocity.

$$\frac{\Delta L'}{L'_0} = \frac{\Delta q}{q_\infty} \tag{37}$$

However, this estimation ignores any effects of the propeller installation angle, which essentially assumes that the angle of attack of the airfoil remains unchanged when immersed in the propeller slipstream. As is clear from inspection of Figure 14, this is a poor assumption, and this model is insufficient to describe the lift augmentation from upstream propellers.

It is assumed that the geometry of any local airfoil section with an upstream propeller can be represented as shown in Figure 15. The propeller diameter is viewed to be large in comparison to the wing chord and the propeller is installed in front of the wing with relatively little offset above or below the zero-lift line such that the wing section will be completely immersed in the slipstream from the propeller. The

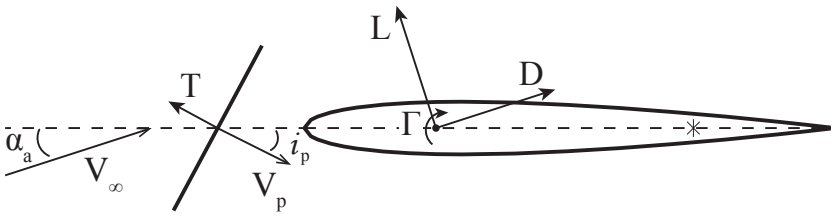

Figure 15: The geometry describing a two dimensional point vortex representation of an airfoil and the incoming local frestream velocity and propeller slipstream velocity relative to the local airfoil section

airfoil is represented by a single point vortex of circulation strength Γ, which is placed at the quarter chord point on the zero-lift line. The circulation strength is determined by requiring flow tangency at a control point located at the 3/4 chord point of the zero-lift line, which is denoted by an asterisk (*) in Figure 15. We will assume that the airfoil is sufficiently thin such that the control point and point vortex are located on the zero-lift line of the airfoil, which implies that the point vortex will induce a velocity, w, downward and normal to the zero-lift line at the control point.

For a known required induced velocity at the control point, the circulation strength of a point vortex can be found from Eq. 38 [111], where c is the chord length of the airfoil.

$$\Gamma = \pi c w \tag{38}$$

Once the circulation strength is known, the lift force per unit span from the vortex can be determined from the scalar form of the Kutta-Joukowski theorem presented in Eq. 39, where the lift per unit span acts perpendicular to the incoming velocity in the plane of the airfoil and the velocity, V, represents the total local velocity at the point vortex.

$$L' = \rho V \Gamma \tag{39}$$

Figure 16 shows the required induced velocity from the point vortex, w_0, if only the freestream velocity is present. The larger the vertical component of the freestream velocity ($V_\infty \sin(\alpha_a)$), the larger the magnitude of the circulation will be required to

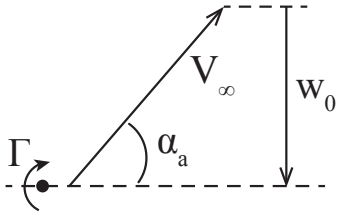

Figure 16: Vector diagram showing the absolute angle of attack and required induced velocity from a point vortex to create flow tangency in the presence of the freestream velocity

enforce flow tangency. Because the local lift per unit span is directly proportional to the circulation strength, this method predicts that increases in α_a will produce increases in lift proportional to the magnitude of the increase of α_a.

If a propeller is installed upstream of the airfoil, an additional velocity component is added to the freestream as was illustrated in Figure 14. In addition to changing the orientation and magnitude of the total velocity vector, there is also a change in the strength of the point vortex, Γ. As with the isolated airfoil, the vortex strength is determined by maintaining flow tangency at the control point. Here, the magnitude of Γ will vary based on the magnitude of the vertical component of the effective velocity aft of the propeller, $V_{ep}\sin(\alpha_{ep})$. The change in the magnitude of the circulation compared to the baseline is determined from the change in the induced velocity required with only the freestream, w_0, and the new induced velocity required in the presence of the new total velocity, w_{ep}. If $w_{ep} < w_0$, then the new circulation strength will be decreased; if $w_{ep} > w_0$, then the new circulation strength will be increased.

3.1.3 Specific Propeller Installations

In this subsection, four propeller installations whose velocity vector diagrams are shown in Figure 17 are considered. For each case, the original lift per unit span resulting from only the freestream velocity is denoted as $L'_0 = \rho_\infty V_\infty \Gamma_0$, where Γ_0 is the circulation strength determined from the induced velocity w_0 (as illustrated in

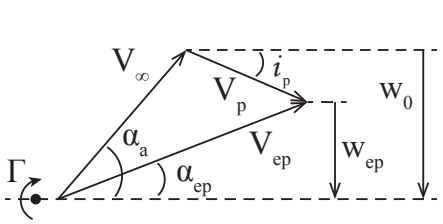

(a) Propeller inclined upward, $i_p > 0$

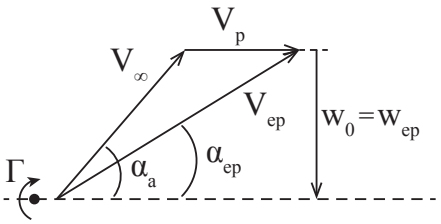

(b) Propeller slipstream aligned with the airfoil zero-lift line, $i_p = 0$

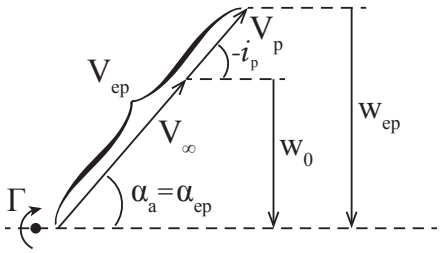

(c) Propeller inclined downward at angle matching angle of attack, $i_p = -\alpha_a$

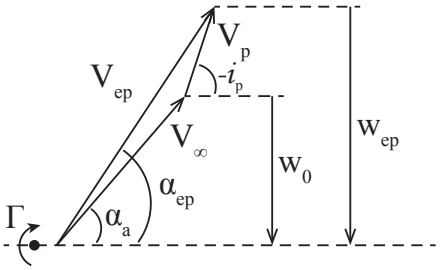

(d) Propeller inclined downward at angle of greater than the absolute angle of attack, $-i_p > \alpha_a$

Figure 17: Vector diagrams showing the effective angle of attack and required induced velocity from a point vortex for various propeller installation angles

Figure 16). The new lift per unit span in the presence of the propeller slipstream will be $L'_{\text{new}} = \rho_{ep} V_{ep} \Gamma_{ep}$, where Γ_{ep} is the circulation strength determined from the induced velocity w_{ep}. Furthermore, incompressible flow is assumed so that $\rho_{ep} = \rho_\infty$. The change in the lift between these two conditions is $\Delta L' = L'_{\text{new}} - L'_0$.

In the following subsections, the implications of the four propeller installations on the lift per unit span are discussed. The direct contribution of the thrust vector to lift is ignored for simplicity in the following analyses unless otherwise noted. Additionally, incompressible flow is assumed.

3.1.3.1 Propeller Slipstream Directed Below the Local Airfoil Zero-Lift Line

For the case shown in Figure 17(a) in which $i_p > 0$, one expects the circulation to decrease relative to the unblown wing because $w_{ep} < w_0$. Additionally, the angle of attack of the airfoil is decreased (i.e., $\alpha_{ep} < \alpha_a$), which has two potentially detrimental

consequences:

1. The local lift per unit span vector is tilted aft in the drag direction by the angle $\alpha_a - \alpha_{ep}$, which implies that not all the force produced by the airfoil is usable for lift, and some directly contributes to drag.
2. In case of propeller loss, the airfoil angle of attack will suddenly increase, potentially causing stall.

If the circulation strength decreases by some factor κ (where $\kappa < 1$), then $\Gamma_{ep} = \kappa\Gamma_0$ and the fractional increase in the lift can be expressed as Eq. 40.

$$\frac{\Delta L'}{L'_0} = \kappa\frac{V_{ep}}{V_\infty} - 1 \tag{40}$$

Note that if $\kappa = 1$, Eq. 40 reduces to $\Delta L'/L'_0 = (V_{ep} - V_\infty)/V_\infty = \Delta V/V_\infty$; therefore, this installation should result in an increase in lift per unit span of *less* than the relative increase in the total velocity because $\kappa < 1$.

Because the induced velocity from a point vortex is directly proportional to the vortex strength, κ can be expressed in terms of induced velocity ratio as shown in Eq. 41.

$$\kappa = \frac{w_{ep}}{w_0} = 1 - \frac{V_p \sin i_p}{V_\infty \sin \alpha_a} \tag{41}$$

The percentage change in the lift can then be expressed in terms of the freestream velocity, local slipstream velocity, local propeller inclination angle, and absolute angle of attack as Eq. 42.

$$\frac{\Delta L'}{L'_0} = \left(1 - \frac{V_p \sin i_p}{V_\infty \sin \alpha_a}\right)\sqrt{1 + 2\left(\frac{V_p}{V_\infty}\right)\cos\left(\alpha_a + i_p\right) + \left(\frac{V_p}{V_\infty}\right)^2} - 1 \tag{42}$$

Finally, the fractional increase in lift per unit span can be represented in terms of the dynamic pressure as shown in Eq. 43, where $q_{ep} = \frac{1}{2}\rho_{ep}V_{ep}^2$ and $q_\infty = \frac{1}{2}\rho_\infty V_\infty^2$.

$$\frac{\Delta L'}{L'_0} = \frac{q_{ep}\left(\sin\alpha_{ep}/\sin\alpha_a\right) - q_\infty}{q_\infty} \tag{43}$$

Here, $\sin\alpha_{ep}/\sin\alpha_a < 1$ because $\alpha_{ep} < \alpha_a$; therefore, Eq. 43 indicates that the lift increase will be less than the percentage change in the dynamic pressure.

3.1.3.2 Propeller Slipstream Aligned with the Local Airfoil Zero-Lift Line

The case shown in Figure 17(b) in which the propeller's slipstream is aligned with the airfoil zero-lift line is identical to that presented above in Section 3.1.3.1 except that the circulation strength is unchanged from the unblown wing (i.e., $\Gamma_{ep} = \Gamma_0$). With this constant circulation strength, the fractional increase in lift is equivalent to $\Delta V/V_\infty$, as shown in Eq. 44.[4]

$$\frac{\Delta L'}{L'_0} = \frac{\rho_{ep} V_{ep} \Gamma_0 - \rho_\infty V_\infty \Gamma_0}{\rho_\infty V_\infty \Gamma_0} = \frac{V_{ep}}{V_\infty} - 1 = \frac{\Delta V}{V_\infty} \tag{44}$$

Additionally, the angle of the incoming propeller slipstream is zero, so the fractional increase in lift can also be expressed as Eq. 45.

$$\frac{\Delta L'}{L'_0} = \frac{\Delta V}{V_\infty} = \sqrt{1 + 2\left(\frac{V_p}{V_\infty}\right)\cos\left(\alpha_a + i_p\right) + \left(\frac{V_p}{V_\infty}\right)^2} - 1 \tag{45}$$

3.1.3.3 Propeller Slipstream Aligned with the Freestream Velocity Vector

For the case shown in Figure 17(c) in which the propeller slipstream is aligned with the freestream velocity (i.e., $i_p = -\alpha_a$) one expects the circulation strength to increase compared to the unblown case because $w_{ep} > w_0$, which will increase the lift produced. Also, the effective angle of attack of the airfoil is the same as the absolute angle of attack (i.e., $\alpha_{ep} = \alpha_a$), which implies that there is no tilting of the lift vector and if a propeller were to fail, the onset of stall is less likely than in the previous scenarios.[5]

In this case, the local velocity seen by the airfoil section is simply the sum of the freestream and propeller induced velocity (i.e., $V_{ep} = V_\infty + V_p$). The circulation required to induce flow tangency at the control point can be found from Eq. 38 and

[4] Recall the assumption of incompressible flow so that $\rho_\infty = \rho_{ep}$.

[5] The propeller slipstream increases the Reynolds number of the flow, which will generally delay stall to a higher angle of attack. If the wing section in the slipstream is at or near stall and the propeller fails, the decrease in Reynolds number could cause a stall to occur even though the angle of attack is unchanged.

the geometry in Figure 17(c) as Eq. 46.

$$\Gamma_{ep} = \pi c \left(V_\infty \sin \alpha_a + V_p \sin \alpha_a \right) = \pi c V_{ep} \sin \alpha_a \tag{46}$$

Because the circulation required to create flow tangency at the control point when only the freestream velocity is present is $\Gamma_0 = \pi c V_\infty \sin \alpha_a$, the resulting fractional increase in lift per unit span in this case can be expressed as Eq. 47.

$$\begin{aligned} \frac{\Delta L'}{L'_0} &= \frac{\rho_{ep} V_{ep} \Gamma_{ep} - \rho_\infty V_\infty \Gamma_0}{\rho_\infty V_\infty \Gamma_0} \\ &= \frac{\rho_{ep} V_{ep} \left(\pi c V_{ep} \sin \alpha_a \right) - \rho_\infty V_\infty \left(\pi c V_\infty \sin \alpha_a \right)}{\rho_\infty V_\infty \left(\pi c V_\infty \sin \alpha_a \right)} \\ &= \frac{\rho_{ep} V_{ep}^2 - \rho_\infty V_\infty^2}{\rho_\infty V_\infty^2} \end{aligned} \tag{47}$$

Consequently, the fractional increase in the lift per unit span is equivalent to the fractional increase in the dynamic pressure. This relationship as well as an equivalent relationship in terms of the incoming velocity in the propeller slipstream and the freestream velocity are given in Eq. 48.

$$\frac{\Delta L'}{L'_0} = \frac{\Delta q}{q_\infty} = \frac{V_p}{V_\infty} \left(\frac{V_p}{V_\infty} + 2 \right) \tag{48}$$

Note that in each of the other cases shown in Figure 17, the expressions developed have ignored propeller thrust. Here, because the thrust is in the direction of the freestream velocity (i.e., perpendicular to the lift), Eq. 48 holds regardless of the thrust level.

3.1.3.4 Propeller Slipstream Directed Above the Freestream Velocity Vector

For the case shown in Figure 17(d) in which $-i_p > \alpha_a$, one expects both the circulation strength and the local angle of attack of the airfoil to increase compared to the case with only the freestream velocity (i.e., $\Gamma_{ep} > \Gamma_0$ and $\alpha_{ep} > \alpha_a$). The increased angle of attack has several ramifications that must be considered including:

1. The lift per unit span is tilted forward (in the "negative drag" direction), which implies that not all the force produced by the airfoil section is usable for lift, and some will produce thrust.

2. In case of propeller loss, the airfoil angle of attack will suddenly decrease. Although it is advantageous that the wing section will not stall, there will still be a noticeable decrease in lift (from both decreased velocity over the wing section and decreased angle of attack).
3. Care must be taken so that α_{ep} does not exceed the local stall angle, which may be difficult because this local effective angle of attack will vary with power setting. Additionally, if any portion of the wing is unblown, these unblown sections will likely be operating considerably below their maximum lift point (because $\alpha_a < \alpha_{ep} \leq \alpha_{\text{stall}}$) unless there is a large geometric twist in the wing.

Eq. 40, which was given above in Section 3.1.3.1 and is repeated below for convenience, is valid for this case, but here $\kappa > 1$.[6]

$$\frac{\Delta L'}{L'_0} = \kappa \frac{V_{ep}}{V_\infty} - 1$$

Similarly, Eq. 41 and Eq. 42 are valid for this case as well; the only difference here is that $i_p < 0$.

As in Section 3.1.3.1, the percentage lift increase can be compared to the change in dynamic pressure with Eq. 43, which is repeated below for convenience.

$$\frac{\Delta L'}{L'_0} = \frac{q_{ep}\left(\sin\alpha_{ep}/\sin\alpha_a\right) - q_\infty}{q_\infty}$$

Here, $\sin\alpha_{ep}/\sin\alpha_a > 1$ because $\alpha_{ep} > \alpha_a$; therefore, the fractional increase in lift will be greater than that predicted when the thrust is aligned with the freestream velocity (Eq. 48). However, it is prudent to remember that this analysis does not capture stall and has ignored the fact that the thrust vector actually produces negative lift.

3.1.4 Extension to Three Dimensions

There are multiple processes that could be followed to apply the two-dimensional methods presented above to determine the lift increase for a three-dimensional wing.

[6]Because $V_{ep} \geq V_\infty$ and $\kappa > 1$, the lift per unit span increase is greater than the velocity increase in this case.

The first and most laborious involves integrating the lift performance over a number of airfoil sections along the wing. This approach requires that the detailed slipstream characteristics be known at every spanwise location. Such an approach may be advantageous because the local velocity V_p and the corresponding flow angle i_p could be based upon both the local axial and tangential velocities induced by the propeller. However, more detailed propeller performance calculations must be performed to determine the variation of the slipstream velocities aft of the disk. Following this first approach is very similar to the types of calculations that are commonly coupled with lifting line theory that were discussed in Chapter II. Not only is the code execution time increased with this approach, but the insights gained by making the simplifying assumption of the propeller inducing a single, average axial velocity is lost.

The second, simpler approach of extending the models to three dimensions relies on the assumption that the propeller slipstream is directed purely in the axial direction and can be abstracted to a single average value as was discussed above in relation to Eq. 33. This assumption has been made extensively in the literature with roots in simple momentum theory [76, 77]. Koning's classic theory [93] and nearly every work performed through the early 1970s accepted this assumption [94, 95, 98, 99, 109]. Although the results from the assumptions of a "jet" blowing a wing have often predicted greater lift increases than observed in experiments, the assumption provides a reasonable starting point from which more detailed analyses can be performed. Additionally, one of the poor assumptions inherent in many of the previous studies will be addressed below in Section 3.2 to greatly increase the accuracy of this method. Consequently, this second approach is adopted for the conceptual design analyses of interest in this dissertation.

A simple extension of the methods above to three dimensions can be performed as follows when adopting the second approach described above. The fractional increase

in the wing lift due to that of a single propeller can be estimated with Eq. 49

$$\frac{\Delta C_L}{C_{L_0}} = \left(\frac{\Delta L'}{L'_0}\right)\left(\frac{S_{\text{blown}}}{S}\right) \tag{49}$$

where $\Delta L'/L'_0$ can be determined from the equation above (either Eq. 42, 45, or 48) that is appropriate for the geometry under consideration, S is the wing area, and S_{blown} is the area of the wing immersed in the slipstream of the single propeller. This equation makes several assumptions in addition to those made above to determine $\Delta L'/L'_0$:

- The slipstream velocity is assumed to be constant behind the propeller. Because of this assumption, this model can very easily be paired with basic momentum theory, which assumes a uniform velocity increase aft of a propeller disk.
- Swirl is either negligible or the effects of swirl on one side of the propeller disk effectively cancel out the effects of swirl on the opposite side of the disk.[7]
- The twist distribution of the wing behind the propeller is constant or nearly-constant. (If it is not constant, an average value for the absolute angle of attack can be used.)
- The lift per unit span is constant over all wing sections blown by the propeller.
- No section of the wing behind the propeller is at or above stall.
- The lift of a three-dimensional wing will be equivalent to a summation of the lift over isolated two-dimensional airfoil sections. This assumption implies that the induced angle of attack is effectively zero. Clearly this assumption is invalid for wing sections near the tips and for low-aspect ratio wings; consequently, care should be exercised if studying high-lift propellers near the wing tip or installed on low-aspect ratio wings. Additionally, it should be noted that the increases in circulation possible from propeller slipstreams may also impact the induced

[7]Swirl will generally act to increase the angle of attack of wing sections downstream of the prop on the upward-moving half of the propeller disk while decreasing the angle of attack behind the downward-moving side. So long as the swirl profile is fairly uniform and the wing has relatively little twist, these effects will cancel one another in terms of lift.

angle of attack distribution over the span considerably. These impacts are not captured in this model.

One question that arises is how the blown area should be calculated. Generally, the slipstream from the propeller will contract as it moves aft, so the span of the blown portion aft of the propeller will be reduced from the diameter of the propeller. The further ahead of the wing the propeller is located the larger the slipstream contraction. One estimate of the slipstream contraction can be made from momentum theory principles and is shown in Eq. 50 [2], where D_s is the contracted diameter, D is the propeller diameter, a is the axial induction factor, and x is the (dimensional) axial distance aft of the propeller.

$$D_s = D\sqrt{\frac{1+a}{1+a\left(1+\frac{x}{\sqrt{x^2+D^2/4}}\right)}} \tag{50}$$

However, this equation should be used with caution as the calculation of the slipstream contraction is not necessarily a simple task. For example, the nacelle can have significant impacts on how much the slipstream contracts. Veldhuis [1] demonstrates that the presence of the nacelle just aft of the propeller will decrease the contraction that occurs initially, but if the nacelle is contoured (i.e., possesses a faired shape moving aft to a point or small radius at the aft end of the nacelle), the slipstream tends to follow this contour, which can increase the slipstream contraction that occurs. Similarly, the presence of the wing will also impact the slipstream contraction. Additionally, Jameson [109] bases his entire theoretical derivation on the approximation that the slipstreams of adjacent propellers will merge to form one wide slipstream, which seems to imply that the propeller slipstreams actually expand spanwise. Furthermore, the effects of a propeller slipstream on the wing lift distribution are not limited to the region immediately aft of the propeller as was discussed in Chapter II.[8] Finally, if the propellers are lightly loaded, the slipstream contraction is only a few

[8]Specifically, see Figure 10.

percent at most [87, 1]. Based on all these considerations, for early-phase design studies and particularly for true "back of the envelope" calculations, the blown area can be approximated assuming that there is no contraction of the propeller slipstream.

Eq. 49 can be generalized to account for wings with N propellers and/or sections for integration as shown in Eq. 51.[9] In this equation, the percentage lift increase of the wing section i and the percentage of the span in the propeller slipstream of section i are combined with all other sections to give the net effect on the entire wing.

$$\frac{\Delta C_L}{C_{L_0}} = \sum_{i=1}^{N} \left(\frac{\Delta L'}{L'_0} \right)_i \left(\frac{S_{\text{blown}}}{S} \right)_i \tag{51}$$

3.1.5 Intermediate Summary of the Two-Dimensional Model

For configurations in which the velocity over the wing is increased by the presence of a propeller slipstream, the orientation of the slipstream relative to the local airfoil sections can play a large role in the lift augmentation. Simple logic that estimates the lift augmentation to be directly proportional to the increase in dynamic pressure may lead to overly optimistic predictions of wing lift. Additionally, designers should not only consider the lift augmentation but also the safety implications of a particular configuration in case of a motor failure.

If the wing is operated so that the angle of attack of many wing sections are near stall, the maximum lift benefit is expected when the propeller is inclined so that the thrust is directly aligned with the incoming freestream velocity vector (i.e., $i_p = -\alpha_a$) as shown in Figure 17(c). This installation has limited impacts on the local angles of attack downstream of the prop,[10] which limits the potential for a propeller failure to induce a stall.

If the wing is operated so that the angle of attack of all wing sections are noticeably below stall, the maximum lift benefit may be experienced when the local propeller

[9] These sections may contain different wing twist or could be sections where the first, laborious approach described above is followed.

[10] only swirl will cause deviations in the angle of attack

slipstream is angled above the freestream velocity vector as shown in Figure 17(d) provided that the negative lift component from the thrust from the propellers is not too great and that the effective angle of attack of wing sections aft of the propeller remain below stall.

If the propeller thrust is very large, it may be most advantageous for the overall lift of the configuration to have a component of the thrust vector tilted in the lift direction (such as in Figure 17(a) or Figure 17(b)). However, these installations may be dangerous in the event of a motor failure due to the high likelihood of sections of the wing stalling that may lead to a spin.

It should be noted that the model will break down in situations where the freestream velocity is zero (or near zero) because the equations are formulated in terms of percentage changes and there would be zero lift at zero forward speed without blowing. Similarly, other conditions where the airfoil would produce zero lift (e.g., a symmetric airfoil at zero angle of attack) are also unable to be evaluated with the model as presented for the same reasons. So long as these conditions are directly avoided, extrapolation from conditions with finite lift in the baseline case can be used as first-cut estimates of performance.

Finally, the two-dimensional model presented above is predicated on the ability to determine the slipstream velocity from the propeller, V_p, which is not a trivial task. As was discussed in Chapter II, the velocity field in a propeller slipstream is complex and varies radially and circumferentially. The slipstream characteristics can be predicted with tools of varying order, and velocity variations in the slipstream can be modeled if a detailed extension of the method to three-dimensions is performed as described in Section 3.1.4.[11] The simpler extension of the method to three dimensions requires only an effective average value for V_p to be estimated. This average V_p value can be obtained in many ways, but caution should be exercised in its determination.

[11] i.e., where the lift over many airfoil sections is integrated to determine the total lift.

Factors such as propeller tip losses and the "dead zone" aft of the nacelle will tend to reduce the effective V_p value that would be calculated from a simple method such as basic momentum theory. However, even with good estimates of the value(s) of V_p generated by a propeller, the method presented above will typically over-predict the lift augmentation. The primary contributing factor to this over-prediction is addressed in the following section.

3.2 Accounting for Propeller Slipstream Height

The above analysis has assumed that the airfoil section is completely immersed in a very wide, incompressible slipstream flow. However, for the designs of interest in this dissertation such as that shown in Figure 6, the diameter of the propeller will likely be small compared to the wing chord. In these cases, the assumptions made in the simple models presented above will not directly hold and must be modified.

The flow around an airfoil in a propeller slipstream can be viewed as a special case of an airfoil in the vicinity of a boundary between multiple non-uniform streams. For cases where the propeller slipstream is aligned with the freestream velocity (i.e., where $i_p = -\alpha_a$), the problem reduces to an airfoil in non-uniform parallel streams. Such flows have been analyzed in the past [112, 4, 3, 113]. The resulting geometry for such a flow is shown in Figure 18. In this figure, the airfoil is placed in a "jet" of finite height with velocity $V_j > V_\infty$. If the increased velocity in the jet is due to a propeller then $V_j = V_{ep} = V_\infty + V_p$ following the notation above. The height of the slipstream is denoted as $2R$ and the chord length of the airfoil is c.

Consider a flat plate in the slipstream of a propeller as shown in Figure 18. If the notation from the previous sections is maintained, then the geometry in the figure implies that $i_p = -\alpha_a$, $\alpha_{ep} = \alpha_a$, and $V_j = V_{ep} = V_\infty + V_p$. If the lift over the flat plate is assumed to be proportional to the dynamic pressure increase (as the geometry and the model presented above in Section 3.1.3.3 imply) and the lift curve slope of the

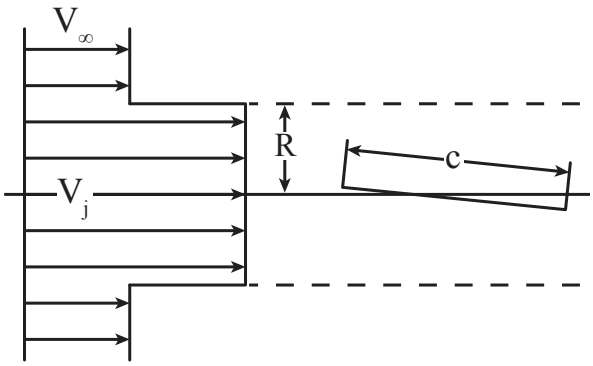

Figure 18: A flat plate airfoil placed in a slipstream of finite height

flat plate is $a_0 = 2\pi$ rad^{-1}, then the section lift coefficient can be expressed as Eq. 52.

$$c_l = \frac{V_j^2}{V_\infty^2}(2\pi)\,\alpha_a \tag{52}$$

To compare the effects of different slipstream velocities on the lift of the flat plate, a lift multiplier, K_L, is defined as the ratio of the lift generated by a flat plate in a slipstream, c_l, and the lift produced by the flat plate in the absence of the slipstream, $(c_l)_\infty$. For the flat plate, which has a lift curve slope of 2π rad^{-1}, a zero-lift angle of attack of 0°, and an absolute angle of attack α_a, the lift multiplier can be expressed in several forms as shown in Eq. 53.

$$K_L = \frac{c_l}{(c_l)_\infty} = \frac{c_l}{2\pi\alpha_a} = \frac{V_j^2}{V_\infty^2} \tag{53}$$

For the case where $V_j = 2V_\infty$, the lift is predicted by the prior theory to increase by a factor of four (i.e., $K_L = 4$); similarly, if $V_j = 1.5V_\infty$, then $K_L = 2.25$.

In reality, these lift multiplier values of 4 and 2.25 are often overly optimistic. Ting et al. [3] show that for a finite slipstream height, the lift produced by an airfoil is less than if the airfoil were located in a single stream with velocity V_j. The effect of slipstream height on the flat plate lift is shown in Figure 19 for two values of V_j: $1.5V_\infty$ and $2V_\infty$ [3]. As shown in the figure, the lift multiplier values predicted by the theory developed above (i.e., Eq. 53) hold only in certain situations where the wing

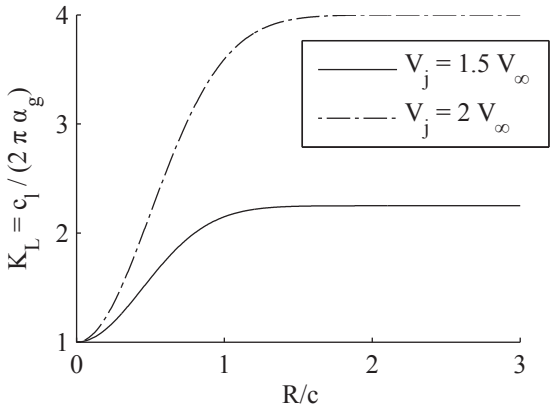

Figure 19: Effect of slipstream height on the lift produced by a flat plate [reproduced from [3]]

chord is relatively small in comparison to the slipstream height. For geometries in which the height of the slipstream is on the order of twice the chord length or less (i.e., $R/c \lesssim 1$), the studies presented by Ting et al. indicate considerably smaller increases in lift as compared to the prior theory. In the limit as the slipstream height becomes infinitely small, the lift becomes equivalent to a flat plate in a freestream velocity of V_∞, and consequently $K_L = 1$.

This decrease in lift with slipstream height was observed by Ting et al. in purely two-dimensional simulations. It is interesting to note that Smelt and Davies [2] observed a similar decrease in lift in three-dimensional experiments when the propeller diameter was small in comparison to the wing chord. They attributed this decreased lift to a three-dimensional effect—i.e., shed vortices from the wing at the edges of the slipstream boundary—but provided no formal theoretical derivation to support their claim. It appears that in reality Smelt and Davies were actually observing the same two-dimensional effect described by Ting et al..

If the λ parameter introduced by Smelt and Davies (which was introduced in Section 2.3.3.1 and shown in Figure 11) that describes the predicted lift increase is viewed in a two-dimensional sense as a function of R/c (where R is approximately

equivalent to the propeller radius) as opposed to the aspect ratio immersed in the slipstream, sigmoid-like curves similar to those shown in Figure 19 results. However, the two curves in Figure 19 from Ting et al. and the λ parameter described by Smelt and Davies all indicate different trends of how lift augmentation varies with the slipstream height. Consequently, a more definitive quantification of this lift variation is desired if the model presented above is to provide accurate results.

3.2.1 Quantifying Slipstream Height Impacts

The trends shown above in Figure 19 indicate that finite slipstream heights can be accounted for in the theory presented above for wide slipstreams by a simple modification to the slipstream velocity—i.e., a reduced slipstream height can effectively be modeled by a reduced slipstream velocity. Specifically, the theory presented in Section 3.1 can be modified by applying a multiplicative factor, β, to the propeller slipstream velocity, V_p, to determine an effective slipstream velocity, βV_p. The impact of slipstream heights can then be quantified if a relationship between the β parameter and the slipstream height is determined.

The lift multiplier results presented by Ting et al. [3] imply the variation of the β parameter as shown in Figure 20. This sigmoid-like variation begins at a value of 0 at $R/c = 0$ and increases to asymptotically approach 1 at $R/c \to \infty$. The two different slipstream velocities imply slightly different variations of β with slipstream height, but each has reached a value of over 0.95 by $R/c = 1.25$.

The λ parameter described by Smelt and Davies implies a different variation of β with the slipstream height than the curves shown in Figure 20. The minimum value given for λ is 1, and when $\lambda = 1$ Smelt and Davies predict the lift increase to be proportional to the velocity increase. This implies that when $R/c = 0$ (i.e., for values of aspect ratio immersed in the slipstream of zero) there is still some finite augmentation to the lift over freestream. The minimum value of β predicted by Smelt

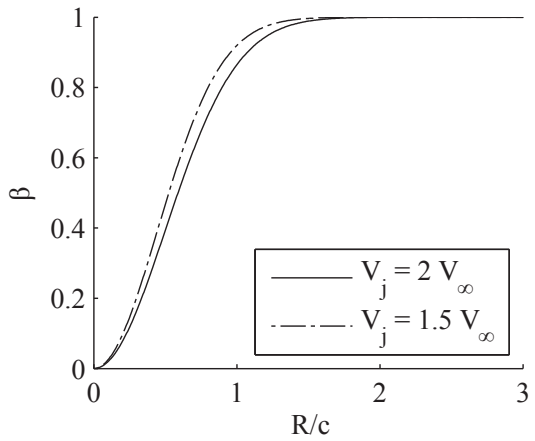

Figure 20: Effective β values determined from the lift multiplier relationships provided by Ting et al.

and Davies is greater than zero, and consequently the variation of the β parameter that could be derived from the work of Smelt and Davies is considerably different than that derived from Ting et al. (i.e., that shown in Figure 20).

Despite the differences in the implied β values between these references, they both imply that there is some variation of the lift when the slipstream height changes. Furthermore, Ting et al. show that the value of β will also vary with the slipstream velocity. Additionally, the distance the disk is placed upstream of the airfoil can impact the lift generated because the slipstream contracts and accelerates moving aft of the propeller. Consequently, it is hypothesized that a model for β can be developed based on the height of the slipstream, the velocity in the slipstream, and the location of the propeller disk upstream of the wing. By applying the β parameter to the equations presented above, the impacts of these three parameters can be incorporated into the simple model.

3.2.1.1 OVERFLOW Simulations

To determine a model for the β parameter, two-dimensional, inviscid simulations of a modified NACA 0012 airfoil[12] with an actuator disk upstream were performed in OVERFLOW, which is a structured overset grid CFD flow solver developed at NASA [114, 115]. The grid was designed so that there was a distance of 100 chord lengths between the airfoil and the outer domain, and visualizations of the grid are presented in Appendix A. Each run is made by specifying a location of the actuator disk relative to the airfoil, the freestream velocity, the pressure increase across the actuator disk, and the angle of attack of the airfoil. The airfoil was pivoted about the quarter chord point and the disk placed perpendicular to the freestream velocity vector.

It should be noted that simple, linearized potential flow models are incapable of accurately describing the flow when the slipstream height is small. Chow et al. demonstrate that to adequately capture the impacts of non-uniform streams such as the scenario shown in Figure 18, nonlinear equations that account for the airfoil's influence on the slipstream[13] must be solved [4]. Additionally, the simulation results presented below in Figure 23 will make clear that the influence of the airfoil on the propeller slipstream cannot be ignored. Although very detailed lower-order methods that model the movement of the shed vorticity from the disk as influenced by the airfoil[14] may be able to model the impacts of small slipstream heights, the increased computational expense of these methods is still likely to preclude employing such models directly in early-phase design studies. Because computations must be performed prior to performing trade studies, more detailed "experiments" with CFD were performed to more accurately model the physics of the problem.

[12] i.e., one with zero trailing edge thickness

[13] This assumption is stated by Chow et al. as follows: "it is usually assumed that the disturbance of an airfoil on the jet stream behind the propeller is small, so that the vorticity and stagnation pressure are carried along the streamline of the undisturbed jet." [4].

[14] e.g., models with freely deforming wakes that require time stepping or wake relaxation

An actuator disk representation of a propeller should be more accurate for predicting lift augmentation from a propeller than the non-uniform freestreams considered by Ting et al. because non-uniform freestreams will only model variations of slipstream velocity profile and do not take into account other effects present behind a propeller such as static pressure changes. Inviscid simulations were performed because Ting et al. showed the decrease in lift with slipstream height to be an inviscid effect, and many more runs could be performed in the same period of time.

Although it would be ideal to run a CFD solution for any configuration of interest, the run time of the code is too long to be practical for use in early-phase design. Furthermore, it is desired to develop a model that will provide a designer general insights about how the behavior of the β parameter and lift augmentation varies. Therefore, a surrogate model of the OVERFLOW simulations is desired so that a designer can rapidly determine the effective velocity in a propeller slipstream (i.e., βV_p) for a given geometry and propeller operating condition. This surrogate model should be a function of easily identifiable design parameters that drive the effective lift augmentation.

A surrogate model for β was developed as a function of three design parameters:

1. the ratio of the disk radius to the chord of the airfoil (i.e., R/c),
2. the velocity of the contracted slipstream far downstream of the disk, and
3. the distance upstream of the leading edge the disk is placed.

For the model developed in this dissertation, the vertical height of the disk and the angle of the disk relative to the freestream were kept constant.

Simulations were performed at a freestream Mach number of 0.2 with total Mach numbers far downstream of the actuator disk in the slipstream (i.e., V_j) of 0.25, 0.3, 0.4, and 0.45, which correspond to values of V_j/V_∞ of 1.25, 1.5, 2, and 2.25, respectively.[15] The ratio of the radius of the actuator disk to the chord length of the

[15]Ideally, the freestream Mach number would have been reduced to approximately 0.1 to more

airfoil (i.e., R/c) was varied from 0.125 to 3.0. The distance the actuator disk was placed upstream of the wing leading edge, which is denoted here as u, was varied from values of 25% of the chord length up to three times the chord (or from $u/c = 0.25$ to $u/c = 3$). The raw lift coefficient results for all these simulations can be found in Appendix A.

The largest number of simulations were run with a pressure jump over the actuator that would create a downstream slipstream velocity of two times the freestream (i.e., $V_j/V_\infty = 2$). This speed was selected because it is on the higher-end of slipstream velocity ratios Borer et al. [68] found to be practically obtainable from high-lift propellers at the speed and diameter ranges of interest here and to maintain some level of parity with the calculations of Ting et al. [3] who studied this velocity ratio.[16]

The results from the simulations are presented here in terms of the effective β parameter implied by the lift coefficient values output by the simulations. To determine β, an isolated airfoil is first run in OVERFLOW at the desired angle of attack. The airfoil is then run at the same angle of attack with an actuator disk upstream of it. The lift multiplier, K_L, is found as the ratio of the lift coefficient with blowing to the c_l of the isolated airfoil. Since the slipstream is aligned with the freestream, the theory presented above indicates that the lift multiplier should be equal to the ratio of V_j^2/V_∞^2 or $(V_p + V_\infty)^2/V_\infty^2$. However, the finite slipstream height (and other effects) may cause the lift to differ from this value. It is desired to find the apparent V_p (i.e., βV_p) that can be used in the above theory to yield the calculated lift multiplier. Said differently, a value of β is sought that will satisfy Eq. 54.

$$K_L = (\beta V_p + V_\infty)^2/V_\infty^2 \tag{54}$$

closely approximate the landing conditions where high-lift propellers will be operating; however, due to the stiffness of the Euler equations and the large changes in the flow field near the edges of the actuator disk slipstream, simulations were unable to adequately converge over the desired range of slipstream velocity values at a freestream speed of less than Mach 0.2.

[16] Recall Figure 20.

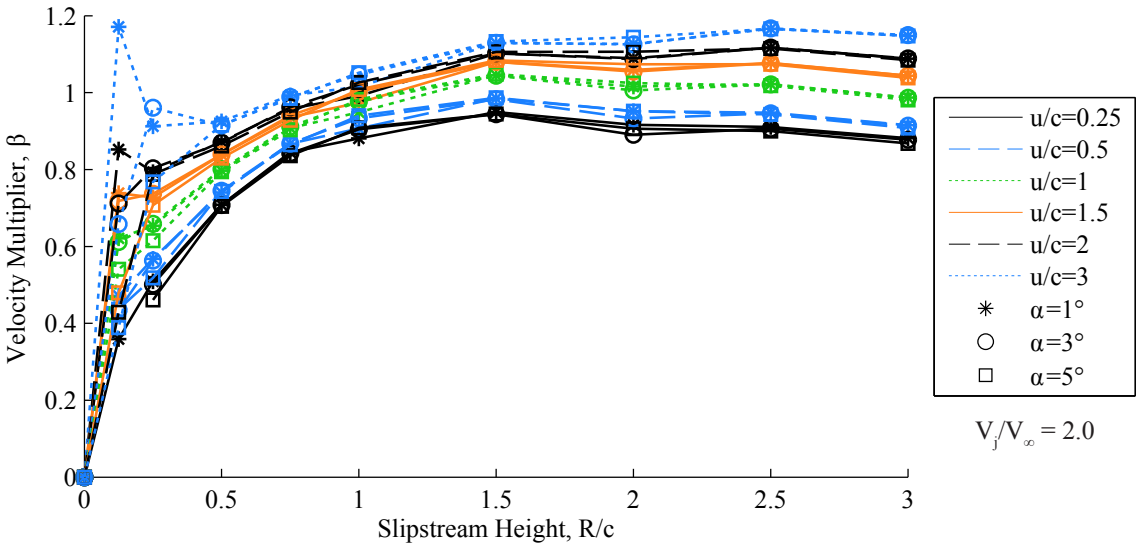

Figure 21: β values as a function of slipstream height and upstream distance of the actuator disk determined from two-dimensional OVERFLOW simulations with the actuator creating $V_j/V_\infty = 2.0$ far downstream at 1°, 3°, and 5° angles of attack

Solving Eq. 54 for β with the understanding that β must be greater than zero yields Eq. 55, which is used to determine the implied β from the OVERFLOW simulations.

$$\beta = \frac{\sqrt{K_L} - 1}{V_p/V_\infty} = \frac{\sqrt{K_L} - 1}{V_j/V_\infty - 1} \tag{55}$$

The results of the OVERFLOW simulations for the $V_j/V_\infty = 2$ case are presented in Figure 21. This figure plots the β value as a function of the ratio of radius of the actuator disk to the chord length of the airfoil (R/c). Nine different R/c values were evaluated: 0.125, 0.25, 0.5, 0.75, 1, 1.5, 2, 2.5, and 3. This figure contains data from runs at six different u/c distances—0.25, 0.5, 1, 1.5, 2, and 3—as well as three angles of attack for each R/c and u/c. The angles of attack of 1°, 3°, and 5° are denoted with asterisks, circles, and squares, respectively. The different line types and colors used in the figure refer to various u/c values as shown in the legend.

Figure 21 demonstrates that there is a strong influence on the lift generated from both the slipstream height and the distance upstream the disk is placed. Generally, increasing the distance of the actuator disk upstream increases the lift augmented by

the airfoil (at a given R/c). This lift increase can be attributed to the increase in velocity that occurs as the slipstream contracts—greater distances upstream lead to increases in slipstream contraction and slipstream velocity.

A potentially vexing observation from Figure 21 is that there are many cases where $\beta > 1$. The theory presented above and the results from Ting et al. shown in Figure 20 indicate that $\beta = 1$ is an effective upper limit. However, these two theories are based on the assumption that the flow properties (i.e., density, temperature, and pressure) in the slipstream are unchanged from the freestream. In the OVERFLOW simulations, a static pressure increase is prescribed across the disk, which also results in changes in the temperature and density. These changes are more representative of what would actually occur in the flow aft of the propeller than the incompressible flow assumptions made by Ting et al. and in the theory discussed above. By incorporating the results from the OVERFLOW simulations into a model for β that will be applied to the simple theory presented above, the resulting model will implicitly incorporate these flow property changes and, consequently, improve in accuracy.

Additionally, Figure 21 indicates that differences in the lift multiplier between angles of attack are quite small with the exception of very low R/c values.[17] This observation helps justify the validity of the simple model presented above that is effectively agnostic to the angle of attack. Practically, this effective elimination of angle of attack as an independent variable is advantageous because it allows an accurate model to be built without including angle of attack as an input variable.[18]

Figure 22 shows the same data as Figure 21, but is zoomed in on the low R/c values to help illustrate the large differences in lift observed at low R/c values. The differences in the effective β values at very low R/c values (i.e., those at $R/c = 0.125$

[17]The reasons for the differences in β between angles of attack at low R/c values are discussed in the following paragraphs.

[18]Once stall is reached the variation of the lift multiplier with angle of attack may be significant. However, it is assumed here that all airfoil sections are not stalled.

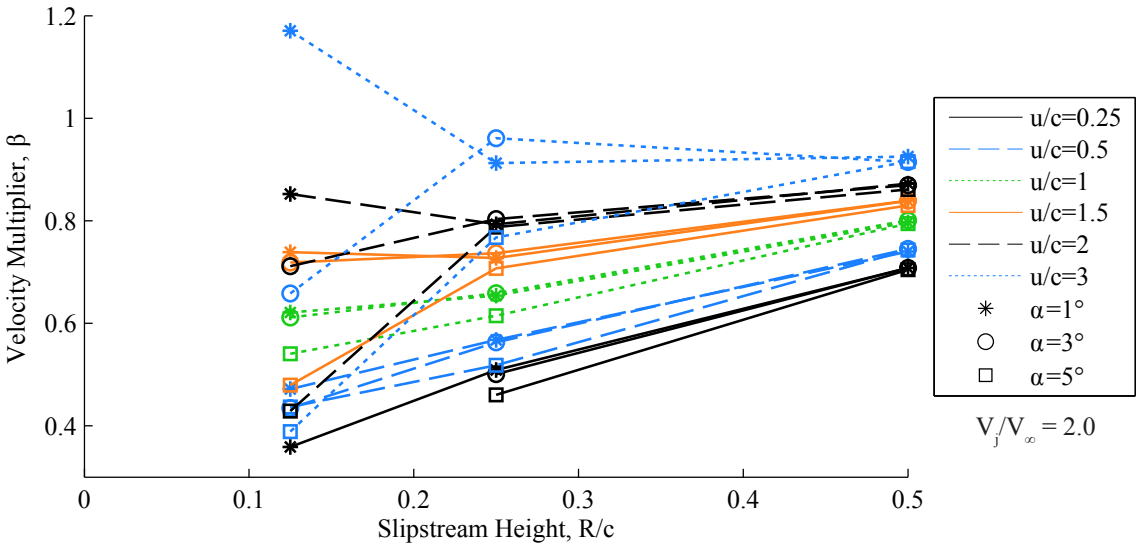

Figure 22: β values as a function of slipstream height and upstream distance of the actuator disk determined from two-dimensional OVERFLOW simulations with the actuator creating $V_j/V_\infty = 2.0$ far downstream at 1°, 3°, and 5° angles of attack

and also at $R/c = 0.25$ for $u/c = 3$) result from large portions of the slipstream being pulled over the airfoil as is illustrated for two specific cases in Figure 23. The greatest differences in β values occur at the largest u/c values because the further ahead of the airfoil the disk is located, the further the slipstream height at the airfoil is reduced (due to slipstream contraction) and the longer the airfoil circulation has to impact the slipstream's direction of travel. The very large β of 1.17 found at $\alpha = 1°$, $u/c = 3$, and $R/c = 0.125$ is caused by an upper-surface blowing-like effect where the slipstream is pulled over the upper surface of the airfoil and continues to follow the upper surface downstream as shown in Figure 23(a). This can be contrasted with the 5° angle of attack case at the same u/c and R/c values that has $\beta = 0.39$ that is shown in Figure 23(b). At the higher angle of attack, the airfoil circulation is increased, which causes the slipstream to be turned upward more noticeably and further ahead of the airfoil. This increased turning pushes the slipstream further above the airfoil, and it does not turn back downward to follow the upper surface of the airfoil in the same manner as observed in the 1° angle of attack case. The slipstream is completely above

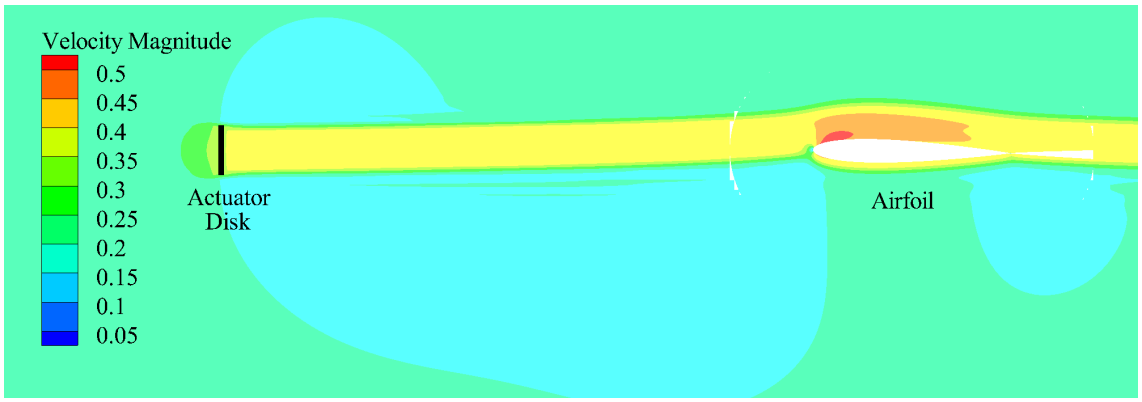

(a) 1° angle of attack

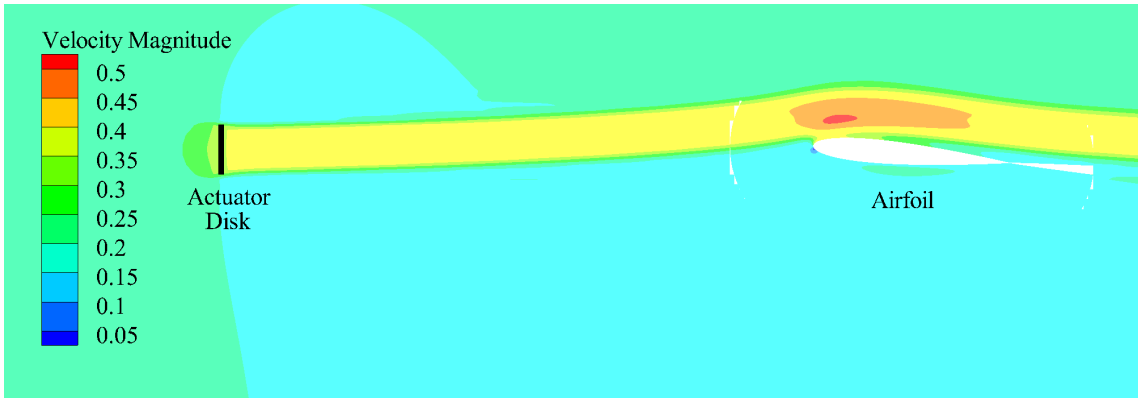

(b) 5° angle of attack

Figure 23: Mach number contours from OVERFLOW simulation with $R/c = 0.125$, $u/c = 3.0$, and $V_j/V_\infty = 2.0$ showing the turning of the slipstream over the upper surface of the airfoil

the airfoil and a region of flow more similar to the case without an actuator disk is present just above the airfoil, which causes the reduced lift.

Ultimately the sort of upper-surface blowing-like effects seen at very low R/c and higher u/c values are not of particular interest for this present dissertation. Although very large increases in lift may occur with an upper-surface blowing effect, this lift increase is quite dependent on the angle of attack at which the aircraft would operate. It is desired that the high-lift propellers be more robust so that they can successfully augment lift over a wide range of angles of attack. Furthermore, it is unlikely that functional high-lift propellers will be placed sufficiently far ahead of the wing so that their slipstreams can effectively be turned over the upper surface by the airfoil's

circulation. Placing propellers very far in front of the wing will incur structural penalties and increase the skin friction drag. It is envisioned that most high-lift propellers will be placed relatively close to one radius ahead of the wing.[19] Therefore, placing the propellers sufficiently far ahead of the wing to obtain appreciable turning of the slipstream over the wing seems a remote possibility.

Another general observation from Figure 21 is that the lift augmentation from increasing slipstream heights is not a simple monotonically increasing function as the simulations of Ting et al. (i.e., Figure 20) suggest. The general decrease in lift for R/c values above approximately 1.5 is caused by the effects of slipstream contraction/acceleration. For larger diameter actuator disks (i.e., larger R/c values), the flow must travel a greater absolute distance downstream of the disk before it is fully accelerated than for a smaller disk. Therefore, if a small diameter actuator disk is placed at the same absolute distance from the airfoil as a large actuator disk, then the flow will have accelerated relatively more aft of the small disk than the large one. Since the curves are shown at constant values of the absolute distance upstream of the airfoil, there is a decrease in lift augmentation as R/c becomes large.

The discussion thus far has focused on a single far downstream slipstream velocity (i.e., $V_j/V_\infty = 2$), but the trends discussed above generally hold true for all other velocities studied. The OVERFLOW simulation results for the lowest velocity case where $V_j/V_\infty = 1.25$ are shown in Figure 24. The effective β values from the simulations for a velocity ratio of 1.5 can be seen in Figure 25, and the results at the fastest slipstream velocity of $V_j/V_\infty = 2.25$ are shown in Figure 26. Each of these figures only plots results for u/c values from 0.25 to 1.5 (at most) because it was determined that larger distances ahead of the airfoil were impractical for high-lift

[19]The exact placement of the propellers will depend on many factors. However, two primary factors include folding of the propeller blades, which requires them to be placed almost one radius ahead of the wing, and structural considerations, which will generally favor propellers placed as close to the wing spar as possible. From these two factors it is assumed here that they will be placed close to one radius ahead of the wing.

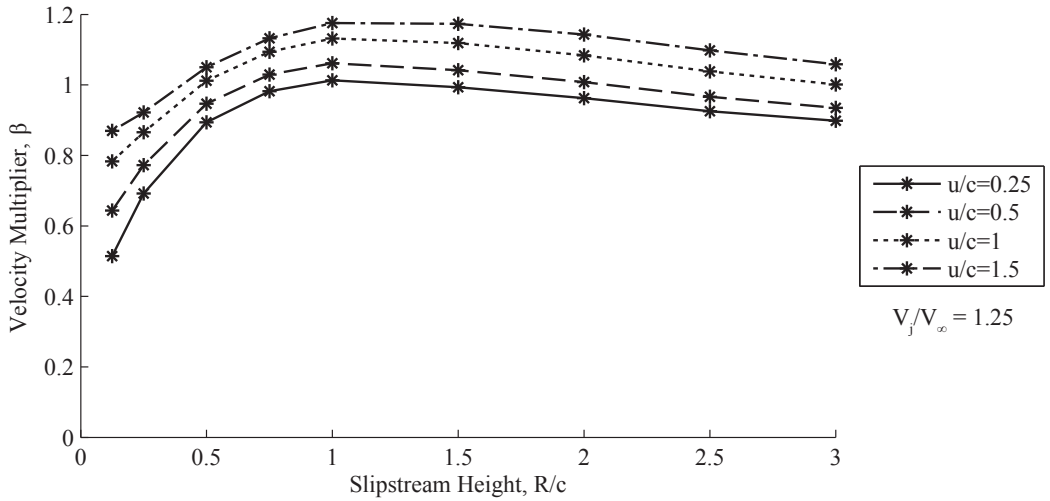

Figure 24: β values as a function of slipstream height and upstream distance of the actuator disk determined from two-dimensional OVERFLOW simulations with the actuator creating $V_j/V_\infty = 1.25$ far downstream at a 1° angle of attack

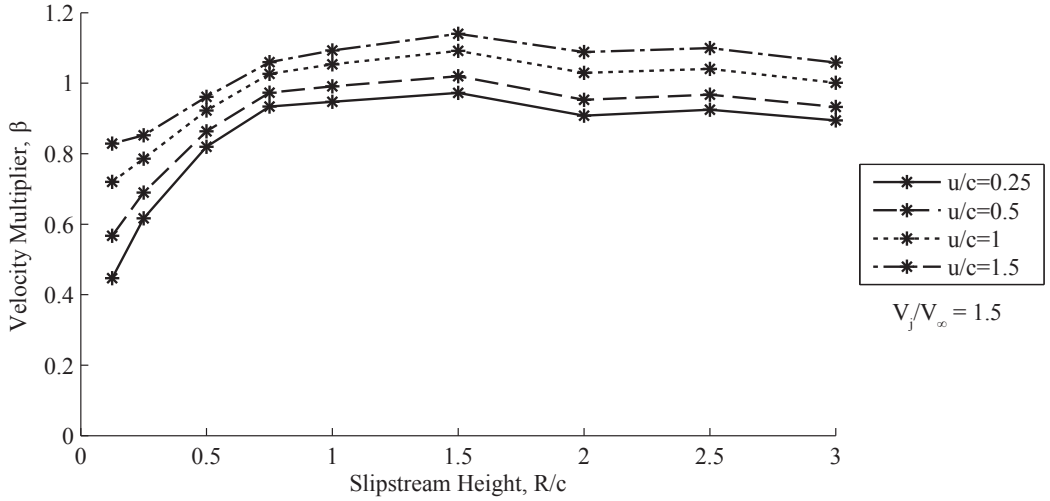

Figure 25: β values as a function of slipstream height and upstream distance of the actuator disk determined from two-dimensional OVERFLOW simulations with the actuator creating $V_j/V_\infty = 1.5$ far downstream at a 1° angle of attack

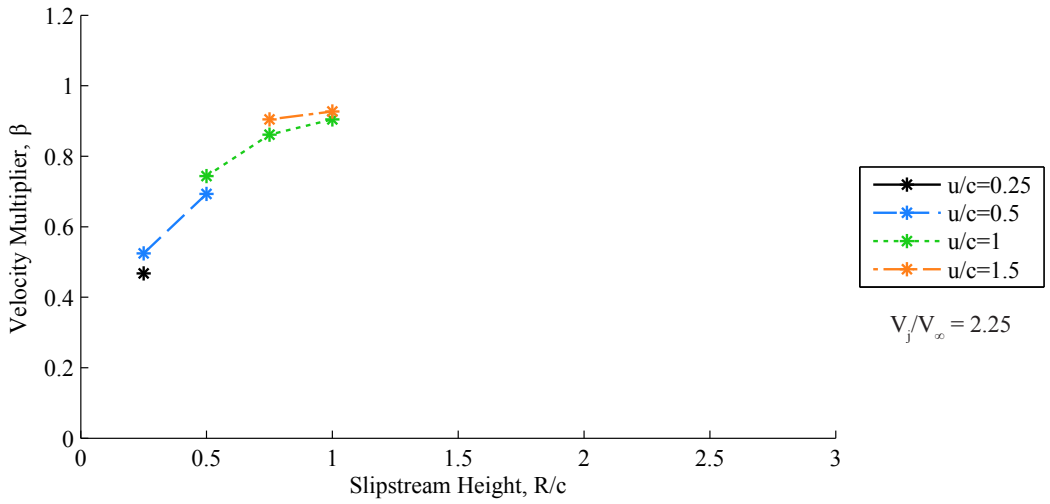

Figure 26: β values as a function of slipstream height and upstream distance of the actuator disk determined from two-dimensional OVERFLOW simulations with the actuator creating $V_j/V_\infty = 2.25$ far downstream at a 1° angle of attack

propeller placement.[20] Additionally, relatively few cases were run at the velocity ratio of $V_j/V_\infty = 2.25$ because the work of Borer et al. [68] indicates that it is difficult to develop practical propeller designs in the speed and diameter ranges of interest here that produce this velocity ratio.[21] The R/c and u/c values selected to run were based on the logic that most high-lift propellers would be placed roughly one radius ahead of the airfoil and that high-lift props will likely be of relatively small diameter.

Another observation from the OVERFLOW simulation results can be made from the runs at $V_j/V_\infty = 1.5$ and $V_j/V_\infty = 2$ (i.e., Figures 25 and 21): there is a decrease in lift at $R/c = 2$ that seems out of place with the other prevailing trends (i.e., generally increasing up to a point then decreasing). Although it is not completely clear what causes this decrease in lift, it is believed to be a result of the interaction of the pressure field around the airfoil with the boundaries of the actuator disk slipstream.

[20]This is primarily a result of the larger structural mass and increased wetted area that will occur the further upstream of the wing the disk is placed. Additionally, most conventional propellers are placed much closer to the wing than 1.5 chord lengths. Consequently, it would have been justifiable to study even less extreme of a limit on u/c.

[21]See Figure 3 in Reference [68]. In fact, Borer et al. found no designs with a dynamic pressure of even 5, which corresponds to $V_j/V_\infty \approx 2.24$.

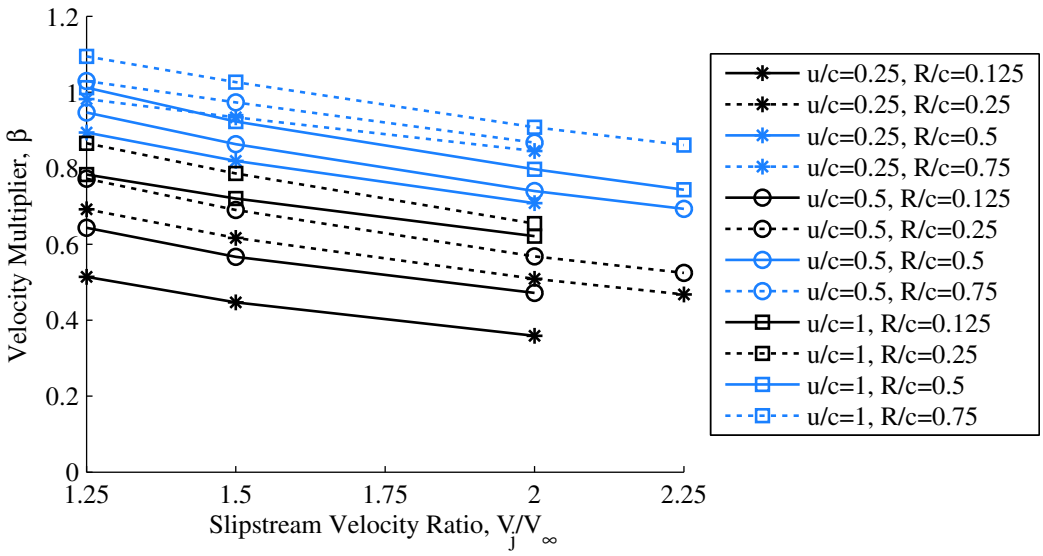

Figure 27: β values as a function of slipstream velocity ratio (V_j/V_∞) for various actuator disk heights and upstream distances of the actuator disk determined from two-dimensional OVERFLOW simulations

The information presented thus far indicates variations in the lift augmentation as the slipstream velocity is varied, but these changes are difficult to ascertain from the separate figures. To help visualize the variations in the effective β parameter with the slipstream velocity, a reduced set of the data presented above is shown in Figure 27.

Figure 27 plots the β value obtained from the OVERFLOW simulations as a function of V_j/V_∞ for three u/c values and four R/c values. It is clear from this figure that there is a general decrease in the β parameter as the slipstream velocity increases for the same disk height and upstream location. This decrease in β implies that the lift augmentation becomes less effective the faster the slipstream velocity. Consequently, it may be more advantageous in certain situations to place the propeller farther upstream and/or use a larger diameter propeller than to attempt to increase the slipstream velocity by a large amount.

3.2.1.2 Surrogate Model

The data obtained from the OVERFLOW simulations and discussed above is useful for understanding the general trends that exist in the design space when varying the disk height and distance from the airfoil as well as the slipstream velocity. To make this data useful in a computational design environment, a surrogate model was fit to the data presented above in Figures 21, 24, and 25.[22] To fit the surrogate model, four separate fourth-order polynomials in the form of Eq. 56 were fit to the data at V_j/V_∞ values of 1.25, 1.5, and 2.0 resulting in 12 total polynomials.

$$\beta = f_0 + f_1\left(\frac{R}{c}\right) + f_2\left(\frac{R}{c}\right)^2 + f_3\left(\frac{R}{c}\right)^3 + f_4\left(\frac{R}{c}\right)^4 \tag{56}$$

The four curve fits at each V_j/V_∞ value correspond to u/c values of 0.25, 0.5, 1.0, and 1.5. Values of u/c greater than 1.5 were ignored in fitting the model because these were deemed larger than would be expected from configurations with high-lift propellers as discussed above.[23]

Next, the variation of the each of the coefficients (f_0, f_1, ..., f_4) was approximated as a second order response surface equation of the u/c and V_j/V_∞ variables as shown

[22]The fastest slipstream velocity—i.e., the data in Figure 26—was ignored in fitting the surrogate model because they represent a higher speed than is expected in practice from high-lift propellers as discussed above. Instead, these points were used as validation points to test the goodness of the fit as will be discussed below.

[23]If folding propellers are desired, then this u/c limit effectively limits the propeller radius to be on the order of $R/c = 1.5$ (which is likely larger than high-lift propellers will be in practice). Larger R/c values are included in the model so that it can be applied to non-folding propeller designs as well.

in Eq. 57.

$$
\begin{aligned}
f_i &= k_{i,0} + k_{i,1}\left(\frac{u}{c}\right) + k_{i,2}\left(\frac{u}{c}\right)^2 + k_{i,3}\left(\frac{u}{c}\right)\left(\frac{V_j}{V_\infty}\right) + k_{i,4}\left(\frac{V_j}{V_\infty}\right) + k_{i,5}\left(\frac{V_j}{V_\infty}\right)^2 \\
&= \begin{bmatrix} k_{i,0} & k_{i,1} & k_{i,2} & k_{i,3} & k_{i,4} & k_{i,5} \end{bmatrix} \begin{bmatrix} 1 \\ u/c \\ (u/c)^2 \\ (u/c)(V_j/V_\infty) \\ (V_j/V_\infty) \\ (V_j/V_\infty)^2 \end{bmatrix} \\
&= K_i X
\end{aligned}
\tag{57}
$$

The resulting values of the coefficient row vectors K_0, K_1, K_2, K_3, and K_4 are given in Eq. 58, and these thirty numbers define the surrogate model.

$$
\begin{aligned}
K_0 &= \begin{bmatrix} 0.378269 & 0.748135 & -0.179986 & -0.056464 & -0.146746 & -0.015255 \end{bmatrix} \\
K_1 &= \begin{bmatrix} 3.071020 & -1.769885 & 0.436595 & 0.148643 & -0.989332 & 0.197940 \end{bmatrix} \\
K_2 &= \begin{bmatrix} -2.827730 & 2.054064 & -0.467410 & -0.277325 & 0.698981 & -0.008226 \end{bmatrix} \\
K_3 &= \begin{bmatrix} 0.997936 & -0.916118 & 0.199829 & 0.157810 & -0.143368 & -0.057385 \end{bmatrix} \\
K_4 &= \begin{bmatrix} -0.127645 & 0.135543 & -0.028919 & -0.026546 & 0.010470 & 0.012221 \end{bmatrix}
\end{aligned}
\tag{58}
$$

The three-dimensional input of the surrogate model makes visualization of the model output somewhat difficult. However, the general trends that result from changes in R/c or u/c can be readily observed from the raw data in Figure 21 (and/or Figures 24, 25, and 26), and the general variation with V_j/V_∞ can be seen in Figure 27. Extensive visualizations of the surrogate model outputs can be found in Appendix A, specifically Figures 71 through 78.

The final surrogate model can be represented in a single equation as Eq. 59, where $X = \begin{bmatrix} 1 & u/c & (u/c)^2 & (u/c)(V_j/V_\infty) & (V_j/V_\infty) & (V_j/V_\infty)^2 \end{bmatrix}^T$ and the coefficients K_i

are defined in Eq. 58.

$$\begin{aligned}\beta &= K_0 X + K_1 X \left(\frac{R}{c}\right) + K_2 X \left(\frac{R}{c}\right)^2 + K_3 X \left(\frac{R}{c}\right)^3 + K_4 X \left(\frac{R}{c}\right)^4 \\ &= \sum_{i=0}^{4} K_i X \left(\frac{R}{c}\right)^i\end{aligned} \tag{59}$$

To ascertain the accuracy of the surrogate model, the model was evaluated at the specified R/c, u/c, and V_j/V_∞ points used to fit the model as well as at other validation points. In some of these comparisons the points for values of $R/c = 0.125$ were excluded because of the wide variability in the results due to the upper-surface blowing-like effects discussed above.[24] The validation points include those shown in Figure 26 as well as the six additional points shown in Table 1. These additional points were selected with similar logic described above for the $V_j/V_\infty = 2.25$ velocity cases (i.e., are representative of likely high-lift propeller characteristics).

Table 1: Validation cases for surrogate model of β from OVERFLOW simulations

R/c	u/c	V_j/V_∞	α	c_l	β
0.35	0.35	2	3°	0.9542	0.6114
0.4	0.8	2	3°	1.0822	0.7161
0.6	0.6	2	3°	1.2032	0.8095
0.8	0.8	2	3°	1.3474	0.9149
0.7	0.75	2	5°	2.1279	0.8646
0.5	0.75	2	1°	0.3850	0.7721

In evaluating all the model fit points and validation cases the surrogate model has an R^2 value of 0.9858 compared to an R^2 of 0.9856 on simply the model fit points. If the $R/c = 0.125$ values are excluded, these R^2 values are 0.9917 and 0.9914, respectively.

The accuracy of the surrogate model can also be evaluated visually. Figure 28 plots the β values found from the OVERFLOW simulations versus the values predicted by the surrogate model. The blue points represent cases, and the black line

[24] In reality, at only two of these points is the prediction different from the actual value by more than 0.04: those at $u/c = 1$ and $u/c = 1.5$ for a 5° angle of attack and $V_j/V_\infty = 2$.

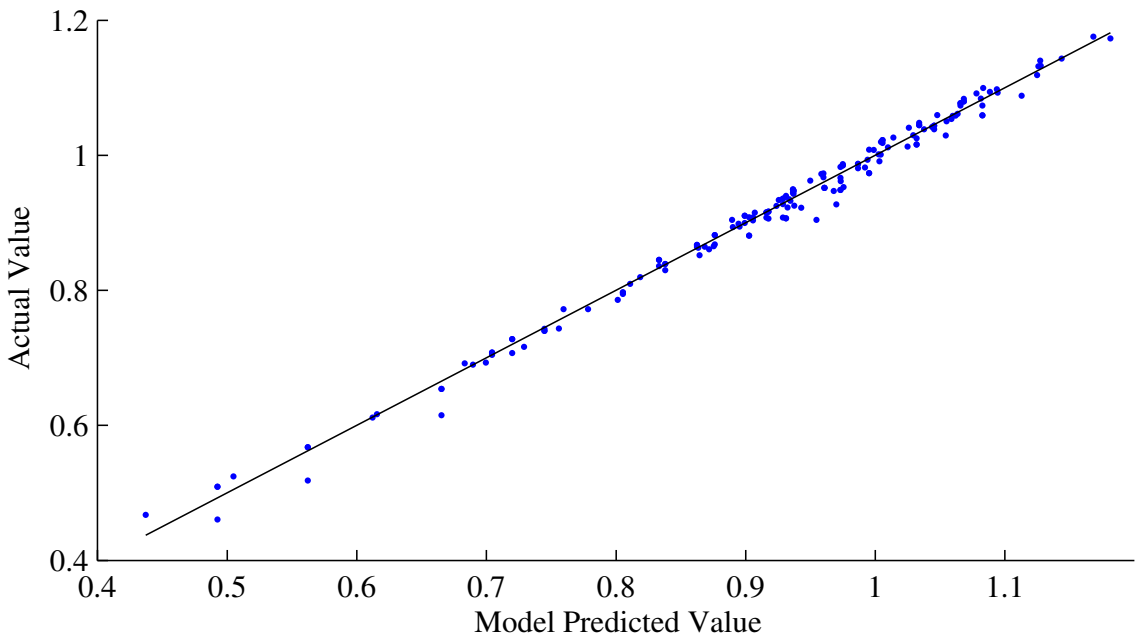

Figure 28: β values from the OVERFLOW simulations vs the values predicted by the surrogate model

indicates where the points should fall if the surrogate model and the OVERFLOW simulations had perfect agreement. The model is clearly not perfect, but it does capture the general trends well and appears to provide a good fit to the data.

Analysis of the residuals—i.e., the difference between the model prediction and the actual values from the OVERFLOW simulations—also provides insight into the accuracy of the model. Figure 29 shows two ways of visualizing the residuals data: Figure 29(a) plots the residuals versus the model predicted values and Figure 29(b) is a histogram of the residuals. The observed relatively even scatter of the points around a mean of zero is desirable and indicative that the surrogate model provides a reasonable fit to the data. Additionally, the relatively even scatter of the residuals also indicates that there is not any major factor for which the model fails to account.[25] The mean of the residuals is 0.001 with a standard deviation of 0.0134. These low

[25] A noticeable pattern in the residuals plot is often a sign that there is a functional dependency of the data on some other variable that is not included in the model.

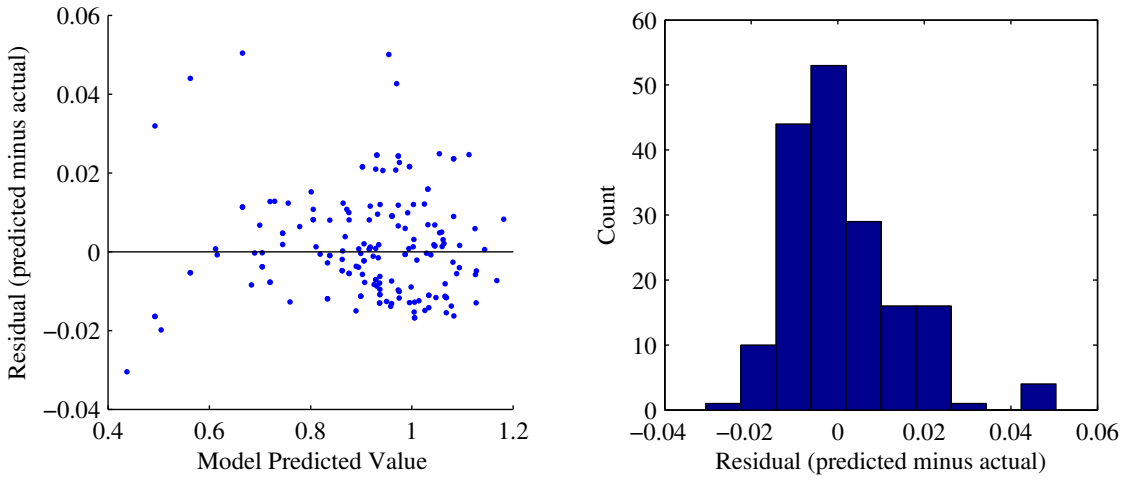

(a) Residual values vs model predicted values

(b) Residuals histogram

Figure 29: Residual error of surrogate model

values are an additional indication that the model provides a good fit to the data.

The data shown in Figures 28 and 29 also provide insight into where the model is least accurate. Specifically, the model deviates most from the OVERFLOW simulations at very low values of R/c. Additionally, larger deviations are observed at very high V_j/V_∞ values (i.e., at 2.25). Consequently, caution should be exercised if the model is desired to be used for cases with very small propellers or very large slipstream velocity increases.

In addition to knowing where the model is least and most accurate, it is appropriate to specify the known limitations of the surrogate model. In order to obtain reasonable fits to the data, limits on the slipstream heights, distances of the disk upstream of the airfoil, and slipstream velocities were imposed as discussed above. Specifically, the value of R/c should be between approximately 0.15 and 3; u/c should be limited to between 0.25 and 1.5; and V_j/V_∞ should be limited to between 1 and approximately 2.25. Although the surrogate model provides results for inputs outside of these limits, the results may be unreasonable.

3.2.1.3 Design Guidance

Reasonable design guidance is to try to identify the "sweet spot" in terms of propeller diameter where β values are not quite at the maximum but where the increase in β with increasing R/c is no longer as steep as at lower R/c values. Generally this seems to occur near R/c values of approximately 0.75. When in doubt, it is likely wise to select slightly smaller diameters to avoid any dips in lift that were observed near R/c values of 2 and to counteract the need to place the propeller further ahead of the wing to obtain sufficient slipstream contraction.

The OVERFLOW simulations suggest that if a propeller is placed too high above or too low below the wing chord line—particularly a very small diameter propeller—then the theory presented above will likely break down. If most of the slipstream moves over the wing, then upper-surface blowing-like effects may dominate, which the theory cannot capture. Additionally, if the slipstream moves mostly below the airfoil, the lift increase will likely be diminished compared to the values predicted by the theory. These detrimental impacts to lift are seen most dramatically in the simulations where the airfoil is at the highest angle of attack and the disk is placed further ahead of the airfoil.

Additionally, as the slipstream velocity increases the effective β value generally decreases for the same R/c and u/c as was illustrated in Figure 27. Consequently, it is recommended to avoid designs that require very high slipstream velocities if possible. If large changes in the slipstream velocity are required for a particular situation, it may be advantageous to instead consider increasing the propeller diameter and/or increase the distance upstream of the wing at which the propeller is placed.

3.2.2 Modifying the Simple Theory

Each of the equations in Section 3.1 predicting the lift increase $\Delta L'/L'_0$ (i.e., Eqs. 40 through 48) should be modified to include the β parameter, which can be found from

the surrogate model described above. The inclusion of this parameter will reduce the lift increase predicted in many circumstances because β is often less than 1.0. For the sake of brevity, only the most general of these equations, Eq. 42, is presented here in Eq. 60 to illustrate how this modification is performed.

$$\frac{\Delta L'}{L'_0} = \left(1 - \frac{\beta V_p \sin i_p}{V_\infty \sin \alpha_a}\right) \frac{\sqrt{V_\infty^2 + 2V_\infty \beta V_p \cos\left(\alpha_a + i_p\right) + \left(\beta V_p\right)^2}}{V_\infty} - 1 \tag{60}$$

The application of the β parameter to three-dimensions requires some explanation since the surrogate model that defines β was developed from two-dimensional simulations. To apply this factor to full three-dimensional propellers, experimentation has indicated that the full propeller radius should be used in Eq. 59 as R as will be demonstrated in the next section. This approximation has been found to be sufficiently accurate for early-phase design calculations and can be explained considering the assumption made above in Section 3.1.4 that the tangential velocity can be ignored.

By neglecting the tangential velocity component present in the slipstream, the magnitude of the local velocity at many two-dimensional locations aft of the propeller will be lower than the wing sections actually experience. Since the lift is proportional to the full local velocity as shown in Eq. 39, taking V_p as the average axial velocity effectively reduces the local velocity, which reduces the lift predicted. If an "average" value for the β parameter was selected aft of the prop, an additional lift-reducing assumption would be made. To avoid applying multiple conservative assumptions, the full propeller radius is considered when calculating β, which effectively counteracts the conservative assumption on the velocity made above. Additionally, this approach for taking the full propeller radius in determining the β parameter follows the assumptions made by Jameson [109] that the slipstreams of adjacent props can merge effectively forming a larger jet with nearly-constant height.

3.3 Comparison of Model to Experimental Results and Other Methods

To test the accuracy of the model described above, the lift augmentation predicted by the method is compared to several experiments and other higher-order computational modeling tools in this section. Additionally, the theory described in this chapter is compared to the theories presented by Jameson and Smelt and Davies that were described in Chapter II. The results in this section suggest that the new method presented above is more accurate than these other theories.

3.3.1 LEAPTech

Perhaps the best test case for the model is the LEAPTech wing that was introduced in Section 1.2.1 in Chapter I. This wing test rig is closest to the configurations of interest for this dissertation since it uses many, smaller diameter high-lift props. Experimental data is unavailable for publication in this dissertation, but comparisons will be made to the results obtained from two separate CFD programs—FUN3D and STAR-CCM+. The FUN3D results were performed at NASA Langley Research Center and the STAR-CCM+ results were obtained from Joby Aviation [63].

A top view of a semi-span of the LEAPTech wing is shown in Figure 30. In the figure, the high-lift propeller nacelles are shown in blue;[26] the flap in its extended position is shown in red; and the main wing is gray. The LEAPTech wing has an area of approximately 55 ft^2, a span of 31 ft, and a mean chord length of approximately 1.72 ft. The wing has full-span fowler flaps, whose airfoil sections have a zero-lift angle of attack of approximately $-24°$.[27] The wing is twisted with the root set at a positive 5° incidence angle relative to the body centerline axis and the tip at a positive 1° incidence (i.e., the wing has 4° of washout). The wing is unswept and untapered

[26] The actual propellers are not shown in the figure.
[27] for the flapped airfoil section

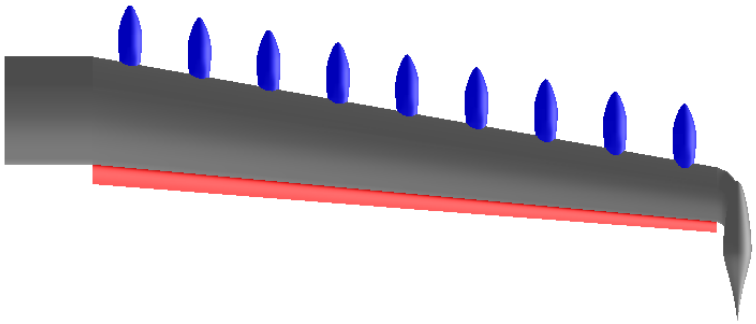

Figure 30: Top view of a semi-span of the LEAPTech wing

from the centerline out to 1.85 ft where the chord length is 2.29 ft. Then there is a 10° leading edge sweep and the chord decrees to 1.15 ft at a spanwise location of 15.1 ft.

The propellers are 1.465 ft in diameter and produce approximately 41 lb of thrust each. Each of the eighteen props is placed 0.65 ft ahead of the wing leading edge at its centerline. The inner-most nacelle is placed 2.65 ft from the wing centerline and the outer-most nacelle is placed at a spanwise location of 14.37 ft. All nacelles are evenly spaced along the span and are placed at a zero degree incidence relative to the vehicle longitudinal axis.[28] The average change in axial velocity produced by the propellers is calculated here with momentum theory.

For comparison purposes, only low angles of attack are considered here. Since the model presented in this chapter is incapable of predicting behavior after stall, low angle of attack data where the lift curve is approximately linear provides the best test of the model. Generally, the presence of high-lift propellers will delay stall to higher angles of attack, which will increase the lift more than predicted by the above theory. Therefore, if the model is sufficiently accurate in the linear regime of the lift curve, then it will likely be a conservative estimate of the true lift multipliers that

[28]This implies that they are angled down relative to the wing chord line by 5° at the root and 1° at the tip.

high-lift propeller systems can practically provide.

Additionally, the comparisons here are made based on the lift multiplier (i.e., K_L) obtained from the unblown condition to the blown condition. This approach eliminates any differences in the unblown C_L predictions that may occur between the baseline lift predictions, which here are taken as the FUN3D and STAR-CCM+ CFD results. Furthermore, the K_L for each of the three theories is unchanged regardless of the original unblown C_L estimate.

Before comparisons to the theories presented by Jameson and Smelt and Davies can be made it should be noted that there are two manners in which their models can be applied to aircraft with multiple, adjacent propellers. Both of these theories requires that the aspect ratio of the wing in the slipstream be specified. This aspect ratio may be calculated for each individual propeller, which is termed here the "individual" calculation, or by assuming that all the propellers combine to provide a wide slipstream, which is termed a "grouped" calculation. Both theories seem to imply that the grouped method is the appropriate selection, but it is somewhat unclear. Therefore, both methods are employed here in comparison to the LEAPTech wing to evaluate which method is most appropriate.

Additionally, there are multiple ways of employing the new models described in this dissertation. Each propeller can be considered individually as described above taking the mean chord length behind the propeller for calculation of β parameter; this is termed a "detailed" approach. Alternatively, since each propeller has the same design, calculations for a single propeller located at a fictitious wing station with an average wing twist (2.5°) and an average chord length (1.72 ft) can be performed and the results applied over all 18 propellers. This alternate approach is termed "simple." Both these approaches are shown below.

A comparison of the lift multiplier values predicted by the three theories and two CFD programs is shown in Figure 31. This data shows only the lift carried by the wing

and ignores any contribution of the propeller thrust to effective lift.[29] The present theory's predictions are shown in the blue solid and dashed lines located near the middle of the figure. The Smelt and Davies model results are shown with the green lines. The dot-dashed line near the center of the figure shows the results of the grouped implementation, and the dotted green line at the bottom of the figure represents the individual implementation. Predictions of the lift multiplier from Jameson's model are shown in orange with the dotted line at the center of the figure representing the grouped calculation and the dot-dashed line at the top of the figure showing the results of the individual calculation.

It should be noted that only a single point from FUN3D is shown because the unblown airfoil is clearly stalled at angles of attack greater than $-2°$ and no data points exist for lower angles of attack. It is unclear if the airfoil is stalled at $-2°$; if it is, then the K_L shown in the figure is higher than would be expected. Similarly, there are only two data points shown for the STAR-CCM+ results because no lower angles of attack were run and stall is predicted on the unblown wing at higher angles of attack.

The results in Figure 31 indicate that the grouped implementation of both the Jameson and Smelt and Davies models is most appropriate. The individual implementation of the Jameson model greatly over-predicts the lift multiplier while the individual implementation of the Smelt and Davies model greatly under-predicts the K_L. These same trends have been observed in other cases; consequently, in the following discussion of Figure 31 and all other comparison cases presented in this chapter, only the grouped implementations will be discussed any further.

The results from the simple and detailed variants of the theory presented in this chapter are virtually identical. This implies that for early-phase design studies the impacts of differing propeller installation angles and wing taper can effectively be

[29] Adding in the thrust contribution would simply apply the same lift addition to all cases.

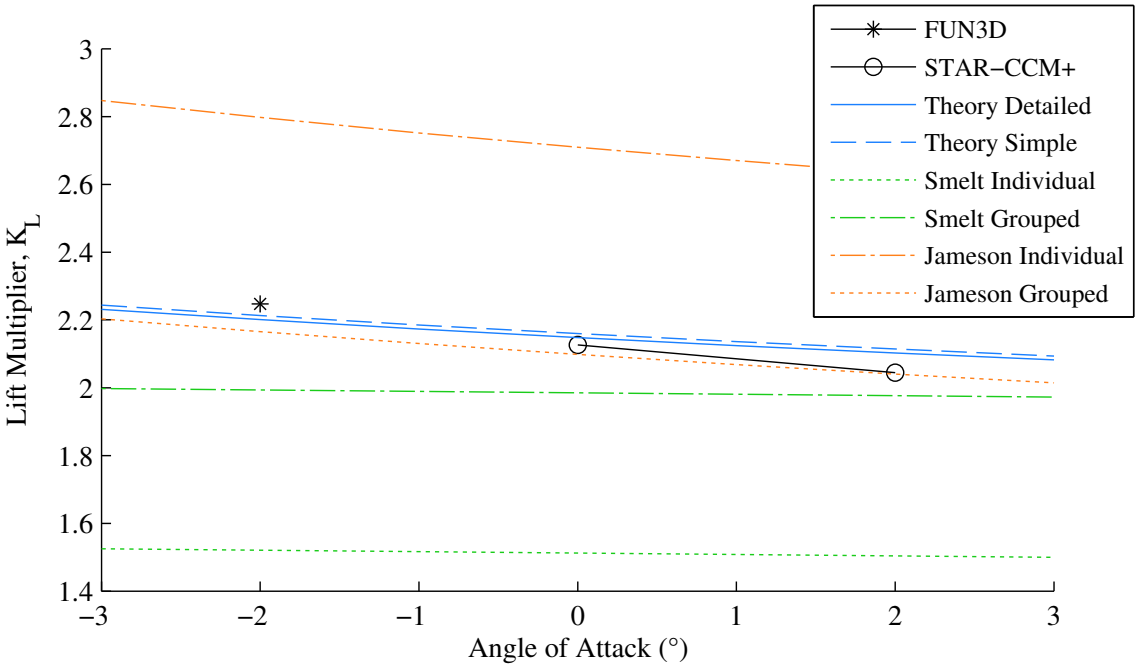

Figure 31: Comparison of the present theory and the theories of Jameson and Smelt and Davies to CFD predictions for the LEAPTech configuration

ignored so long as there are not large changes between these values along the wingspan and a single high-lift propeller design and airfoil are used. (If there are differences in the airfoil—e.g., if a portion of the high-lift prop system is blowing a flapped portion of the wing while other props blown unflapped wing sections—then utilizing the simple variant of the new method is not likely to be as accurate.)

Both the theory presented in this chapter and Jameson's model show decreases in K_L with increasing angle of attack while the Smelt and Davies model predicts results that are virtually constant with angle of attack. The STAR-CCM+ results indicate that there should be a slight decrease in K_L with increasing angle of attack, which implies that the present theory and the Jameson model are superior to the Smelt and Davies model. Furthermore, the Smelt and Davies model predicts lift multipliers noticeably lower than the CFD results indicate. The slope of Jameson's model appears to match the STAR-CCM+ results more closely than the present

theory. Both Jameson's model and the theory presented in this chapter under-predict the FUN3D results. However, Jameson's model is both slightly low compared to the STAR-CCM+ results while the present theory predicts slightly higher lift multipliers than STAR-CCM+.

Ultimately the results of Figure 31 indicate that either Jameson's theory or the theory presented in this chapter are superior to the theory of Smelt and Davies for this type of configuration. However, the results from this comparison are insufficient to state definitively whether the novel method presented here or Jameson's model is most appropriate. Both appear to give answers of sufficient accuracy for early-phase design.

3.3.2 Kuhn and Draper Experiments

The experiments of Kuhn and Draper [56] represent a good test case for the method. These experiments tested a wing with NACA 0015 airfoil sections with a propeller upstream. The tests were performed at various freestream velocities from zero up to 82 ft/sec (just under 49 knots). These velocities are slightly slower than the primary use case for the model described above, and the model is incapable of providing results for the cases with zero freestream velocity. For evaluation of the model, cases where the freestream velocity is 73, 58, and 44 ft/sec (or 43, 34, and 26 knots) are considered here. The model presented above as well as the models of Jameson and Smelt and Davies are also compared to the data.[30]

Because the airfoil is symmetric in this test case and the propeller is installed with its rotational axis in line with the chord, the theory presented above in Section 3.1.3.2 applies to this case. Kuhn and Draper remark that the lift increase agrees best with Smelt and Davies theory when the assumption is made that the circulation around the

[30]The data obtained in the experiments contains impacts of the propeller thrust. Particularly at higher thrusts and angles of attack, a large portion of the C_L increase is due directly to the propeller thrust. The results presented below include this thrust contribution to the lift predicted.

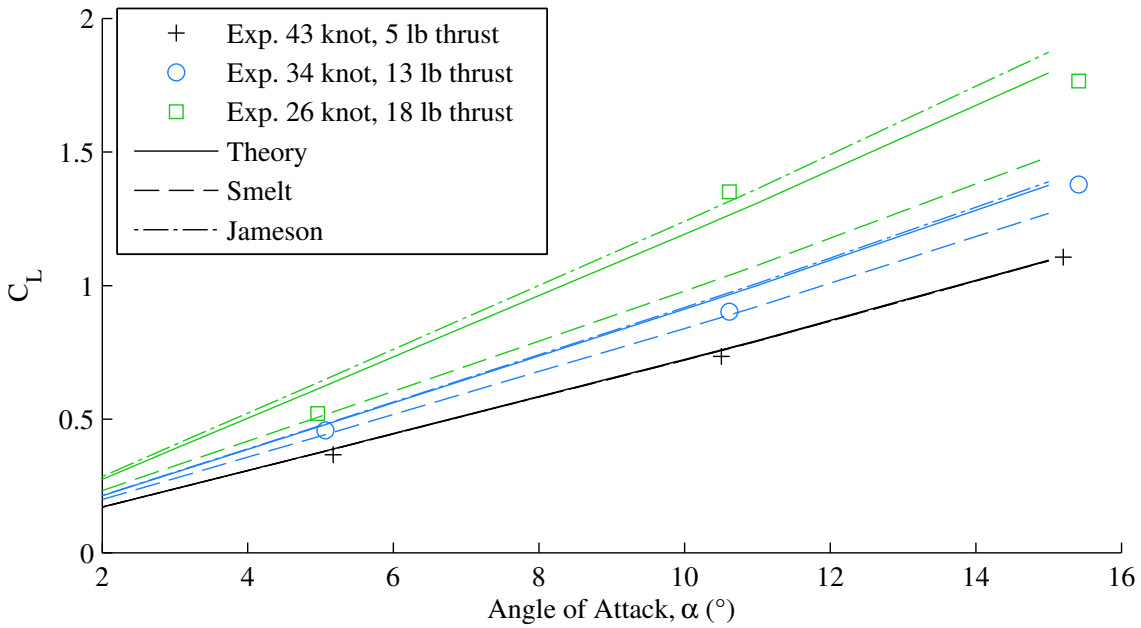

Figure 32: Comparison of the experimental data of Kuhn and Draper to the present theory and the theories of Jameson and Smelt and Davies

wing is unchanged by the presence of the slipstream. This is precisely what the model presented above in Section 3.1.3.2 predicts would occur for the propeller installation studied in these experiments. Qualitatively, this agreement of the experimental results with the theory indicates that the theory is indeed reasonable.

Comparisons of the lift increase observed in the experiments and that predicted by the present theory, Jameson's theory, and the theory of Smelt and Davies are shown in Figure 32. The experimental data is shown with the marker types indicated in the legend and the predictions of all three theories have the line types denoted in the legend. The lowest C_L values are observed for a freestream velocity of 43 knots and are shown in black. The blue lines and markers correspond to the 34 knot runs, and green is used to denote the 26 knot cases.

As can be seen in Figure 32 the present theory predicts the lift increases reasonably well. All three models predict virtually identical lift increases for the lowest

thrust/highest freestream velocity case. Although the Smelt and Davies model predicts the moderate thrust case more accurately than the other two models, it vastly under-predicts the lift increase for higher angles of attack at the highest thrust level. The theory presented in this document slightly over-predicts the lift augmentation at the medium thrust case, but follows the data closely at the higher thrust setting. Jameson's model is generally close to the present theory's prediction, but begins to predict more lift at higher thrust settings.

It should be noted that the results presented above from Kuhn and Draper were obtained through digitizing the figures located in the paper and transforming the data provided to the lift coefficient. In addition to experimental error sources, there are likely small errors in the location of the experimental points for these reasons.

3.3.3 Gentry et al. Experiments

To ascertain how well the model predicts increases in lift with varying propeller installation angles, experiments of Gentry et al. [71] were compared to the model predictions. In their experiments, Gentry et al. studied a turboprop placed 12 inches upstream and 5 inches below the chord line of a semispan wing of 20 inch chord and varied the inclination angle of the nacelle relative to the wing. The wing was equipped with full-span, double-slotted flaps that were deployed 60°. The highly-loaded, 12 inch diameter propeller was operated at two different rotational speeds: 11,000 RPM and 14,000 RPM.

In order to estimate the slipstream velocity aft of the propeller that is required for comparison to the theories, the propeller thrust coefficient versus advance ratio curves were taken from an earlier paper by Gentry et al. [116]. Based on the stated dynamic pressure and freestream velocity in their later experiments (i.e., those of interest for lift comparisons in Reference [71]), the thrust of the propeller at the two stated RPM conditions was determined. Finally, the average induced axial velocity was estimated

from momentum theory taking into account the reduced disk area from the propeller hub.

The results of the experiments and the predictions of the three theories are shown in Figures 33 and 34 with Figure 33 corresponding to the 11,000 RPM propeller operating conditions and Figure 34 showing results from 14,000 RPM setting. These figures show the lift coefficient versus angle of attack for four separate nacelle inclination angles: $i_p = 0°$, $i_p = -2°$, $i_p = -4°$, and $i_p = -8°$, where here i_p is measured relative to the wing chord line. Each line in the figures corresponds to one of these inclination angles with $0°$ being solid, $-2°$ being dashed being dotted, $-4°$, and $-8°$ being dot-dashed. The experimental data is shown in black with markers denoting the actual data points.[31] Only two angles of attack from the experiment are shown because the unblown wing experienced stall at higher angles of attack and only positive lift is of interest in the comparisons. The blue lines closest to the experimental data result from the theory presented in this chapter. The green lines near the bottom of the figure are the predictions of the Smelt and Davies model, and the orange lines at the top of the figure result from Jameson's model.

Here, the Jameson model greatly over-predicts the lift augmentation, Smelt and Davies greatly under-predict the lift, and the theory presented in this chapter slightly under-predicts the lift. Although none of the models performs exceptionally well, the present theory is most accurate as it is at most 8% different from the experiment in the 11,000 RPM case but 18% different in the 14,000 RPM case. Jameson's model is 56% different from experiment at worst for the 11,000 RPM runs and over 91% different for the 14,000 RPM case. Smelt and Davies model is 23% low for the 11,000 RPM case and approximately 30% different at 14,000 RPM.

The large over-prediction by Jameson's model is similar to the over-prediction

[31] The data points were obtained from digitizing the figures in the paper, so they may be slightly off from the actual experimental measurements.

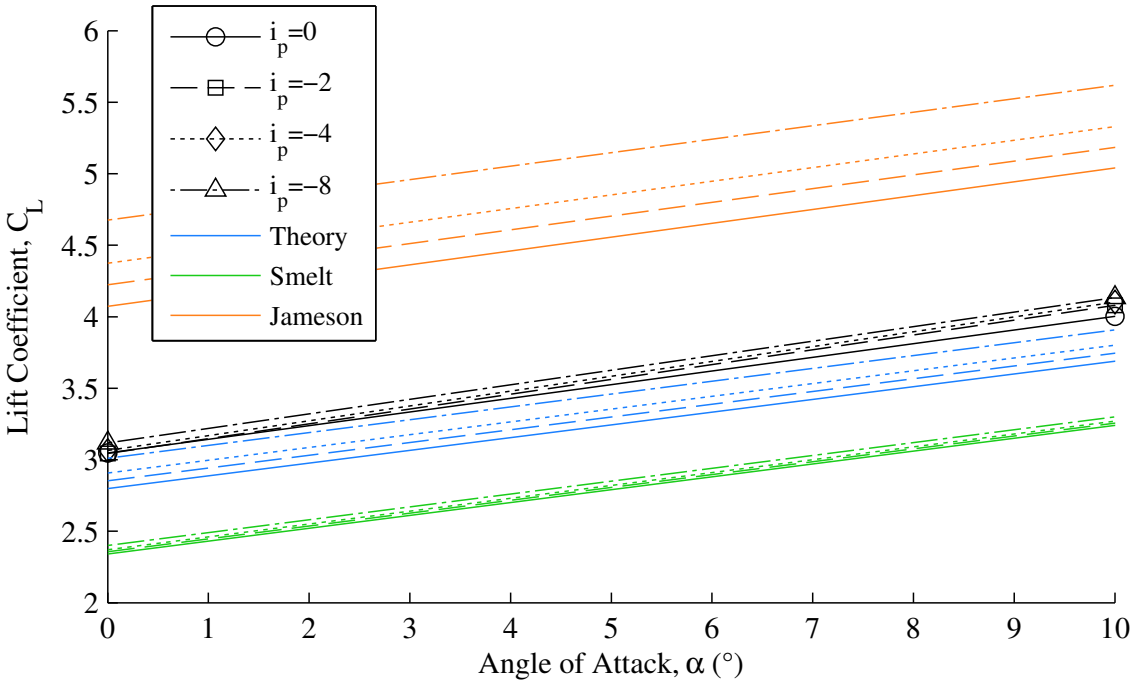

Figure 33: Comparison of the experimental data of Gentry et al. with a propeller RPM of 11,000 to the present theory and the theories of Jameson and Smelt and Davies

that was seen in Figure 31 when using the detailed implementation. Here, only a single propeller exists, so there is no difference between the simple and detailed implementations. This seems to indicate that Jameson's model is not appropriate if only single propellers are used, and the model is likely most accurate in the case of full-span blowing. Such a conclusion is logical because the method was developed assuming the wing was fully immersed in a single, wide slipstream. Similarly, the model of Smelt and Davies was developed assuming lightly loaded propellers, so it is also not surprising that it does not provide satisfactory results for this case.

It is assumed that one of the primary reasons the novel theory presented in this chapter under-predicts the lift is due to the beneficial interaction of the propeller slipstream with the flap, which works to delay stall over the flap. This effect is not modeled.

Additionally, the increase in lift in the experiments observed in going from a

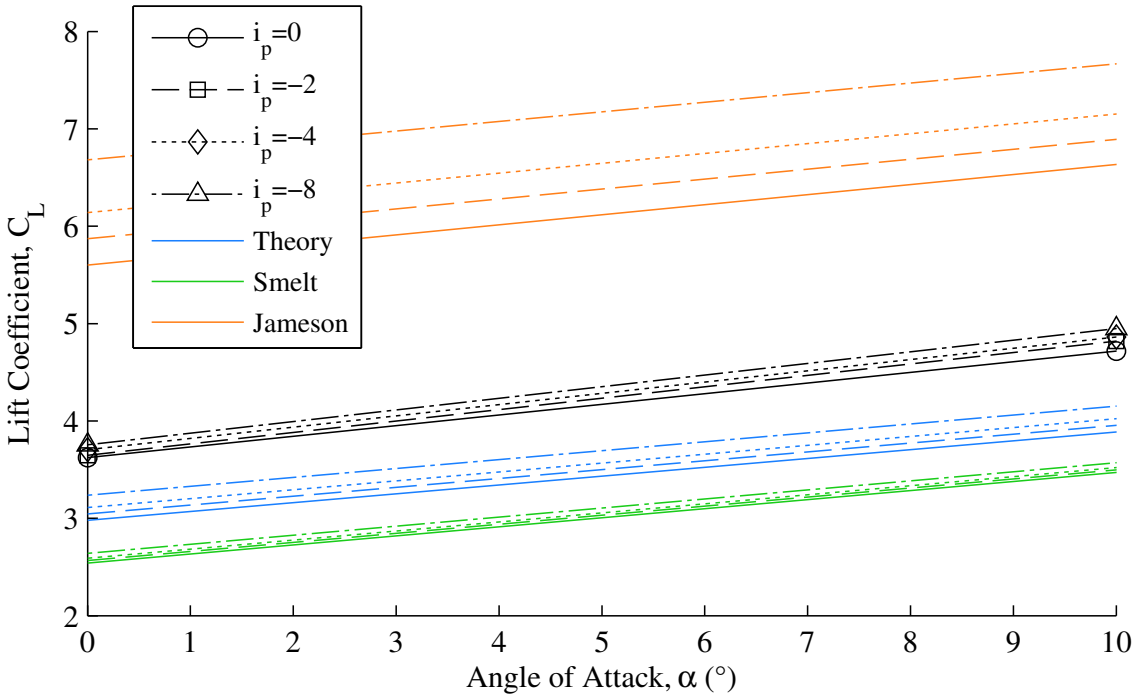

Figure 34: Comparison of the experimental data of Gentry et al. with a propeller RPM of 14,000 to the present theory and the theories of Jameson and Smelt and Davies

nacelle inclination angle of $-4°$ to $-8°$ is less than the lift increase predicted by the theory of this chapter. One potential reason for this decreased lift lies in how externally blown flaps generate additional lift. In addition to delaying stall over the upper surface, these flaps seek to direct a large portion of the slipstream downward, which will generate a reaction lift force. With larger negative nacelle angles, the direction of the slipstream is initially directed upward at a greater angle than would typically occur. If this angle is too great (i.e., the local angle of attack on the flap is too high), the effectiveness of the flap in turning the flow can be reduced (i.e., the flap may experience beyond its stall angle of attack).

However, the novel model also may simply be too sensitive to changes in the propeller installation angle particularly for cases where the propeller center is offset from the wing chord line. Since the OVERFLOW simulations from which the model

for β was derived did not include a vertical propeller offset or offset of the slipstream direction from freestream, the model is being applied outside of its region of greatest accuracy. Consequently, caution should be exercised if the theory presented in this chapter is applied to problems with propellers offset too far from the wing or at large nacelle incidence angles relative to the wing chord.

3.3.4 Summary of Simple Models

The simple models of Jameson, Smelt and Davies, and the novel method presented in this chapter have been compared to multiple experimental results. The method of Smelt and Davies consistently under-predicts the lift augmentation from propeller blowing. Jameson's model predicts the lift generated well in certain situations but deviates greatly in other experiments. The novel method presented in this chapter generally shows good agreement with experiments though it under-predicts the lift in cases with large flap deflections.

The semi-empirical model proposed by Smelt and Davies assumes lightly loaded propellers. Ultimately, it is primarily this light loading assumption causes the predictions of this method to consistently be reduced from actual values for the three configurations shown above. Additionally, Smelt and Davies indicate that their model should not be employed for configurations with flaps.[32] Consequently, the under-predictions of the lift for the experiments of Gentry et al. and the LEAPTech wing are not surprising considering the methods invalidity to flapped configurations.

The assumption behind of Jameson's model that the wing is completely immersed in an elliptic slipstream is likely never to be realized in practice. Despite this assumption, it has been shown to work well in certain situations. However, the very large over-predictions of the model for the experiments of Gentry et al. indicate that this model should be used with extreme caution. Generally, it can be expected that this

[32]They state that the basic premise of the model—i.e., that the circulation may remain unchanged in the blown portion of the wing—is not generally the case with flaps.

model will provide the most accurate results for configurations where larger portions of the wing are blown.

The novel method presented in this chapter performs better for early-phase design than the models of Jameson or Smelt and Davies. The method provides good agreement overall with experiments, and the greatest deviations are observed in situations where there are slotted flaps with large deflections. The under-prediction of the lift in the case of a slotted flap is expected since the model does not incorporate the delays in stall that slotted flaps can provide. Furthermore, it is desired that early-phase design methods provide conservative results when they deviate from reality, and the novel method is conservative in these cases with slotted flaps. Consequently, the novel method is superior to Jameson's method not only because it more closely predicts the lift augmentation but also because it under-predicts the lift where there is a slotted flap with a large deflection whereas Jameson's model greatly over-predicts the lift.

3.4 Implications of Model

The simplified aerodynamics models presented in this chapter have been developed to rapidly assess the effects of upstream propellers on wing lift in a manner that can help provide a designer intuition. The models predict only the effects of leading edge propellers on wing lift while neglecting any influence of the wing on the propeller. Despite the assumptions made, the models are shown to have reasonable accuracy across a variety of comparison cases, and these results are much more consistent than either of the models presented by Jameson or Smelt and Davies. Although the present modeling at times over-predicts lift augmentation while at other times under-predicts it, the deviations are not nearly as drastic as those seen from the other models. Furthermore, the novel model can help provide a designer greater intuition about the impacts of propeller diameter and installation angle than existing simple methods.

The model developed in this chapter indicates that the angle at which the upstream propellers are installed may have significant impacts on the wing lift augmentation; therefore, propeller installation angles must be considered in early design to obtain accurate performance estimates. It is likely most advantageous both from lift augmentation and safety viewpoints to install the propellers such that the propeller slipstream velocity closely aligns with the freestream angle of attack during conditions where the high-lift propellers operate so long as the resulting inclinations of the propeller relative to the wing chord are not too large. Other factors such as propeller thrust contribution to lift and nacelle drag in cruise must also be considered and may affect the choice of installation angle. Nonetheless, this simple model provides a mechanism to rapidly assess how various installations may affect wing lift augmentation.

Designers of aircraft with high-lift propellers will face inherent tradeoffs in the ideal diameter of the propellers. Simple momentum theory indicates that very small diameters are likely advantageous for increasing the slipstream velocity, which is beneficial for lift augmentation. However, if the propeller diameter is too small, then the lift augmentation from the increased slipstream velocity may be drastically reduced from what may otherwise be expected. Incorporation of finite slipstream height effects via the β parameter can provide designers with a simple tool to find an appropriate propeller diameter that balances increased axial velocity with sufficient slipstream height.

3.5 Chapter Summary

The simple theory developed in this chapter was developed to provide an answer to the motivating question presented at the beginning of this chapter:

How can the lift augmentation from high-lift propellers be rapidly assessed to facilitate conceptual design?

This model is most succinctly described by Eqs. 60, 51, 58, and 59. However, the special cases considered in Section 3.1.3 and the visualizations of the variation of the β parameter in Figures 21, 24, 25, 26,and 27 are likely the most useful for building a designer's intuition.

Other important notes from this chapter include:

1. Simply assuming that lift augmentation will be proportional to the dynamic pressure increase in a propeller slipstream is an overly simplistic assumption that will often result in a very poor prediction of the lift augmentation.
2. The installation angle of the propeller relative to the wing will have large impacts on the lift augmentation. This installation angle directly affects the circulation change in the wing sections affected by the propeller slipstream.
3. The first-order lift impacts of high-lift propellers on downstream wings can be determined by abstracting the propeller slipstream to a single, average induced axial velocity.
4. The propeller diameter and the distance of the propeller from the wing can have large impacts on the lift augmentation. When speaking generally about high-lift propellers that will typically have relatively small diameters and be located relatively close to the wing, the lift augmentation will typically be reduced as the diameter of the propeller is decreased and as the propeller is moved closer to the wing.
5. A simple surrogate model of two-dimensional CFD simulations has been developed to describe the impacts of the propeller diameter, distance from the wing, and magnitude of the slipstream velocity. Additionally, this surrogate model effectively removes the incompressible flow assumption that was made in developing the initial models.

CHAPTER IV

A SIMPLE METHOD FOR HIGH-LIFT PROPELLER CONCEPTUAL DESIGN

The work presented in this chapter can be motivated with the following question:

Since the purpose of high-lift propellers differs from traditional propellers, should high-lift propellers be designed differently, and if so, how?

In this chapter a simple method is presented for designing high-lift propellers. The primary purpose of these propellers is to increase lift rather than produce thrust, and indeed thrust production is not desirable during certain high-lift operating conditions such as landing approach. This chapter therefore addresses the research questions of whether and how the design process for high-lift propellers should differ from that of traditional propellers, which are typically designed based on consideration of classical metrics for efficient thrust production such as minimum induced loss. The theory presented below describes how these props can be designed to provide a relatively uniform axial velocity increase along the radius, which is hypothesized to be advantageous for lift augmentation based on a literature survey. Computational modeling indicates that such propellers can generate the same average induced axial velocity while consuming less power and producing less thrust than conventional propeller designs. For an example problem based on specifications for NASA's Scalable Convergent Electric Propulsion Technology Operations Research (SCEPTOR) flight demonstrator, a propeller designed with the new method requires approximately 15% less power and produces approximately 11% less thrust than one designed for minimum induced loss. Higher-order modeling and/or wind tunnel testing are needed to verify the predicted

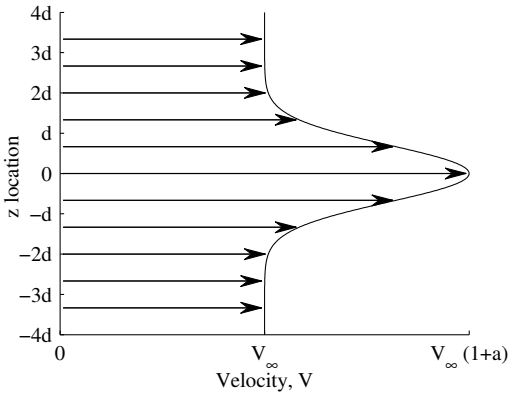

Figure 35: Generic Joukowski velocity profile with $z_c = 0$

performance.

4.1 Motivation for a New Propeller Design Method

A series of papers from Liu et al. from New York University in the late 1960s and early 1970s studied the effects of airfoils placed in non-uniform parallel velocity streams [112, 4, 3, 117]. One of the major applications of these papers was to approximate the impact of a propeller slipstream—specifically the impact of the axial velocity increase produced by the propeller—on a wing. In addition to studying step changes in velocity as would occur with an idealized jet blowing on a wing, they also investigated the impacts of Joukowski velocity profiles to approximate the non-uniformity present in a typical propeller slipstream. These Joukowski velocity profiles are of the form of Eq. 61 where V_∞ is the freestream velocity outside of the jet, a defines the maximum velocity (where $V_{\max} = V_\infty (1 + a)$), d defines a characteristic width of the velocity increase, and z_c specifies the height relative to the airfoil chord line (i.e., the z-coordinate) where the maximum velocity occurs [4].

$$V(z) = V_\infty \left(1 + ae^{-(z-z_c)^2/d^2}\right) \tag{61}$$

A generic representation of this velocity profile is shown in Figure 35.

Based on the Joukowski velocity profiles, Chow et al. defined a "non-uniformity parameter" as a/d^2 to indicate how far a particular profile deviates from a uniform value; the larger the non-uniformity parameter, the larger the deviation from a uniform stream. They also defined an "adjusted lift coefficient," $\bar{C}_L$, which is an alternative form of the conventional lift coefficient normalized by the maximum velocity in the non-uniform stream. The adjusted lift coefficient can be written in terms of the conventional form of the lift coefficient via the a parameter as shown in Eq. 62.

$$\bar{C}_L = C_L \frac{V_\infty^2}{V_{\max}^2} = \frac{C_L}{(1+a)^2} \tag{62}$$

Through numeric simulations Chow et al. empirically determined that there existed a relationship between the maximum adjusted lift coefficient and the non-uniformity parameter that could be approximated with the curve fit given in Eq. 63, where $\bar{C}_L^*$ is the adjusted lift coefficient of a uniform stream (i.e., where $a = 0$ or $d = \infty$) [4].

$$\left(\bar{C}_L\right)_{\max} = \bar{C}_L^* \left[1 - 0.18909(a/d^2) + 0.04883(a/d^2)^2 - 0.00479(a/d^2)^3\right] \tag{63}$$

The simulations that led to the curve fit given in Eq. 63 included varying the height of the velocity profile relative to the airfoil (z_c), the maximum velocity (a), and the characteristic width of the velocity profile (d).[1]

The variation of the maximum lift as a function of the non-uniformity parameter is shown in Figure 36. Figure 36(a) shows the variation of the maximum adjusted lift coefficient (i.e., Eq. 63) and Figure 36(b) shows the variation of the conventional lift coefficient for various values of the a parameter, which defines the maximum velocity in the profile.

It is clear from Figure 36(a) that there is a large decrease in the maximum adjusted lift coefficient as the non-uniformity of the stream increases; however, the variation of

[1]It is unclear if the simulations performed by Chow et al. accounted for varying airfoil shapes. I believe that these results were generated for a single airfoil, but are assuming that the effects for any given airfoil will follow the same general trends.

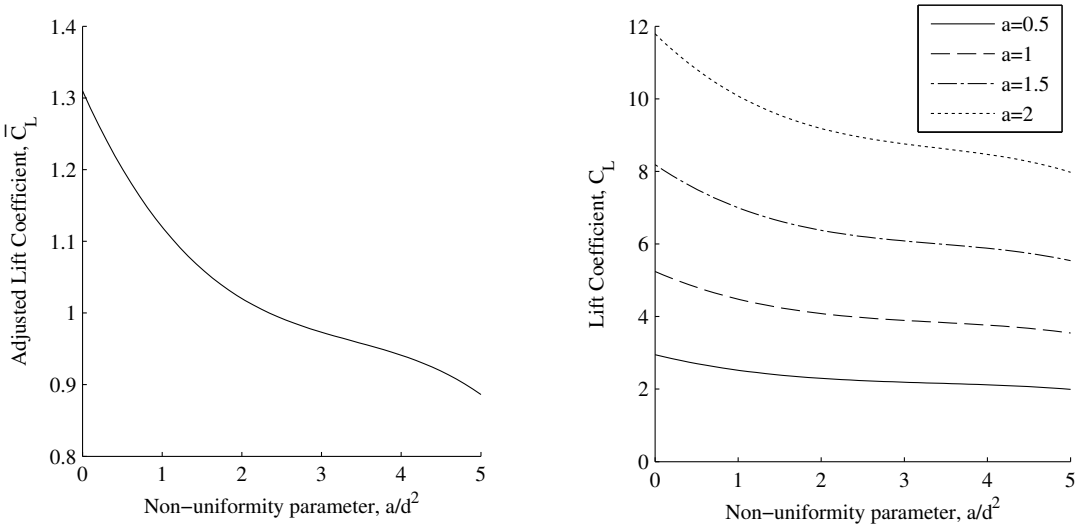

(a) Maximum adjusted lift coefficient (reproduced from Reference [4])

(b) Maximum lift coefficient for four velocity profiles with differing maximum velocities

Figure 36: Empirically determined maximum lift coefficient as a function of the non-uniformity in the upstream velocity profile based on the work of Reference [4]

the total lift produced is somewhat unclear from Figure 36(a) because $\bar{C}_L$ is normalized by the maximum velocity as opposed to the freestream. To provide insight into how the actual lift generated varies with the non-uniformity parameter, Figure 36(b) shows the value of the conventional lift coefficient associated with Eq. 63 for four values of a. (Note that since a is specified, each curve in Figure 36(b) is simply a function of d. The horizontal axis is kept as the non-uniformity parameter as opposed to d for comparison clarity.) There are three major observations that can be made from Figure 36(b):

1. The lift coefficient decreases as the non-uniformity increases regardless of the maximum velocity of the profile (i.e., regardless of a)
2. More lift is produced as the maximum velocity in the slipstream (i.e., a) increases
3. The impact of non-uniformity increases as the maximum velocity in the slipstream increases

These observations imply that a well-designed high-lift propeller should produce a

highly-uniform slipstream with a high maximum velocity. Additionally, maintaining a near-uniform velocity increase becomes relatively more important as the slipstream velocity generated by high-lift propellers increases. Because conventional propellers have a high degree of non-uniformity in their induced velocity distributions, conventional propeller design methods are not likely to yield ideal high-lift propeller designs. Consequently, a new high-lift propeller design method will be developed in the following section that seeks to minimize the non-uniformity in the induced axial velocity distribution.

It should be noted that there is synergy between designing a blade to minimize non-uniformity in the axial velocity profile and classic propeller design theory. Betz's optimality condition states that the induced losses from a propeller can be minimized if the vortex sheets shed from the blades move downstream as rigid "screw" surfaces [81, 80]. For such a situation to occur, a truly constant velocity profile in the slipstream must exist. Designing blades with near-uniform axial velocity profiles may, therefore, approximate this condition and result in relatively efficient propeller designs.[2] However, the intention of the following design method is to generate uniform axial velocities to maximize lift augmentation not thrust production.

4.2 High-Lift Propeller Design Method

In this section a high-lift propeller design method is presented that is intended to provide a near-uniform axial velocity increase aft of the propeller. The method is based on blade element momentum theory (BEMT), which was described in detail in Chapter II, and a brief review is presented here. BEMT is a combination of blade element theory and momentum theory. In blade element theory the propeller blade is divided into segments ("blade elements"), and each segment is analyzed as a single 2-D airfoil section. The total force on a segment is found from the 2-D force per unit

[2] where efficiency is defined in the usual manner as useful power output over power input

span times the span of the section, and the total force on the blade is the sum of the forces over each segment. In momentum theory, the propeller is viewed as a disk that is split into many annular rings. The force over each annulus is found from the mass flow rate times the velocity increase of the fluid through the annulus. The total force from the propeller is the sum of the forces from each annulus.

For the purposes of this dissertation it will be assumed that a propeller will be designed to a specified diameter, rotational velocity, number of blades, and average induced axial velocity from the propeller. The blade geometry will be defined by chord and twist distributions at an arbitrary number of radial stations. For simplicity, the discussion will focus on blades with a single airfoil, but a blade may be designed with an arbitrary variation of airfoil shape, which can be accounted for by varying the aerodynamic properties assumed at each radial station.

4.2.1 Blade Design for a Desired Induced Velocity Distribution

In this section the theory for determining a propeller blade design to produce a desired induced axial velocity distribution is presented. Although the same theory can apply to any desired induced axial velocity distribution, the discussion will focus on designing to produce a near-constant axial velocity distribution based on the discussion above in Section 4.1. In developing the theory, it is assumed that the angular velocity added to the propeller slipstream is negligibly small compared to the angular velocity of the propeller for the momentum theory portions of the equations as described by Glauert [80].

The total local velocity at any blade element, $\boldsymbol{W}$, consists of the local incoming axial velocity, $\boldsymbol{V_a}$, and the local rotational velocity, $\boldsymbol{V_t}$, at that element; the magnitude of this total local velocity is given by Eq. 64.

$$W = \sqrt{V_a^2 + V_t^2} \tag{64}$$

Both the axial and tangential velocity components vary over the blade radius due

to changes in the local rotational velocity and induced velocity. In BEMT these velocity components are typically written in terms of the axial induction factor, a, and tangential induction factor, a', which indicate the magnitude of the velocity induced by the rotor in the axial and tangential directions, respectively. The tangential and axial induction factors were defined previously as Eqs. 15 and 16, and are repeated below for easy reference.[3] Both of these quantities are functions of the radial location and are typically not constant over a propeller blade.

$$a' = \frac{\omega}{2\Omega}$$

$$a = \frac{v_i}{V_\infty}$$

With these definitions, the local axial and tangential velocities can be expressed as Eqs. 17 and 18, respectively, which are repeated here for reference.

$$V_a = V_\infty (1 + a)$$

$$V_t = \Omega r (1 - a')$$

4.2.1.1 Axial Induction Factor Distribution

Designing propellers to have near-constant induced axial velocity distributions implies that the axial induction factor, a, should be nearly constant. If momentum theory is accepted as valid and the angular velocity of the propeller slipstream is approximated as negligibly small compared to the angular velocity of the propeller, then the axial induction factor and tangential induction are directly related by Eq. 65 [80].

$$V_\infty^2 (1 + a) a = \Omega^2 r^2 (1 - a') a' \tag{65}$$

If a designer wishes to specify a particular induced axial velocity distribution, then a can be determined from Eq. 17. The value implied for the tangential induction factor

[3] Recall also that v_i is the induced axial velocity from the prop, Ω is the angular velocity of the propeller, and ωr is the local induced tangential velocity at radial station r.

can be found by solving Eq. 65 for a' as shown in Eq. 66. The a and a' parameters will be sufficient for determining the blade chord and twist distributions.

$$a' = \frac{1 - \sqrt{1 - \frac{4V_\infty^2(1+a)a}{\Omega^2 r^2}}}{2} \tag{66}$$

It should be noted that Eq. 66 may imply imaginary values of a'. In these circumstances, the tangential induction factor is limited to a value of 0.5—the maximum non-imaginary value that can be obtained from the relationship in Eq. 66. When limiting a', the relationship between a and a' (i.e., Eq. 66) is violated; therefore, if a' is 0.5, the relationship is inverted and solved for the axial induction factor implied by the tangential induction factor using Eq. 67.

$$a = \frac{-1 + \sqrt{1 + \frac{4\Omega^2 r^2(1-a')a'}{V_\infty^2}}}{2} \tag{67}$$

It should be noted that when values of a' approach the theoretical limit of 0.5, the assumption that the angular velocity added to the propeller slipstream is negligibly small compared to the angular velocity of the propeller begins to be violated.

Optional Step 1: Maintaining more-uniform induced axial velocities near the tip

If a constant value for the axial induction factor is applied, the tip of the propeller will not be loaded as much as possible because of tip losses, and these tip losses decrease the uniformity of the velocity profile. If one desires to maintain more load toward the tip, an increase to the axial induction factor near the tip can be applied. Prandtl's tip loss factor, F, is applied here to account for tip losses in order to maintain continuity with conventional blade-element momentum theory calculations. However, a small modification of the factor is made in order to generate blade designs that produce near-uniform induced axial velocity distributions.

The tip loss factor can be calculated from Eq. 68, where the term f is given in

Eq. 69 [80].[4]

$$F = \frac{2}{\pi}\cos^{-1}(e^{-f}) \tag{68}$$

$$f = \frac{B}{2}\frac{R' - r}{r\sin(\phi)} \tag{69}$$

In Eq. 69, R' is conventionally taken as the tip radius and ϕ is the inflow angle at radial station r, which is discussed below in Section 4.2.1.2. If the inflow angles (ϕ) are known, the modified axial induction factor can be found from Eq. 70.

$$a_{\text{modified}} = \frac{a}{F} \tag{70}$$

This modified value for the axial induction factor is then carried through the rest of the method in lieu of a. Iteration is required to determine the proper values of ϕ and a_{modified} such that Eq. 71 described below is satisfied. For the first iteration, the value of F is assumed to be 1.0 at all radial stations for simplicity.

An example of the variation of the tip loss factor can be seen in Figure 37.[5] The solid curve shows the variation of the tip loss factor as it is conventionally applied with $R' = R$. As can be seen in the figure, the value of F remains near 1.0 for much of the propeller's radius, but begins to decrease sharply toward the tip. In this particular scenario, this steep decrease occurs beyond a radial location of approximately 80% of the propeller's radius.

Because the value of the tip loss factor approaches a very small value near the blade tip, applying the traditional form of F directly to the axial induction factor as described in Eq. 70 causes very large increases in a near the tip. If these very

[4]Note that the tip loss factor presented here is technically an approximation to Prandtl's original formulation, which was presented in Eq. 21 in Chapter II. Here, the modification is made in Eq. 69 where the local inflow angle, ϕ, is used in place of the helix angle at the tip and the sine of this angle is multiplied by the local radial station value in lieu of the full propeller radius. This approximation is suggested by Glauert as being "sufficiently accurate" (i.e., within a few percent) for the ability to directly apply this factor as opposed to the unknown value of $R\sin(\phi_T)$ [80].

[5]This figure assumes the propeller geometry described below in Section 4.2.2 where both Optional Steps 1 and 2 are employed.

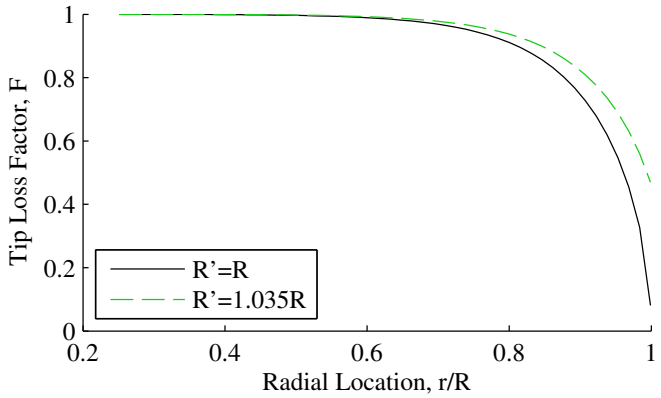

Figure 37: Variation of the tip loss factor over the blade radius for an example problem with two different values of R'

large values of a are maintained throughout the rest of the method, unrealistically large twists and chord lengths near the tip of the blade may result; therefore, it is recommended that a value of R' in Eq. 68 greater than R be used.

Experimentation has indicated that R' values of approximately $1.035R$ provide the desired result of increasing the loading near the tip without creating unrealistic blade shapes.[6] The impact of this increased value of R' is shown in Figure 37 as the dashed curve. Increasing values of R' increase the minimum value of F and push the radial location where the steep decrease in F occurs further outboard. In general, values of R' should be selected that maintain the near-uniform induced axial velocity as close to the tip as practical. Specifically, invoking this optional step can maintain a near-uniform velocity out to approximately the 90% radial station or beyond while conventional minimum induced loss designs and the designs that result without this modification of the axial induction factor begin to exhibit sharp decreases in the induced axial velocity near the 80% radial station.[7]

Optional Step 2: Limiting the rate of change of the tangential induction factor

[6] Additional discussion of the blade shapes and velocity distributions that result from varying values of R' can be found in Section 4.2.3.

[7] The impacts of this optional step will become apparent later when the induced axial velocity distributions from different propellers are compared in Figure 41.

Through experimentation it has been found that values of the tangential induction factor often begin to increase rapidly and approach the limit of 0.5 near the root because the assumptions of the method—specifically that the angular velocity added to the slipstream is small—is violated in this region.[8] These large axial induction factors can lead to blade shapes with large, sudden increases in chord length and twist angle. Such blade shapes may be difficult to manufacture in practice. Additionally, it has been observed that these large chords and twists often result in a velocity peak near the root of the blade. Because the intent of the method is to produce blades with near-uniform induced velocity distributions, a simple means of limiting the blade chord and twists is desired.

Through experimentation with the method it was observed that the large chord and twist changes near the root directly corresponded to large changes in the tangential induction factor. To mitigate these issues, one can apply a limit on the rate of increase of the tangential induction factor.[9] This limit is applied here as a maximum change in a' over a unit change in the non-dimensional radial location (r/R), or $\mathrm{d}a'/\mathrm{d}(r/R)$. When moving from the outer portion of the blade toward the root from one discrete radial station to another, if the change in a' divided by the change in r/R is greater than this limit, then a' is restricted to the maximum value that satisfies the desired slope limit. After the entire distribution of a' values is made to satisfy this limit, Eq. 67 is applied to find the implied modified axial induction factors. It has

[8]Note from Eq. 15 that the angular velocity added to the flow is simply $\omega = 2a'\Omega$, where Ω is the angular velocity of the propeller. Consequently, a' indicates half the fraction of the propeller's angular velocity that is added to the slipstream. If $a' = 0.5$, the angular velocity added to the slipstream is equivalent to the angular velocity of the propeller, which is a blatant violation of the assumption that ω is small in relation to Ω. If the assumption of small ω is taken as less than 10% of Ω, then the assumption is violated when $a' > 0.05$.

[9]There are certainly other means of reducing the large chord lengths and twists that result with large a' increases. For example, direct constraints on the absolute chord length or twist could be applied. Similarly, the rate of change of the chord length and twist could also be limited. Limiting the tangential induction factor is selected here for simplicity since only a single parameter is required to limit both twist and chord length (whereas at least two parameters would be required if limiting the blade geometry directly).

been observed that $\mathrm{d}a'/\mathrm{d}(r/R)$ values of approximately 1.25 are generally sufficient to smooth the blade geometry and reduce the induced velocity peak near the root. Additional discussion of the impacts of different values of $\mathrm{d}a'/\mathrm{d}(r/R)$ can be found below in Section 4.2.3.

4.2.1.2 Blade Twist Angle Distribution

After the axial and tangential induction factors are defined, the blade twist distribution can be specified. The local inflow angle, ϕ, of each blade section is defined as the angle between the plane of rotation and the local velocity vector. Using Eqs. 17 and 18, the local airflow angle can be expressed as Eq. 71.

$$\phi = \tan^{-1}\left(\frac{V_\infty\left(1+a\right)}{\Omega r\left(1-a'\right)}\right) \tag{71}$$

The inflow angle (ϕ), angle of attack (α), and twist angle (β) of each blade element are related as shown in Eq. 72. If the desired angle of attack at each blade element is known, then Eq. 72 can be used to set the twist angle distribution of the blade at each radial location (r).

$$\beta = \phi + \alpha \tag{72}$$

Generally speaking, for the propeller to operate most efficiently at its design point, each local airfoil section should be operating at its maximum lift-to-drag ratio. For this to occur, the local angle of attack for each section must be that which produces the highest lift-to-drag ratio, which is denoted $\alpha_{(L/D)_{\max}}$. Airfoil section data can be analyzed to determine this angle of attack as a function of radial station based on the local section Reynolds numbers and the appropriate values of $\alpha_{(L/D)_{\max}}$ substituted into Eq. 72 to determine the blade twist distribution.

If the propeller will be fixed pitch, it is not always advantageous to have the twist of the blade set such that each section operates at its maximum lift-to-drag ratio. The designer should then select appropriate values for the design angle of attack to

account for off-design operation of the propeller. These design angles of attack when substituted into Eq. 72 will determine the blade twist distribution.

4.2.1.3 Blade Chord Distribution

To determine the chord distribution for the blade, two separate expressions for thrust, T, developed from blade element theory and momentum theory can be equated. These expressions for the thrust produced by a blade annulus covering a radial length of dr are shown in Eqs. 73 and 74 [80, 118], where F is the tip loss factor, B is the number of blades, c_l is the local blade section lift coefficient, c_d is the local blade section drag coefficient, and c is the local chord length.

$$dT = 4\pi r \rho V_\infty^2 \left(1 + a\right) aF \mathrm{d}r \tag{73}$$

$$dT = \frac{B}{2} \rho W^2 \left[c_l \cos\left(\phi\right) - c_d \sin\left(\phi\right)\right] c \mathrm{d}r \tag{74}$$

In calculating the tip loss factor for Eq. 73, the actual propeller tip radius should be used for R' in Eq. 69. If Eqs. 64, 16, and 15 are substituted into Eq. 74 and the resulting equation is equated with Eq. 73, the chord length can be found as shown in Eq. 75.

$$c = \frac{8\pi r V_\infty^2 \left(1 + a\right) aF}{B\left[\left\{\Omega r \left(1 - a'\right)\right\}^2 + \left\{V_\infty \left(1 + a\right)\right\}^2\right]\left[c_l \cos\left(\phi\right) + c_d \sin\left(\phi\right)\right]} \tag{75}$$

4.2.1.4 Verification and Iteration

Once a propeller has been designed, the performance should be verified. It is unlikely that the method described above will produce exactly the desired results due to

(a) the assumptions inherent in BEMT,

(b) the assumption that the rotational velocity added to the slipstream is small,

(c) tip and root losses, and

(d) the modification to the desired axial induction factor near the hub.

The prop performance is verified with the open-source propeller analysis and design tool from Drela and Youngren called XROTOR [119] (in vortex mode).[10] If the average axial velocity predicted by XROTOR is different from what the designer specified, an iterative procedure is followed until convergence. In these iterations, the axial induction factor distribution is modified until the method produces a propeller with the desired average axial velocity. In practice, convergence is typically reached in approximately 2-3 iterations.

4.2.2 Example Propeller Design and Comparison to a Minimum Induced Loss Propeller

As an example of how the design method described above can be applied, the process is applied to design notional propellers for NASA's Scalable Convergent Electric Propulsion Technology Operations Research (SCEPTOR) flight demonstrator aircraft in this section. The candidate configuration for the SCEPTOR aircraft that will be considered here is comprised of 12 high-lift propellers each with 5 blades, a diameter of 1.89 ft (22.7 in), and a hub diameter of 5.7 in. For simplicity, each blade is designed with a single airfoil: the MH 114 [120], which is shown in Figure 38.[11] Early conceptual design studies indicated that these propellers should be designed to provide an average induced axial velocity of 23.2 ft/sec at a freestream speed of 55 knots while rotating at tip speeds of 450 ft/sec (4549 RPM).

[10] It has been found that the induced axial velocity profiles predicted by XROTOR in the potential or graded momentum modes may be unrealistically high near the root for some designs.

[11] The MH114 airfoil was designed by Martin Hepperle for propeller blades and has a 13% thickness to chord ratio. The high-lift propeller blades of the LEAPTech aircraft described in Chapter I were comprised of this same airfoil section, and it is selected here to maintain consistency with the LEAPTech configuration. In general, the selection of the airfoil will impact the specific blade chord and twist distribution that results from the design method, but similar performance often results at the design condition [69]. Airfoil selection affects the off-design performance of the propeller more substantially. To maintain a focused discussion on the novel aspects of the high-lift propeller design method, airfoil selection is not covered here.

Figure 38: MH114 airfoil shape

4.2.2.1 Axial Induction Factor Distribution

The first step of the new design method is to determine the axial and tangential induction factors as described in Section 4.2.1.1. Since there are two optional steps within this initial step, four different designs that utilize different combinations of these optional steps are presented. These propellers are designed with a) neither of the optional steps (termed the "base" method), b) only Optional Step 1, c) only Optional Step 2, and d) both Optional Steps 1 and 2.

For each of these designs, the first step is begun with a constant axial induction factor of 0.25 over all radial stations, and this value of a implies a distribution of a' values defined by Eq. 15. For designs invoking Optional Step 2, these initial values are then immediately modified based on the maximum desired value of $\mathrm{d}a'/\mathrm{d}(r/R)$. For designs invoking Optional Step 1, no further modifications can yet be made because the inflow angles, ϕ, are not yet known. (Said differently, the tip loss factor, F, is initially assumed to be 1.0 at all radial stations of the blade.) The resulting initial axial and tangential induction factors are shown in Figure 39. All designs have the same tangential and axial induction factors above radial locations of approximately 3.75 inch. Those designs invoking Optional Step 2 have decreased values of a and a' at radial locations near the root based on the maximum desired value of of $\mathrm{d}a'/\mathrm{d}(r/R) = 1.25$.

4.2.2.2 Blade Twist Angle and Chord Distributions

Once the axial and tangential induction factors are known, the inflow angles can be determined from Eq. 71. If Optional Step 1 is invoked, the following iterative procedure is then begun:

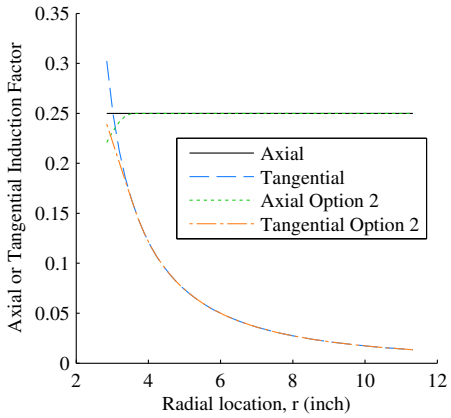

Figure 39: Initial axial and tangential induction factors for the example problem

1. The calculated values of ϕ are substituted into Eq. 69.
2. The tip loss factor is found from Eq. 68 (where $R' = 1.035R$).
3. Modified axial induction factors are calculated from Eq. 70.
4. Implied values of a' are determined from Eq. 66.
5. Any modifications required to the values of a' are made (either capping them at a maximum value of 0.5 or limiting the rate of change of a' in Optional Step 2)
6. If needed, a values are recalculated from Eq. 67.
7. New values of the inflow angles are calculated from Eq. 71.
8. Finally the new values of ϕ are compared to the values calculated previously. If the change is within a tolerance, then the iterative process is ended. If the values have changed more than desired, new values of ϕ are selected and the process is repeated.

For the two example propellers invoking Optional Step 2, four iterations of this procedure were required before the value of ϕ at all radial stations changed less than 1° from the prior iteration.

Airfoil information is required to determine the design angle of attack as well as the lift and drag coefficients. For the example SCEPTOR propellers, a design lift coefficient of 1.1 was desired, which led to local angles of attack of approximately 2° to 4° over the range of Reynolds numbers for all blade sections. The inflow angles found above and the angle of attack information were then sufficient to determine the twist angle distribution from Eq. 72. The airfoil information was also used to determine the chord distribution from Eq. 75, where the value of F was determined with $R' = R$.

4.2.2.3 Verification and Iteration

With an initial blade design defined, each propeller was then analyzed in XROTOR (in vortex mode) to verify the performance. In all cases, the initial blade designs only produced induced axial velocities of between 20.1 ft/sec and 21.8 ft/sec, which are all lower than the desired 23.2 ft/sec. The entire design process was then repeated using a higher initial value of the axial induction factor; these new initial values of a were approximately 0.27 or 0.29 for each propeller based on the difference between the desired average induced axial velocity and value determined after the first iteration through the method. All designs converged after one subsequent iteration through the entire method to produce the same average induced axial velocity of 23.2 ft/sec to within a 0.1 ft/sec tolerance.

The axial and tangential induction factors that result in the final iteration of the new design method are presented in Figure 40. Figure 40(a) shows the final axial induction factors for the four propellers designed with the new method while Figure 40(b) shows the associated tangential induction factors. Note that the green dashed curve for Optional Step 1 and the blue solid curve denoting both optional steps are essentially coincident for radial locations greater than approximately 3.5 inches. Similarly, the solid black curve for the base version of the method and the

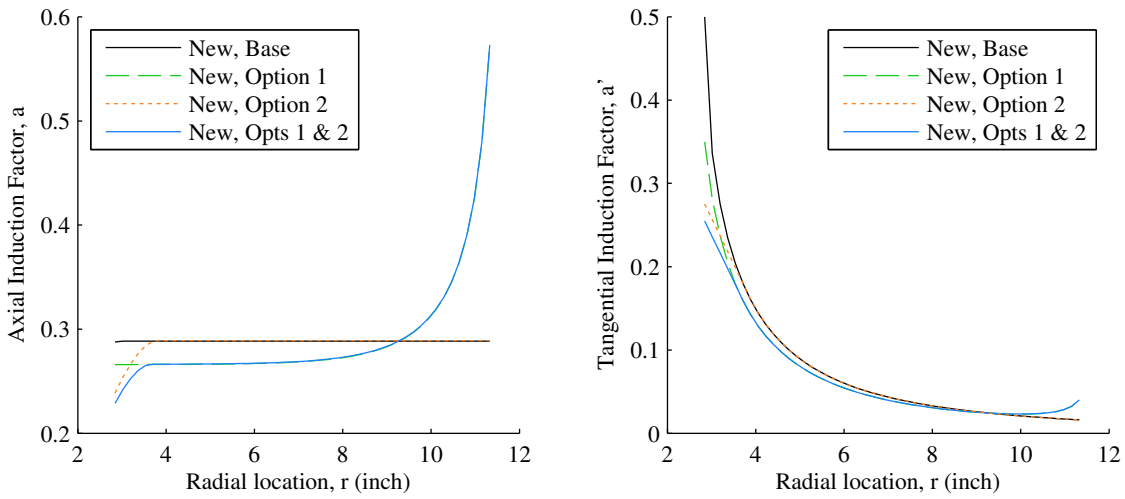

(a) Axial induction factors

(b) Tangential induction factors

Figure 40: Axial and tangential induction factor values after the final iteration of the design method for all designs

dotted orange line representing Optional Step 2 are also coincident for radial stations beyond approximately 3.7 inches.

The two propellers not invoking Optional Step 1 have nearly constant axial induction factors of 0.29, and have nearly identical tangential induction factors for most radial locations. The two propellers invoking Optional Step 1 have axial induction factors of approximately 0.27 for much of the blade before rising sharply near the tip; similarly, the tangential induction factors for these two propellers also mirror one another for most of the blade and rise slightly near the tip. The increase in the axial induction factor near the tip causes proportionally more load toward the tip so that the values of a over much of the blade are lower than the propellers that do not attempt to increase the loading near the tips.

The two blades invoking Optional Step 2 each display decreases in their axial induction factors down to values of approximately 0.23 and 0.24 near the root. The impact of limiting the slope of the tangential induction factor vs. radial location curve can clearly be seen in Figure 40(b) when the solid blue and dotted orange curves depart from the dashed green and solid black curves, respectively, near the 3.5

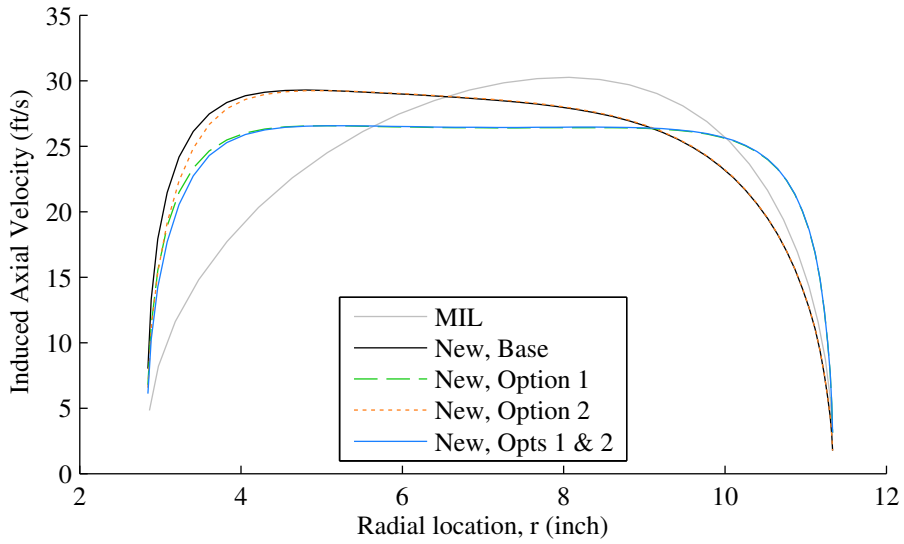

Figure 41: Predicted induced axial velocity distributions for the five propellers designed to produce the same average induced axial velocity

to 4 inch radial locations.

4.2.2.4 Propeller Performance and Comparison to a Minimum Induced Loss Propeller

To assess the potential merits of the design method, a minimum induced loss propeller was designed with XROTOR's minimum induced loss (MIL) design procedure, which is based on the theory of Larrabee [84, 85]. This minimum induced loss propeller was designed to provide the same average induced axial velocity as the designs described above. Because the design procedure in XROTOR does not allow for a direct input of the desired average induced axial velocity, the thrust of the propeller was estimated and an iterative procedure was followed until the resulting average induced axial velocity matched the desired value of 23.2 ft/sec.

Figure 41 shows the final induced axial velocity distributions from all five of the propellers—the four designed with the new method and the single minimum induced loss design. Recall that the initial motivation in developing the method was to produce propellers that induce a near-uniform axial velocity profile. The XROTOR modeling

indicates that propellers designed with the new method using Optional Step 1 achieve this goal. There are decreases in the velocity at the tip and root of the blade, but these losses are most likely unavoidable.

Although Figure 41 indicates that the most-uniform velocity profiles result from new design method when invoking Optional Step 1, even those propellers designed from the new method that do not invoke Optional Step 1 still appear to produce a more uniform axial velocity profile than the MIL propeller. As expected, the MIL propeller induces an axial velocity that displays a distinct peak near the 8 inch or 70% radial station. The propellers designed without invoking Optional Step 1 also display a peak, though this peak is less pronounced than for the MIL prop. Interestingly, the base form of the new design method produces propeller designs that exhibit peak induced velocities near the root.

It is unclear if it is more advantageous in terms of lift augmentation to locate the peak velocity near the tip or root of the blade. It is hypothesized that different propeller placements relative to the wing would benefit from the peak being placed in a different location, but wind tunnel testing and/or higher-order modeling would be required to test this hypothesis. However, because the theory presented in Section 4.1 indicates that near-uniform velocity distributions should improve lift augmentation, it is hypothesized that propellers designed with the new method invoking Optional Step 1 will provide superior lift augmentation compared to designs that exhibit peaks near the root or tip.

The final blade designs for all five propellers are shown in Figures 42 and 43. Figure 42 displays the chord lengths of the propellers while the twist distributions are presented in Figure 43.

Perhaps the most striking features of Figures 42 and 43 are the sudden increases in chord length and twist angle that result near the root from the base version of the new design method. The large chord lengths and twist angles that result from these

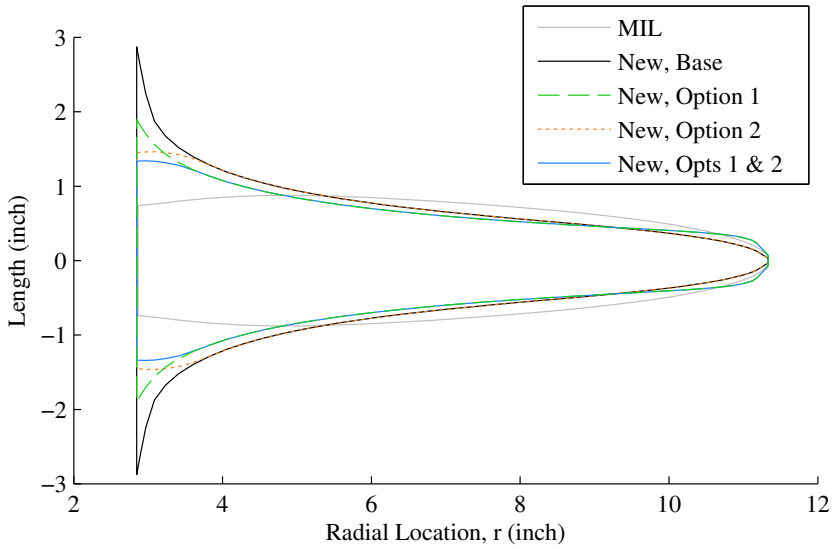

Figure 42: Comparison of the chord lengths of the final blade designs for the five propellers designed to produce the same average induced axial velocity

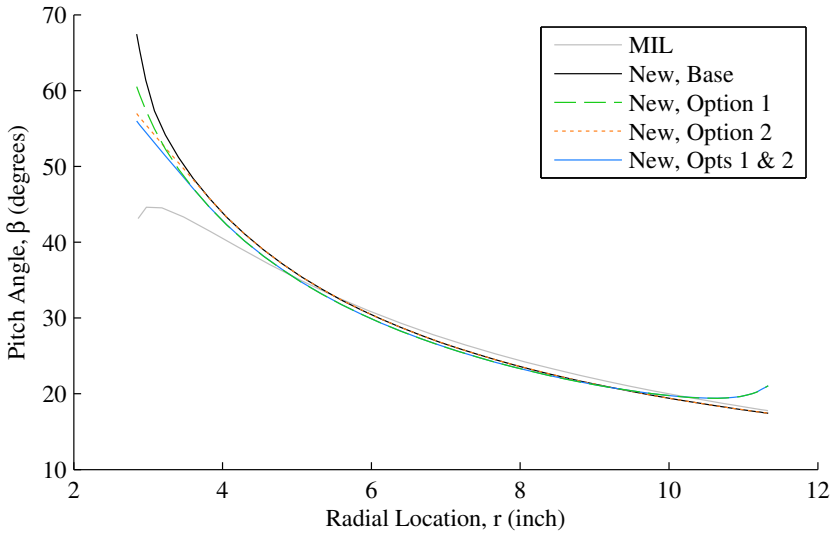

Figure 43: Comparison of the twist distributions for the final blade designs for the five propellers designed to produce the same average induced axial velocity

sudden increases are likely the result of the assumption that the rotational velocity added to the flowfield is small in comparison to the rotational velocity of the blade, which is a poor assumption near the root.[12] The large chord lengths and twist angles also cause the velocity peak near the root in the base version of the method. Optional Step 2 was implemented in order to reduce the sharp increases in chord length and twist, and it appears to be effective for that purpose. It does slightly decrease the induced axial velocities near the root, but the decreases are small and are likely an acceptable penalty to pay in order to make the blades more easy to manufacture. Additionally, even though Optional Step 1 was designed to increase the propeller loading near the tip, it also serves to reduce the chord length and twist angle near the root slightly.

The typical propeller performance measures—i.e., power, thrust, and torque—for these propellers should also be considered; however, one must consider that the purpose of high-lift propellers is not to generate thrust but rather to augment lift. Although one can compare the performance of all five propellers, it is unclear precisely how much lift each of these propellers would augment on a downstream wing. Before definitive comparisons between the effectiveness of these designs as high-lift propellers can be made, wind tunnel testing and/or higher-order unsteady computational fluid dynamics simulations of these propellers are required.

Because no experimental data is currently available, it will be assumed that each propeller will augment approximately the same lift. This assumption is almost certainly incorrect (for many reasons, including the theory in Section 4.1), but making this assumption enables us to directly compare the typical propeller performance parameters between props. Furthermore, it is likely a reasonable assumption since each propeller induces the same average axial velocity.

[12] Also, large twists and chord lengths near the root may also induce more significant radial flow, which represents another violation of the assumptions.

The performance characteristics of each of the five propellers were evaluated with XROTOR, and the results are summarized in Table 2. The power, torque, and thrust for each design are listed, and the percent difference in these values from the minimum induced loss (MIL) design is also presented. As is clear from the table, each of the

Table 2: Comparison of propeller performance characteristics for the five propellers designed to produce the same average induced axial velocity

	MIL	Base	Optional Step 1	Optional Step 2	Optional Steps 1 & 2
Power, kW	7.21	6.13	6.17	6.10	6.16
Power % Difference	–	-15.0%	-14.4%	-15.4%	-14.6%
Torque, N-m	15.1	12.9	12.9	12.8	12.9
Torque % Difference	–	-14.6%	-14.6%	-15.2%	-14.6%
Thrust, N	170	149	151	149	151
Thrust % Difference	–	-12.4%	-11.2%	-12.4%	-11.2%

propellers produced with the new design method requires less power and torque and produces less thrust than the MIL propeller. Each of these trends is advantageous. Although it may be counterintuitive that decreased thrust would be preferred, the SCEPTOR aircraft will have to operate all 12 of these high-lift propellers in order to approach and land at the desired flight speeds. These current propellers are predicted to add between 1790 N (402 lb) and 2040 N (457 lb) of thrust to the configuration when it is attempting to descend and decrease its speed. (It is possible these propellers will lead to relatively large amount of drag through modifying the lift distribution and increased friction drag over the wing due to scrubbing.)

If each of these propellers does augment approximately the same lift, then the new design method is capable of producing propellers that are superior to conventional minimum induced loss designs. The ability to generate the same lift augmentation with approximately 15% less power would not only directly decrease vehicle energy consumption, but also provide the potential to reduce weight by employing smaller motors.

For the sake of brevity only a single example implementing the method has been presented here; however, many other propellers with diameters ranging from 13 inches to over 3.6 ft have been designed following the same procedure described above. (Several additional design examples will be discussed later in Chapter VI.) For all of these cases, the propellers designed for minimum induced loss are predicted to require between approximately 10% and 20% more power and produce between approximately 10% and 20% more thrust than propellers designed with the new method to achieve the same average induced axial velocity.

4.2.3 Additional Comments on the Optional Steps

Guidance was provided above for reasonable values of R' and $\mathrm{d}a'/\mathrm{d}(r/R)$. In this section, propellers designed with differing values of these parameters for the example problem described in Section 4.2.2 are presented to provide better insight into the effects of these parameters. Similar types of studies can be performed for any specific problem to determine the most appropriate value of these parameters for that problem.

The impacts of varying the R' parameter from R to $1.1R$ are shown in Figures 44, 45, and 46. The induced axial velocity distributions are shown in Figure 44. The chord and twist distributions are plotted in Figures 45 and 46, respectively.

As can be seen in Figure 44, values of R' at or near the radius create large increases in the axial velocity distribution near the tip. Additionally, unrealistically large increases in chord length and twist angle result near the tip when $R' = R$ as can be observed from Figures 45 and 46. Although the purpose of including Optional Step 1 was to increase the loading near the tip, employing this optional step leads to changes in the blade design over the entire blade. Changes in the chord and twist near the root are most pronounced with smaller values of R'.

When values of R' are 2.5% or 5% greater than the propeller radius, the large

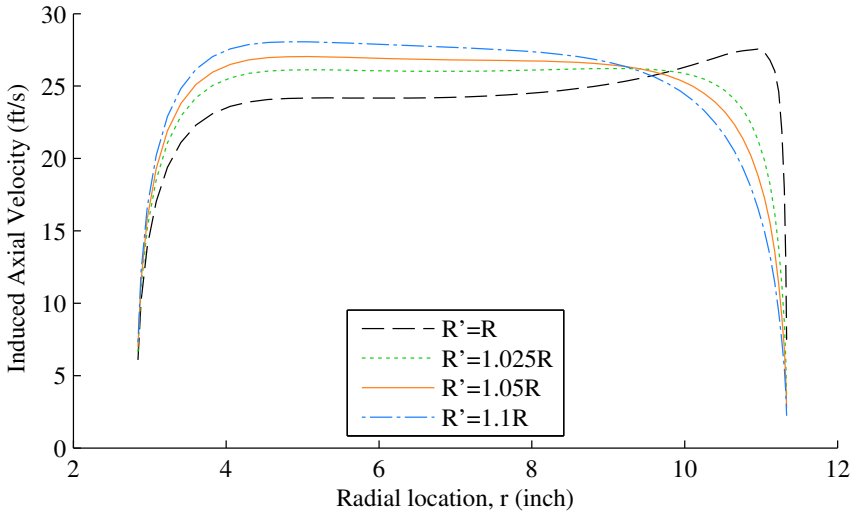

Figure 44: Predicted induced axial velocity distributions for propellers designed with varying values of R'

increase in axial velocity at the tip is eliminated while the velocity near the hub is simultaneously increased. These changes result in considerably more uniform velocity profiles than those generated with $R' = R$ or without application of Optional Step 1 as can be seen in Figure 44. Additionally, the chord length and twist angle increases at the tip for R' values of $1.025R$ or $1.05R$ are greatly reduced and much more realistic

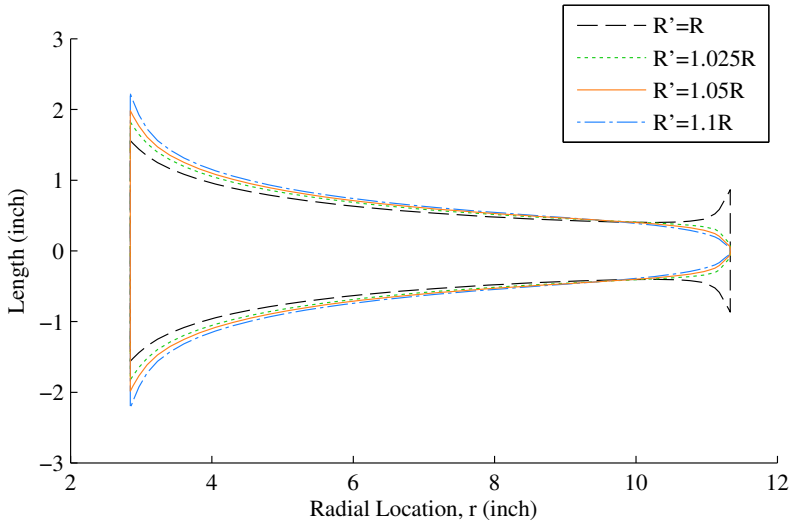

Figure 45: Comparison of the chord lengths of blades designed with varying values of R'

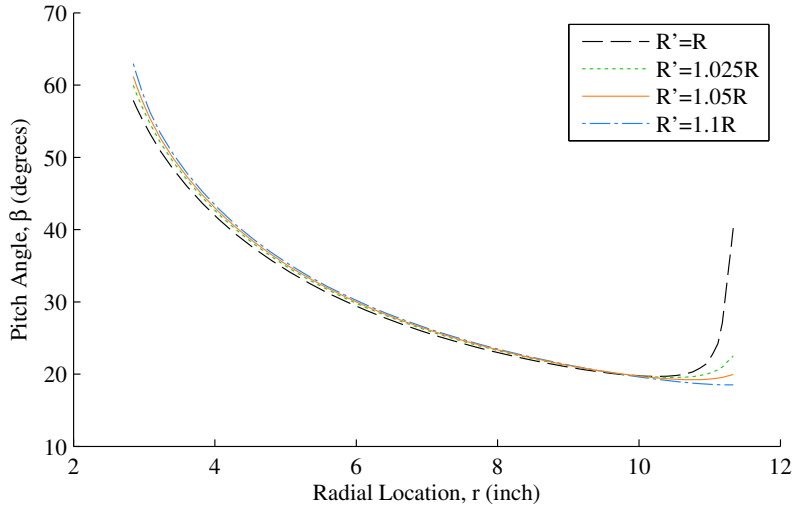

Figure 46: Comparison of the twist distributions of blades designed with varying values of R'

than those observed for $R' = R$. Consequently, it was recommended above that R' values should be approximately $1.035R$.

As the value of R' is increased to $1.1R$ and beyond, the velocity profiles as well as the chord length and twist angle distributions begin to become more and more similar to the base version of the method (i.e., that without employing either of the optional steps). In these cases, peaks in the induced axial velocity are observed near the root, and the induced velocity continually decreases to the tip.

To provide perspective on how Optional Step 2 can modify the blade designs, four propellers were designed with values of $\mathrm{d}a'/\mathrm{d}(r/R)$ ranging from 0.25 to 2. The resulting axial velocity distributions are shown in Figure 47. The chord lengths are shown in Figure 48, and the twist distributions are presented in Figure 49.

When values of $\mathrm{d}a'/\mathrm{d}(r/R)$ are low, the chord lengths and twist angles near the blade root are greatly reduced, which leads to reductions in the induced axial velocity near the root. The reduced velocity near the root necessitates that the induced axial velocities increase near the tip to provide the same average induced axial velocity. Additionally, small $\mathrm{d}a'/\mathrm{d}(r/R)$ values produce blades that exhibit more gradual changes

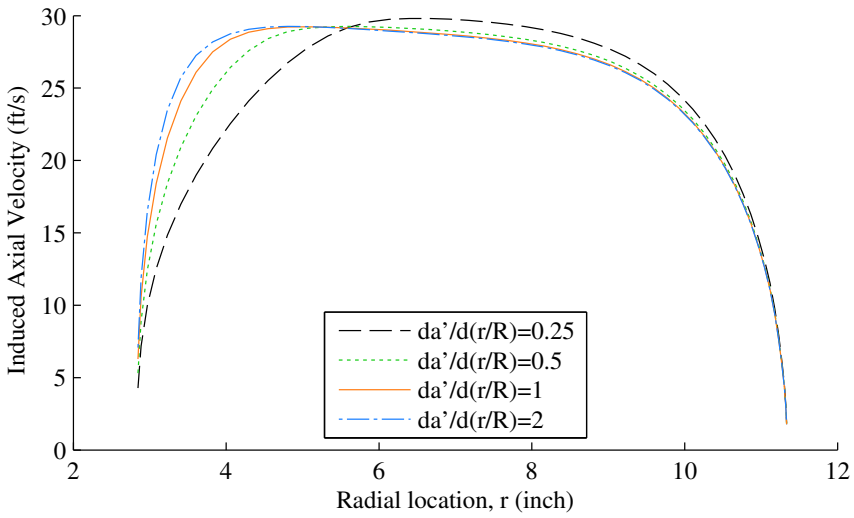

Figure 47: Predicted induced axial velocity distributions for propellers designed with varying values of $\mathrm{d}a'/\mathrm{d}(r/R)$

in the chord length and twist angle than those with higher $\mathrm{d}a'/\mathrm{d}(r/R)$ values.

As the values of $\mathrm{d}a'/\mathrm{d}(r/R)$ increase, the propeller designs become more similar to the base version of the method. Depending on the value of $\mathrm{d}a'/\mathrm{d}(r/R)$ that is specified, it is possible that the blade design may be unchanged from the base method. Consequently, higher $\mathrm{d}a'/\mathrm{d}(r/R)$ values generally produce blades with higher induced

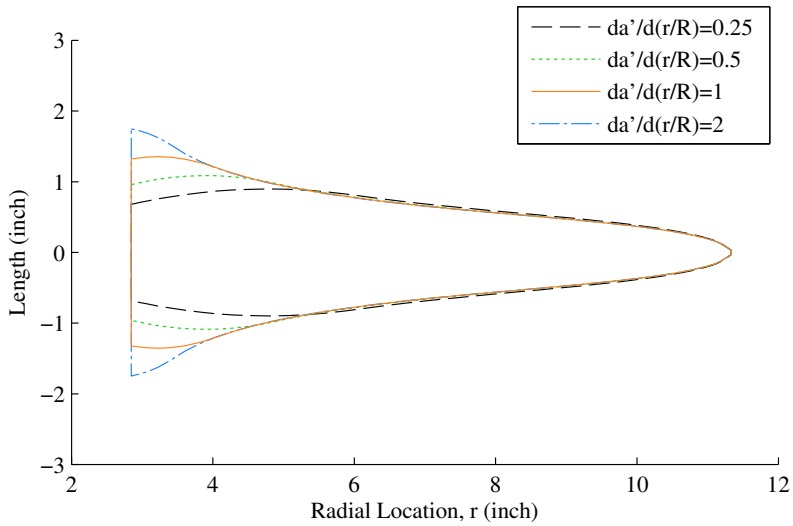

Figure 48: Comparison of the chord lengths of blades designed with varying values of $\mathrm{d}a'/\mathrm{d}(r/R)$

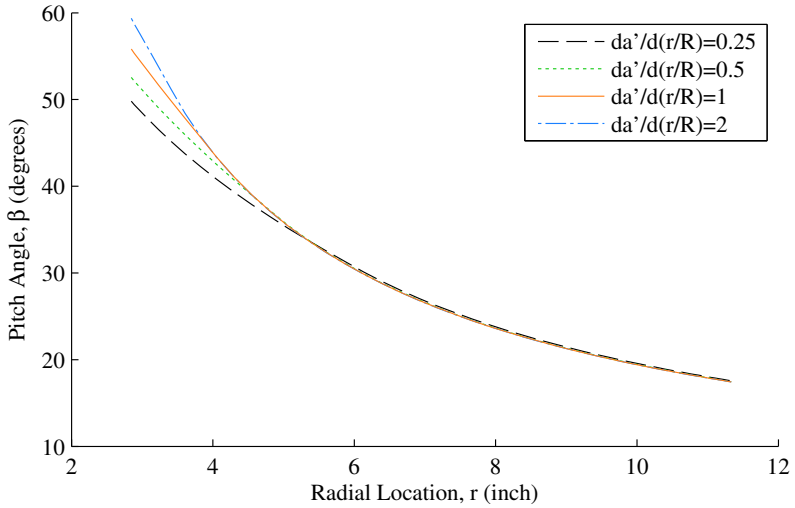

Figure 49: Comparison of the twist distributions of blades designed with varying values of $\mathrm{d}a'/\mathrm{d}(r/R)$

velocities near the root than blades with lower $\mathrm{d}a'/\mathrm{d}(r/R)$ values.

4.3 Cautionary Statements

The benefits observed from the propellers produced by the novel propeller design method presented above rely on the assumption that the lift augmentation from a propeller of a given diameter can effectively be abstracted to the average induced axial velocity generated by that propeller. This is almost certainly not the case precisely in reality, but the modeling and comparison to experiments performed in Chapter III indicate that it is a reasonable assumption. Additionally, since the axial velocity distributions generated by the new method exhibit less variation over the propeller radius than a conventional minimum induced loss design method, literature indicates that the novel propellers should actually be more effective than conventionally designed propellers. Consequently, wind tunnel testing and/or unsteady higher-order computational fluid dynamics simulations are required to verify if potential performance benefits of the novel propeller designs can be realized in practice.

Further refinement to the proposed design method may be required before using

it to design practical high-lift propellers. First, the assumption that the rotational velocity added to the slipstream is small does not appear to be a valid assumption near the root. Although the method as presented can produce propellers with the desired near-uniform induced axial velocities, modification of the theory to eliminate this assumption may result in superior designs without the need to implement any optional steps to the procedure. Second, the large chords and twists that can result from the method near the blade root may prove difficult to manufacture and/or fold. Although Optional Step 2 of the method reduces the magnitude of these chord and twist changes, the resulting chord lengths and twist angles are still larger than in conventional propeller designs. The impacts of limiting twist angle and chord lengths on the resulting propeller performance should be explored. It is likely that airfoil changes near the root will be required to achieve the desired loadings with limits imposed. Finally, the relatively short chord lengths that can be produced by the method near the mid-radial location toward the tip may result in aeroelastic deformations that could reduce the effectiveness of the blade. Consideration of varying the airfoil along the blade and/or utilizing stiff materials in manufacturing may result in sufficient structural rigidity to avoid significant deformations.

4.4 Chapter Summary

Recall the motivating question for this chapter:

Since the purpose of high-lift propellers differs from traditional propellers, should high-lift propellers be designed differently, and if so, how?

The answer to the first part of the question is 'yes,' and a method was presented for designing more effective high-lift propellers. The following points summarize the method:

1. The literature indicates that lift can be most effectively augmented by high-lift propellers if their induced axial velocity profiles are uniform or as closely

uniform as possible.

2. A novel high-lift propeller design method has been developed that seeks to maintain a near-uniform induced axial velocity profile over the propeller blade.
3. The design method presented is built on blade element momentum theory including Prandtl's tip loss factor to account for vortex losses.
4. The novel design method produces propellers that, according to computational models, can induce the same average axial velocity as propellers designed for minimum induced loss while requiring approximately 15% lower power and producing approximately 11% lower thrust. These characteristics indicate that the new designs would be superior to conventional minimum induced loss propellers if they augment approximately the same lift as is predicted by the model presented in Chapter III.

CHAPTER V

DETERMINING THE DESIGN POINT FOR THE HIGH-LIFT PROPELLERS

The design method presented in the previous chapter assumed that the design point for the propellers was known. It is logical, then, to ask the following question:

What is the appropriate design point for high-lift propellers?

Answering this question is the main topic of this chapter.

Although it may seem that the most critical operating condition for high-lift propellers will be the lowest desired operating speed of the aircraft (i.e., the stall speed with high-lift propellers operating), this is not necessarily the case. The manner in which the aircraft will be operated at low speeds can have a considerable impact on the design point that should be selected. In this chapter, the issues associated with practical, low-speed operation are discussed. For the discussions in this chapter it will be assumed that the high-lift propellers are fixed pitch. Although it is possible to install constant speed (or other form of variable pitch) high-lift propellers, the additional weight and complexity associated with these propellers is assumed to outweigh the benefits for the purposes of this dissertation.

5.1 Approach Considerations

The most critical low-speed performance requirement on many aircraft is the ability of the aircraft to approach and land at a reasonable speed. Generally, small wings are desirable for cruise flight because the drag of a small wing is less than that of a large wing and still capable of producing sufficient lift at higher speeds. However, too

small of a wing may lead to high approach and landing speeds, which can increase landing distances and decrease the safety of the aircraft since the increased kinetic energy carried with a higher speed must be dissipated in the event of an emergency landing.

Conventional aircraft generally trade some high-speed performance for acceptable low-speed performance through a combination of larger-than-optimal wings for cruise flight along with conventional high-lift devices such as flaps. These aircraft are able to approach and land with little to no thrust required since the potential energy of the vehicle can be traded for kinetic energy as the aircraft descends. In contrast, aircraft with high-lift propellers will likely be designed with smaller wings, which will require blowing from the high-lift props to meet the stall and approach speed requirements. These props will inherently produce thrust in low-speed conditions, and it is possible that the thrust generated to provide sufficient lift will make it impossible for the aircraft to descend at the desired speed. The modeling described in this section will provide insight into this interesting new problem.

Additionally, the regulations associated with low-speed flight will be discussed in this section. Current regulations will be examined and modifications of these regulations based on the novel performance characteristics of aircraft with high-lift propellers will be proposed. Ultimately, these regulations will dictate how high-lift propeller systems should be designed.

5.1.1 Regulations Related to Stall and Approach Speeds

Current Federal Aviation Regulations (FARs) dictate that many small aircraft certified under Part 23[1] must exhibit a stall speed of no more than 61 knots unless certain other criteria designed to improve the crashworthiness of the aircraft are met [53]. The conditions at which the stall speed must be determined are explicitly stated in

[1]specifically, any single engine aircraft or a multi-engine aircraft less than 6,000 lb that cannot meet certain critical engine out climb requirements

the regulations, and these conditions currently do not allow any credit for blowing from high-lift propellers (i.e., the stall speed must be determined without any positive thrust from the propellers). Additionally, the current regulations also only cover "reciprocating engine-powered airplanes" or "turbine engine-powered airplanes" [53] so an electric aircraft with no reciprocating or turbine engine cannot be certified. It is clear that the concepts discussed in this document, which rely on both electric motors and high-lift propellers, will require new regulations before they can be certified.

The Federal Aviation Administration (FAA) and the aerospace industry as a whole are well aware of the limitations of the existing FARs in certifying new technologies and are working to improve the process. The advent of practical electric aircraft in recent years has been one of the factors leading to this realization. ASTM International's Committee F44 on General Aviation Aircraft was established to develop consensus standards that will contain more flexible means of compliance than the existing FAR Part 23 regulations, which should allow for new technologies such as electric propulsion to be certified [121]. If the F44 Committee's standards are adopted by the FAA (as is anticipated), the possibility of certifying electric aircraft with high-lift propellers may become a reality.

Because the F44 Committee is still developing the new consensus standards, no definitive statements can be made as to the conditions that must be met for high-lift propellers and electric motors to be certifiable. Therefore, the discussion here will be based on maintaining the "spirit" of existing regulations as closely as possible although the concepts proposed will not meet the current "letter of the law" (i.e., the current FARs). When deviations from existing regulations are proposed, justification for the safety of the overall system will be provided.

The current FARs dictate a minimum threshold for a reference approach speed, V_{REF}, which depends on the stall speed of the configuration [122]. Although the reference approach speed does not denote the speed at which an approach must

actually be flown by a pilot, it does dictate how a manufacturer can represent the performance of the aircraft (and provides solid guidance for how pilots should actually fly an approach). Generally, the FARs specify that the reference approach speed is 30% higher than the stall speed (i.e., $V_{REF} = 1.3V_{S1}$) [122].[2]

Although the regulations do not explicitly state the reasons for maintaining a higher speed in approach, the 30% velocity margin likely exists to provide a sufficient buffer between the stall and approach speeds to account for both pilot error and factors beyond the pilot's control such as wind gusts and low-level wind shear. The pilot must be able to react to any changes in aircraft attitude or airspeed without stalling or otherwise losing control of the airplane (e.g., having insufficient control surface authority due to decreased dynamic pressure from a tailwind gust). This view is at least partially supported by the fact that the regulations for larger, transport category aircraft certified under Part 25 require a reduced velocity margin of only a 23% increase over the stall speed [123].[3] This reduction in the required margin is likely due to the higher approach speeds of transport aircraft. The impact of a sudden change in wind velocity of 15 knots, for example, will be less pronounced on a transport category aircraft approaching at 150 knots than a small aircraft approaching at 65 knots.

As a short aside, it should be noted that the difference in the regulations dictating the definition of V_{REF} for small (i.e., Part 23) versus large (i.e., Part 25) aircraft is a prime example of how certain assumptions about the vehicle characteristics for different categories of aircraft were made in writing the current regulations. Historically,

[2]Technically V_{REF} may actually be set by the minimum control speed with a critical engine inoperative if that speed is higher than 1.3 times V_{S1}. However, the stall speed provides a minimum value of V_{REF}. See 14 CFR §23.73. Additionally, for landing performance calculations, the stall speed is typically taken to be the stall speed in the landing configuration (i.e., with full flaps in a conventional aircraft) although the regulations only specify that the configuration must be specified. See 14 CFR §1.2 for the definition of V_{S1} and additional clarification in 14 CFR §23.49.

[3]As with Part 23, there are other circumstances where V_{REF} may actually be set by other factors, but it cannot be any lower than 1.23 times the reference stall speed. See 14 CFR §25.125 for details.

these assumptions have been sufficient to certify new aircraft and maintain the high safety levels desired. However, aircraft equipped with new technologies that break from the traditional assumptions made in the regulations may either be penalized by these assumptions or be completely uncertifiable.

From a technical perspective, the 30% velocity margin dictated by FAR §23.73 is likely more appropriately viewed as a lift coefficient margin. Since $C_L = 2L/(\rho V^2 S)$ and the lift produced at the approach speed ($V_{REF} = 1.3V_{S1}$) and stall speed (V_{S1}) must be the same, the lift coefficient at the approach speed must be $C_{L_{\text{REF}}} = C_{L_{\max}}/1.3^2 \approx 0.59 C_{L_{\max}}$ (where $C_{L_{\max}} = 2L/(\rho V_{S1}^2 S)$). Therefore, the lift coefficient margin between the stall speed and approach speed, $(\Delta C_L)_{\text{approach}}$, is

$$(\Delta C_L)_{\text{approach}} = \left(1 - 1/1.3^2\right) C_{L_{\max}} \approx 0.41 C_{L_{\max}}. \tag{76}$$

Eq. 76 indicates that the required C_L margin between approach speed and stall speed varies with the aircraft's $C_{L_{\max}}$. An aircraft with a higher maximum lift coefficient is required to carry a larger margin than one with a lower $C_{L_{\max}}$. The required C_L margin for values of the maximum lift coefficient ranging from 1 to 5 is shown in Table 3. For conventional general aviation high-lift systems that produce maximum

Table 3: Lift coefficient margins required by current Part 23 regulations for various maximum lift coefficient values

$C_{L_{\max}}$	1.0	1.5	2.0	2.5	3.0	3.5	4.0	4.5	5.0
$(\Delta C_L)_{\text{approach}}$	0.41	0.615	0.82	1.025	1.23	1.435	1.64	1.845	2.05

C_L values of approximately 2, a C_L margin of approximately 0.8 is required. However, for novel high-lift systems such as those with high-lift propellers that could produce lift coefficients of 5, a C_L margin of over 2 is required. This margin is greater than the maximum lift capability of many current small aircraft! It is difficult—and arguably impossible—to justify that such high $(\Delta C_L)_{\text{approach}}$ values are actually necessary to maintain safety.

Conventional aircraft create the required C_L margin entirely by controlling the angle of attack (for given flight conditions and vehicle configuration).[4] Therefore, one can also view the 30% velocity margin as an angle of attack margin, which is denoted as $(\Delta\alpha)_{\text{approach}}$. The angle of attack margin will more directly relate to the safety of the aircraft than a velocity margin because stall is much more closely related to the angle of attack than it is to velocity.[5]

Since every aircraft will have a different lift curve slope and maximum lift coefficient, the velocity margin does not equate directly to a single $(\Delta\alpha)_{\text{approach}}$. Instead, the angle of attack margin will vary for every aircraft, and these variations can be significant. Figure 50 indicates how the angle of attack margin varies for aircraft with lift curve slopes of 2π, 5, and 4/radian[6] over a range of $C_{L_{\max}}$ values from 1 to 5.

As indicated in Figure 50, the angle of attack margin required by the current FARs can vary widely depending on the aircraft. The $(\Delta\alpha)_{\text{approach}}$ values for the cases in the figure range from less than 4° to nearly 30°. The rationale for requiring such varied angle of attack margins is open to interpretation, but the author sees no solid safety reasons for requiring such large variations in $(\Delta\alpha)_{\text{approach}}$. It is assumed here that relative velocity margins were specified in the regulations rather than angle of attack or C_L margins primarily because velocity is much more easily measured than angle of attack or C_L. However, Figure 50 makes it clear that requiring all aircraft

[4]There are many small aircraft with propellers installed upstream of the wing leading edge (e.g., a typical light twin-engine aircraft). The slipstreams from these propellers can have significant impacts on the lift generated. However, since these propellers are not specifically designed to augment lift, current regulations prohibit the use of propulsive thrust in determining the stall speed, and very low powers are typically used in approach, these aircraft control lift during approach (at a given speed) almost entirely via angle of attack.

[5]Certainly the velocity will play a role in determining the stall angle of attack since the Reynolds number will vary directly with velocity and the stall angle of attack changes with Reynolds number. However, for the small ranges of velocity being discussed here, the changes in Reynolds number for a given configuration are small so there will be negligible variations of the stall angle of attack with velocity.

[6]These lift curve slopes are representative of different aircraft with varying wing planforms. Although airfoils may have lift curve slopes on the order of 2π, three-dimensional effects reduce the effective lift curve slope so that values closer to 5/radian are more representative of real aircraft.

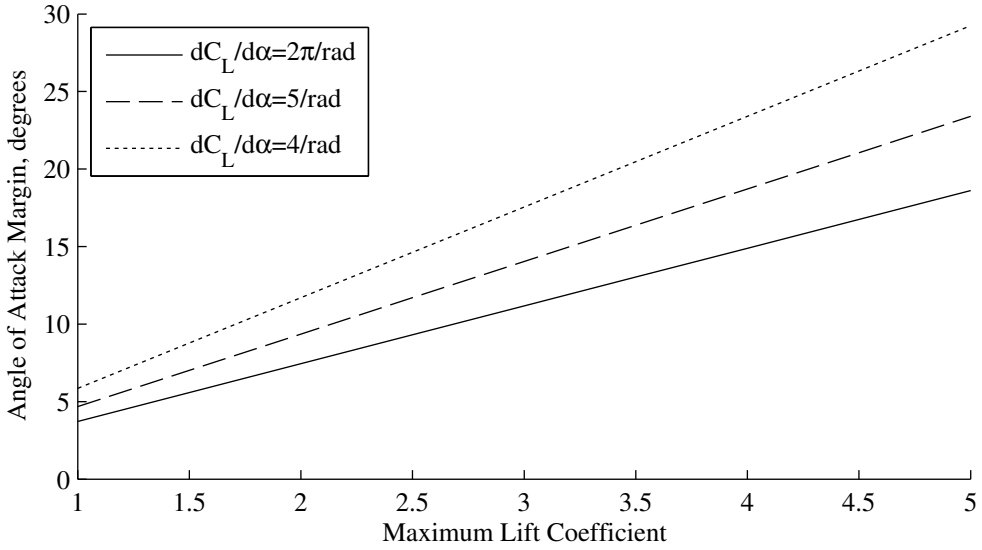

Figure 50: Variation of the required angle of attack margin between stall and approach speeds for various maximum lift coefficients and lift curve slopes

to maintain the same velocity margin does not equate to maintaining an equivalent level of safety (assuming that an angle of attack margin equates more-or-less directly with safety).

In defense of the existing regulations, conventional Part 23-certified small aircraft typically have maximum lift coefficients near 2.0, so the current regulations in practice have only required aircraft to maintain angle of attack margins ranging from approximately 5° to 10°. However, for new technologies or vehicle concepts that may enable very high maximum lift coefficients on the order of 5.0, the current regulations would require angle of attack margins of approximately 15° to 30°—or up to six times more than required for conventional aircraft! So long as approximately the same approach and landing speeds are being considered for these aircraft with higher $C_{L_{\max}}$ values, it is difficult to justify margins so much higher than with conventional technologies. This is another example of how existing regulations have certain assumptions "baked in" that may not be appropriate for new technologies.

Apart from being able to generate much higher maximum lift coefficients, aircraft

with high-lift propellers generate lift differently than conventional aircraft. Whereas a conventional aircraft in a specified configuration at a certain airspeed and altitude can only increase lift through increasing the angle of attack,[7] aircraft with high-lift propellers can create additional lift at the same angle of attack through increasing the blowing from the props. The induced velocity from the propellers adds a new degree of freedom to produce lift and thus generate a safe C_L margin.

Because these two mechanisms for producing lift in an aircraft with high-lift propellers can be modified independently, it is helpful to decompose the total lift generated into two components: the angle of attack contribution and the blowing contribution. Mathematically, this relationship can be expressed as Eq. 77, where C_{L_α} is the C_L contribution from the angle of attack (i.e., the lift coefficient without any blowing) and $C_{L_{\text{blowing}}}$ is the additional lift generated by the high-lift propellers' slipstreams (i.e., the total lift less the unblown lift). (It should be noted that the notation of C_{L_α} adopted here is *not* the lift curve slope.)

$$C_L = C_{L_\alpha} + C_{L_{\text{blowing}}} \tag{77}$$

Similarly, the total lift coefficient margin is comprised of the C_L margin available from the angle of attack, $(\Delta C_{L_\alpha})_{\text{approach}}$, and the C_L margin available from increasing propeller blowing, $\left(\Delta C_{L_{\text{blowing}}}\right)_{\text{approach}}$, as shown in Eq. 78.

$$(\Delta C_L)_{\text{approach}} = (\Delta C_{L_\alpha})_{\text{approach}} + \left(\Delta C_{L_{\text{blowing}}}\right)_{\text{approach}} \tag{78}$$

The discussion around Figure 50 assumed all the C_L margin would be required to come from the angle of attack (i.e., that $C_{L_{\text{blowing}}} = \left(\Delta C_{L_{\text{blowing}}}\right)_{\text{approach}} = 0$). Since high-lift propellers offer a new degree of freedom to generate C_L, the need for angle of attack margins on the order of 3 to 6 times conventional aircraft is not necessarily required to maintain the $(\Delta C_L)_{\text{approach}}$ values currently required by the regulations.

[7] See Footnote 4 above.

However, as noted above in relation to Table 3, the current regulations also require C_L margins that are likely higher than justifiable no matter how they are generated. Is it really necessary for an aircraft with a $C_{L_{\max}}$ of 5 to have over 2.5 times the C_L margin of conventional aircraft and carry more margin than lift capability of conventional aircraft?

It is proposed here that high-lift propeller systems should be able to be certified if they can be shown to maintain roughly the same overall C_L margins as many existing general aviation aircraft provided the new aircraft will approach and stall at approximately the same speeds. Because many general aviation aircraft have $C_{L_{\max}}$ values on the order of 1.5 to 2.0, a reasonable range for $(\Delta C_L)_{\text{approach}}$ is approximately 0.6 to 0.85 as indicated by Table 3. This total lift margin can be created from any combination of an angle of attack margin and a blowing margin (as calculated from Eq. 78) with one caveat: the reference approach speed must be greater than the unblown stall speed of the wing to account for the case of a full system power loss. Stated in another manner, at the reference approach speed $(\Delta C_{L_\alpha})_{\text{approach}}$ must be greater than 0.[8] The safety implications of certifying aircraft with high-lift propellers in a different manner than conventional aircraft is explored below. This exploration can provide justification for creating a new certification pathway for these novel aircraft.

5.1.2 Exploration of Lift Coefficient Margin and Potential Approach Profiles of Aircraft with High-Lift Propellers

The total C_L margin required and the division of this margin between the angle of attack and blowing components in high-lift propeller aircraft will have implications on both the maximum power required from the high-lift propeller system and the flight condition at which the critical power requirement to the system will be set. In this

[8]The exact value required for $(\Delta C_{L_\alpha})_{\text{approach}}$ is debatable. The probability that there is a complete power failure at the exact instant when a wind gust is encountered is small, so relatively small (but certainly still greater than zero) values for $(\Delta C_{L_\alpha})_{\text{approach}}$ may still ensure safe aircraft operations. The value of $(\Delta C_{L_\alpha})_{\text{approach}}$ selected should provide margin for pilots to react to off-nominal conditions such as power failures or wind gusts.

section the variation of the lift coefficient and lift coefficient margin with velocity are discussed. The general variations of these parameters both with and without high-lift propellers is explored using the SCEPTOR flight demonstrator aircraft as an example case to illustrate how the sizing conditions for the high-lift propellers change with lift coefficient margin.

5.1.2.1 Approach Profiles

Current regulations only imply a C_L margin at a single speed: the reference approach speed. In an operational setting, the aircraft will initially approach at this speed, but will decrease its speed before landing. To reduce the landing distance, the speed should be decreased to near stall before touchdown. The act of decreasing speed through the approach is accompanied by an increase in the lift coefficient, and, consequently, a reduction in the C_L margin. The variation of the lift coefficient through the act of decreasing the velocity is termed here the "approach profile," and the C_L margin that is associated with an approach profile is called the "lift coefficient margin profile." These profiles are most easily visualized as plots of either the C_L or $(\Delta C_L)_{\text{approach}}$ as a function of flight speed such as those shown in Figure 51. The approach profile can be seen in Figure 51(a), and the associated margin is plotted in Figure 51(b). Each of these profiles assume a conventional configuration without any high-lift propellers.

The approach profile in Figure 51(a) follows an inverse square curve since the same total lift must be maintained at all speeds and C_L is proportional to the square of the velocity. The lift coefficient is steadily increased as the velocity is decreased until the stall speed of the aircraft is reached.[9] The C_L margin in Figure 51(b) is highest

[9]It should be noted that the aircraft does not necessarily have to reach the stall speed before touching down. (In the author's own limited experiences flying, he has never actually stalled an aircraft when landing.) Therefore, the lower speed regions in the approach profile may never actually be flown in practice. Also, the aircraft could be operated at velocities less than the stall, but would then have insufficient lift to maintain level flight. These conditions are ignored here, since in practice aircraft maintain some positive margin above the stall speed throughout their approach.

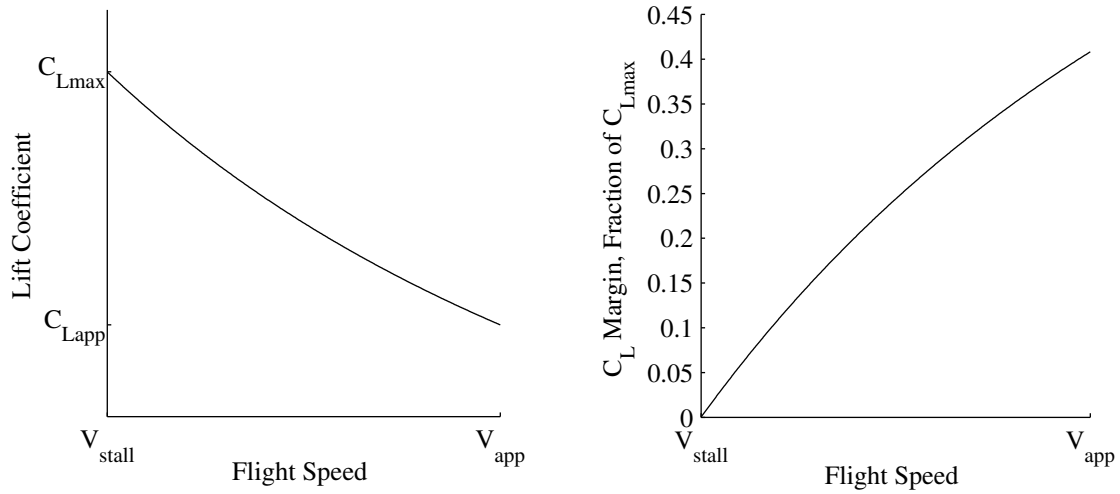

(a) Approach profile

(b) Lift coefficient margin profile

Figure 51: Generic representation of an approach profile and the associated lift coefficient margin for conventional aircraft

at the approach speed (with the value specified in Eq. 76), and the margin decreases as the velocity is decreased until reaching zero at the stall speed. These two profiles represent a baseline to which aircraft with high-lift propellers will be compared.

There are many possible approach profiles that can be flown in aircraft with high-lift propellers because the blowing can be varied to augment different amounts of lift. In contrast, conventional aircraft must increase lift by increasing the angle of attack, so only a single profile can be flown. The following five example profiles will be presented here:

1. Aggressive two-phase approach,
2. Conservative two-phase approach,
3. Constant lift multiplier (a.k.a., "Constant K_L") approach,
4. Linear variation of C_L generated by angle of attack with velocity (a.k.a., "Linear C_{L_α}") approach, and
5. Maximum blowing approach.

These examples are certainly not an exhaustive list of all possible profiles, but they should effectively "bound" the realm of possible approach profiles that can be flown.

The first four of these example approach profiles are illustrated in Figure 52.[10] The plots in this figure show velocities ranging from the blown stall speed, $(V_{\text{stall}})_{\text{blown}}$, up to the unblown approach speed, which is the reference approach speed that the current FARs would require for an aircraft with high-lift propellers (i.e., $(V_{\text{approach}})_{\text{unblown}} = 1.3(V_{\text{stall}})_{\text{unblown}}$). In each profile, the total required C_L is generated through a combination of angle of attack and blowing (as discussed above in reference to Eq. 77), and these combinations are described below.[11]

The aggressive two-phase approach creates as much lift from angle of attack as possible, and is depicted graphically in Figure 52(a). From the unblown approach speed to the unblown stall speed, no blowing is utilized so $C_L = C_{L_\alpha}$. Once reaching $(V_{\text{stall}})_{\text{unblown}}$, no additional lift can be produced from angle of attack, so blowing must be utilized to maintain sufficient lift at lower speeds. This approach forms an absolute lower bound on the blowing power that may be required because it utilizes as little blowing as possible.[12]

Figure 52(b) illustrates the conservative two-phase approach. This approach follows the same principle of splitting the approach into two phases as the aggressive approach discussed above, but less C_L is generated from angle of attack. In this approach, C_{L_α} is held constant from the unblown approach speed down to a speed of $1.3(V_{\text{stall}})_{\text{blown}}$ (which corresponds to an approach speed for an aircraft with conventional high-lift system that achieved the same maximum C_L as $(C_{L_{\max}})_{\text{blown}}$), and the additional C_L is generated exclusively by the high-lift propeller blowing. For lower speeds, the same total lift force (not lift coefficient) is generated from angle of attack

[10] The maximum blowing profile cannot be illustrated generically because it depends on the amount of blowing available. See discussion below.

[11] Certain profiles will dictate that certain amounts of blowing be utilized at the unblown reference approach speed. No discussion of the blowing required above this speed will be presented here, but the reader should be aware that the approach profile selection may have implications on the lift generated outside of the velocity region shown.

[12] It should be stressed that this approach is described here strictly to provide a lower bound on the required blowing. Operating at the maximum unblown C_L over a range of speeds is unsafe and should never be done in practice.

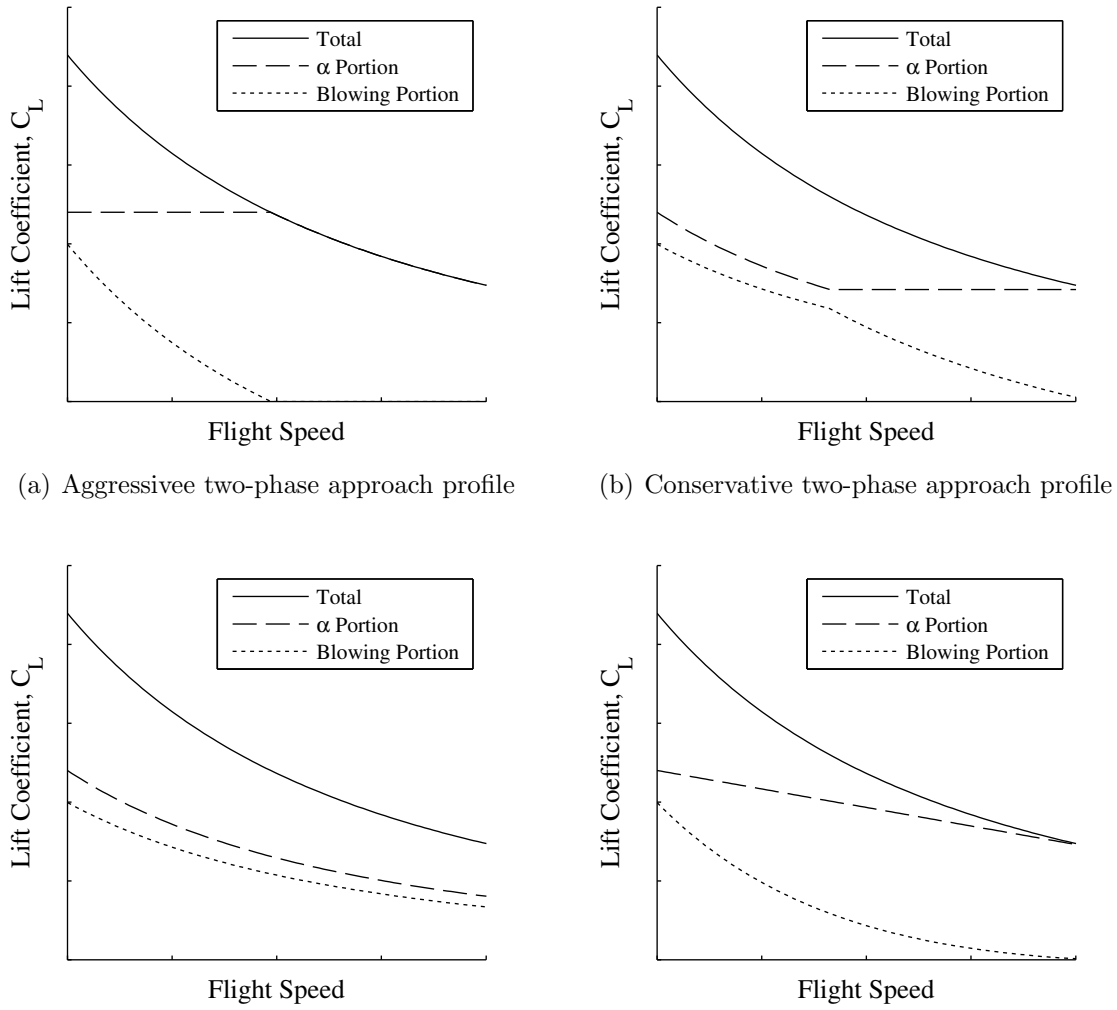

(a) Aggressivee two-phase approach profile

(b) Conservative two-phase approach profile

(c) Constant K_L approach profile

(d) Linear C_{L_α} approach profile

Figure 52: Generic representations of example approach profiles for aircraft with high-lift propellers

down to the blown stall speed, which increases the C_{L_α} in a inverse square relationship with velocity. In this lower velocity regime, the C_L from blowing also increases.

The constant lift multiplier approach is shown generically in Figure 52(c). This approach requires that the ratio of the total lift to the lift generated via angle of attack remain constant, which makes K_L a constant value throughout the profile. The value of K_L is set from value required at the desired blown stall speed when $C_{L_\alpha} = (C_{L_{\max}})_{\text{unblown}}$. Both C_{L_α} and $C_{L_{\text{blowing}}}$ follow an inverse square variation with

velocity.

The linear C_{L_α} approach is illustrated in Figure 52(d). In this approach profile, the C_L from angle of attack is increased linearly as the velocity is decreased. The blowing is also increased with decreasing velocity to maintain the same overall lift.

The final example approach profile is the maximum blowing approach. In this approach, the propellers are operated at their maximum torque limit throughout the approach. The precise lift augmentation from this operation depends on the detailed wing and propeller geometries as well as the torque limits of the motors. Consequently, no generic plot of this profile can be made. In contrast to the other profiles where the desired blowing is first specified, in this profile the blowing "falls out" from the existing geometry and motor capabilities. So long as the blowing is sufficient to produce the required lift throughout the approach profile, this approach is the most conservative approach in that it will require the least amount of lift from angle of attack of any of the approach profiles.

In each of the five example profiles, the C_L margin and the contributions of angle of attack and blowing to this margin vary. In the discussion below, the SCEPTOR aircraft is analyzed in each of these approach profiles to demonstrate these changes and the implications of the approach profile on the high-lift propeller design point.

5.1.2.2 Baseline Lift Coefficient Margins

Because it is unclear what sort of C_L margins (both at the reference approach speed and throughout and approach) may be required in future regulations, four potential ways of viewing the C_L margin will be referenced in the work below. The conditions are as follows (where HLPA refers to the configuration with high-lift propellers[13]):

1. An unblown approach and landing in the HLPA following the current regulations as written (i.e., not allowing any credit for the high-lift propellers, which means

[13]HLPA = high-lift propeller aircraft

the aircraft must approach at a higher speed based on the unblown stall speed of the wing)

2. An approach and landing in a conventional aircraft of lower weight than the HLPA that stalls at the blown stall speed of the HLPA. This lower-weight aircraft has a $C_{L_{\max}}$ equal to unblown $C_{L_{\max}}$ of the HLPA.
3. An approach and landing in a conventional aircraft of equivalent weight to the HLPA stalling at the blown stall speed of the HLPA with a fictitious, conventional high-lift system capable of producing the required $C_{L_{\max}}$ without blowing. If the high-lift propeller system could be certified as a high-lift system, then this profile is indicative of what the current regulations would require.
4. An approach and landing in a HLPA with a lift coefficient margin at the blown reference approach speed (i.e., at $(V_{\text{approach}})_{\text{blown}} = 1.3(V_{\text{stall}})_{\text{blown}}$) approximately equivalent to current C_L margins of Part 23-certified aircraft (i.e., $0.6 \lesssim (\Delta C_L)_{\text{approach}} \lesssim 0.85$).

5.1.2.3 Approach Thrust Issues and High-Lift Drag Model

The approach profile flown will have implications on the blowing required from the high-lift propellers and, therefore, the thrust produced by these props. If the thrust is greater than the drag of the aircraft, then the aircraft will accelerate. Consequently, high-lift propeller thrust may make descent and landing when flying the desired profile impossible. Before the performance of the aircraft in approach can be analyzed, the drag of the aircraft in high-lift conditions with propeller blowing must be estimated because this drag will determine an effective ceiling on the total thrust allowable from the high-lift propellers.

Unfortunately, the drag generated from propeller blowing is very difficult to predict—particularly in the early design phase. Not only is the flow velocity increased over only certain sections of the wing, which will act to increase the friction drag of those

sections, the induced flow from the propeller will also modify the location of the transition from laminar to turbulent flow over the wing and/or cause transitions from laminar to turbulent flow and back. The swirl induced by the propellers will create very "jagged" lift distributions, which will generally act to decrease the span efficiency of the wing. The peaks and valleys in the lift distribution with propeller blowing are caused by the swirl inducing increases in the local angle of attack of wing sections on the upward moving side of the prop disk and a decrease in the local angle of attack on the other side. Stoll shows examples of these very "peaky" lift distributions for the LEAPTech aircraft [124]. Furthermore, the lift distribution will vary as both the flight speed and blowing power are modified. Additionally, if the wing is operating near the stall angle of attack, the swirl may induce local areas of separated flow, which will increase the pressure drag of those sections. Finally, the wing will likely have high-lift devices (e.g., flaps) deployed, which makes the drag prediction even more difficult.

For the purposes of demonstrating the general trends that may occur and the types of information pertinent to the designer, two simple high-lift drag models are adopted in this document. Each of these models is based on a simple, two-parameter drag polar of the form $C_D = C_{D0} + KC_L^2$, where C_{D0} is assumed to be constant and K varies with propeller blowing. These models are very approximate and should be used only as initial screening tools to estimate the likelihood of the vehicle producing excess thrust. If the total drag is potentially lower than the high-lift propeller thrust, higher-order modeling should be performed to more accurately estimate the drag.

For both methods, the parasite drag coefficient, C_{D0}, is estimated with handbook component drag buildup methods incorporating form factors and wetted areas along with an estimate for the additional parasite drag from the flap proposed by Raymer [125]. For the SCEPTOR aircraft with fully deployed flaps (which cover approximately 70% of the span), the C_{D0} is estimated to be 0.0782, where approximately

311 counts are related to the flap and the rest of the aircraft comprises the other 471 counts.

The two drag models differ in their calculation of the K parameter for the induced drag. The first method calculates K from Eq. 79, where the Oswald efficiency factor, e_0, decreases with high-lift propeller blowing.

$$K = 1/(\pi e_0 AR) \tag{79}$$

The variation of e_0 in this model is derived from observations of the induced drag and span efficiency predicted by various members of the SCEPTOR project team for the LEAPTech and SCEPTOR aircraft. Although many of these results are unpublished, Stoll presents some of these calculations for the LEAPTech configuration [124]. Ultimately, these simulations indicate that the effective Oswald efficiency could reach values on the order of 0.5 or lower in situations with high-lift propeller blowing. These low span efficiencies are the result of the propeller slipstream creating very "jagged" wing lift distributions.

To estimate how the Oswald efficiency may vary with blowing, simulations were performed for a twelve-propeller version of the SCEPTOR aircraft with VSPAero, which is a vortex lattice aerodynamic solver developed by Kinney at NASA Ames [126, 124]. For these simulations, the propellers were modeled as elliptically loaded actuator disks based on an inviscid formulation by Conway [127] with viscous corrections included for the swirl [128]. The rotational speed and thrust of the actuator disks were varied at a fixed flight speed and angle of attack, and the span efficiency was calculated. The results from these simulations are shown in Figure 53. The black curves indicate the results from the VSPAero simulations at freestream speeds of 60 and 75 knots and angles of attack ranging from 3° to 10°.

Although the magnitudes of the span efficiency values from the VSPAero simulations change with operating condition, similar general trends are observed. Specifically, there is a relatively steep decrease in the span efficiency as the blowing is

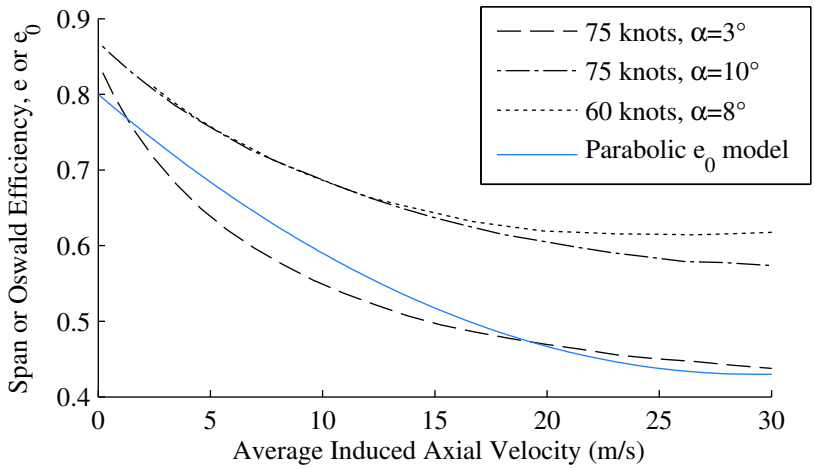

Figure 53: Span efficiency variation at two speeds and multiple angles of attack as predicted by VSPAero for a twelve high-lift propeller SCEPTOR configuration with parabolic model overlaid

first increased from zero, then the decreases in e become more gradual as the blowing velocity is increased. This variation of span efficiency can be explained through considering the modification of the lift distribution. Even with small axial velocity increases, the swirl from the propellers creates relatively large deviations from the baseline lift distribution. As the blowing is further increased, the swirl increases causing even greater departures from an ideal lift distribution; however, the general shape of the lift distribution changes less drastically as this additional blowing is applied. Consequently, the span efficiency begins to exhibit relatively little variation once large values of the induced axial velocity are reached.

Based on these observations, the first drag model estimates the variation of e_0 as a parabolic function of the average induced axial velocity from the high-lift propellers[14] as shown in Eq. 80 where $(V_a)_{\max} = 29.2\text{m/s}$, $e_{\max} = 0.8$, $e_{\min} = 0.43$, and V_a is the average axial velocity from the propeller far-downstream.

$$e_0 = \frac{\left(V_a - (V_a)_{\max}\right)^2}{(V_a)^2_{\max}} \left(e_{\max} - e_{\min}\right) + e_{\min} \tag{80}$$

[14]which are assumed to all generate the same velocity

The implied values for the Oswald efficiency from this model are shown in Figure 53 by the solid blue line beginning at $e_0 = 0.8$ at no blowing.

It should be noted that the Oswald efficiency factor, e_0, differs from the span efficiency factor, e. The span efficiency factor only captures the changes in drag from non-elliptic lift distributions. The Oswald efficiency factor considers both the deviation of the lift distribution from the elliptic shape as well as the increases in wing profile drag with lift. For operations at high lift coefficients, which will be experienced in situations when the high-lift propellers are operating, the profile drag will generally be increased from its values at lower lift coefficients. Because the high-lift propellers will increase the lift coefficient as blowing increases, there will be an increase in the wing profile drag. Therefore, the variation of e_0 in this first drag model is intended to capture both decreased span efficiency and increased profile drag. Consequently, the values for the parameters $(V_a)_{\max}$, $e_{\max}$, and $e_{\min}$ in Eq. 80 were selected to be more in-line with the lower values of the span efficiency calculated in the VSPAero simulations shown in Figure 53.

The second method of determining the induced drag is adapted from Jameson [109] who develops a theory for induced drag by modifying conventional lifting line theory as was described in Chapter II. This method defines a new effective aspect ratio for the wing when experiencing blowing from the propellers, AR_μ, which can be found from Eq. 28 (repeated below) where Λ is taken here as the number of high-lift propellers[15] and $\mu = V_\infty/V_j$.

$$AR_\mu = AR\frac{1+\Lambda\mu^2}{\Lambda+\mu^2}$$

This effective aspect ratio is then used in a similar manner as the typical aspect ratio in the calculation of the parameter K as shown in Eq. 81, where the ratio V_∞^2/V_j^2 is

[15]Technically Λ is the ratio of the slipstream width to height. Taking the slipstream width as the number of high-lift propellers times the prop diameter and the height as the prop diameter leads Λ to be the number of propellers.

required to normalize the coefficient to the freestream velocity and e_0 is held constant at 0.8.

$$K = V_\infty^2/(\pi e_0 A R_\mu V_j^2) \tag{81}$$

Jameson's model may under-predict the drag because it ignores the effects of propeller swirl on the lift distribution. Although a reasonable assumption for the calculation of lift,[16] this assumption ignores the jagged, highly non-elliptic shape of the lift distribution, which as described above is likely to increase the induced drag. However, the swirl recovery from the wing, which was discussed in Chapter II, may lead to effective reductions in the drag despite the jagged lift distributions. This second drag model, therefore, effectively assumes that the swirl recovery at least somewhat compensates for the non-elliptic lift distributions.

Ultimately there is a high degree of uncertainty in the drag models. The differences in drag estimated from the two models will provide an idea of the uncertainty in the drag prediction with the second drag model serving as a likely lower-bound on the expected drag. These models are used here primarily to provide examples of the trades that are of interest to a designer. When available, more refined models should be utilized, particularly if the high-lift propeller thrust is identified as a likely active constraint.

5.1.2.4 Creating Additional Drag

For aircraft with high-lift propellers, additional drag sources may be required to mitigate the effects of thrust from the high-lift props. Despite the fact that it is relatively easy to increase the drag of an aircraft, these additional drag sources are only potentially desirable in the approach and landing phase of flight where both high lift and low thrust production is required. Therefore, it is desirable to add drag sources that can be stowed (to reduce drag in other flight phases such as cruise) and

[16] because the increase in lift on one half of the disk will be nearly equivalent to the decrease in lift on the opposite side of the disk

that do not interfere with the flow creating lift. Such potential drag sources include, but are not limited to:

1. windmilling the "cruise propeller(s)" (i.e., the non-high-lift propeller(s)),
2. deploying speed brakes that do not impact the lift generated by the wing (which could be located on both the sides of the fuselage to eliminate any yawing moments created by such devices), or
3. installing landing gear doors so that the largest area is deployed perpendicular to the flow (as opposed to parallel to the flow as is conventionally done).

It should be noted that there are safety implication of installing deployable drag-producing devices. Specifically, if a "go-around" (i.e., a missed approach) is required, it is no longer advantageous to have additional drag-producing devices deployed. So long as these devices can be quickly stowed, then a go-around should be easily accomplished since the high-lift propellers will already be producing excess thrust for the configuration in the absence of the extra drag (and the main propulsors could be powered to increase thrust even further). However, this places requirements on these devices to be able to be quickly stowed. Additionally, additional drag sources on portions of the aircraft may create large moments (potentially about any axis) that could destabilize the aircraft. Although installing deployable devices symmetrically around the airframe can eliminate these moments in the nominal case, a failure of a single deployable device to stow (while its companion device does retract as desired) may still create an undesired moment. These moments may necessitate that larger control surfaces or stabilizers (e.g., a vertical tail) be installed, which could have negative impacts on the overall aerodynamic efficiency of the vehicle. Consequently, it is highly recommended that deployable drag devices be avoided if possible. If it is determined that they are required, trade studies should be conducted that consider increasing the wing size (to reduce the thrust required from the high-lift props), which may result in a higher overall vehicle efficiency (perhaps by reducing the required tail

size).

Perhaps the best way to increase the drag of the configuration is to operate any cruise propellers as windmills. Windmilling the cruise propeller(s) can not only create additional drag but also recapture energy from the flow. Because electric motors can be operated "in reverse" as generators, some (likely small) amount of energy can be harvested from propellers that act like wind turbines diffusing the flow.[17] Researchers at the Japan Aerospace Exploration Agency (JAXA) have demonstrated this ability to create drag and regenerate energy from a propeller-electric motor combination in flight as a part of the FEATHER project [129, 130, 131]. To be most effective, constant speed (or some other form of variable pitch) cruise propellers are required so that these propellers can be effective both for producing (positive) thrust in cruise and creating drag (i.e., negative thrust) in approach.

When attempting to create drag with a propeller driven by an electric motor, various levels of drag can be produced depending on the rotational speed of the propeller and the pitch of the blades. To illustrate the impacts of blade pitch on the drag and power, the custom-designed cruise propeller for the SCEPTOR aircraft shown in Figure 54 was examined. This three-bladed prop is 5 ft in diameter and has a single airfoil, the MH 117 [132], along the entire blade. The potential drag obtainable from the SCEPTOR cruise propeller when rotating at 1719 RPM was estimated with XROTOR [119].[18] Specifically, the thrust and power of a single cruise propeller are shown in Figure 55, where the prop was operated at various blade root pitch angles at a freestream speed of 55 knots and sea level standard conditions. The solid line denotes the thrust produced by the propeller while the power required or

[17] Windmilling propellers to produce drag is also possible with conventional engines, but the author is unaware of any systems that use prop windmilling in conjunction with a conventional engine to actually recover and store energy.

[18] The rotational speed corresponds to a low tip speed of 450 ft/sec. Because noise is roughly proportional to the tip speed to the 5th power [133], operating at 1719 RPM should produce a low noise signature.

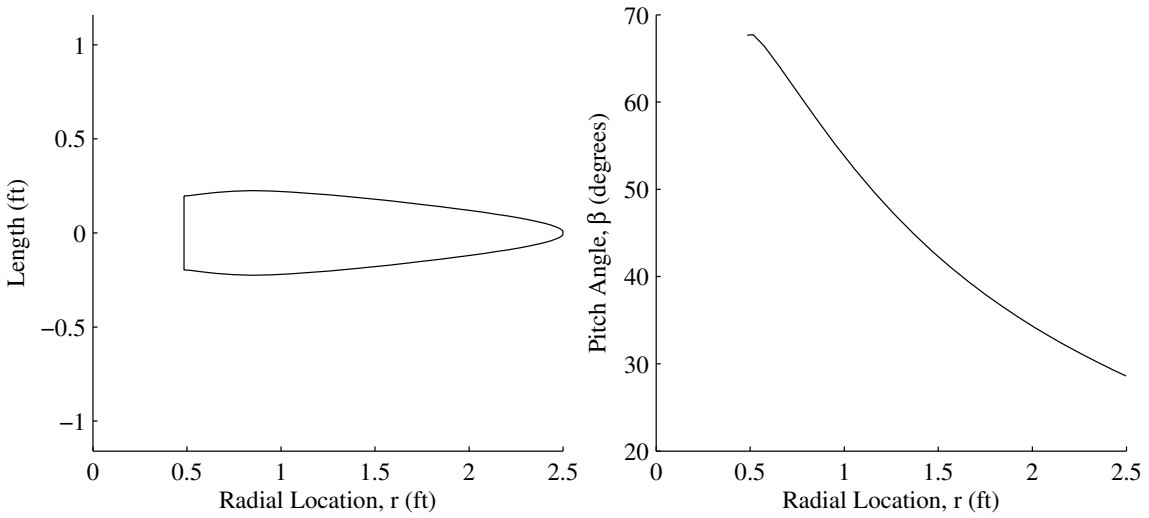

Figure 54: Geometry of a cruise propeller for an early variant of the SCEPTOR aircraft

produced by the propeller is shown in the dashed line. The gray areas from root pitch angles of 10° to 37° and 61° to 80° indicate areas where XROTOR predicts that at least one section of the blade will be stalled. The pitch angles shown correspond to the limits of an existing, commercially-available, electrically-actuated constant speed hub produced by MT Propeller, the MTV-7 [134].

As can be seen in Figure 55, the propeller begins to produce drag at root pitch angles below approximately 42°, and the drag production continually increases as the pitch angle decreases down to the minimum pitch angle. Although the general trend of increasing drag is likely correct, the accuracy of the drag values too far below where stall first occurs is suspect because of the low-order post-stall modeling employed in XROTOR. The minimum power for the propeller is seen at a pitch angle of approximately 33°, which is only slightly below stall. At this point, the propeller is actually generating power (as opposed to requiring it) since the power value is negative. The power extracted by the prop can recharge the batteries if the electric motor and power system are configured for this scenario.

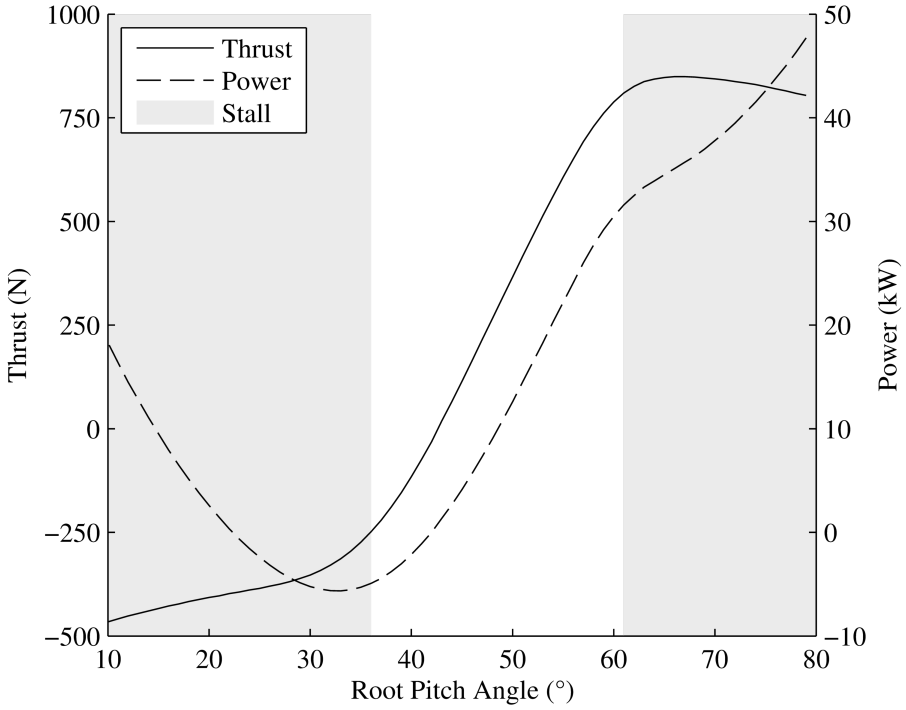

Figure 55: Power and thrust variation with blade pitch angle for a SCEPTOR cruise propeller at a rotational speed of 1719 RPM at 55 knots and standard sea level conditions

If the pitch angle of the propeller is decreased beyond the minimum power point, the power extraction from the prop decreases, and eventually positive power is again required to drive the propeller due to the large number of stalled blade sections. Additionally, there are "diminishing returns" in terms of drag production as the pitch is decreased below the minimum power point—i.e., the extra drag produced when going from the minimum power pitch angle to 5° below that angle is much less than the additional drag produced when changing the pitch from 5° above the minimum power angle to that angle. Unless extreme amounts of drag are required, operating the propeller at the minimum power point will likely provide the most "bang for the buck" since the most power can be extracted from the flow and a fairly large amount of drag can still be produced.

For the studies shown below, a more conservative approach is taken: the drag is estimated at the pitch angle just above where stall is first predicted to occur, which for the case shown in Figure 55 is 37°. By avoiding any stalled blade sections, the noise of the propeller should be less than if any sections were stalled. It should be noted that XROTOR's stall prediction is likely also conservative since it is based on the two dimensional section lift coefficients, and in practice stall is typically delayed over rotors. However, the author's experiences with XROTOR have shown that it tends to over-predict thrust; therefore, the additional margin above stall can help mitigate an over-predicted drag in addition to avoiding stall.

The total drag, power extraction, and pitch angle at which maximum power extraction or stall occurs will vary with flight condition; however, the same trends seen in Figure 55 will apply in general. When applying the logic described above, the drag and associated pitch angle where this drag occurs of a SCEPTOR cruise propeller are shown in Figure 56.[19]

As can be seen in Figure 56, both the pitch angle and drag produced increase with velocity. The higher mass flow rate through the propeller disk at higher speeds enables more drag to be produced. The smaller drag production at lower velocities is unfortunate, because drag will most likely be required at low speeds where more lift augmentation is needed from the high-lift props. Regardless, the two cruise propellers for the SCEPTOR aircraft can offset between approximately 460 and 720 newtons (100 to 160 pounds) of thrust from the high-lift props depending on the flight condition.

As discussed above in regards to deployable high-lift devices, there are also potential safety implications when windmilling the cruise propellers. Since these propellers are the primary source of thrust on the aircraft, in the event that a go-around is necessary, the cruise propellers need to be capable of quickly producing thrust as opposed

[19]The jaggedness of the curves are due to rounding in the XROTOR outputs.

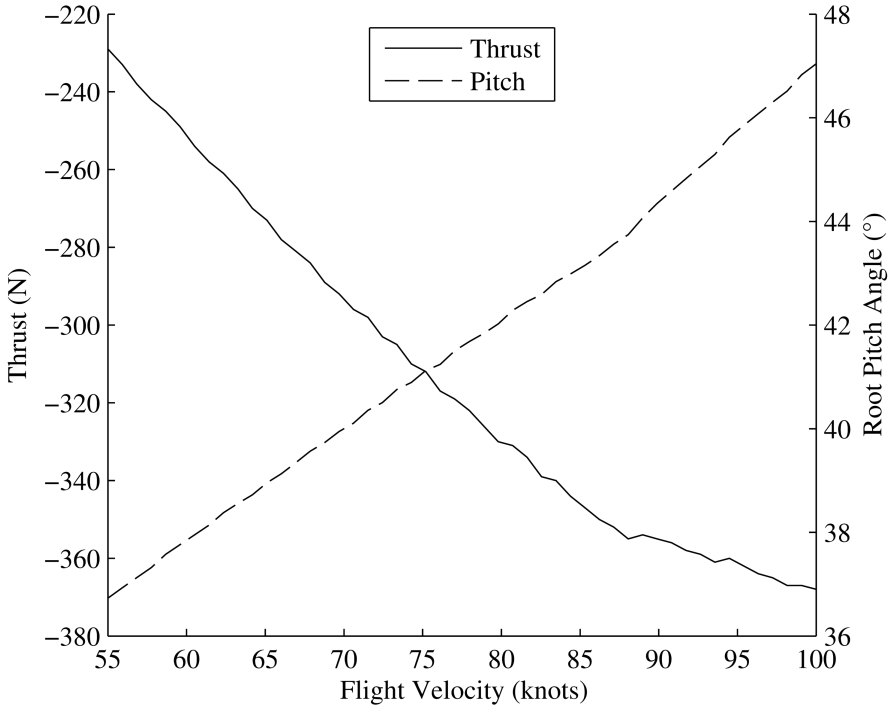

Figure 56: Thrust and root pitch angle variation with velocity for a SCEPTOR cruise propeller at a rotational speed of 1719 RPM and standard sea level conditions

to drag. Unlike other forms of deployable drag devices, eliminating the drag from the cruise props is very simple to do and would be the pilot's first step in a go-around procedure already: increase the "throttle" setting. If a constant speed mechanism is employed, the blade pitch would automatically adjust to begin producing thrust; the only delays would be the reaction time of the pilot and the constant speed mechanism's actuation of the blade. However, unlike in conventional aircraft with constant speed propellers, the speed control may not be set to "full forward" (i.e., maximum speed)[20] as would be prescribed in a typical pre-landing checklist. Although changing the speed control would be necessary to produce maximum thrust, this step is likely unnecessary because the high-lift props would already be producing enough thrust to make the aircraft accelerate (which was the purpose of windmilling the cruise props

[20]if the suggested approach of limiting tip speed for noise abatement is followed

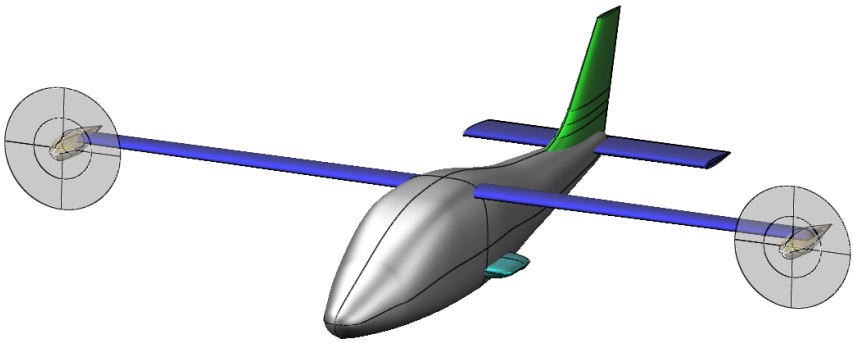

Figure 57: Rendering of the SCEPTOR aircraft with cruise propellers shown as disks and no high-lift propellers shown

in the first place).

The most critical safety issue associated with windmilling propellers to produce drag is likely an asymmetric drag condition that could result from a failure of a single cruise prop in multi-prop configurations. In a configuration like the SCEPTOR aircraft shown in Figure 57 where the cruise props are located far outboard, very large yawing moments could result. However, this asymmetric drag condition would likely not cause any more critical of a scenario than an asymmetric thrust condition in takeoff or climb where the cruise props would be at very high thrusts. Theoretically the tail and rudder would already be sized to stabilize the aircraft at similar flight speeds with positive thrust, so it is unlikely that windmilling drag would add a new critical sizing condition. Regardless, both the maximum asymmetric drag and maximum asymmetric thrust conditions should be considered when sizing the tail.

For the studies shown in this document, only windmilling of the cruise propellers will be considered as an additional drag source since the SCEPTOR aircraft and other aircraft under consideration will have at least one cruise propeller in addition to the high-lift props. If this additional drag is found to be insufficient, other mechanisms for producing drag could be considered, but these solutions will vary from one aircraft to another and are consequently difficult to generalize. Results below

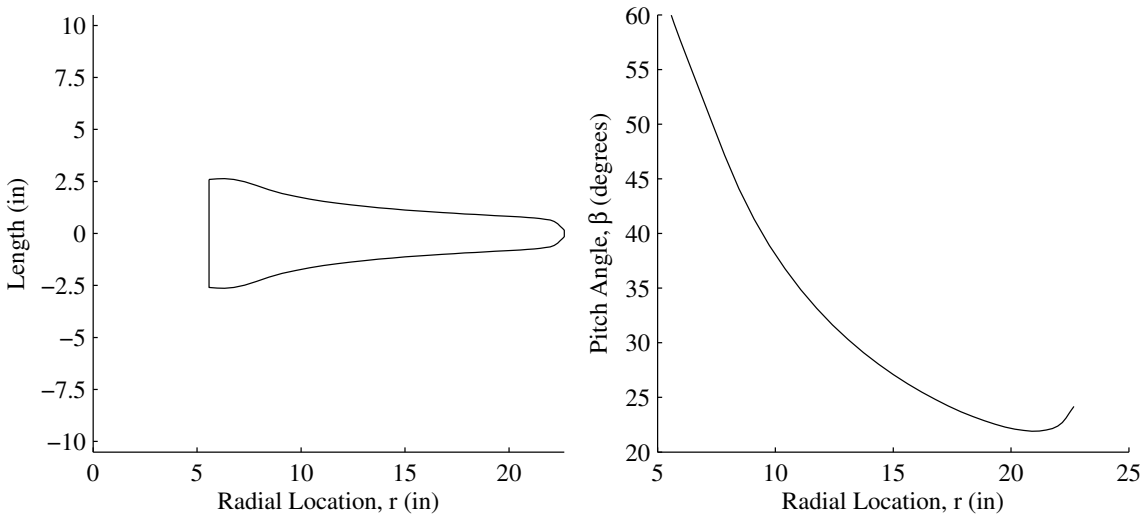

Figure 58: Blade design of a 5-bladed high-lift propeller analyzed for approach calculations

will be presented both with and without the estimated drag contribution from the windmilling propellers for the SCEPTOR aircraft. Such an approach is instructive because it will help indicate if windmilling is required and how much additional drag the cruise propellers can provide.

5.1.2.5 Results

In this section, the performance of a preliminary geometry of the SCEPTOR aircraft[21] when flying various approach profiles is presented. The propeller operating conditions required for the example approach profiles discussed above in Section 5.1.2.1 are analyzed assuming that a 5-bladed propeller designed with the method presented in Chapter IV is installed. The blade geometry is shown in Figure 58. The origin of this propeller design will be discussed later in Chapter VI.[22]

For the following results, the aircraft is analyzed as a point mass at an instant in

[21]This geometry is the same as the "Rev3Mod3" configuration (as it is referred to within the project team), but has a different high-lift propeller design.

[22]Note that the results presented in this chapter apply to the configuration discussed in more detail in Chapter VI.

time, and the forces are balanced only in the direction perpendicular to the freestream velocity. The aircraft weighs 3,000 lb and is flying a conventional 3° glide slope. The high-lift propellers are installed at a $-1°$ incidence angle relative to the wing mean chord line, and the wing mean chord line is inclined at an angle of 1° to the reference point for measuring angle of attack. This installation implies that at positive angles of attack there will be "flow turning" from the propellers—i.e., the wing will see a reduced angle of attack relative to the freestream. Although this will reduce the effective lift from the wing (see Chapter III) the prop thrust will directly contribute to lift.

The following analyses of the example approach profiles are presented here to help describe how the approach profile will impact the high-lift propeller design point. However, for a specific aircraft and a known desired approach profile, the following analyses would be performed primarily to indicate if there would be any resulting acceleration or deceleration of the aircraft. Any thrust imbalance would indicate that the cruise propeller(s) would need to provide either positive or negative thrust depending on the vehicle drag and thrust from the high-lift propellers to enable a steady-state approach at a given speed. In the following examples, if the excess thrust from the high-lift propellers alone is greater than zero, windmilling of the cruise propellers will be required. If the total excess thrust (including drag from windmilling the cruise propellers) is greater than zero, then such an approach is impossible with the given high-lift propellers. The implications of such a situation will be discussed further in Chapter VI.

Several assumptions were made for the following analyses. First, the propellers are analyzed in isolation at a zero-degree angle of attack with XROTOR. In reality they will likely experience a decrease in performance from the calculated values from operating near the wing and at an angle of attack. Second, the aircraft operates along a linear lift curve where zero lift is obtained in the flapped configuration at $-20°$

(without propeller blowing) and an unblown $C_{L_{\max}}$ of 2.6 occurs at 10°. Third, the presence of the cruise propellers and whether or not they are feathered or windmilling has no effect on the wing lift or drag. (The isolated drag from windmilling the cruise propeller is considered separately from the wing as described above in reference to Figure 55.)

The results for the five example approach profiles are shown in Figures 59 through 63. Each of these figures contains six sub-figures that show the

(a) lift coefficient profile;

(b) lift coefficient margin profile;

(c) high-lift propeller excess thrust (i.e., the thrust from the high-lift propellers minus the drag of the aircraft assuming the first drag model explained above where the Oswald efficiency exhibits a parabolic variation with propeller blowing), total excess thrust (which is the high-lift propeller excess thrust along with additional drag from windmilling the cruise propellers), and thrust of a single high-lift propeller;

(d) same parameters as (c) except the induced drag is calculated with Jameson's model;

(e) high-lift propeller RPM and tip speed; and

(f) torque for each high-lift prop, total power for all the high-lift propellers, and total power including regenerative windmilling of the cruise propellers.

The performance of the aircraft is plotted in all sub-figures from the desired stall speed of 55 knots up to 90 knots, which is approximately 1.3 times the unblown stall speed.

In the lift coefficient margin sub-figure, the first three baseline lift coefficient margin profiles discussed above in Section 5.1.2.2 are included, and the fourth baseline margin can be read from the y-axis directly (i.e., values of C_L margin of approximately 0.6 to 0.85). The unblown approach is shown by the blue curve that starts at a

C_L margin of approximately 1.1 at 90 knots[23] and decreases to zero C_L margin at 71.5 knots. An approach with a lower weight aircraft moves between these same lift coefficient margins from velocities of 71.5 knots to 55 knots and is shown in green. The orange curve beginning at approximately 1.8 C_L margin at 71.5 knots and decreasing to zero at 55 knots corresponds to the margin required by the current regulations for an aircraft with the same maximum lift coefficient.

It should also be noted that the blowing contribution to the total C_L margin is calculated assuming that the motors are sized for the highest torque experienced for that specific profile (with the exception of the maximum blowing profile, which assumes a maximum torque of 21 N-m). Consequently, there is no blowing margin at the most critical condition for the high-lift propellers, and the maximum torque available varies between all different approach profiles.

The aggressive two-phase approach results are shown in Figure 59. This example profile is the least conservative of all those analyzed and represents an absolute lower-bound on the high-lift propeller requirements. Although theoretically possible to fly, this approach is unsafe and should never be flown in practice because there is no margin to account for sudden angle of attack changes over much of the approach. The profile is useful, however, for determining a minimum torque or power requirement for the electric motors; furthermore, if this approach cannot be flown without excess thrust, then no approach profile will be feasible.

In this approach, the high-lift propellers are inoperative from 90 knots to 71.5 knots. As speeds decrease below 71.5 knots there is a gradual increase in the required RPM, torque, and power. The most-critical point of operation for the high-lift props is the blown stall speed, which implies that if this profile is to be flown, then the design point of the system is the desired stall speed.

[23]Note that this C_L margin is higher than the values quoted above for typical GA aircraft because the SCEPTOR aircraft has a higher unblown maximum lift coefficient than conventional aircraft.

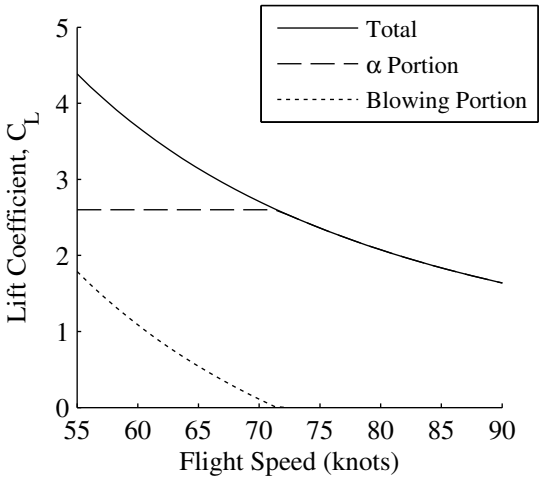

(a) Approach profile

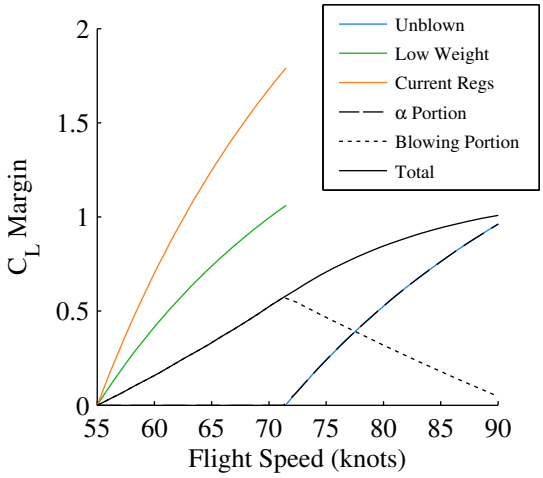

(b) Lift coefficient margin profile

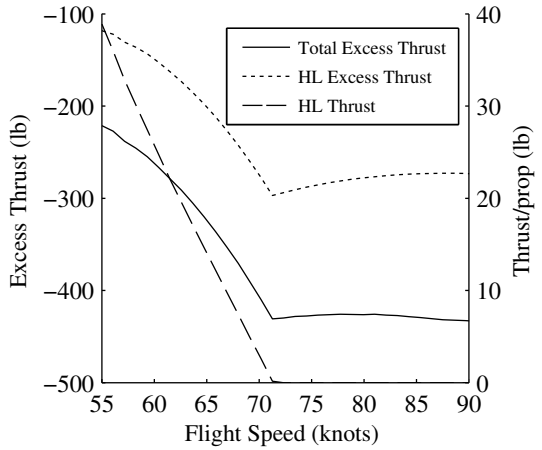

(c) Total excess thrust with parabolic e_0 drag model and high-lift propeller thrust

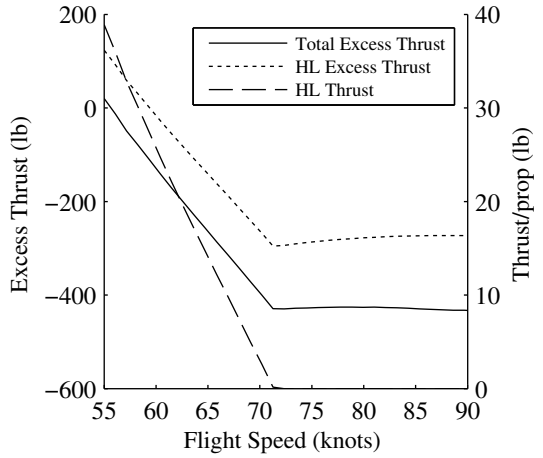

(d) Total excess thrust with Jameson drag model and high-lift propeller thrust

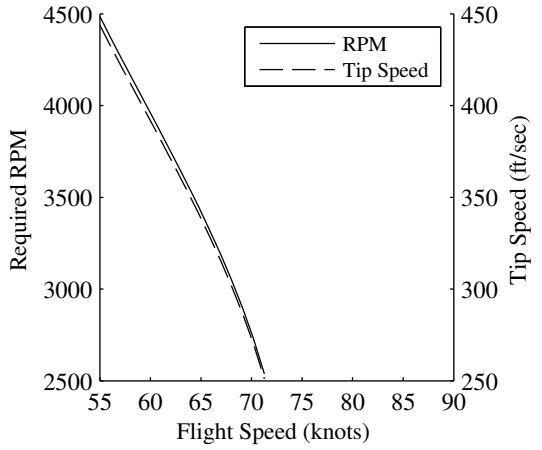

(e) High-lift propeller RPM and tip speed

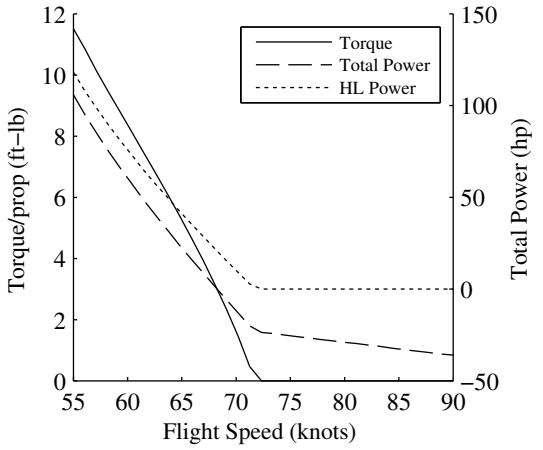

(f) High-lift propeller torque and total power

Figure 59: Aggressive two-phase approach profile simulation results

As shown in Figure 59(b), the total C_L margin for this approach profile falls above the unblown curve at all speeds, but below the low weight baseline curve and substantially below the current regulations. However, the aircraft could still maintain the same lift coefficient margins as many existing aircraft (i.e., on the order of approximately 0.6 to 0.85) if its approach speed was between approximately 72 and 78 knots.

Figures 59(c) and 59(d) indicate that this approach profile could likely be flown with the current high-lift propeller design. Although Figure 59(c), which estimates drag with a parabolic variation of e_0, indicates some positive thrust from the cruise propellers will be required for the entire speed range, Figure 59(d) indicates that in order to slow below approximately 59 knots, windmilling from the cruise propellers will be required.

Figure 60 plots the performance of the SCEPTOR aircraft over the conservative two-phase approach. The differences between this approach and the aggressive two-phase approach are substantial. Here, the high-lift propellers are required over the entire speed range. The torque and power levels required increase as the flight speed decreases down to 71.5 knots then decrease as the speed is further reduced down to stall. Apart from the maximum torque/power condition for the high-lift props occurring at a different speed, the maximum torque and power are increased as compared to the aggressive two-phase approach. Here, approximately 15.6 ft-lb of torque per prop are required, which is nearly 36% more than the 11.5 ft-lb required at stall speed. This increased torque implies that the appropriate design point for this approach profile is the speed below which the C_L from angle of attack begins to increase, which here is $1.3(V_{\text{stall}})_{\text{blown}} = 71.5$ knots.

For the conservative two-phase approach, the total C_L margin is greater than both the unblown and lower weight vehicle baselines as can be seen in Figure 60(b). For most of the speed range the margin falls below current regulations except for low

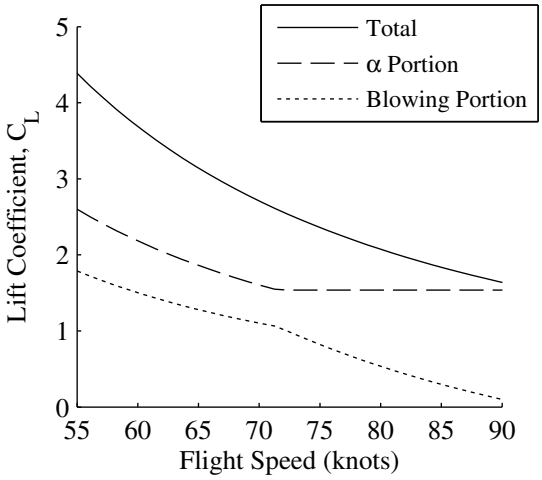

(a) Approach profile

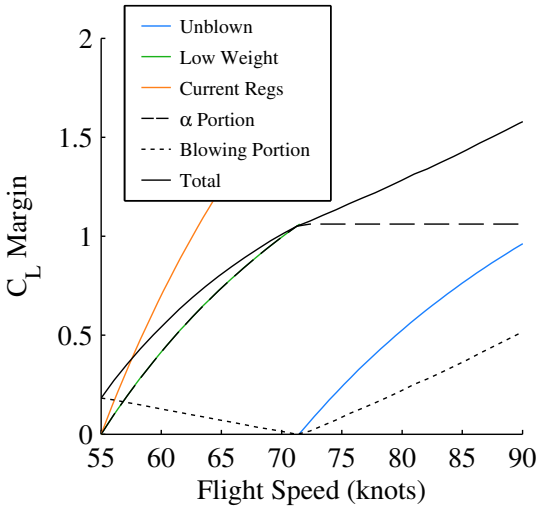

(b) Lift coefficient margin profile

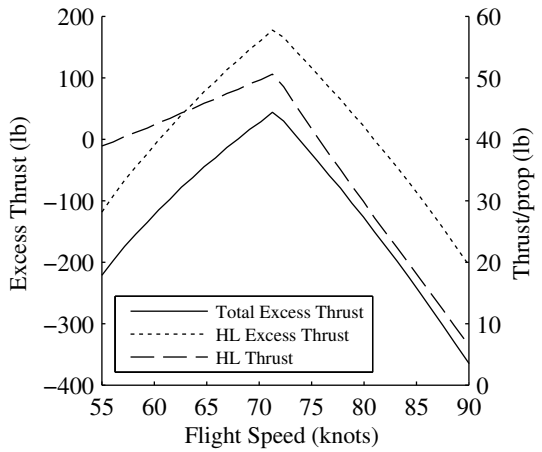

(c) Total excess thrust with parabolic e_0 drag model and high-lift propeller thrust

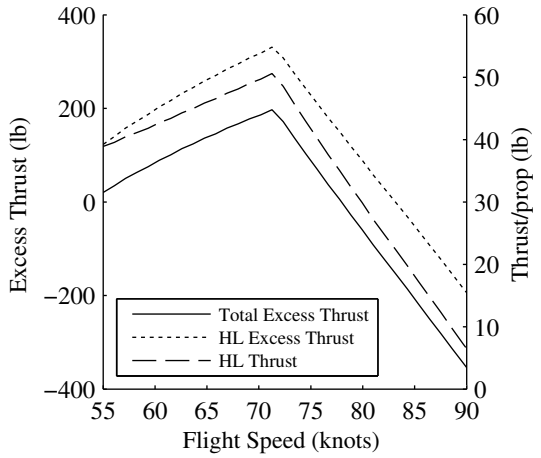

(d) Total excess thrust with Jameson drag model and high-lift propeller thrust

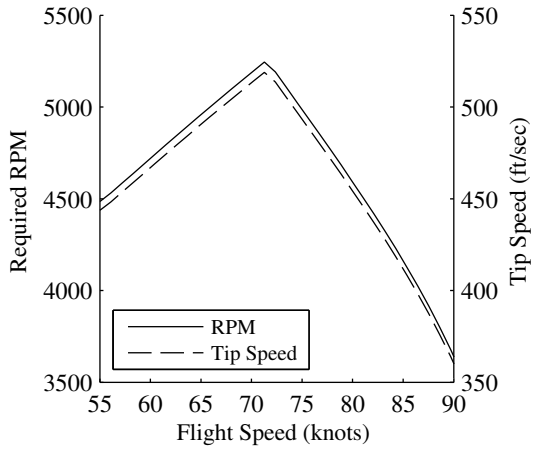

(e) High-lift propeller RPM and tip speed

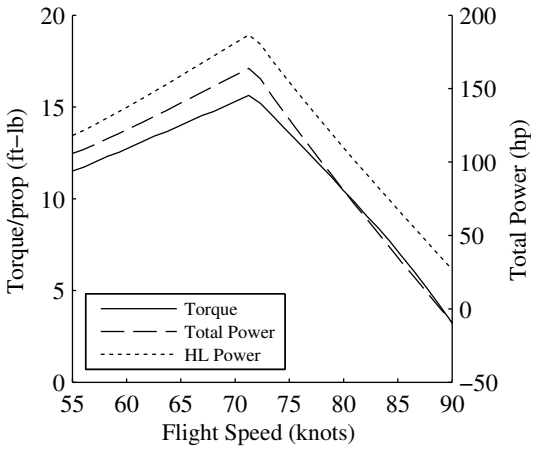

(f) High-lift propeller torque and total power

Figure 60: Conservative two-phase approach profile simulation results

speeds. The blowing margin is increased at these low speeds because the motors are sized for higher torque than is required. Approach speeds of approximately 61 to 66 knots provide total C_L margins on the order of conventional GA aircraft.

Figures 60(c) and 60(d) indicate that for speeds near 71.5 knots where the propellers are operating at high torques the high-lift system is likely to produce excess thrust. It does not appear that the aircraft will be able to slow below approximately 73 or 78 knots (depending on the drag model) even with windmilling of the cruise propellers to produce additional drag. The feasibility of this approach in the SCEPTOR configuration is doubtful.

It should also be noted that tip speed of the propellers is increased in the conservative two-phase approach when compared to the aggressive two-phase approach as can be seen when comparing Figures 59(e) and 60(e). Since propeller noise is highly correlated to the tip speed (in general, it has been shown to vary with tip speed to the fifth power [133]), the aircraft will likely be louder when flying the conservative two-phase approach than the aggressive two-phase approach.

The constant lift multiplier approach profile results are displayed in Figure 61. In this approach, considerably more lift is derived from blowing than the previous approach profiles in order to maintain a lift multiplier of 1.69 at all speeds. Consequently, the maximum torque and power levels are increased substantially over the previous two profiles. Here, a maximum torque of approximately 20.2 ft-lb is required, which is over 75% greater than the torque required for the conservative two-phase approach. This maximum torque is required at the maximum speed analyzed, and it decreases along with the power and RPM as the speed is reduced down to the stall speed as can be seen from Figures 61(f) and 61(e). Therefore, in this scenario, the design point for the motor is the maximum speed condition.

The lift coefficient margin is greater in this approach than in either of the two previous cases. While the angle of attack portion of the C_L margin decreases as the

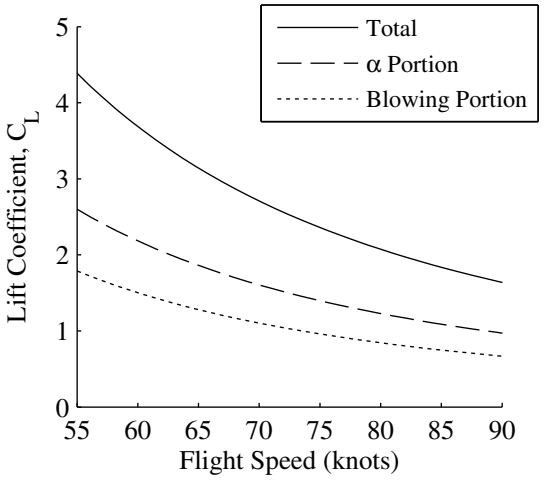

(a) Approach profile

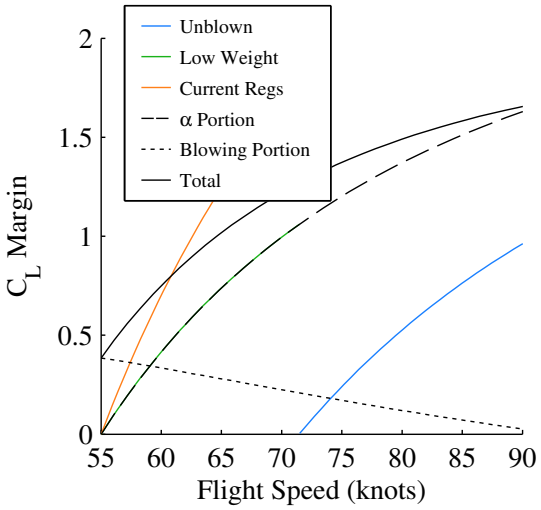

(b) Lift coefficient margin profile

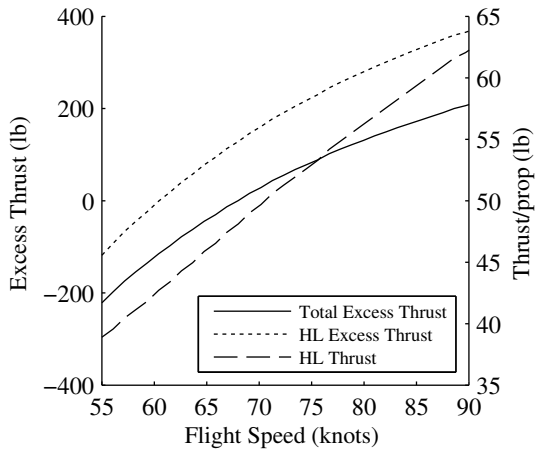

(c) Total excess thrust with parabolic e_0 drag model and high-lift propeller thrust

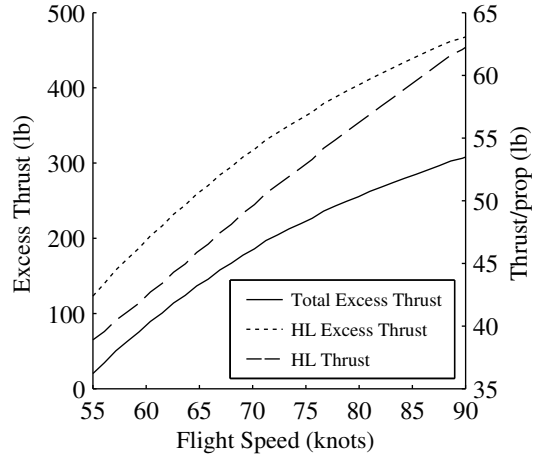

(d) Total excess thrust with Jameson drag model and high-lift propeller thrust

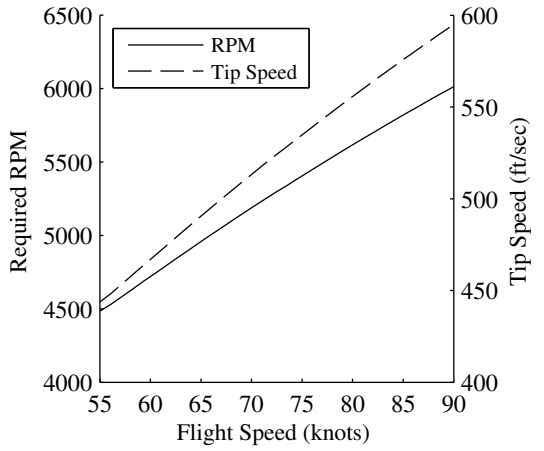

(e) High-lift propeller RPM and tip speed

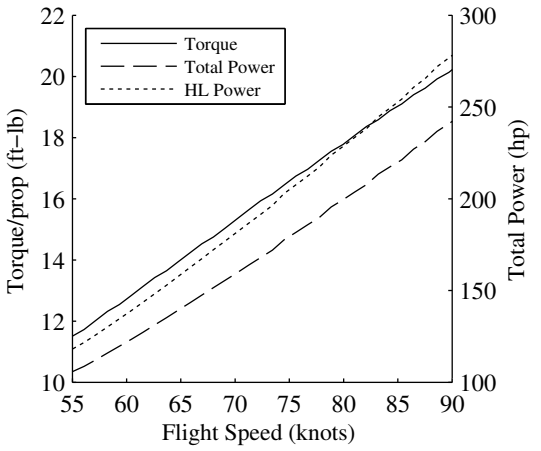

(f) High-lift propeller torque and total power

Figure 61: Constant lift multiplier approach profile simulation results

speed decreases, the blowing margin increases. There is noticeable margin even at the stall speed, which implies an even lower stall speed could be obtained with the aircraft if it were operated with a different approach profile. Parity in C_L margin with typical GA aircraft is achieved at speeds near 58 to 61 knots.

Although the large C_L margins may make this approach profile seem appealing, the configuration exhibits noticeable excess thrust at most speeds for both drag models as shown in Figures 61(c) and 61(d). Windmilling of the cruise propellers may enable this configuration to fly at lower speeds, but the aircraft would not be able to reach those lower speeds if this complete profile were flown because it could not decelerate from the higher speeds. Consequently, this approach profile is simply infeasible for this specific configuration to fly. Counterintuitively, if an aircraft did have sufficient drag to fly such an approach profile, thrust would have to be added by the cruise propeller(s) as the velocity decreased.

The linear C_{L_α} approach profile results are shown in Figure 62. In this approach, the blowing is gradually increased throughout the entire profile with the maximum torque/power condition (i.e., the sizing point) occurring at the stall speed. A near-linear variation of torque with airspeed is required to maintain adequate lift, and the power and RPM exhibit near parabolic variation with speed.

The total C_L margin is comprised of a combination of blowing and angle of attack over all speeds, with the angle of attack portion being greater than the blowing portion throughout as shown in Figure 62(b). Unlike previous profiles that have had much greater margin from one source over the other, this approach provides a balanced margin between angle of attack and blowing, which provides flexibility in adjusting to disturbances. In previous profiles—particularly the aggressive two-phase approach—the pilot would need to know where margin existed at every speed to correct for a disturbance. At some speeds, it may only be appropriate to increase power to the props while at other speeds only angle of attack variations would be possible.

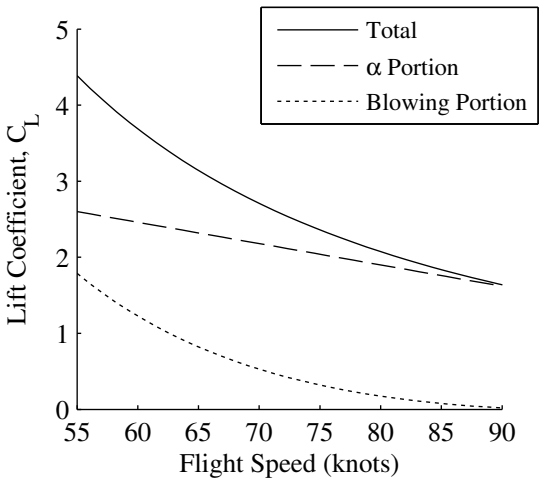

(a) Approach profile

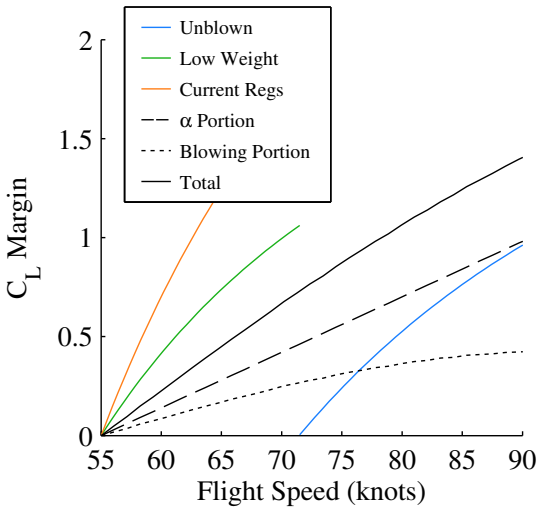

(b) Lift coefficient margin profile

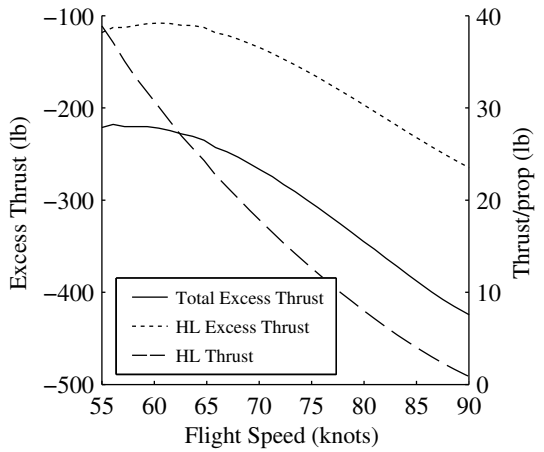

(c) Total excess thrust with parabolic e_0 drag model and high-lift propeller thrust

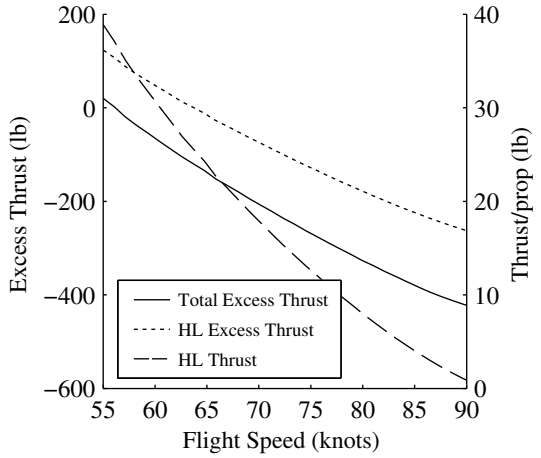

(d) Total excess thrust with Jameson drag model and high-lift propeller thrust

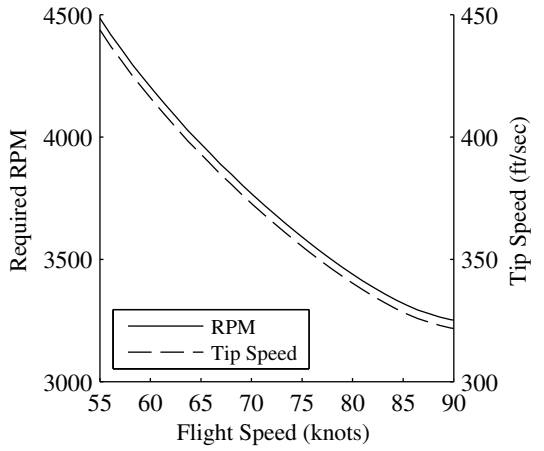

(e) High-lift propeller RPM and tip speed

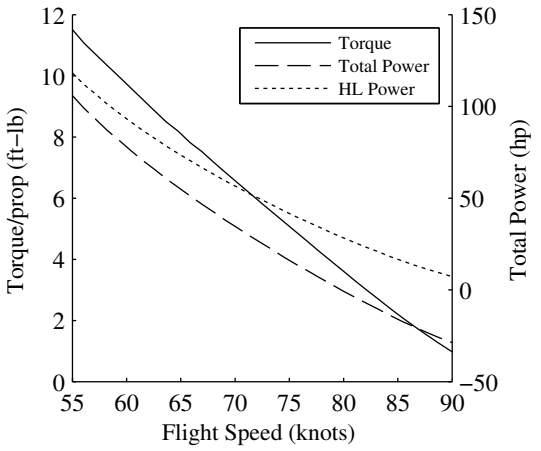

(f) High-lift propeller torque and total power

Figure 62: Linear C_{L_α} approach profile simulation results

However, with the linear C_{L_α} profile, the pilot could always adjust either angle of attack or high-lift power to account for lift variations. Total C_L margins similar to typical GA aircraft occur at speeds between approximately 69 and 73 knots.

The excess thrust of the Linear C_{L_α} profile is less of a concern than for the conservative two-phase or constant K_L approaches as shown in Figures 62(c) and 62(d). Both drag models indicate that the profile is likely feasible, though the second model predicts that cruise propeller windmilling is required to slow below about 64 knots and the configuration would need additional drag to slow below approximately 56 knots. (The first drag model suggests that no windmilling is required to fly the entire approach.) Also, this approach is preferred to the aggressive two-phase approach because the changes in propeller operating conditions and excess thrust with velocity are less drastic for the linear C_{L_α} profile.[24] These more gradual changes can aid the pilot in adjusting the cruise propeller throttle settings as speed is varied.

[24] not to mention the fact that the aggressive two-phase approach is unsafe

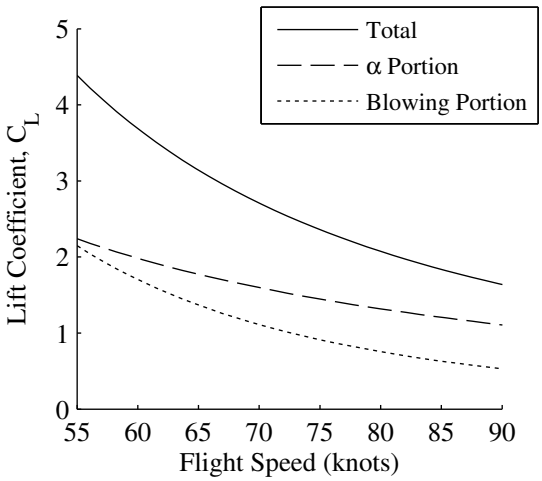

(a) Approach profile

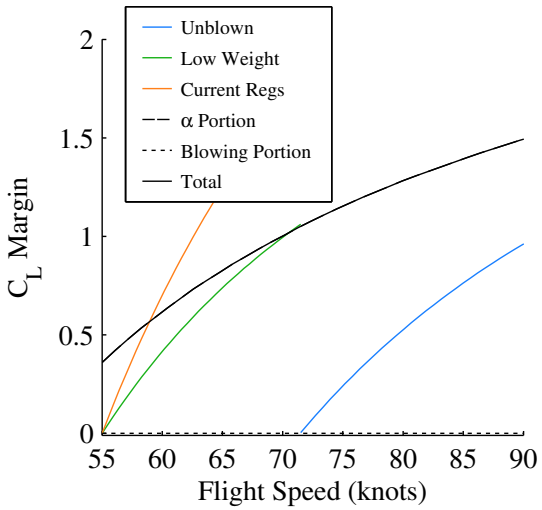

(b) Lift coefficient margin profile

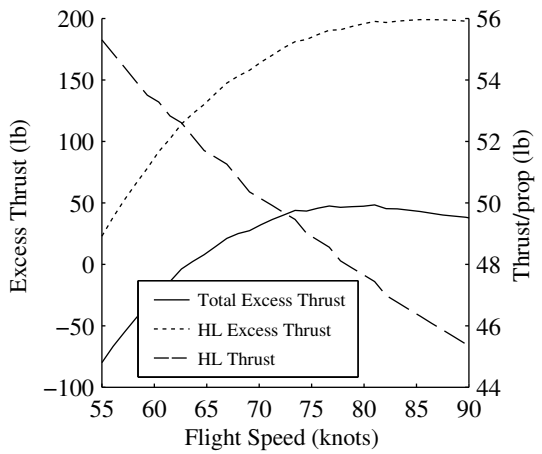

(c) Total excess thrust with parabolic e_0 drag model and high-lift propeller thrust

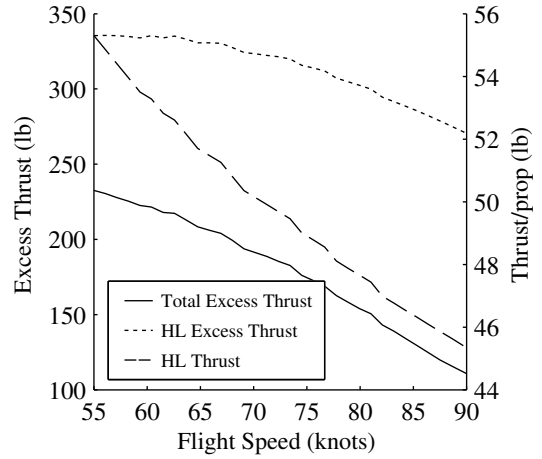

(d) Total excess thrust with Jameson drag model and high-lift propeller thrust

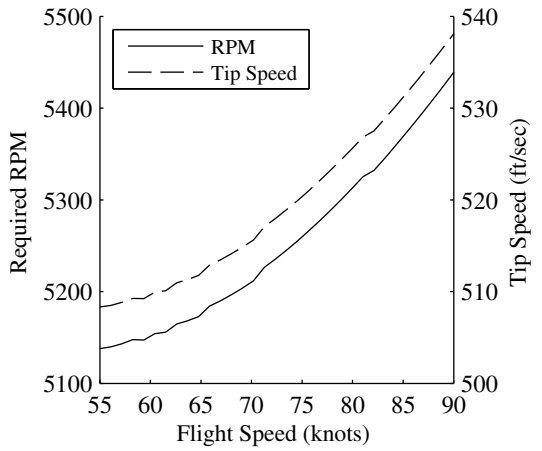

(e) High-lift propeller RPM and tip speed

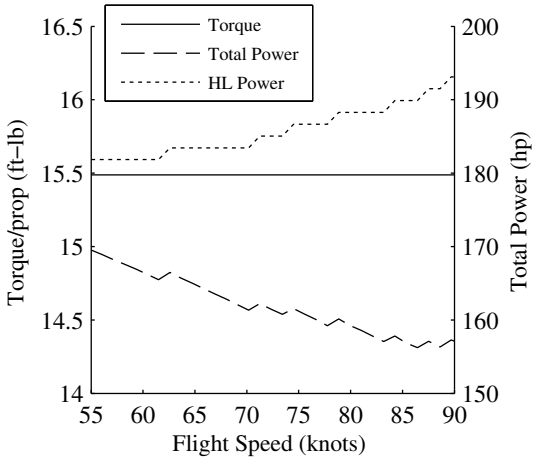

(f) High-lift propeller torque and total power

Figure 63: Maximum blowing (i.e., constant 21 N-m of torque) approach profile simulation results

Figure 63 shows the aircraft performance assuming a maximum blowing approach profile where the motor has a maximum torque of 21 N-m (or approximately 15.5 ft-lb), which was selected because this corresponds to the maximum torque of the Joby JM1 motor [135]. Unlike all the previous approach profiles, the maximum blowing approach does not technically have a sizing condition. Rather, a specific maximum torque is specified and it is assumed that the motor operates at this torque throughout the profile. With this assumption, the power required decreases slightly as the speed is decreased.[25]

Figure 63(b) indicates that there is a good C_L margin throughout the entire profile, and all of the margin comes from angle of attack (since by definition there is no additional blowing that can be utilized). Although this would appear to indicate that the maximum blowing approach is a desirable option, Figures 63(c) and 63(d) both indicate that the maximum blowing approach is impossible to fly since the excess thrust is noticeably above zero.[26]

5.1.2.6 Summary and Recommendations

In summary, the design point for each approach profile is as follows:

- the desired blown stall speed for the aggressive two-phase approach,
- the unblown stall speed for the conservative two-phase approach,
- the unblown approach speed (i.e., highest speed) for the constant lift multiplier approach,
- the desired blown stall speed for the linear C_{L_α} approach,
- and undefined for the maximum blowing profile.

[25]The "stair-step" nature of the power curves result from rounding in the outputs of XROTOR. In reality, a smooth profile is to be expected from the maximum to minimum power required.

[26]Technically Figure 63(c) shows that slow speeds could be flown with maximum torque, but windmilling the tip propellers is required. However, it is at best difficult to conceive how one could fly anything resembling a controlled, steady approach with maximum blowing and be able to slow to these speeds.

Note that even though these five profiles do not cover every possible manner of flying an approach they still exhibit design points that span from the lowest to highest speeds. It is conceivable that an approach profile could be selected where the associated design point occurs at any airspeed from stall up to the unblown approach speed. Therefore, the approach profile must be selected before a high-lift propeller system can be designed.

It is recommended that an approach profile similar to the linear C_{L_α} approach (i.e., one with a linear variation of C_L from angle of attack with velocity) be flown. Such an approach maintains some degree of margin from both the angle of attack and the high-lift propellers so that there are multiple degrees of freedom to account for unexpected changes in condition (e.g., wind gusts). This profile also has the benefit that the high-lift motors do not have to be oversized for operation at the blown stall speed like the constant lift multiplier or conservative two-phase approaches. The reduction in motor requirements also implies that the high-lift props will require less power to operate over the approach, which will leave more energy available for other phases of flight.[27] Finally, the aggressive two-phase approach profile and this linear C_{L_α} profile are least likely to exhibit excess thrust from the high-lift propellers at any speed, which makes these two approaches have the highest probability of being feasible. However, because the aggressive two-phase approach carries zero angle of attack margin for a portion of the approach, the linear C_{L_α} approach profile is inherently safer and is therefore recommended.[28]

[27] Reduced energy used in approach could lead to smaller aircraft sizes for a fixed range or to longer range capability in the same aircraft.

[28] In this particular case, if the Jameson drag model is considered (i.e., Figure 62(d)), the linear C_{L_α} approach also exhibits an interesting safety feature: without any additional drag from the cruise propellers, the aircraft can only decelerate to about nine knots over the desired stall speed. Consequently, it would be difficult to accidentally stall the aircraft since the pilot would have to set the cruise propellers to windmill in order to even slow to the stall speed. This observation provides an interesting potentially advantageous feature that can result from the high-lift propellers generating excess thrust.

It is also recommended that the high-lift propellers be controlled automatically (i.e., a "fly-by-wire" system for the "throttles" to the high-lift propellers is recommended). Specifically, this control system should be based on a torque schedule with airspeed (i.e., the torque to each high-lift propellers is automatically set based on the airspeed following a schedule similar to that presented in Figure 62(f)). There are several reasons for employing a control system. First, it is simply impractical to expect the pilot to control 14 (or potentially more) "throttle levers" for each of the motors.[29] Additionally, even if an experienced pilot could manage each of these levers and/or each high-lift prop could be controlled with a single lever, it would be incredibly difficult for a pilot to match the desired approach profile when manually flying the aircraft. An automatic high-lift propeller controller would allow the pilot to fly an approach in virtually the same manner as is currently done. Furthermore, an automated high-lift propeller torque control with airspeed would automatically adjust the high-lift propellers' "throttle" to account for wind gusts or other disturbances. This automated system is likely to respond much more quickly than the pilot, which should increase the safety of the aircraft. Such an automated response to disturbances may enable reduced C_L margins as compared to current regulations since the existing regulations assume the pilot is solely responsible for responding to disturbances.

Finally, it is recommended that the reference approach speed be set as no less than $(V_{\text{stall}})_{\text{unblown}} + \Delta V$, where $\Delta V \gtrsim 5$ knots. Although several of the approach profiles analyzed above indicated lift coefficient margins on the order of conventional GA configurations could be obtained at speeds relatively near the desired stall speed, setting the reference approach speed at these low speeds is likely unwise. At speeds below the unblown stall speed if there were a sudden total loss of power the aircraft would experience a stall. Therefore, it would be prudent to set a reference approach

[29]The SCEPTOR aircraft will have 12 high-lift props and 2 cruise propellers, but other configurations could have even more propellers. The trades associated with selecting the number of propellers will be discussed in Chapter VI.

speed that is at least as high as the unblown stall speed. To account for the possibility of a disturbance (e.g., a wind gust) that occurs simultaneously with a power failure, some margin above the unblown stall speed is recommended. There are many potential ways to reason what the ΔV margin should be. Here, it is recommended that ΔV be at least 5 knots. However, this margin may need to be increased to assure that the total C_L margin is at least on the order of conventional GA aircraft (i.e., $(\Delta C_L)_{\text{approach}} \gtrsim 0.6$). Note that in all of the example profiles shown above, ΔV would be 5 knots since each profile has a total C_L margin of greater than 0.6 at a speed of 76.5 knots (i.e., $(V_{\text{stall}})_{\text{unblown}} + 5$ knots).

5.2 Altitude Considerations

The discussion in this chapter has assumed an altitude was specified. Before the final sizing condition can be selected, one must consider how the performance of the high-lift propeller system will vary with altitude. If the lift augmentation or thrust production from the high-lift propellers changes substantially at different altitudes, then the appropriate sizing condition may need to be modified. Additionally, if the high-lift propellers are controlled automatically as recommended above, the appropriate control commands must be sent to these high-lift propellers at all altitudes.

Before altitude variations can be considered, one must specify the performance variation that is desired as altitude changes. Because Part 23 of the FARs specify that the stall speeds (V_{S0} and V_{S1}) are in calibrated airspeed, it is assumed here that the same stall speed in calibrated airspeed with altitude is to be maintained. From an analysis perspective, the calibrated airspeed will be treated as the equivalent airspeed because the two are typically the same in small aircraft.[30]

To study the impacts of varying altitude on the high-lift propellers, simulations

[30]The calibrated airspeed, which is the indicated airspeed corrected for instrumentation errors, technically differs from equivalent airspeed due to compressibility effects. Since the speeds of concern here are low, these compressibility effects are negligible and are ignored.

with XROTOR were performed varying altitudes from sea level to 10,000 ft.[31] These simulations determined the required propeller operating conditions to maintain a constant 55 knot equivalent airspeed stall in the Linear C_{L_α} approach profile, and the results are shown in Figure 64. Each of the sub-figures plots the metrics versus the altitude in feet.

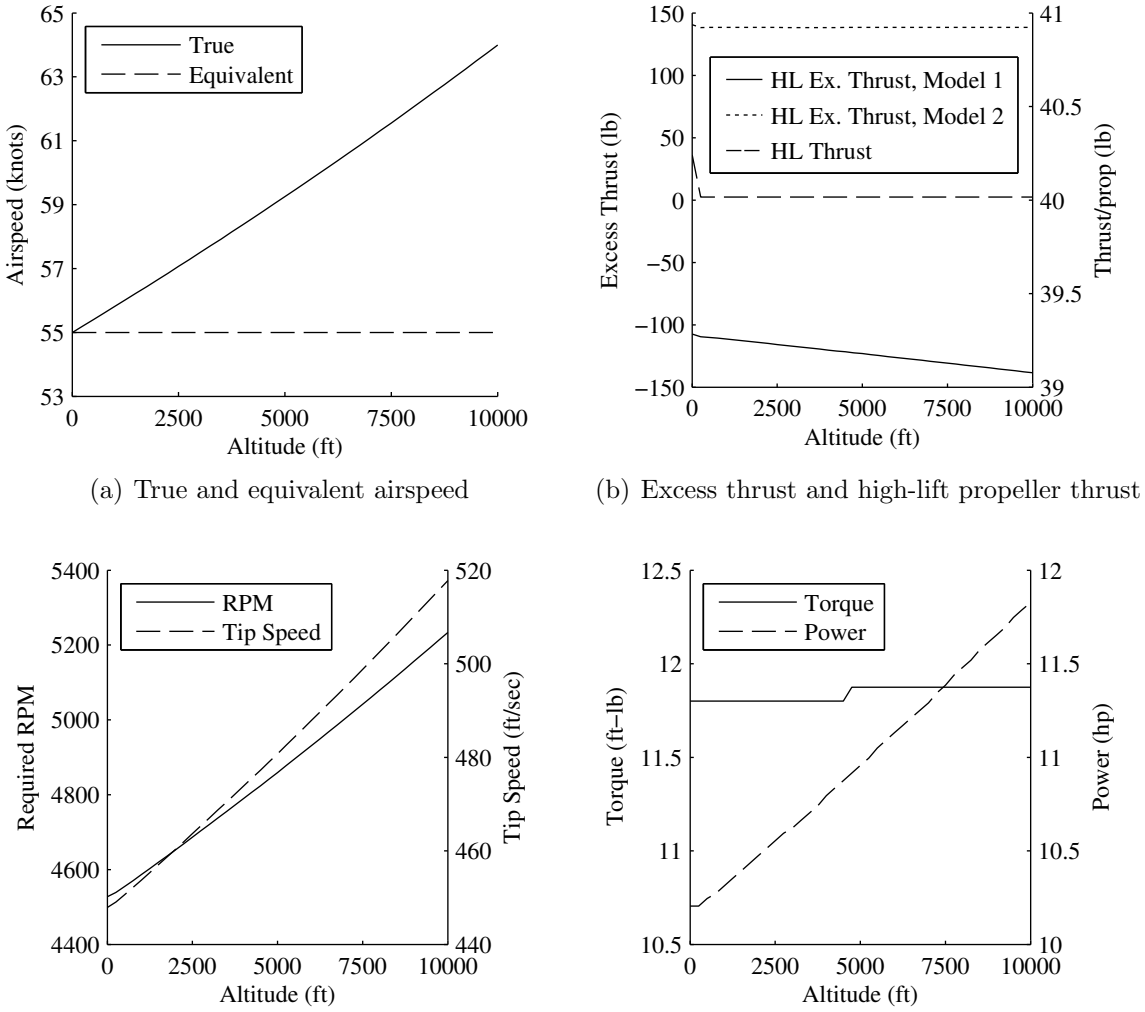

(a) True and equivalent airspeed

(b) Excess thrust and high-lift propeller thrust

(c) High-lift propeller RPM and tip speed

(d) High-lift propeller torque and total power

Figure 64: Variation of propeller operating conditions and performance with altitude to maintain a 55 knot equivalent airspeed stall

[31] 10,000 ft was selected as the maximum because landing conditions are of interest, and few airports will have density altitudes greater than 10,000 ft.

Figure 64(a) shows the variation of the true airspeed for a constant equivalent airspeed with altitude. The true airspeed increases with altitude as the density decreases to maintain the same equivalent airspeed.[32]

The thrust of each high-lift propeller and an estimate of the excess thrust of the configuration (based only on the high-lift propeller thrust) is plotted in Figure 64(b) for both drag models. Interestingly, the thrust from each propeller is approximately constant with altitude. The two drag models predict not only different absolute values of drag and excess thrust (as was observed above), but also slightly different trends. The first drag model where the Oswald efficiency varies with propeller blowing indicates that the pilot will need differing values of thrust (or drag) from the cruise propellers as approaches are flown at varying altitudes. The second drag model, however, predicts that excess thrust is constant with altitude, which implies the pilot would observe no practical change in cruise propeller control as altitude is changed.

Figure 64(c) indicates that the high-lift propeller RPM must be increased as altitude is increased in order to maintain stall at a constant equivalent airspeed. Similarly, the power required increases with altitude as shown in Figure 64(d). However, the torque required to maintain stall at the desired equivalent airspeed as altitude changes is essentially constant. This observation is incredibly important if an automatic control system to the high-lift props is desired. *High-lift propeller controllers can be set up to control torque simply as a function of equivalent airspeed.* This implies that once an approach profile is selected, the torque required from the high-lift props can be determined at a single altitude (with standard sea level conditions likely being the most logical place to analyze performance). Since all aircraft already effectively measure the equivalent airspeed, little additional hardware apart from the high-lift propeller system will be required in the aircraft to implement such a control system.

[32] since $V_{\text{equivalent}} = V_{\text{true}}\sqrt{\rho/\rho_0}$ where ρ_0 is sea level density and ρ is the density at altitude

It is important to note that the power requirements to maintain a constant equivalent airspeed stall increase with altitude (as shown in Figure 64(d)). If sizing an aircraft with high-lift propellers, the highest density altitude at which the aircraft is desired to land should be used for the approach and landing analysis. The larger power required will affect the total energy usage, which may have implications on the vehicle size.

5.3 Chapter Summary

This chapter was begun with the motivating question of

What is the appropriate design point for high-lift propellers?

A succinct answer to this question is that the design point depends on how the aircraft will be operated in approach, but it is likely that the design point will be the lowest desired speed of operation with high-lift propellers. A more detailed answer to this question along with other related important points from this chapter are stated below.

1. Regulations must change before electric aircraft or aircraft with high-lift propellers can be certified.
2. Current regulations require a 30% velocity margin between the reference approach speed and the stall speed, which equates to a C_L margin of approximately 41% of the maximum lift coefficient (or precisely $(1 - 1/1.3^2)\, C_{L_{\max}}$).
3. The reference approach speed for aircraft with high-lift propellers should be no less than the unblown stall speed and likely slightly higher than the unblown stall speed (to account for a complete loss of power occurring concurrently with a disturbance such as a wind gust).
4. The certification requirements and/or operational considerations related to flying an approach (i.e., which approach profile is desired) will set the high-lift propeller design point. However, a likely design point for the system is the desired blown stall speed.

5. There are many potential approach profiles that can be flown in an aircraft with high-lift propellers. The "Linear C_{L_α}" profile is recommended because it balances the lift coefficient margin between blowing and angle of attack throughout the profile and requires the smallest possible motor maximum torque.
6. There is a derived requirement in aircraft with high-lift propellers that the high-lift props should be controlled automatically via torque commands that vary with equivalent airspeed. The precise "torque schedule" must be linked to the desired approach profile, and ultimately must be determined via flight testing (although predictions of the appropriate profile can be estimated with the modeling presented in this document).
7. The presence of an automatic control system for the high-lift props may justify a reduced C_L margin than currently required because the pilot is no longer solely responsible for maintaining a safe degree of lift coefficient margin.
8. Additional drag may be required to approach and land at desired speeds depending on the thrust produced by the high-lift propellers and the approach profile flown.
9. Windmilling the cruise propeller(s) can produce additional drag and provide a tailorable drag increase if there is the ability to vary the propellers' pitch angles.

CHAPTER VI

SELECTING THE NUMBER AND POSITION OF HIGH-LIFT PROPELLERS

In the preceding chapters of this document it has been assumed that the diameter of the high-lift propellers was known, which implies that the number of propellers and the blown span are also known. The material in this chapter will remove these assumptions by addressing the question

How can the appropriate number of high-lift propellers be determined?

To answer to this question, the high-lift propeller system must be analyzed in the context of the overall aircraft system design. The modeling techniques and methods presented in the preceding chapters of this document enable the design trades associated with selecting the number of propellers for a particular design to be practically assessed. Although the work in this chapter in some ways represents an application of the methods presented elsewhere in this document, other methods for exploring and visualizing the design space are presented, and insights about the general characteristics of the design space for high-lift propeller systems are provided.

In this chapter, trade studies that can be performed to select an appropriate number of high-lift propellers for a specific wing design are discussed, and sample design space explorations for the SCEPTOR aircraft are presented. The results indicate that there is a vast design space with many interesting trades. Designers of high-lift propeller systems will have many metrics that should be considered, and often different metrics indicate that different high-lift propeller system designs are advantageous.

The specific propeller design method and number of blades selected can have significant impacts on the resulting performance, and consequently, must be considered when selecting the desired number of high-lift propellers.

The methods presented in this chapter are focused on selecting the number of propellers for a certain wing design but can also be coupled with a wing design process to evaluate the benefits of high-lift propellers in a design study. The high-lift propeller system adds new constraints to the design process and may directly influence the wing design. Potential ways of integrating the high-lift prop system design with the wing design process and the anticipated impacts of high-lift propellers on the design of the wing are discussed.

6.1 High-Lift Propeller Installation Considerations

6.1.1 Propeller Orientation Relative to the Wing

The theory presented in Chapter III indicates that there is a strong relationship between the lift augmentation and the angle the propeller is oriented relative to the wing. Therefore, the performance of the high-lift propeller system will be highly dependent on the propeller installation. Different installation schemes will provide different benefits and may lead a designer to select a different number of propellers altogether. In this section, the general benefits and drawbacks of various propeller installations are discussed.

The theory presented in Chapter III suggests that angling the propellers downward relative to the wing chord can lead to increased lift. This increase in lift with negative nacelle inclination is confirmed by experimental results including those of Gentry et al. [71] and Veldhuis [1]. Although the simple theory developed earlier indicates that very large angles are advantageous, this theory ignored stall, which will place a practical limit beyond which further reduction of the nacelle inclination angle will no longer provide benefits. This upper limit is difficult to generalize, but Veldhuis

suggests in most cases a practical upper limit is reached prior to a 15° downward inclination of the nacelle [1].

It is hypothesized that smaller diameter propellers will dictate that a practical maximum downward inclination angle will be even smaller than 15°. The direction of travel of smaller diameter slipstreams can be influenced more easily by the wing than larger diameter slipstreams as was discussed in conjunction with Figure 23 in Chapter III. If a large negative inclination angle is installed, the slipstream is more likely to be diverted completely over or under the wing, which can have negative impacts on the lift augmentation. Additionally, the experiments of Gentry et al. [71] discussed in Section 3.3.3 seem to show that there are diminishing returns as the nacelle inclination is decreased from −4° to −8° when compared to modifying the inclination from 0° to −4°. Consequently, for early-phase design studies it is recommended to maintain nacelle installations of no more than 10° below the wing chord line.

Although it may be beneficial from a lift standpoint to angle the nacelles downward, such installations may not be beneficial for other reasons. First, the nacelle drag at cruise conditions is likely to be increased if the nacelle is angled downward too far from the wing. Such installations will either require larger nacelles to mount motors at an angle or cause the nacelle to have a larger frontal area facing the flow direction at cruise (when angles of attack are typically noticeably reduced from high-lift scenarios). The potential benefits of the high-lift propeller system in shrinking the wing may effectively be offset by the nacelle drag increase. Second, once the propellers are angled below the freestream velocity, the thrust force from the propellers begins to have a component in the negative lift direction. This force will directly offset at least some of the lift generated by the wing.

It was suggested previously in Chapter III that the best "bang for the buck" could be obtained by aligning the propeller axis with the freestream direction. Since wings

are likely at a noticeable positive angle of attack in high-lift scenarios, a negative nacelle inclination is implied in such a scenario, which is beneficial for lift augmentation. Furthermore, the thrust from the propellers will not directly counteract any lift from the wing. Such installations will also likely have relatively clean inflow to the propeller disk, which is beneficial for the propeller performance. However, such an installation may suffer from a cruise drag penalty because the nacelles are more likely to be angled relative to the freestream direction in cruise.

In order to provide the benefits of downward angled nacelles without taking a penalty in cruise nacelle drag, an installation where the nacelle angle could be varied would be ideal. Such a system is suggested by Gentry et al. [71]. However, allowing the nacelles to pivot would require additional motors and actuators, which would add weight and complexity to the high-lift system. It is likely only advantageous to install such a system if extremely large amounts of lift are required and the vehicle is relatively insensitive to weight increases.

Ultimately, the benefits of downward-angled nacelles for increased lift must be weighed with the cost of increased nacelle cruise drag in the design of the high-lift propeller system. For near-term electric aircraft that are energy constrained, the lift increases possible from installing nacelles at a noticeable downward angle is likely outweighed by the probable increases in cruise drag that would result. Similarly, the added weight of active nacelle angle modification systems likely outweighs the benefits of additional lift.

6.1.2 Propeller Placement Relative to the Wing

In conventional aircraft design, the centerlines of propellers have generally been placed near the chord line of the wing. Such placements allow the engines to be mounted to the main wing structure easily and limit the amount of wetted area added to the aircraft. For low-wing aircraft, the props are often in-line with or above the chord line

while high-wing aircraft often place the propellers below the wing chord. So long as the high-lift propeller diameters are not sufficiently large, it may be possible to mount the propellers so that the props' centerlines are below the wing in all configurations (including low-wing aircraft). Consequently, a designer can likely consider both high and low propeller placements and would prefer to place the high-lift propellers in a location that is most advantageous for lift augmentation.

There is some seemingly conflicting information in the literature as to the optimal placement of the propeller in the vertical direction relative to the wing: some references suggest placement above the wing is advantageous while others indicate that placement below the wing is preferred. In this section, the reasons cited for various propeller placements are examined, and additional considerations for the placement of the high-lift props are discussed.

Vidal [136] and Veldhuis [1] suggest based on their experiments with unflapped wings that maximum lift can be obtained if the propeller centerline is placed above the chord line (i.e., $z_p > 0$). Vidal attributes this benefit to a higher-order slipstream shear effect though he was unable to develop a satisfactory theory to explain the phenomenon. Veldhuis attributes the observed benefit of high propeller placement primarily to slipstream contraction: with a high propeller placement, the contraction of the slipstream underneath the wing results in an increased angle of attack on the wing sections [1]. One important observation about their results is that they each only considered unflapped wings. In flapped configurations the position of the propeller disk relative to the flap (which is effectively an additional wing) should also be considered. Furthermore, Veldhuis's results show increases in the lift coefficient when the propeller is placed below the wing (i.e., $z_p < 0$). At some angles of attack, the lift increases with prop centerlines below the wing are greater than those where the prop centerline is above the wing; at other angles of attack this trend is reversed.[1]

[1]See Veldhuis's Figure 5.29 [1].

The peaks in lift augmentation are noticed when the propeller is placed approximately half a radius above or below the wing (i.e., when $z_p/R \approx 0.5$ or $z_p/R \approx -0.5$). Veldhuis attributes the local peaks in lift augmentation to the amount of maximum dynamic pressure that impacts the wing. Particularly with the large nacelles required for conventional engines, placing the propeller centerline in line with the wing chord leaves a noticeable portion of the wing effectively unblown due to the dead area aft of the nacelle. Additionally, traditional propellers have slipstreams with peaks in dynamic pressure near the 70% radial location as was discussed in Chapter II.[2] By placing the propeller somewhat below or somewhat above the wing centerline, more of the wing can effectively be exposed to the highest velocity flow.

There are three major differences between the configurations studied by Vidal and Veldhuis and the proposed high-lift propeller systems. First, if the high-lift propellers are designed with more uniform velocity distributions as described in Chapter IV, smaller offsets from the wing will enable the wing to be blanketed by a larger dynamic pressure. Second, the smaller nacelle sizes that are possible with electric motors will likely reduce the effective dead area aft of the nacelle, which again is likely to make smaller offsets from the wing advantageous. Finally, high-lift propellers should be coupled with flaps to obtain the maximum benefit, and the studies performed by Vidal and Veldhuis did not consider flaps.

Other literature suggests that placing the propeller centerline below the wing is advantageous. In two-dimensional simulations of non-uniform freestreams, Chow et al. [4] found that placing the velocity peak below the airfoil resulted in higher lift than placing it above. Additionally, Veldhuis found that the propulsive efficiency was increased with low propeller installations because there is less flow distortion by the wing [1]. The cleaner (though still far from clean) flow field below the wing may also lead to lower stresses on the blades, which can improve blade life. Perhaps the

[2]Specifically, see Figure 9.

most significant reason for placing high-lift prop centerlines below the wing chord is to enable the externally blown flap. The propeller slipstream blowing over the flap helps the flow to remain attached to the upper surface of the flap element and aft section of the main wing element, which can significantly increase lift. Additionally, with more of the slipstream below the wing the flap can more effectively turn the slipstream downward, which increases the lift. By placing more of the propeller disk below the wing, the projected area of the propeller disk onto the combined wing-flap system is increased, and the amount of projected disk area has been shown to have an significant impact on the lift augmentation [71, 1].[3] By exposing a larger portion of the flap to the slipstream, more benefits are noticed.

There are other considerations that suggest placing the high-lift propeller centerlines below the wing chord are advantageous. First, if the nacelle is attached to the wing upper surface, the suction peak of the airfoil is more likely to be affected than if the nacelle is attached to the lower surface. Since the suction peak is a significant factor in determining the lift from an airfoil, nacelle placement above the wing may have an adverse effect on the lift generated by the airfoil. Although this may be "made up for" with propeller blowing, a lower blowing power would likely be required if this suction peak could be unaffected.[4] Second, the static pressure increase aft of the high-lift prop disks is more beneficial on the lower surface of a wing (i.e., the pressure side). A larger portion of the slipstream underneath the wing will create a higher pressure on the lower surface than the upper surface, directly contributing to lift. Third, it is easier to turn the flow on the lower surface of a wing. Since lift

[3]Note that this is effectively the same observation made by Veldhuis for the main wing which suggests placing the propeller either above or below the wing chord. His conclusion about placing the prop above the wing did not account for the additional area created by a flap since he was primarily concerned with cruise performance.

[4]Because conventional engines require large nacelles, there are likely relatively small changes in wing lift whether the nacelle is centered above or below the wing in conventional aircraft. However, the electric motors for high-lift propellers will be considerably smaller, which may lead the nacelle placement above or below the wing to have much larger impacts on the lift.

can be thought of as turning a mass flow rate of air downward, this may be more easily accomplished if the flow is directly impacting the lower wing surface, which will be most noticed if the propeller is angled downward relative to the wing chord. Fourth, the potential benefits of upper surface blowing that could be observed with high propeller placements are likely diminished in high-angle of attack situations. As was shown in Chapter III[5] the lift augmentation from the slipstream was highly dependent on the angle of attack when upper-surface blowing-like effects were present. Fifth, the high-lift motor nacelles are likely to shed vortices in cruise. If the nacelles are placed too close to the wing chord line, these shed vortices may cause considerable decreases in the span efficiency of the wing. Mounting the nacelles on pylons below the wing may reduce the impacts of the shed vortices on the wing lift distribution. Finally, maintenance on the motors and high-lift propellers will likely be easier if the propellers are placed below the wing—particularly for high-wing aircraft.[6]

Based on all the above discussion, it is recommended for early-phase design that high-lift propellers be placed below the wing at a height such that the projected area of the disk onto the wing-flap system is maximized. The exact positioning of the propellers can then be modified in later-phase design when higher-order tools that are capable of capturing the mutual interference between the nacelles, props, and wing can be employed. The final nacelle placement should consider not only the lift augmentation but also other metrics such as total system weight and cruise drag.

[5]See the discussion around Figure 23.

[6]It is very likely that aircraft with wingtip propellers will have a high-wing placement to provide sufficient clearance to avoid tip prop ground strikes.

6.2 Design Space Exploration for Selecting the Number of High-Lift Propellers

Once a general propeller installation approach has been selected, analysis can be performed to determine what the most advantageous number of propellers is for a specific configuration. There are many metrics that will be important to a designer in determining the preferred number of propellers; these metrics include but are not necessarily limited to the total power required, total thrust generated, individual motor torque/power required, performance after a critical motor or propeller failure (which, for example, may cause a yawing moment and a loss of lift), total system weight (including motors, controllers, nacelles, wiring, etc.), nacelle (cruise) drag, reliability, cost, and complexity. Ideally, the analysis will be able to determine an overall "optimum" design through accurately assessing each of the metrics of interest. However, when one considers that the design space is very large and contains many different components (e.g., propellers, motors, nacelles, etc.) as well the fact that some of the desired characteristics are difficult to quantify (e.g., complexity), developing truly "optimum" designs is a daunting task!

Because the design space with high-lift propeller systems is so large, the SCEPTOR aircraft will be used in this section as an example of how the appropriate number of propellers can be selected. Although limiting the following discussion to the SCEPTOR aircraft and the design assumptions inherent with it will not describe the entire design space, this limited scope is necessary to make the problem tractable and will still provide insight into the trades that designers of high-lift propeller systems must consider. Through this example, the richness of the design space is evident and important observations are made about the types of simplifying assumptions that can practically be made in the design process.

6.2.1 Design Assumptions and SCEPTOR Aircraft Information

In designing the SCEPTOR aircraft, the team first selected initial wing and cruise propeller designs (i.e., the propellers that provide cruise thrust and are located at the wing tips) under the assumption that a high-lift propeller system could be designed to provide sufficient lift at low speeds. In practice, an approach similar to the following should be implemented in parallel with the wing design process to obtain a more advantageous overall aircraft design.

The details of the overall configuration and the design process followed to develop this configuration will be published in an AIAA Aviation 2016 paper by Borer et al. [137]. For the purposes of the present study, the following geometric parameters are all that are required to be known:

- the trapezoidal wing has a span of 31.6 ft, an average chord of 2.11 ft, and a taper ratio of 0.7 (as defined from the wing root at the aircraft centerline);
- the wing has 2° of washout and the root of the wing is inclined upward at 2° (so that at cruise the aircraft should fly at approximately a 0° angle of attack);
- the fuselage occupies 3.95 ft of the center wing span;
- the wing is flapped beginning just outside the fuselage junction and moving out 10.4 ft along the span;
- the wing section is a custom airfoil and single slotted flap, which together exhibit a zero-lift angle of attack of approximately −20° and a maximum sectional lift coefficient of approximately 2.75 at a 10° angle of attack; and
- the cruise (wingtip) propeller diameter is 5 ft.

Additionally, the aircraft is being designed to achieve a 55 knot stall speed (at standard sea level conditions) and will have a gross weight of 3,000 lb. A final consideration of note is that the SCEPTOR aircraft's high-lift nacelles will not be able to pivot in flight. This implies that a specific installation angle relative to the wing must be selected. It is assumed that the nacelles are oriented so that when the aircraft is at a

0° angle of attack, the nacelles are at a 0° inclination relative to the aircraft reference frame.[7]

To put practical limits on the design space for the high-lift propeller system for the SCEPTOR aircraft, the following assumptions were made:

- All high-lift propellers have the same design (i.e., the same diameter, chord distribution, twist distribution, etc.), and the prop blades use a single airfoil, the MH114 [120].
- The configuration has an equal number of high-lift props on either side of the fuselage.
- The high-lift propellers fill the entire span of the wing from the edge of the fuselage to the edge of the wingtip propellers without overlapping any of the propellers (in order to reduce the acoustic signature produced by interacting prop tip vortices).
- The high-lift propellers are placed upstream of the leading edge a distance of one radius (i.e., $u = R$) to enable folding
- Propeller tip speeds at the design condition are set to 450 ft/sec, which is about half the typical tip speed of similarly-sized GA aircraft, to reduce noise.
- The unblown maximum lift coefficient of the wing (with flaps) is 2.6.
- The aircraft will operate with the "Linear C_{L_α}" approach profile described in Chapter V. This implies that the design point for the high-lift propellers is the desired blown stall speed.
- The propellers are placed relatively close to the wing chord line so that the surrogate model developed in Chapter III will provide accurate results.
- The propellers should have an odd number of blades to reduce the acoustic

[7]This implies that a nacelle placed directly at the wing root would be angled downward relative to the wing chord by 2° and a nacelle placed directly at the tip would be directly aligned with the chord line.

signature.[8]

In order to obtain reasonable estimates of the motor weight and diameter, simple models were developed based on the Joby JM1, JM1S, JM2, and JM2S motors [135]. The JM1 motor is a candidate motor for the SCEPTOR flight demonstrator. Because the torque and power levels of the JM1 are likely not sufficient for all the high-lift propeller systems under consideration, a "rubberized" JM1 model is developed.

Because the design of electric motors is beyond the scope of the present work, it is assumed here that, as the power requirements of the high-lift propellers increase, the diameter of the motor (and thus the nacelle size) will also increase. Such an approach should capture the general trends of increased power requirements and allows for a simple model to be developed whose only input is the required power level.[9] Based on the specifications of the Joby motors, a specific power of 2 horsepower per pound[10] and a specific diameter of 1.1 inch per pound were selected. To determine the motor weight, the power required at the sizing condition is divided by the specific power. Similarly, the diameter of the motor is determined by multiplying the estimated motor weight by the specific diameter. To avoid potentially unrealistic results, limits on the maximum and minimum motor diameters were set to 18 inches and 3 inches, respectively.[11]

[8] If the propeller has an even number of blades, the wake from the up-moving side of the propeller and the wake from the down-moving side of the prop will both impact the wing at approximately the same time since one pair of blades are always 180° apart. The prop wake-wing interaction is a noticeable source of noise, and the peak noise level is increased with the wakes intersecting the wing at the same time. However, with an odd number of blades, the blades on either side of the prop pass in front of the wing out of phase with one another. This phase difference should reduce the peak noise level caused by the wake-wing interaction.

[9] It should be noted that, in general, electric motors can be made of varying weights and diameters to achieve the same torque or power. For example, a smaller diameter motor can provide the same torque or power as a larger diameter motor, but generally the larger diameter motor will be lighter.

[10] The specific power assumed here is slightly lower than the Joby Motor data would suggest to account for the additional weight of a controller. For simplicity of explanation, this total weight is referred to as the motor weight.

[11] Motor sizes could potentially be smaller than the minimum, but the nacelle must have sufficient volume to hold the motor and likely the controller as well. Additionally, motor sizes may realistically become larger, but this would come with a change in motor architecture, which would likely increase the specific power. This maximum limit is not reached in any of the design studies performed below.

The motor diameter affects the propeller design and the nacelle drag. Propeller blades cannot be designed for radial stations less than the motor radius, and larger motor diameters will reduce the effective disk area, which will impact the power and/or thrust of the prop. Additionally, the motor diameter will effectively set the nacelle size, which will directly impact the drag of the configuration. For the studies presented here, Raymer's [125] component drag buildup method—a simple handbook method based on skin friction coefficients, form factors, wetted areas, and interference factors—is used for estimating the nacelle drag. The nacelle is modeled in OpenVSP [138, 139] with a pod component assuming a fineness ratio[12] of 6 to obtain the wetted area. Raymer's suggested interference factor (1.3) and form factor equation for nacelles are employed to estimate the drag of the configuration at cruise.[13]

6.2.2 Design Space Exploration Process

With a given wing design and the above assumptions, the high-lift propeller system can be defined by selecting the number of props (which implies a prop diameter), a blade shape (i.e., twist and chord distributions), and the number of blades. To select these parameters, an exploratory design method is followed in this dissertation—i.e., many candidate designs are created and evaluated, then a "preferred" design is selected. Although this method may not produce a strictly "optimal" solution, greater intuition about the design space can be gathered through such an exploratory method than by employing a numeric optimization scheme. There is certainly no reason an optimization algorithm could not be used in a practical design process, but the exploratory method is instructive for showing the tradeoffs that exist in the

[12]The fineness ratio is defined as the ratio of the length to the maximum diameter. Currently the fineness ratio in OpenVSP's pod component uses the radius in its calculation instead of the diameter. This error is accounted for in the modeling presented here so that the resulting component has the appropriate actual fineness ratio.

[13]Cruise drag is selected rather than drag at stall because the primary objective of the SCEPTOR project is to demonstrate very efficient cruise flight. Therefore, the nacelle drag at cruise should be minimized.

design of high-lift propeller systems as will be shown below.

The overall exploratory design procedure consists of the following steps:

1. Select the number of high-lift props
2. Estimate the motor/hub diameter
3. Design many props (by varying the design section lift coefficient) that provide the required induced velocity to produce the desired blown stall speed
4. Analyze all props at off-design conditions
5. Select the most-preferred prop design for this particular number of props
6. Repeat this procedure (back to step 1) for all numbers of props
7. Compare the most-preferred design for each number of props, and select the number of props with the most-preferred overall performance

The following sub-sections describe these steps in more detail.

6.2.2.1 Designing Propellers

Two separate propeller design methods are studied here: one traditional minimum induced loss (MIL) design method and the novel method presented earlier in Chapter IV. By studying both design methods, further verification of the benefits shown previously for the new design method can be obtained and estimates of the uncertainty bounds on the performance of the system can also be developed.

The propellers are designed to operate at the stall speed of the aircraft because a "Linear C_{L_α}" approach profile is assumed. The required lift augmentation for level flight at the 55 knot stall speed taken with the geometry of the wing provide a value of the required average axial velocity that must be produced by each high-lift propeller. This required axial velocity is used as an input to the propeller design process.

Additionally, both propeller design methods require inputs for the blade element airfoil properties. Specifically, lift and drag estimates of the airfoil sections as well as a design section lift coefficient are required. To select an appropriate section lift

coefficient, a sweep of 40 different design lift coefficient values ranging from 0.1 to 1.77 (the approximate stall c_l) is performed. For each of these design lift coefficient values, a new propeller design is generated, and these designs are evaluated at off-design conditions as described below before selecting the desired section lift coefficient.

The traditional propeller designs are generated with the open-source propeller analysis and design tool XROTOR [119], which is based on the MIL theory of Larrabee [84, 85]. To design a minimum induced loss rotor, XROTOR requires inputs for the desired thrust from the propeller and blade element section properties in addition to freestream flow conditions. An iterative procedure is performed to determine the appropriate input thrust value to XROTOR to produce the needed average axial velocity. The initial guess of the thrust is determined from simple momentum theory. If this thrust estimate does not produce the correct average axial velocity, the thrust input to XROTOR is varied until the desired average induced axial velocity is produced. It is possible that such an iterative procedure may never converge because the required thrust is simply too high for the other input parameters. In these cases, no feasible solution can be found with the MIL design method.

Novel high-lift propeller designs are generated for each number of props and design c_l following the method outlined in Chapter IV. It is possible that this design process will be unable to design a propeller in certain situations, but in general the method can provide designs for many different inputs. This robustness is both a strength and a weakness of the method. If left unchecked, the designs generated can have unrealistically large chord lengths or twist angles in an attempt to generate the desired forces. To ensure that relatively reasonable designs resulted during the design process, the chord length of all designs generated with the simple high-lift prop design method are limited to have chord lengths of no more than 40% of the radius, and pitch angles are limited to stay between $-90°$ and $90°$. If these limits are reached, the iterative procedure described as a part of the method is employed to modify the overall designs

for subsequent iterations.

6.2.2.2 Off-Design Evaluation

After each propeller is designed, it is also evaluated at off-design conditions of 30 and 90 knots to ensure reasonable performance exists in these off-nominal cases. A velocity of 30 knots approximates the conditions that would be present over the takeoff ground roll, and flight at 90 knots is likely close to an upper-limit on the speed range in which the high-lift propellers will ever be practically operated for the SCEPTOR aircraft.[14] By analyzing the propellers at these two off-nominal conditions, the general variations in performance over a range of practical operating speeds can be assessed to ensure that the designs provide acceptable performance.

6.2.2.3 Selecting the Most-Preferred Propeller Design for a Given Number of Propellers

In the design exploration process, many propeller designs are generated for a given number of blades, number of propellers, and prop design method by varying the design lift coefficient. If only point-design characteristics are of interest, then the "optimum" design c_l will likely be the lift coefficient for maximum lift-to-drag ratio. However, when off-design conditions are evaluated, the best design c_l may be substantially different than the c_l for maximum L/D. Because the high-lift propellers are fixed pitch, as the freestream velocity is changed the local angle of attack of the blade sections will vary (for a constant RPM). This change in local angle of attack can lead to stalled blade sections and/or reduced performance at off-design conditions.

Generally, the most preferred propeller design for a given number of props and number of blades can be determined in a myriad of ways including an optimization algorithm or the selection of a preferred design by an expert. For the purposes of the design exploration process presented here, the performance of many propellers

[14]The wing is capable of generating more than sufficient lift without the high-lift propellers at this higher-speed condition.

designed with different design section lift coefficients is visualized, and general trends in performance are observed. Based on the observed trends, a preferred propeller is selected based on a simple rule that is described below.

To visually explore the changes in performance as the design section lift coefficient is varied, the change in six metrics of interest are plotted as a function of the design c_l in Figure 65. These metrics are the thrust, power, torque, number of stalled airfoil sections, average swirl angle, and average induced axial velocity, which are plotted in Figures 65(a), 65(b), 65(c), 65(d), 65(e), and 65(f), respectively. The variations of these metrics with the design c_l at the design point of 55 knots standard sea level conditions are denoted by black asterisks. The off-design performance characteristics at velocities of 30 knots and 90 knots are shown with gray circles and triangles, respectively.

The information in Figure 65 applies to a case where five-bladed propellers were designed with a minimum induced loss method for a version of the SCEPTOR aircraft that has twelve high-lift props. Forty separate propellers were designed with design lift coefficients ranging from 0.1 to 1.77, and each point in the figure refers to one of these propellers. Although this figure applies to only one specific case, the trends observed here generally apply to all other numbers of props and blades when sweeping over the design c_l.

Each of the propellers is designed to produce the same average induced axial velocity at the design condition as shown in Figure 65(f). Interestingly, the thrust, power, torque, and swirl are virtually constant for all propellers at the design condition with the exception of props designed with low design lift coefficients (i.e., less than approximately 0.5). This is a testament to the intuition that momentum theory can help build (though momentum theory under-predicts the thrust and power required to produce this desired average induced axial velocity).

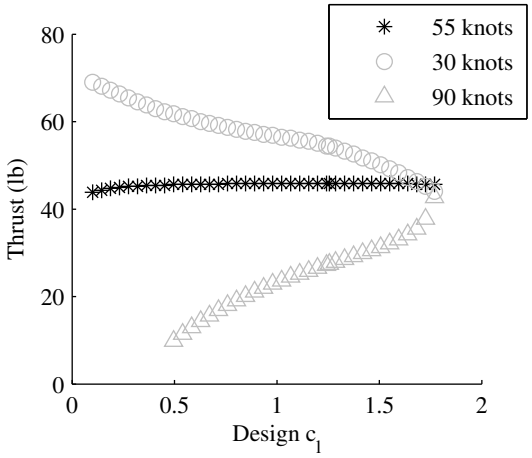

(a) Thrust

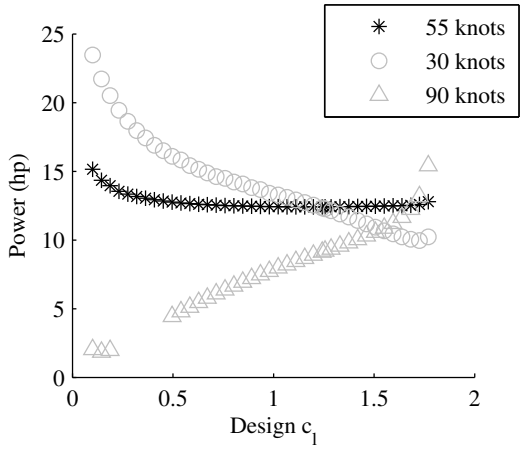

(b) Power

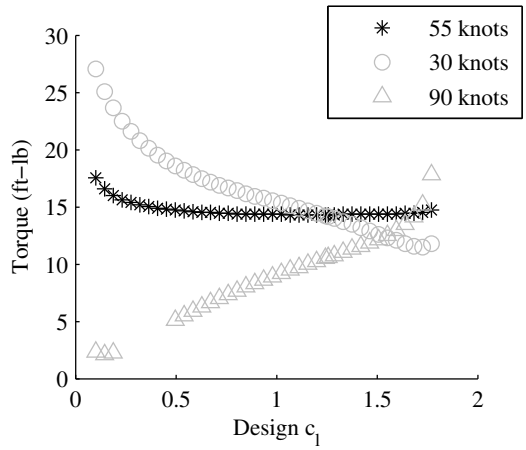

(c) Torque

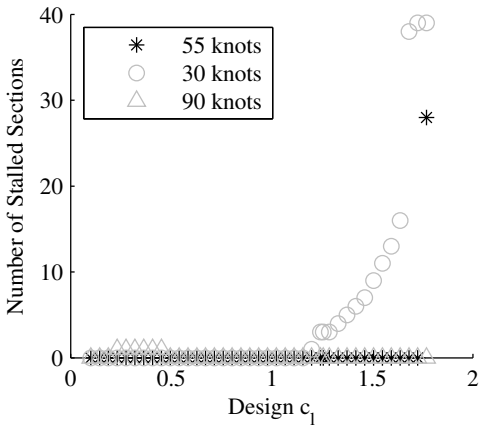

(d) Number of stalled airfoil sections (where the blade is designed with 40 sections)

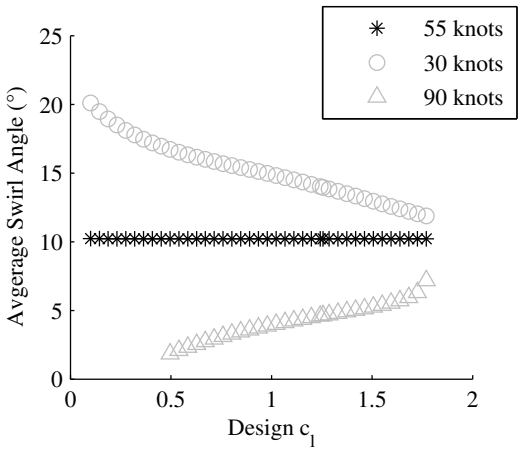

(e) Average swirl angle

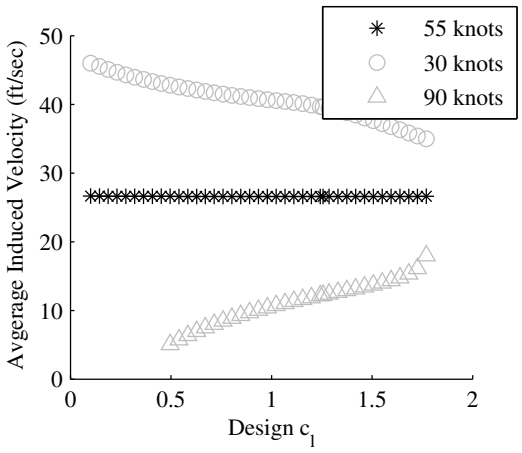

(f) Average induced axial velocity

Figure 65: Comparison of six metrics of interest when varying the design c_l of a five-bladed propeller in a minimum induced loss design method for a 12 propeller configuration on the SCEPTOR aircraft

In selecting the most preferred propeller design, both the on- and off-design performance of the prop are considered. An ideal high-lift propeller would produce the desired average induced axial velocity with very low thrust, power, torque, and swirl while not experiencing stall over any blade sections (to reduce the acoustic signature of the props) at all flight conditions. Additionally, it may be advantageous for the propeller performance to show relatively little variation from on-design to off-design conditions. Based on these desired characteristics, high design lift coefficients can be eliminated because they lead to stalled blade sections at low-speed operations. Similarly, low design c_l values lead to increased torque and power requirements. Furthermore, Figure 65 indicates that the least variation between on- and off-design conditions occurs at moderate to high design c_l values. With these trends in mind, the most-preferred design c_l in the design space exploration process is selected as the highest design c_l that does not cause stall over any blade sections at any of the conditions evaluated. For the case shown in Figure 65, a design c_l of 1.15 is selected. All other cases (i.e., number of high-lift propellers and number of blades) are evaluated in the same manner, and the most-preferred propeller design is determined for all of these conditions.

6.2.2.4 Selecting the Number of Propellers

Once the most-preferred high-lift propeller design is determined for each number of props, these designs are then compared to one another to select the most advantageous number of propellers. As with selection of the most preferred design c_l, the number of propellers can ultimately be selected in many ways. Here, a design space visualization procedure similar to that performed to determine the design c_l is followed to provide insight into the trades that exist with high-lift propeller systems. An optimization algorithm or other method could be used if desired as part of a full aircraft design process.

In selecting the number of propellers, the aircraft's performance under off-nominal circumstances must be considered in addition to on-design performance because this performance may change the resulting aircraft design. For example, in the design of a conventional twin-engine general aviation aircraft, the aircraft's performance with the critical engine inoperative can be a driving factor in the design of the empennage and/or power requirements of an engine. In the case of high-lift propellers, the most critical single-point failure corresponds to the high-lift propeller that ultimately generates the most lift. Interestingly, this "critical high-lift motor" is likely the inner-most motor, since it will drive a propeller that typically blows the largest area of the wing and has a flap.[15] Additionally, there could be a second critical motor in relation to the yawing moment that is more similar to the conventional "critical engine." If a reasonably high thrust is required from the high-lift propellers, the relatively large spanwise distance at which high-lift motors may be placed could result in a large yawing moment in the event of a motor failure. This "critical yawing motor" is the one that generates the most yawing moment, which under many circumstances will be the farthest outboard motor.[16] The yawing moment with the critical yawing motor inoperative and the change in stall speed with the critical high-lift motor inoperative are both tracked in the following design space exploration.

The results from the design space exploration for the SCEPTOR aircraft are shown in Figures 66 and 67. To provide insight into the design space, ten separate metrics are tracked for each design.[17] These metrics are

1. the total thrust of all high-lift propellers (Figure 66(a)),
2. the total power required from all high-lift motors (Figure 66(b)),
3. the required torque for each propeller (Figure 66(c)),

[15]It is certainly possible other motors could be the critical high-lift motor. For example if the inner-most high-lift propeller blows a section of wing without a flap while other props blow flaps.

[16]The critical yawing motor for the SCEPTOR aircraft is indeed the farthest outboard motor.

[17]These metrics are all evaluated at the design condition of 55 knots standard sea level conditions unless otherwise noted.

4. the required power for each prop (Figure 66(d)),
5. the average swirl angle (Figure 66(e)),
6. the total motor weight (Figure 67(a)),
7. the nacelle parasite drag estimate at cruise (Figure 67(b)),
8. the yawing moment that would result from the loss of the critical yawing motor (Figure 67(c)),
9. the total yawing moment generated by all propellers on one side of the aircraft (Figure 67(d)), and
10. the stall speed resulting from the loss of the critical high-lift motor (Figure 67(e)).

These ten metrics are not an exhaustive list of the metrics of interest; rather, they are provided as a subset to help illustrate the tradeoffs inherent in the design of high-lift propeller systems. In each of the sub-figures, six different propeller designs are shown for each number of high-lift propellers. These six designs correspond to 3-bladed, 5-bladed, or 7-bladed propellers that were designed with one of the two different propeller design methods. The minimum induced loss designs are shown with black markers and denoted with 'MIL' while those designed with the high-lift propeller design method presented in Chapter IV are shown in blue and denoted by 'HLP.'

One may notice that for each number of high-lift propellers not all design methods and/or number of propellers are represented in the figures. For example, for 14 and more propellers, there is no MIL, 3-blade design shown. The lack of a marker indicates that no propeller was designed successfully for these conditions that meets the constraints mentioned above in Section 6.2.2.3. As the number of propellers is increased, generally fewer combinations of design method and number of blades generate feasible designs.

When studying Figures 66 and 67, the many competing tradeoffs inherent in the design of high-lift propeller systems become apparent. Certain metrics (e.g., swirl)

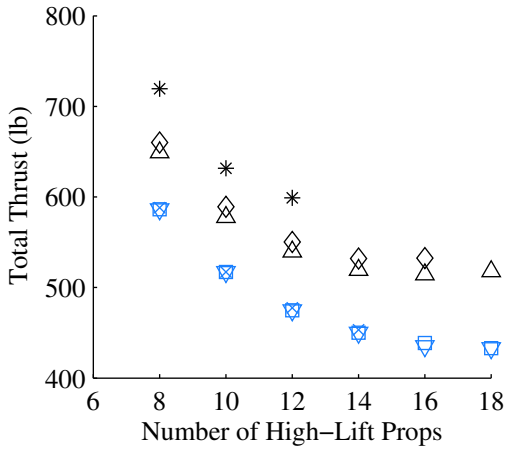

(a) Total thrust

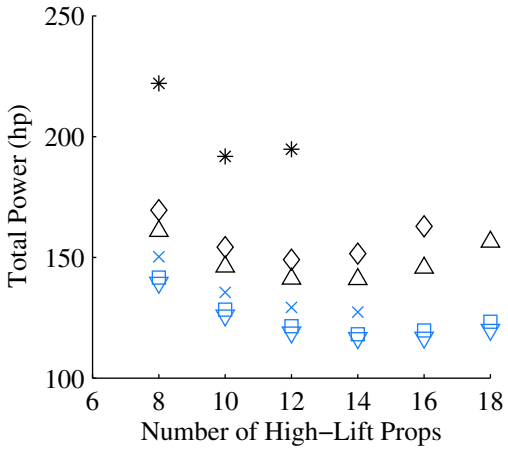

(b) Total power

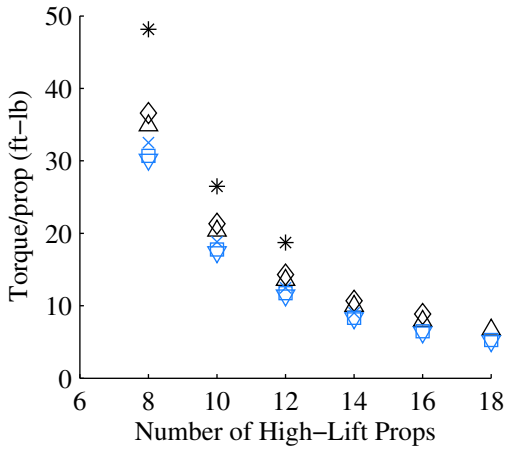

(c) Torque per prop

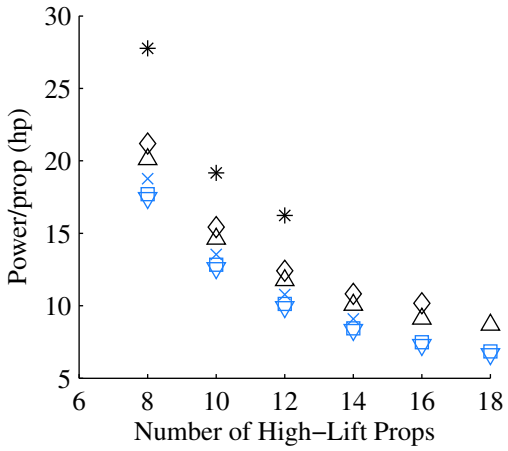

(d) Power per prop

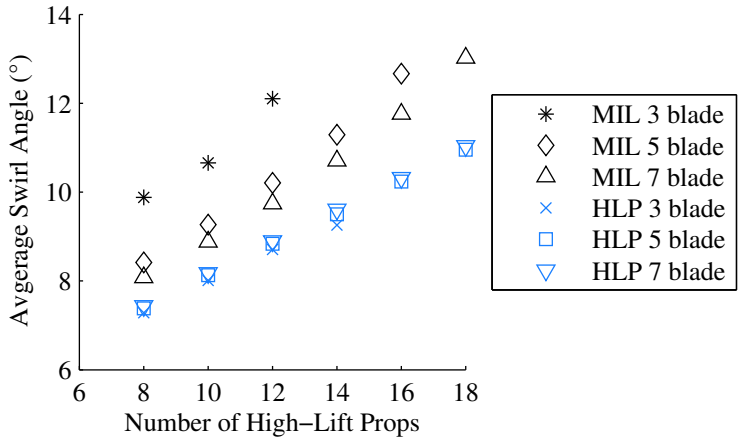

(e) Average swirl angle

Figure 66: Part 1 of 2: Comparison of metrics of interest when varying the number of propellers and the number of blades per propeller for conventional and high-lift prop design methods

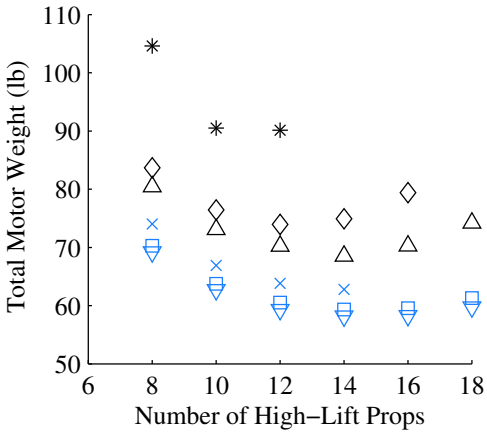

(a) Motor weight

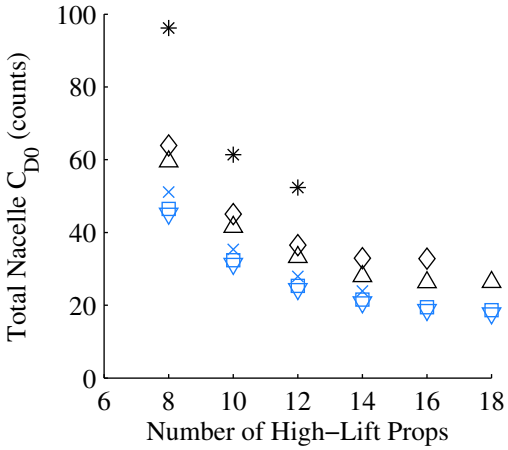

(b) Total nacelle parasite drag at cruise (150 knots, 8,000 ft)

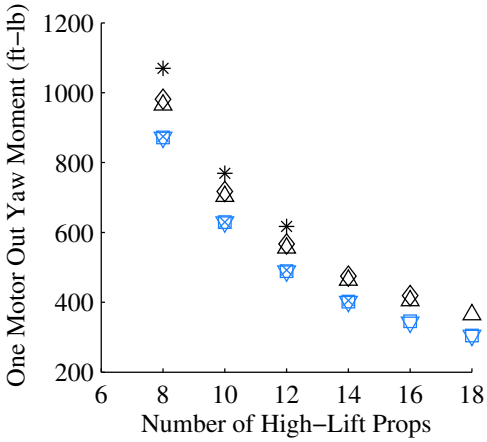

(c) Yawing moment with critical motor inoperative

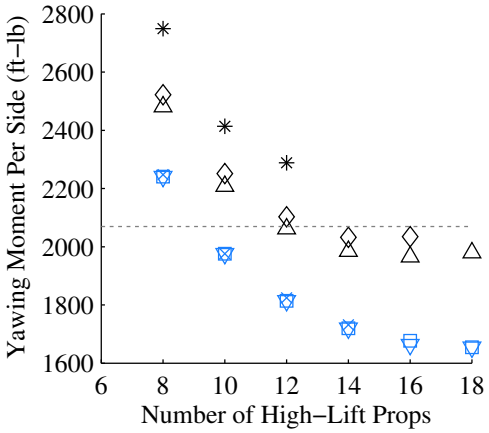

(d) Yawing moment of all motors on one side. (The dotted line is an estimate of the Tecnam P2006T yawing moment with one engine out.)

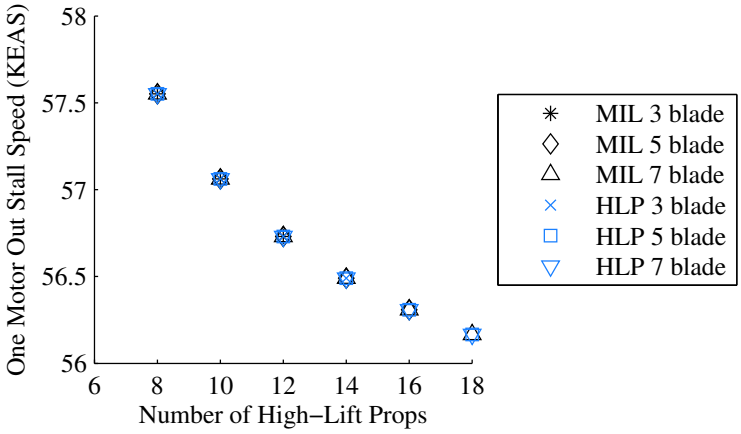

(e) Stall speed with critical motor inoperative

Figure 67: Part 2 of 2: Comparison of metrics of interest when varying the number of propellers and the number of blades per propeller for conventional and high-lift prop design methods

indicate that the fewest number of high-lift propellers should be selected; other metrics (e.g., stall speed with one motor inoperative) indicate that the highest number of props is most advantageous; other metrics (e.g., total power) suggest that some number of props between the extremes is best. One could justify selecting almost any number of propellers based on this information!

Additionally, although many metrics have clear directions of optimality (e.g., a minimum power propeller is desired), other metrics may not have a clear "optimal" direction, which makes the selection of an appropriate number of propellers even more difficult. One example metric without a clearly optimal direction is the yawing moment per side, which is shown in Figure 67(d). It may be advantageous for the high-lift propellers to be capable of generating a large yawing moment to counteract the adverse yawing moment that would arise if a cruise propeller failed. However, if there were to be a failure of all high-lift propellers on one side of the wing (a scenario that with a proper electrical system architecture should be very low probability), it would be more advantageous if a small yawing moment resulted. To provide a reference for the relative magnitudes of the yawing moments shown in Figures 67(c) and 67(d), an estimate of the one engine out yawing moment that the Tecnam P2006T[18] would generate at 55 knots and takeoff power is shown with a dotted line in Figure 67(d).[19] It appears that most MIL designs would generate approximately the same yawing moment as the base Tecnam while most HLP designs would generate less moment in this case. This indicates that the tail of the Tecnam is appropriately sized to handle the worst-case yawing moment from the high-lift props. However, if it is desired that these high-lift props counteract the yawing moment from one of SCEPTOR's wingtip cruise props, then they will be woefully inadequate since the wingtip propellers will

[18]Recall that the SCEPTOR aircraft is a modified version of the P2006T. The empennage of the SCEPTOR aircraft will be unchanged from the baseline aircraft.

[19]This is a simple calculation assuming a 67.5% propeller efficiency and the engine operating at full power of 73.5 kW.

generate substantially larger yawing moments than the baseline Tecnam propellers because they are placed further outboard.[20]

Another off-nominal situation of note is the change in the stall speed if the critical high-lift motor fails, which is shown in Figure 67(e). Because the high-lift propellers are all designed to provide the same lift augmentation, the loss of lift when a motor fails is equivalent[21] between all propeller designs at a set number of propellers. Configurations with fewer high-lift props will experience greater changes in lift, but the likelihood of a motor failing is reduced.[22]

The nacelle parasite drag estimate in cruise, which is shown in Figure 67(b), indicates that larger numbers of propellers are likely advantageous; however, the parasite drag impact of the nacelles is not the only drag metric that is of interest. The influence of the nacelles on the lift distribution in cruise may also have a significant impact on the induced drag of the wing. The nacelles may shed vortices or otherwise influence the pressure field around the wing in such a manner as to modify the lift distribution from what would be expected if the nacelles were not present. It is anticipated that fewer numbers of nacelles will be advantageous from an induced drag perspective because there will be fewer locations where the lift distribution will be modified. Additionally, the wing design could likely be modified to account for these effects so that the impacts of the nacelles on the lift distribution are minimized. However, higher-order analyses of more detailed nacelle and wing geometry are required to adequately assess these impacts and make any desired modifications the wing design to minimize the impact of the nacelles on the lift distribution.

It is also interesting to note from Figures 66 and 67 that the optimum number of propellers for many metrics changes based on the propeller design method employed.

[20] A rough estimate is that one of the wingtip propellers at the 55 knot condition will generate a yawing moment of approximately 5,275 ft-lb if operated at full power.

[21] based on the models employed here; in reality there will be small changes between propeller designs

[22] assuming the motors and propellers have equivalent reliabilities

For example, Figure 66(b) indicates that the minimum total power is obtained with 12 high-lift props when using the MIL method while 14 props provides the lowest power solution from the HLP method. Similarly, the number of blades can also impact the optimum number of propellers for certain metrics—particularly for the MIL design method. For example, the minimum motor weight occurs with 12 motors for the MIL 5-bladed designs, but the MIL 7-bladed designs suggest 14 motors leads to the lowest motor weight as shown in Figure 67(a). These observations suggest that the propeller design method employed and the number of blades selected can have significant impacts on the performance characteristics of the high-lift prop system.

Figures 66 and 67 provide further evidence that the novel high-lift propeller design method presented in Chapter IV is indeed superior for designing high-lift propellers. Power savings on the order of 15% and decreases in thrust of 10-15% are observed across all numbers of propellers. The HLP design method is also capable of designing a wider range propellers than the MIL design method in XROTOR. For example, there are no feasible 5-bladed MIL designs for the 18 prop configuration, but the HLP method was able to produce feasible designs there. Additionally, the variability in performance between the different MIL designs for a given number of props is considerably greater than the HLP designs. For most metrics, it is difficult to distinguish between the markers denoting propellers designed with the HLP method. However, for many metrics, there are substantial performance differences between the number of blades in the MIL method. The relative closeness in performance of the HLP designs may imply that a designer can effectively eliminate the number of blades as a design variable if employing the HLP method. However, this is not generally recommended since the number of blades does have a significant impact on the MIL designs. The relative closeness of the HLP designs may be an artifact of this particular design space and not indicative of general high-lift propeller design spaces.

Ultimately, a decision on the number of high-lift propellers (and likely the propeller

design method and number of blades) must be made. Ideally the number of propellers with the lowest power would also have the lowest total motor weight, nacelle drag, and induced swirl as well as the smallest change in stall speed if the critical motor is lost. Unfortunately, this is not the case. To further complicate matters, there are other factors to consider when selecting the number of high-lift propellers that may not be easily quantified in the early conceptual design phase such as

- complexity (e.g., additional motors require more parts),
- cost (including acquisition, maintenance, and disposal costs),
- reliability (e.g, the more motors/propellers the system has, generally the higher the probability of failure of any single component, but the lower the consequences if there is a failure),
- availability of commercial off-the-shelf components (e.g., an electric motor with the proper torque/power requirements) for use in the design,

and so forth.

Overall, it seems that either 12 or 14 high-lift propellers are likely the most advantageous number of propellers to select in this case. Depending on the prop design method and number of blades, either 12 or 14 propellers provides the lowest power and lowest motor weight; additionally, the total thrust and nacelle drag values for 12 and 14 props are close to the lowest values predicted. Finally, 12 and 14 propellers provide a "happy medium" in terms of average swirl angle, resulting stall speed with the critical high-lift motor inoperative, and complexity. The current design of the SCEPTOR aircraft has 12 high-lift propellers.

6.2.3 Linking the Process to Wing Design

Ultimately, the selection of the number of propellers should feed back into the design of the overall wing and aircraft. Most of the trades that should be considered are discussed above in Sections 6.2.2.3 and 6.2.2.4, but a new, important metric is not

directly present: the excess thrust. As was discussed in Chapter V, the thrust from the high-lift propellers may preclude the aircraft from slowing down and descending to land. The practicality of high-lift propellers depends on there being no excess thrust with the high-lift props operating over the desired speeds of operation.

6.2.3.1 Excess Thrust Constraint

To estimate the excess thrust of the SCEPTOR aircraft with 12 high-lift propellers, the same two drag models discussed in Chapter V were used along with the propeller performance presented in the preceding section. The resulting excess thrust is shown in Figure 68, which has four different colors of markers to refer to different drag models and prop design methods. The black and green markers refer to the propellers designed with the MIL method while the blue and orange markers correspond to the HLP design method. The two lower groupings of markers (i.e., black and blue) are the excess thrust predictions with the parabolic variation of Oswald efficiency and the two upper groupings of markers (i.e., green and orange) represent the excess thrust as predicted with the Jameson model for induced drag.

There are also two vertical axes shown in Figure 68. The left axis is the excess thrust calculated when only considering the high-lift propellers, and the right axis shows the excess thrust when the cruise propellers are operated as windmills to produce drag. The dotted line is drawn for easy identification of zero high-lift propeller excess thrust and the dashed line shows the zero excess thrust location when the cruise propellers are windmilling.

If the parabolic e_0 drag model is considered, most designs including all those with 12 propellers or more exhibit no excess thrust from the high-lift propellers, which indicates that these designs are feasible in relation to an excess thrust constraint. However, if the Jameson drag model is used, there are no designs that are feasible without cruise propeller windmilling. Furthermore, only the 14 prop configurations

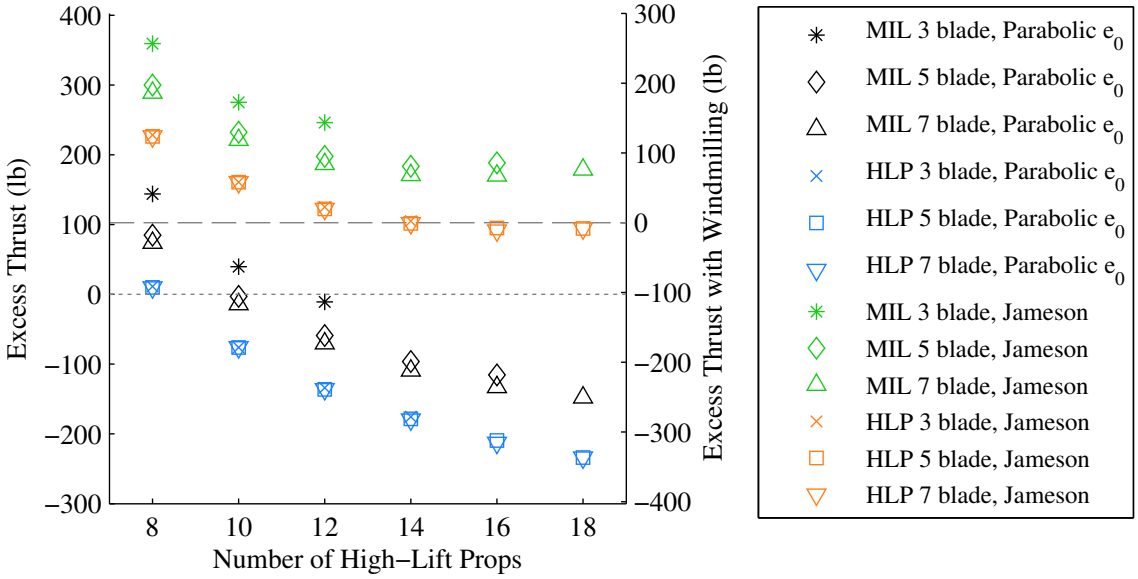

Figure 68: Excess thrust calculated with two different drag models for the candidate high-lift propeller designs

with 5 or 7 blades designed with the HLP method as well as all the 16 and 18 high-lift prop configurations designed with the HLP method have less than zero excess thrust. Therefore, if the Jameson drag model is accepted as accurate, then the desired number of propellers would likely need to change (from 12 to 14 or more) in order to satisfy the excess thrust constraint.

It is important to note that the results in Figure 68 only show the excess thrust at a single speed—i.e., the design point, which corresponds to the 55 knot blown stall speed in this case. Depending on the approach profile (and vehicle drag variation), the most critical condition for excess thrust may occur at a different speed. Therefore, to ensure that the aircraft will be able to descend, the excess thrust must be evaluated at the most critical condition if not over a portion of the desired approach profile.

There are multiple approaches that can be taken if the excess thrust is found to be greater than zero. A new design that demands less lift augmentation from the high-lift propeller system could be considered. A larger wing, more advanced flap system (to provide higher unblown $C_{L_{\max}}$), or increased stall speed requirement are

all manners by which the design could be modified to potentially become feasible. Additionally, it is important to remember that the performance of the high-lift propeller system is directly tied to the geometry of the wing. For example, increasing the wing aspect ratio may help a design become feasible since the effective R/c ratio could be increased, which generally will act to increase the lift augmentation.[23] Similarly, increasing the distance of the propeller from the leading edge of the wing may also increase the lift augmentation. However, increasing wing aspect ratio and propeller distance from the wing are not without other penalties (namely increased weight) that must be considered in a full wing or aircraft design process.

A final method by which a design with positive excess may be made feasible is by adding additional drag sources to the aircraft as discussed in Chapter V. Since drag in any other phase of flight is likely undesired, these drag devices would likely need to be deployable so that they can be stowed in other phases of operation. The increased weight and complexity of the drag producing systems must be considered in the design process if such systems are required to eliminate excess thrust.

6.2.3.2 Other Design Considerations

Unfortunately, the design of a high-lift propeller system cannot be performed effectively without knowledge of the wing dimensions. Unlike a conventional stall speed constraint that is a function of the wing loading, W/S, the effectiveness of a given high-lift propeller system cannot be abstracted in terms of the wing loading, but requires a sized wing. It is recommended that the wing be sized to the smallest required area considering all other constraints to begin the design process. Beginning with a small wing effectively assumes that a high-lift propeller system can be designed to meet the required lift augmentation, which may or may not be valid. This small wing should be used in the first iteration of a design loop of the high-lift propeller system,

[23] See Chapter III, specifically the figures showing the variation of the β parameter with R/c.

and the trades demonstrated above should be performed. If practical propellers are designed and the total excess thrust of the configuration is less than zero after this first loop, then a feasible system is achieved. If a feasible design is not achieved, then the wing design must change. Assuming the same flap system and aspect ratio are desired, then the wing area should be increased until a feasible solution is found.

It is important to remember that even if a feasible solution is found, this solution may not represent the most advantageous aircraft design. The increased power requirements, weight, and drag of a high-lift propeller system that augments more lift may offset the gains in cruise drag reduction that can be obtained by reducing the size of the wing. Therefore, the design of the high-lift propellers and the selection of the number of propellers should be included in the wing design process. Incorporating the high-lift propeller system design into the wing design process will act to increase the dimensionality of the design space, but may lead to noticeably improved overall aircraft designs.

6.3 Chapter Summary

This chapter was motivated with the following question:

How can the appropriate number of high-lift propellers be determined?

A succinct answer to this question is that the number of propellers can be selected by weighing the benefits and drawbacks of different numbers of propellers. The assessment of these pros and cons is not necessarily straightforward, however. As with all of design, there are tradeoffs of many different metrics that can be explored, these trades depend on the design assumptions made, and the design space is incredibly large. The example design space exploration of the SCEPTOR aircraft presented in this chapter has provided insight into the types of trades that can be made and the richness of the high-lift propeller design space.

Some of the key points from this chapter are as follows:

1. It is likely most advantageous to install the nacelles for high-lift propellers slightly below the wing chord line in a position where the projected area of propeller disk onto the combined wing-flap system is maximized.
2. From a lift perspective it is best to install high-lift propellers with a slight negative incidence relative to the wing chord. However, such an approach is likely to create additional cruise drag. Actively tilting nacelles could be considered to circumvent these tradeoffs, but such systems would increase the weight and complexity of the high-lift propeller system.
3. The design process demonstrated here should be linked with a wing design process so that the high-lift propeller system is able to influence the design of the wing.
4. It is unlikely that there will be an abundantly clear "optimum" number of high-lift propellers to select for any given configuration. Therefore, it may be necessary to develop some form of composite objective function that takes into consideration many metrics of interest (e.g., total power, cruise drag, motor weight, complexity, etc.) into the overall wing design process.
5. The propeller design method and the number of blades selected for the prop design may have large impacts on the performance of the high-lift system and, consequently, the appropriate number of high-lift propellers that should be selected.
6. A likely new constraint on the design of the system is the total thrust. The system should be analyzed with methods similar to those presented in Chapter V (including improved drag models as available) to verify if there is indeed too much thrust to fly the desired approach.
7. If a design is infeasible from excess thrust, additional drag sources can be added or the wing design can be changed to make the design close. Potential wing design changes include increasing the wing area, decreasing wing chord (which

implies increasing the aspect ratio), or adding a more effective flap system.

8. The novel high-lift propeller design method presented in Chapter IV provides propeller designs that require consistently less power and torque than traditional minimum induced loss methods.
9. The performance of the most preferred design (and/or several of the most preferred designs) should be verified with tools of increased order (e.g., CFD). Of particular importance is the the excess thrust prediction because it could be critical to the feasibility of the design.

CHAPTER VII

CONCLUSIONS

7.1 Summary and Implications of Results

Electric motors open new degrees of freedom for aircraft designers, including the ability to distribute propulsors over the airframe. There are many ways in which this "distributed electric propulsion" may benefit the overall efficiency of the aircraft. The concept at the heart of this dissertation is one in which many propellers are placed upstream of the wing leading edge to augment lift. Because these propellers are operated only at low speeds and are folded back against the nacelles at higher speeds, they act as a new form of high-lift device and, consequently, have been termed "high-lift propellers."

One of the primary purposes of this dissertation was to develop tools and methods to rapidly assess the lift impacts of high-lift propellers on downstream wings. A novel theory describing the impact of tractor propellers on wing lift was developed. This model is based on considerations of thin-wing theory and predicts variations in wing lift due to changes in the circulation and dynamic pressure caused by the propellers. One of the primary benefits of this model is its ability to help build the intuition of a designer. Specifically, the impacts of propeller inclination angle, diameter, and placement in front of the wing can be rapidly be assessed, and general trends in performance variation with these parameters were presented visually to aid in building the designer's intuition. The model is designed to be used as an initial estimate of the wing lift in the presence of the propellers, and consequently should be used in very early phases of design to arrive at reasonable initial propeller designs that can later be refined and analyzed with higher-order models. Although the model has shown good

agreement with experimental and higher-order computational results, more detailed models should be applied as the design process continues and the design space is narrowed.

Ultimately, the application of propellers as high-lift devices represents a shift in mentality for an aircraft designer. Although propellers have been applied to increase lift in the past, these same propellers were required to be efficient thrust-producing devices. In contrast, high-lift propellers need only to efficiently augment lift.

A shift in the purpose of propellers from efficient thrust producers to efficient lift augmenters requires that the design approach be reconsidered. A novel method based on blade element momentum theory principles was introduced in the dissertation to design efficient high-lift propellers under the hypothesis that a uniform axial velocity distribution aft of the propeller would provide the most advantageous lift augmentation. This method produces propellers that consistently require less power and produce less thrust than conventional propellers designed with minimum induced loss design methods that provide the same average induced axial velocity. These novel designs achieve near-uniform induced axial velocity profiles by increasing the loading of the propeller blades both near the root and somewhat toward the tip compared to conventional propellers.

Before propellers can effectively be designed, a design point must be selected. Although it would seem intuitive that the appropriate design point for a high-lift propeller system would be the lowest desired operating speed (i.e., the blown stall speed), this may not always be the case. There is an interdependence between the manner in which a vehicle with high-lift propellers will be operated and the design point. Specifically, the operation of the aircraft in the approach and landing phases of flight will dictate the appropriate design point.

The operation of aircraft in approach and landing is closely tied to regulations. Current regulations dictate a 30% velocity margin over the power-off stall speed

of the aircraft at the reference approach speed. From a technical perspective, this velocity margin can be equated to a lift coefficient margin above stall, which implies aircraft can be made sufficiently safe if they can operate with an adequately high C_L margin. Unlike conventional aircraft that achieve a target C_L in a given configuration solely by adjusting the angle of attack at set flight conditions, high-lift propellers provide another degree of freedom in achieving a target C_L: adding power to the high-lift props. Equivalent C_L margins to existing aircraft can be obtained in aircraft with high-lift propellers through many combinations of angle of attack and propeller blowing. Consequently, there are many potential ways in which safe C_L margins can be achieved in approach, which implies the aircraft can fly many different "approach profiles" in which the C_L margin is divided differently between angle of attack and blowing.

Five representative approach profiles have been explored that cover the full range of potential combinations of angle of attack and blowing. The results from these studies indicate that the highest propeller torque may be required over a range of flight speeds. Consequently, the desired operation during approach must be specified in the design of the high-lift propeller system so that an appropriate design point can be selected. The approach profile recommended here is one in which there is a balance of C_L margin from blowing and from angle of attack, with a gradual (i.e., linear) decrease of C_L margin from angle of attack with decreasing flight speed. This particular approach profile dictates the propeller design point to be the desired blown stall speed.

Before finalizing a design point, the variation in high-lift system performance with altitude must be considered to determine if the critical design condition occurs at a specific altitude. Since typical aircraft experience stall at effectively the same equivalent airspeed regardless of altitude and current regulations specify stall speeds in calibrated airspeeds (which are the same as equivalent airspeeds in the absence

of compressibility effects), it is desirable to produce high-lift propeller systems that provide the same effective performance regardless of altitude at a specific equivalent airspeed. The studies performed show that performance parity can be achieved at a given equivalent airspeed if the torque supplied to the propeller remains constant with altitude. This observation suggests that any altitude can be selected as a design point for the high-lift propeller system (so long as the airspeed analyzed correlates to an equivalent airspeed).

The constancy of required torque with altitude also has implications on the viability of controlling the high-lift propellers. It is unlikely that a pilot will practically be able to manually control individual "throttle" levers for each high-lift motor. Furthermore, it would be exceedingly difficult for a pilot to maintain the desired balance of blowing margin and angle of attack margin specified by a particular approach profile even if a single throttle lever controlled all the high-lift props. Therefore, some form of automatic control algorithm is likely required for the high-lift propellers. The finding that torque should remain constant with altitude implies that a simple control algorithm for the high-lift propellers can be implemented where the motors are controlled by torque commands that vary with equivalent airspeed. Implementing such an automatic control algorithm would allow a pilot to fly an approach in much the same way as is currently done.

After the design point (i.e., an equivalent airspeed and the required lift augmentation there) has been selected, a high-lift propeller system can be designed for a specific wing. It is important to note that high-lift propellers cannot be effectively designed without a dimensional wing due largely to the strong coupling of the lift augmentation and the effective height of the slipstream from the propeller. Perhaps the most important decision that must be made related to the high-lift propeller system design is the selection of the number of high-lift propellers.

In determining the desired number of propellers, many metrics are of interest

including but not limited to the total power required, system weight, nacelle drag, performance with critical motor failures, and complexity. The variations of the metrics of interest with the number of high-lift propellers for the SCEPTOR aircraft indicate that depending on the objective function (i.e., which metric(s) is/are most important for a particular aircraft), different numbers of high-lift propellers should be selected. Furthermore, the number of blades and the method by which the blades are designed have both been shown to have large impacts on the resulting performance of the system and, consequently, the number of high-lift propellers that is most advantageous for a particular design. Therefore, employing simple approaches of estimating propeller performance that are agnostic to the blade design (e.g., momentum theory) may result in an unrealistic picture of the tradeoffs in the design space and lead to the selection of a clearly non-optimal high-lift propeller system design.

The design of the high-lift propeller system must fit into the wing and overall aircraft design processes. An iterative procedure may be required to determine a practical wing design. It is recommended that the wing design process begin by sizing the wing as small as possible considering all constraints other than those specifying the low-speed lift requirements and assuming that the high-lift propeller system can provide the required lift augmentation. Then, the methods presented in this document can be employed to design a high-lift propeller system and determine if the system is feasible. If the system is found to be infeasible, the wing design can be modified (likely by increasing the wing area), and a new iteration of the high-lift system design performed. This procedure can continue until a feasible solution is found.

Infeasibility may be identified in one of two manners. First, it is possible that the methods may fail to provide practical propeller designs capable of providing the desired lift augmentation. Second, the propeller designs and installations that produce the needed lift augmentation may result in too much excess thrust during approach.

Perhaps one of the most novel aspects of high-lift propeller system designs is the

fact that the thrust from the propellers may actually be undesirable. If thrust levels higher than the total drag of the aircraft are required to generate the needed lift, the aircraft will be unable to fly at the desired low speed condition(s). Consequently, an excess thrust constraint must be incorporated into the design process. If the high-lift propellers produce too much excess thrust, the design could simply be considered infeasible or additional drag-producing devices such as fuselage-mounted speed brakes could be added to the aircraft to balance the excess thrust. Any drag producing devices added to the aircraft should be deployable so that drag is not increased throughout all phases of flight. These deployable devices will likely increase the weight and complexity of the overall system, and these impacts must be considered in an overall aircraft design process.

To demonstrate the methods presented in this dissertation and provide insights into the design trades that exist in aircraft with high-lift propellers, the flight demonstrator aircraft being developed as a part of NASA's SCEPTOR project was studied throughout this dissertation. To fit within the practical constraints of the project, the design space has been reduced by assuming that all high-lift propellers will assume the same design and be distributed along the entire exposed wing span. Even with this simplified design space there are still many interesting tradeoffs involved with the design of the resulting high-lift propeller system that have been explored in this document.

Ultimately, propellers employed as high-lift devices open many new degrees of freedom in both the design and operation of the aircraft. In designing and operating these systems a mentality shift is required from thinking of propellers as thrust producers that may augment lift to lift augmenters that produce thrust. If a designer can accept this mentality, then a wide new design space can be explored, and the potential exists to achieve novel aircraft designs that far exceed the performance of modern small aircraft.

7.1.1 Summary of Contributions

The primary contributions of this thesis are as follows:

1. Development of a model that estimates the lift augmentation from high-lift propellers. The model was developed from considerations of thin wing theory and the impacts of propeller slipstreams on dynamic pressure and circulation and was calibrated with computational fluid dynamics results. This model is capable of providing intuition to a designer about the impacts of various propeller installation angles, diameters, and installation locations relative to the wing.
2. Development of a novel method to design high-lift propellers based on blade element momentum theory with a systematic procedure to specify induction factor distributions. This design method was shown to reduce the required propeller power by approximately 15% relative to conventional minimum induced loss design methods in addition to providing other performance benefits.
3. Identification of implied requirements and potential regulatory changes required for aircraft with high-lift propellers. In particular, multiple plausible operating schedules (i.e., propeller torque and aircraft angle of attack) for approach and landing were proposed and evaluated with respect to current FAA requirements for landing reference speed margin.
4. Identification of the appropriate sizing conditions for high-lift propeller systems based on the desired low-speed operation of the aircraft.
5. Demonstration of how the models and methods developed in this dissertation enable the exploration of the vast design space and many tradeoffs that exists in designing high-lift propeller systems.

7.2 Potential Directions for Further Research

This dissertation has only begun to explore the many new design trades that are possible in aircraft with high-lift propeller systems. There are many possible avenues to extend the work and continue exploring the wide design space associated with these systems.

A likely next step in the research of high-lift propeller-equipped aircraft is to perform design trade studies of an entire aircraft that includes a high-lift propeller system. The methods presented in this dissertation can be incorporated into an existing wing design process to further explore the impacts of the high-lift prop system on the overall aircraft design.

Just as the design of propellers has been modified in this dissertation to design more effective axial velocity-producing props, work remains to design propellers that are capable of folding smoothly against a nacelle. There may be practical folding constraints that directly impact the design of the propeller, which could reduce the effectiveness of the designs generated by the methods presented in this document.

Because the excess thrust has been identified as one of the most important new constraints in the design of high-lift propeller systems, high-lift drag estimation with propeller blowing may become of prime importance. Initial studies may be performed with higher-order model tools such as CFD, but novel, highly-accurate drag prediction methods with very fast execution times would prove immensely helpful in the early phases of design of high-lift propeller systems to ensure that excess thrust is not generated.

The stability and control of an aircraft with high-lift propellers may be vastly changed from conventional aircraft, and should be studied in detail. Unlike many high-lift devices, high-lift propellers in and of themselves do not generate higher lift strictly by aft-loading a wing (though they may indirectly work to increase flap

loading). Consequently, lower nose down pitching moments than with other high-lift devices may result, but this needs to be verified. However, the location of the propellers relative to the center of gravity and the forces produced by the propeller (including the normal force, which is directed in the plane of the propeller) may cause destabilizing effects. Additionally, increased downwash from higher lift on the wing as well as propeller slipstreams propagating downstream may have considerable impacts on the tail that should be studied.

Aircraft with high-lift propeller systems may also be prone to potentially detrimental aeroelastic behavior. The distribution of masses along the wing span and in front of the wing may modify the structural modes of the wing. Similarly, the forces generated by the propellers and the unsteady loadings of the propeller slipstreams on the wing will likely also impact the wing's structural dynamics. These impacts have not been addressed in this dissertation, but should be analyzed to ensure the structure is sound. Although the current SCEPTOR team is analyzing the flight demonstrator design to ensure safety, more efficient overall aircraft designs could result if aeroelastic analyses could be effectively incorporated into early design space exploration. Including aerostructural analysis in early-phase design is particularly important for these systems because the primary purpose of high-lift propellers is to reduce the wing size. This reduced wing size implies that there will be less volume for structural mass, which will generally tend to reduce the stiffness of the structure. Additionally, the lift augmentation from high-lift propellers is most effective when paired with wings of shorter chord. Consequently, if the high-lift prop design is incorporated into the wing design process, higher aspect ratio wings may be favored, which may further reduce structure stiffness. Further work is needed to include both static and dynamic structural analyses in early-phase design to effectively "push back" against these tendencies toward very small, high-aspect ratio wings and ensure the resulting designs are structurally sound.

APPENDIX A

OVERFLOW SIMULATION RESULTS AND SURROGATE MODEL

In this appendix additional information about the two-dimensional OVERFLOW CFD simulations including raw lift coefficient results and visualizations of the surrogate model described in Chapter III are presented.

Visualization of the grids used in the simulations are shown in Figures 69 and 70. Figure 69 shows the near-body grids around the airfoil and actuator disk along with velocity contours for a case where $V_j/V_\infty = 1.5$, $R/c = 0.5$, and $u/c = 0.5$. A view of the grids over the entire domain is shown in Figure 70. The total grid size is 200 chord lengths by 200 chord lengths, and the airfoil is located in the center of the domain.

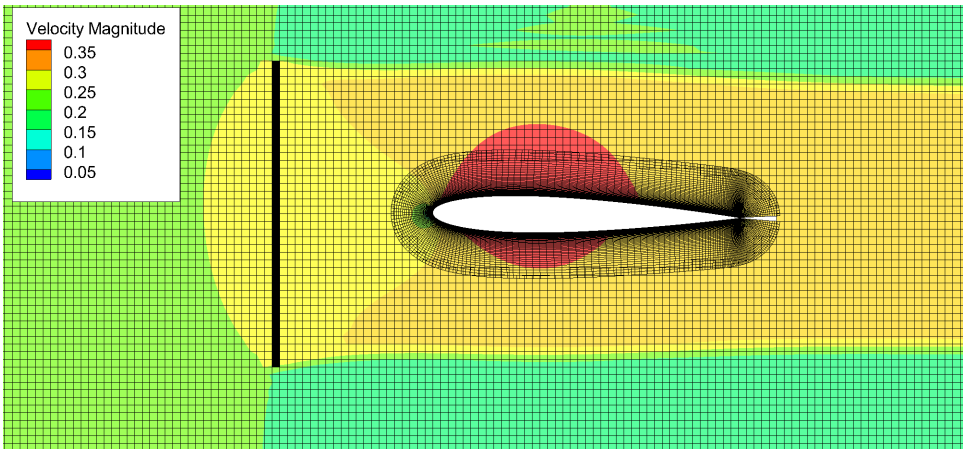

Figure 69: Visualization of the near-body grids used in the OVERFLOW simulations with contours of the local Mach number plotted for a case with $V_j/V_\infty = 1.5$

Tables 4, 5, 6, 7, 8, and 9 show the raw lift coefficient data for the various runs at the specified R/c and u/c values. Each table refers to a different slipstream Mach

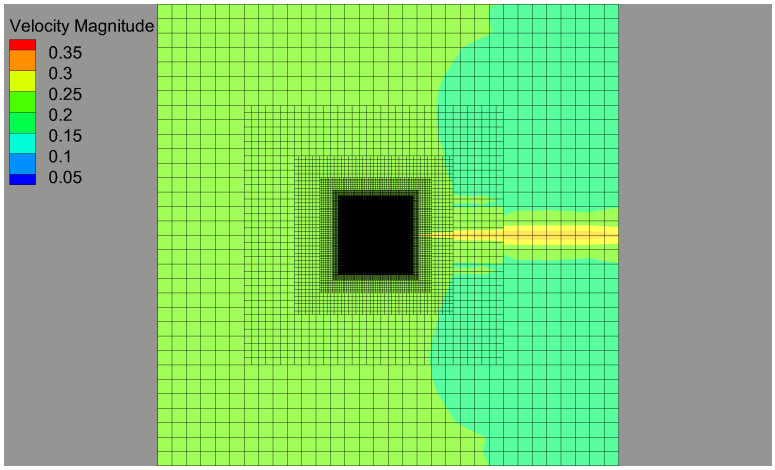

Figure 70: Visualization of the grid for the entire domain used in the OVERFLOW simulations with contours of the local Mach number plotted for a case with $V_j/V_\infty = 1.5$

number and/or angle of attack.

Visualizations of the surrogate model developed from the simulations are shown in Figures 71, 72, 73, and 74 as surfaces for each V_j/V_∞ along with the data points from the OVERFLOW simulations as black lines with data points depicted by asterisks. Similarly, surfaces depicting the surrogate model output for each of the u/c values are shown in Figures 75, 76, 77, and 78.

Table 4: Lift coefficients at 1° angle of attack and a slipstream Mach number of 0.25 for various R/c and u/c values

	$u/c = 0.25$	$u/c = 0.5$	$u/c = 1$	$u/c = 1.5$
$R/c = 0$	0.12259405	0.12259405	0.12259405	0.12259405
$R/c = 0.125$	0.15613221	0.16519881	0.17529094	0.18171508
$R/c = 0.25$	0.16866195	0.17449586	0.1813828	0.1856368
$R/c = 0.5$	0.18349857	0.18746797	0.19246702	0.19542132
$R/c = 0.75$	0.19018328	0.19382611	0.19882665	0.20183654
$R/c = 1$	0.19254193	0.1962981	0.20177528	0.20523931
$R/c = 1.5$	0.19104049	0.19478202	0.20076999	0.20505103
$R/c = 2$	0.1886915	0.19214728	0.19804934	0.20268262
$R/c = 2.5$	0.18589041	0.18899497	0.19451675	0.19912568
$R/c = 3$	0.18385174	0.18661155	0.19165918	0.19605531

Table 5: Lift coefficients at 1° angle of attack and a slipstream Mach number of 0.3 for various R/c and u/c values

	$u/c = 0.25$	$u/c = 0.5$	$u/c = 1$	$u/c = 1.5$
$R/c = 0$	0.12259405	0.12259405	0.12259405	0.12259405
$R/c = 0.125$	0.18347453	0.20194509	0.22674401	0.24525604
$R/c = 0.25$	0.20980502	0.22176407	0.23789559	0.24930327
$R/c = 0.5$	0.24360991	0.25126185	0.26180362	0.26880084
$R/c = 0.75$	0.26380276	0.27093146	0.28071914	0.28687166
$R/c = 1$	0.26622636	0.27423477	0.28581665	0.29315841
$R/c = 1.5$	0.27076373	0.27946971	0.29297946	0.30222511
$R/c = 2$	0.25911406	0.26725145	0.28128285	0.2922948
$R/c = 2.5$	0.26218528	0.26986507	0.28338589	0.29445247
$R/c = 3$	0.25678286	0.26361005	0.27603197	0.28674407

Table 6: Lift coefficients at 1° angle of attack and a slipstream Mach number of 0.4 for various R/c and u/c values

	$u/c = 0.25$	$u/c = 0.5$	$u/c = 1$	$u/c = 1.5$	$u/c = 2$	$u/c = 3$
$R/c = 0$	0.12259405	0.12259405	0.12259405	0.12259405	0.12259405	0.12259405
$R/c = 0.125$	0.22642229	0.26554245	0.3222054	0.370685	0.4206516	0.5777405
$R/c = 0.25$	0.27914323	0.30125195	0.33537375	0.36589985	0.3942579	0.4484116
$R/c = 0.5$	0.35765825	0.3712145	0.395913	0.41455565	0.42994115	0.45431985
$R/c = 0.75$	0.4173797	0.4274192	0.44625975	0.4593948	0.46998705	0.48685445
$R/c = 1$	0.43376219	0.4456119	0.4656127	0.47752505	0.48600225	0.4979574
$R/c = 1.5$	0.46590938	0.48307935	0.5125915	0.5303125	0.5417025	0.555559
$R/c = 2$	0.45028437	0.46700235	0.4982383	0.5197645	0.5351525	0.5542885
$R/c = 2.5$	0.44752347	0.4650835	0.501366	0.5288725	0.549398	0.575279
$R/c = 3$	0.43409154	0.4497383	0.48419065	0.512136	0.534568	0.5654465

Table 7: Lift coefficients at 3° angle of attack and a slipstream Mach number of 0.4 for various R/c and u/c values

	$u/c = 0.25$	$u/c = 0.5$	$u/c = 1$	$u/c = 1.5$	$u/c = 2$	$u/c = 3$
$R/c = 0$	0.3674695	0.3674695	0.3674695	0.3674695	0.3674695	0.3674695
$R/c = 0.125$		0.756218	0.954228	1.085278	1.0764695	1.010477
$R/c = 0.25$	0.8278906	0.897792	1.0108185	1.1086195	1.195147	1.413002
$R/c = 0.5$	1.07189268	1.1189675	1.191713	1.2432655	1.2846795	1.34734
$R/c = 0.75$	1.24714849	1.2816625	1.341923	1.3837225	1.414049	1.453187
$R/c = 1$	1.33306431	1.3734055	1.4361585	1.473572	1.500636	1.53949
$R/c = 1.5$	1.38817504	1.4443455	1.5351795	1.589332	1.62404	1.666369
$R/c = 2$	1.31314256	1.3721995	1.478347	1.551029	1.600901	1.660071
$R/c = 2.5$	1.33483004	1.391478	1.5013325	1.584356	1.6466535	1.725913
$R/c = 3$	1.29512961	1.3460905	1.4506315	1.5351435	1.60329	1.6978595

Table 8: Lift coefficients at 5° angle of attack and a slipstream Mach number of 0.4 for various R/c and u/c values

	$u/c = 0.25$	$u/c = 0.5$	$u/c = 1$	$u/c = 1.5$	$u/c = 2$	$u/c = 3$
$R/c = 0$	0.6120075	0.6120075	0.6120075	0.6120075	0.6120075	0.6120075
$R/c = 0.125$		1.2633075	1.452938	1.3392215	1.249168	1.180068
$R/c = 0.25$	1.30563165	1.4107985	1.596059	1.783669	1.95562	1.9121165
$R/c = 0.5$	1.77810896	1.859302	1.9707265	2.049338	2.1198015	2.245759
$R/c = 0.75$	2.06304551	2.1272035	2.2178105	2.274575	2.326117	2.411593
$R/c = 1$	2.22862691	2.302779	2.406173	2.4680955	2.5127525	2.575999
$R/c = 1.5$	2.31379983	2.415691	2.566883	2.657166	2.7145185	2.783444
$R/c = 2$	2.22351493	2.3311315	2.5095305	2.631874	2.7155345	2.8138835
$R/c = 2.5$	2.20881159	2.310806	2.493104	2.6320385	2.736694	2.8717785
$R/c = 3$	2.13576603	2.2278935	2.401232	2.5433875	2.6590155	2.8219115

Table 9: Lift coefficients at 1° angle of attack and a slipstream Mach number of 0.45 for various R/c and u/c values

	$u/c = 0.25$	$u/c = 0.5$	$u/c = 1$	$u/c = 1.5$
$R/c = 0$	0.12259405	0.12259405	0.12259405	0.12259405
$R/c = 0.25$	0.30779298	0.33609192		
$R/c = 0.5$		0.42692876	0.45636112	
$R/c = 0.75$			0.52845113	0.55649614
$R/c = 1$			0.55649614	0.57148281

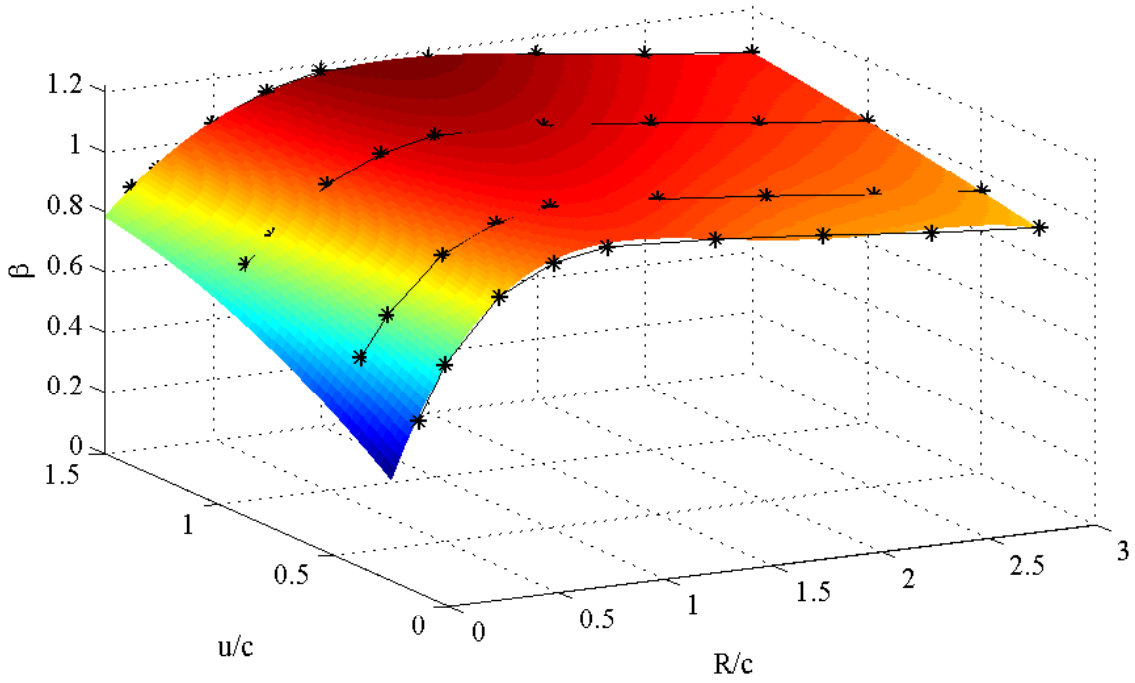

Figure 71: Visualization of the surrogate model for β and OVERFLOW simulation results for $V_j/V_\infty = 1.25$

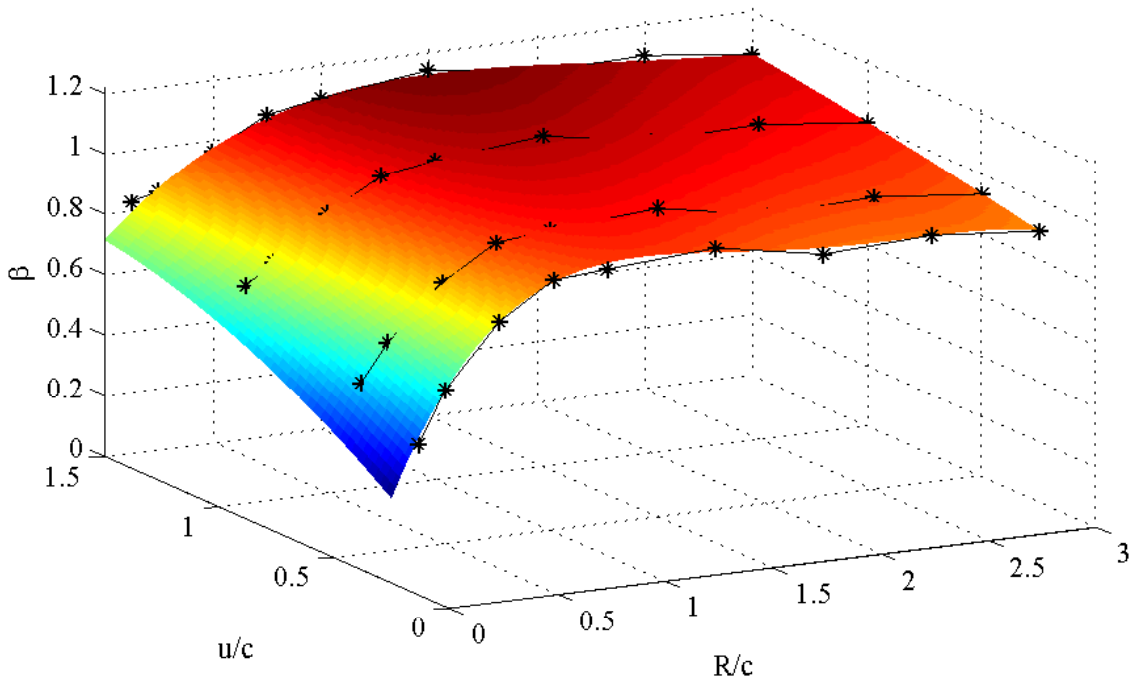

Figure 72: Visualization of the surrogate model for β and OVERFLOW simulation results for $V_j/V_\infty = 1.5$

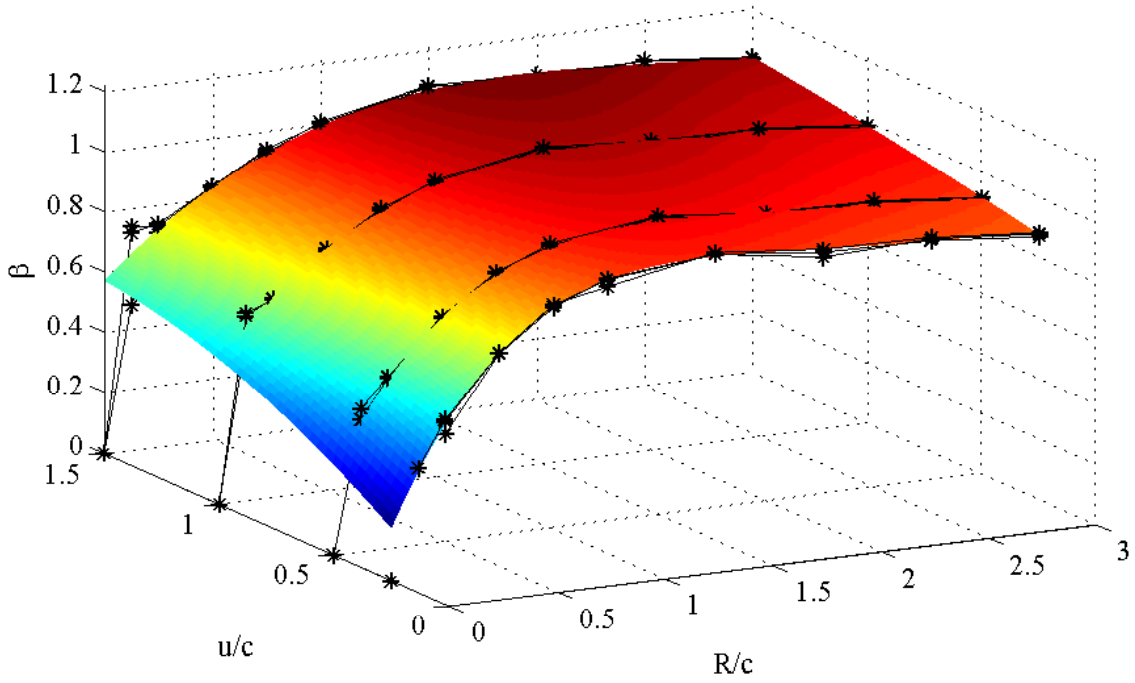

Figure 73: Visualization of the surrogate model for β and OVERFLOW simulation results for $V_j/V_\infty = 2$

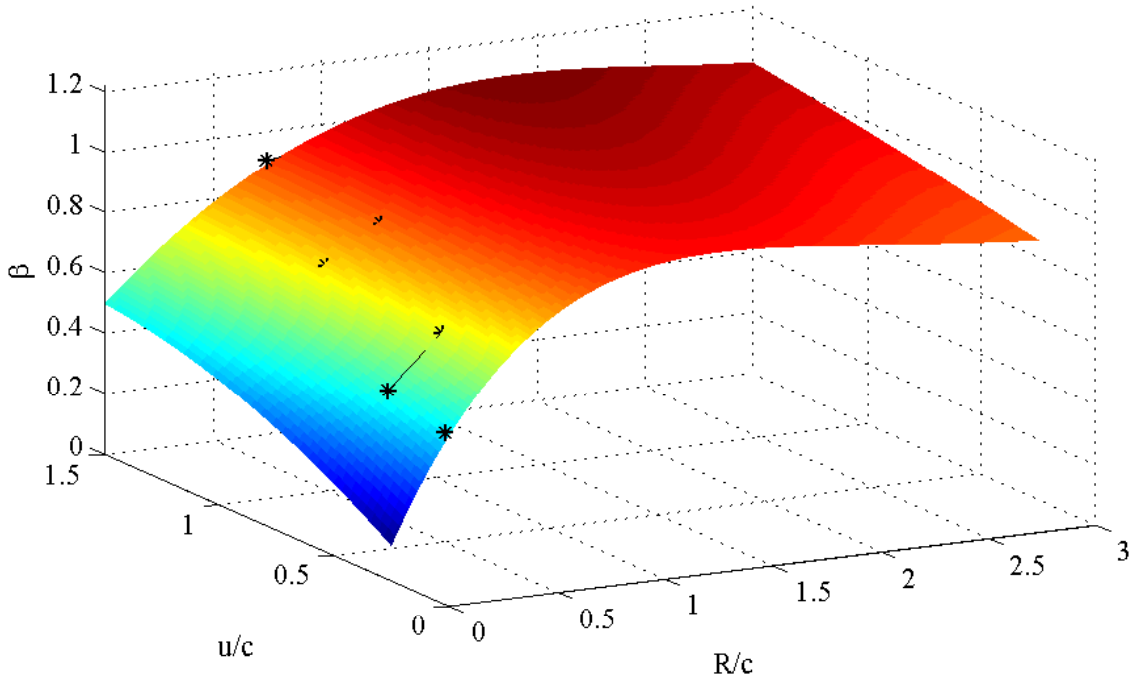

Figure 74: Visualization of the surrogate model for β and OVERFLOW simulation results for $V_j/V_\infty = 2.25$

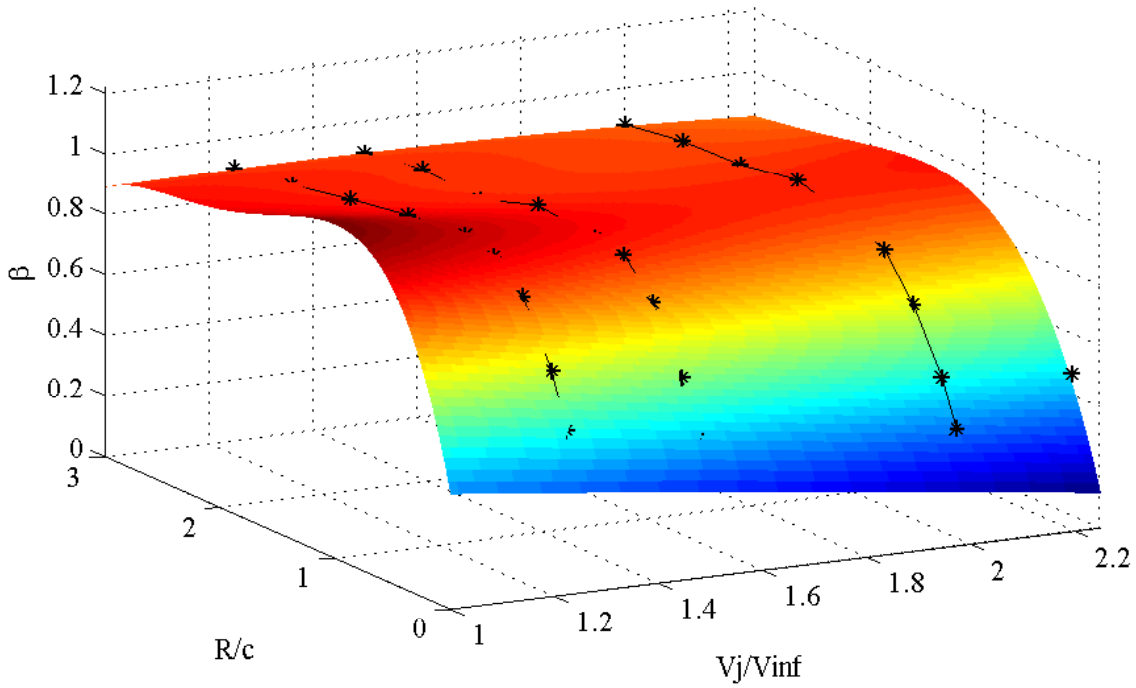

Figure 75: Visualization of the surrogate model for β and OVERFLOW simulation results for $u/c = 0.25$

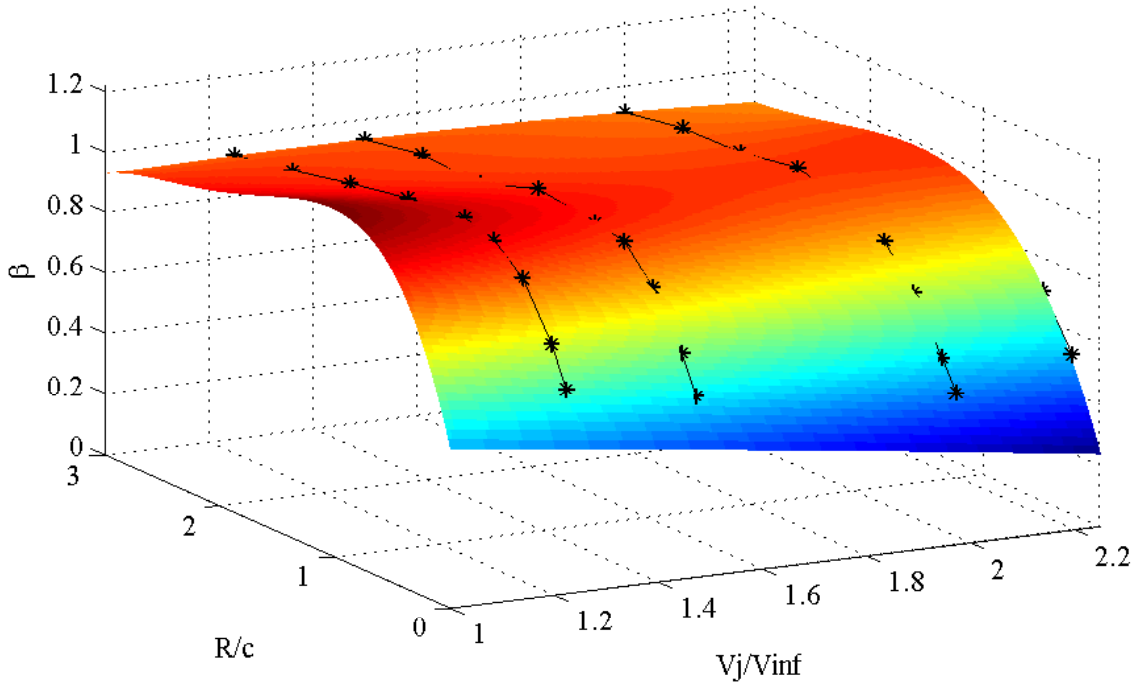

Figure 76: Visualization of the surrogate model for β and OVERFLOW simulation results for $u/c = 0.5$

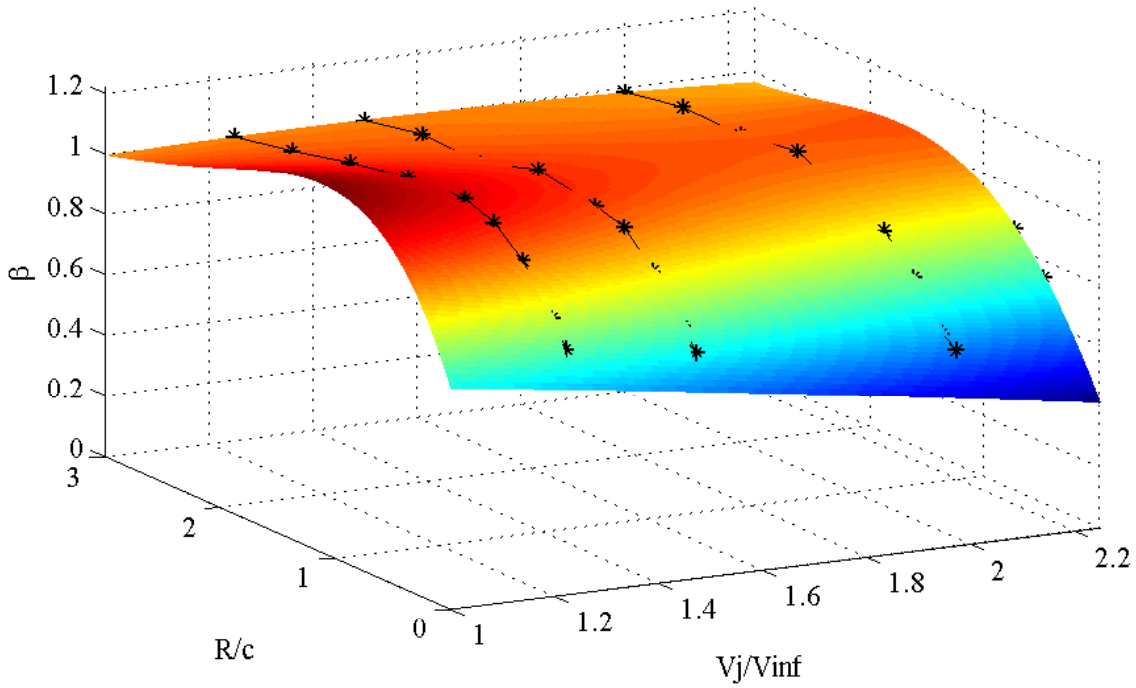

Figure 77: Visualization of the surrogate model for β and OVERFLOW simulation results for $u/c = 1$

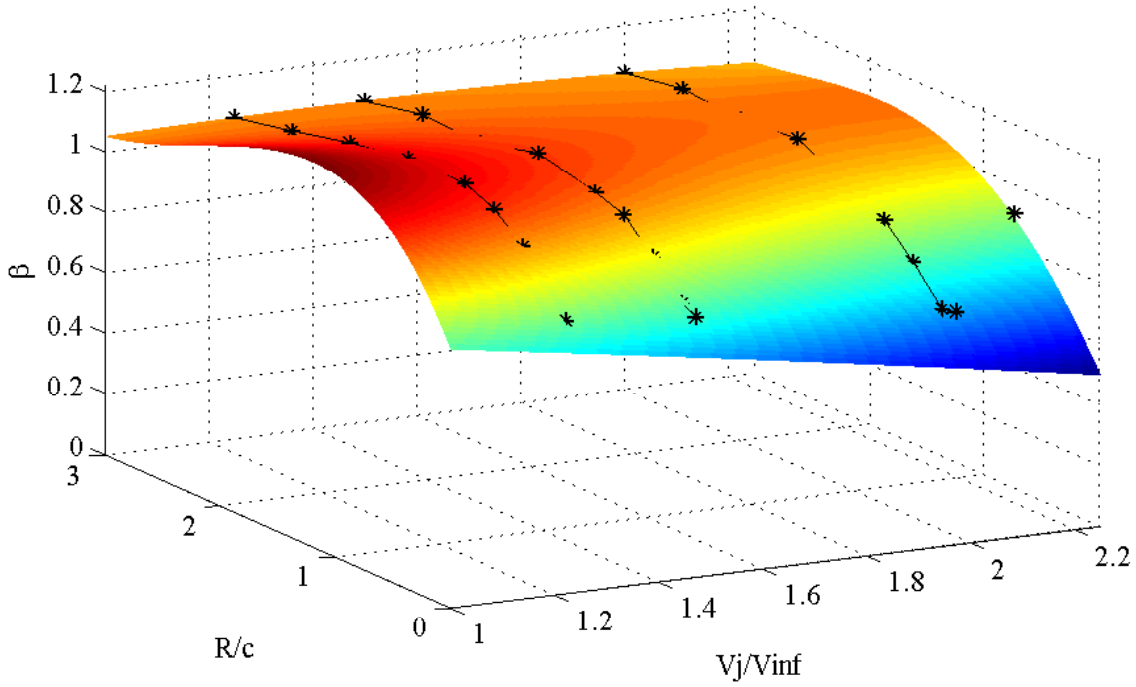

Figure 78: Visualization of the surrogate model for β and OVERFLOW simulation results for $u/c = 1.5$

REFERENCES

[1] Veldhuis, L. L. M., *Propeller Wing Aerodynamic Interference*, Ph.D. thesis, Delft University of Technology, June 2005.

[2] Smelt, R. and Davies, H., "Estimation of Increase in Lift Due to Slipstream," Reports and Memoranda 1788, British Aeronautical Research Council, 1937.

[3] Ting, L., Liu, C. H., and Kleinstein, G., "Interference of Wing and Multipropellers," *AIAA Journal*, Vol. 10, No. 7, 1972, pp. 906–914.

[4] Chow, F., Krause, E., Liu, C. H., and Mao, J., "Numerical Investigations of an Airfoil in a Nonuniform Stream," *Journal of Aircraft*, Vol. 7, No. 6, 1970, pp. 531–537.

[5] Ashcraft, S. W., Padron, A. S., Pascioni, K. A., Stout, G., and Huff, D. L., "Review of Propulsion Technologies for N+3 Subsonic Vehicle Concepts," TM-2011-217239, NASA, 2011.

[6] Kim, H. D., "Distributed Propulsion Vehicles," *27th International Congress of the Aeronautical Sciences*, Nice, France, September 19–24 2010.

[7] Wells, D., "NASA Green Flight Challenge: Conceptual Design Approaches and Technologies to Enable 200 Passenger Miles per Gallon," *11th AIAA Aviation Technology, Integration, and Operations (ATIO) Conference, including the AIAA Balloon Systems Conference and 19th AIAA Lighter-Than-Air Technology Conference*, Virginia Beach, VA, Sept 20–22 2011, AIAA-2011-7021.

[8] Tomažič, T., Plevnik, V., Veble, G., Tomažič, J., Popit, F., Kolar, S., Kielj, R., Langelaan, J. W., and Miles, K., "Pipistrel Taurus G4: on Creation and Evolution of the Winning Aeroplane of the NASA Green Flight Challenge 2011," *Strojniški vestnik - Journal of Mechanical Engineering*, Vol. 57, No. 12, 2011, pp. 869–878.

[9] Langelaan, J. W., Chakrabarty, A., Deng, A., Miles, K., Plevnik, V., Tomazic, J., Tomazic, T., and Veble, G., "Green Flight Challenge: Aircraft Design and Flight Planning for Extreme Fuel Efficiency," *Journal of Aircraft*, Vol. 50, No. 3, 2013, pp. 832–846.

[10] CAFE Foundation, "Green Flight Challenge Sponsored by Google - Final Results," http://cafefoundation.org/v2/gfc_2011_results.html, accessed 18 Dec 2015.

[11] Steitz, D. E., "NASA Awards Historic Green Aviation Prize," Press Release 11-334, NASA Headquarters, Oct 3 2011, http://www.nasa.gov/home/hqnews/2011/oct/HQ_11-334_GFC_Winners.html.

[12] Moore, M. D. and Fredericks, B., "Misconceptions of Electric Aircraft and their Emerging Aviation Markets," *52nd Aerospace Sciences Meeting*, 2014, AIAA 2014-0535.

[13] McDonald, R. A., "Electric Propulsion Modeling for Conceptual Aircraft Design," *52nd Aerospace Sciences Meeting*, National Harbor, Maryland, 13–17 January 2014, AIAA 2014-0536.

[14] UQM Technologies, "PowerPhase 125 Specification Sheet," 4120 Specialty Pl., Longmont CO 80504, 13–17 January 2010, AIAA 2014-0536.

[15] Patterson, M. D., German, B. J., and Moore, M. D., "Performance Analysis and Design of On-Demand Electric Aircraft Concepts," *12th AIAA Aviation Technology, Integration, and Operations (ATIO) Conference and 14th AIAA/ISSMO Multidisciplinary Analysis and Optimization Conference*, Indianapolis, IN, Sept 17–19 2012, AIAA-2012-5474.

[16] Moore, M. D., "Concept of Operations for Highly Autonomous Electric Zip Aviation," *12th AIAA Aviation Technology, Integration, and Operations (ATIO) Conference and 14th AIAA/ISSMO Multidisciplinary Analysis and Optimization Conference*, Indianapolis, IN, Sept 17–19 2012, AIAA-2012-5472.

[17] Gallagher, K., "Envia Systems Achieves World Record Energy Density for Rechargeable Lithium-Ion Batteries," Press release, Gallagher Group Communications, Newark, CA, Feb 27 2012, http://enviasystems.com/pdf/Press_Release_400WHK.pdf.

[18] Energy, A. R. P. A., "Batteries for Electrical Energy Storage in Transportation," http://arpa-e.energy.gov/?q=arpa-e-programs/beest, accessed 10 Oct 2013.

[19] Beyond Aviation, http://www.beyond-aviation.com/, 2012, accessed 13 Dec 2012.

[20] Yuneec International Ltd., "e430 Electric Aircraft," http://yuneeccouk.site.securepod.com/Aircraft.html, accessed 3 Oct 2013.

[21] Pipistrel USA, http://www.pipistrel-usa.com/, accessed 3 Oct 2013.

[22] Lange Aviation, "ANTARES 20E," http://www.lange-aviation.com/htm/english/products/antares_20e/antares_20E.html, accessed 3 Oct 2013.

[23] Warwick, G., "Slovenias Pipistrel Takes Lead In Electric Aircraft Development," *Aviation Week & Space Technology*, September 8 2014, pp. 52.

[24] Pope, S., "Meet Airbus E-Fan: Coming soon to an airport near you," *Flying Magazine*, July 15 2015.

[25] "Small Community Air Service," *49 U.S. Code Sections 41731-41748*, 2011.

[26] U.S. Department of Transportation, "Essential Air Service," https://www.transportation.gov/policy/aviation-policy/small-community-rural-air-service/essential-air-service, November 2015, accessed 20 Dec 2015.

[27] U.S. Department of Transportation, "Essential Air Service Alaskan Subsidized EAS Report," October 2015, https://www.transportation.gov/office-policy/aviation-policy/essential-air-service-reports.

[28] U.S. Department of Transportation, "Essential Air Service Non-Alaska U.S. Carrier Subsidy Report," October 2015, https://www.transportation.gov/office-policy/aviation-policy/essential-air-service-reports.

[29] McDonald, R. A., "Establishing Mission Requirements Based on Consideration of Aircraft Operations," *Journal of Aircraft*, Vol. 50, No. 3, 2013, pp. 741–751.

[30] Moore, M. D., "Aviation Frontiers - On Demand Aircraft," *10th AIAA Aviation Technology, Integration, and Operations (ATIO) Conference*, Fort Worth, Texas, 13–15 September 2010, AIAA-2010-9343.

[31] Smith, J. C., Viken, J., Guerreiro, N. M., Dollyhigh, S. M., Fenbert, J. W., Hartman, C. L., and Kwa, T.-S., "Projected Demand and Potential Impacts to the National Airspace System of Autonomous, Electric, On-Demand Small Aircraft," *12th AIAA Aviation Technology, Integration, and Operations (ATIO) Conference and 14th AIAA/ISSMO Multidisciplinary Analysis and Optimization Conference*, Indianapolis, IN, Sept 17–19 2012, AIAA-2012-5595.

[32] Smith, Leroy H., J., "Wake Ingestion Propulsion Benefit," *Journal of Propulsion and Power*, Vol. 9, No. 1, Jan – Feb 1993, pp. 74–82.

[33] Sanders, N. D., Diedrich, J. H., Hassell, Jr., J. L., Hickey, D. H., Luidens, R. W., and Stewart, W. L., "V/STOL Propulsion," *Aircraft Propulsion: Proceedings of a conference held at NASA Lewis Research Center*, No. NASA-SP-259, Cleveland, Ohio, November 18-19 1970.

[34] Yaros, S. F., Sexstone, M. G., Huebner, L. D., Lamar, J. E., McKinley, Robert E., J., Torres, A. O., Burley, C. L., Scott, R. C., and Small, W. J., "Synergistic Airframe-Propulsion Interactions and Integrations: A White Paper Prepared by the 1996-1997 Langley Aeronautics Technical Committee," TM 1998-207644, NASA, 1998.

[35] Ko, A., Schetz, J. A., and Mason, W. H., "Assessment of the Potential Advantages of Distributed-Propulsion for Aircraft," *XVI International Symposium on Air Breathing Engines*, 2003, ISABE-2003-1094.

[36] Hill, G. A., Brown, S. A., and Geiselhart, K. A., "Integration of Propulsion-Airframe-Aeroacoustic Technologies and Design Concepts for a Quiet Blended-Wing-Body Transport," *AIAA 4th Aviation Technology, Integration, and Operations Forum*, Chicago, IL, September 20–22 2004, AIAA-2004-6403.

[37] Kim, H., Berton, J., and Jones, S., "Low Noise Cruise Efficient Short Take-Off and Landing Transport Vehicle Study," *6th AIAA Aviation Technology, Integration and Operations Conference (ATIO)*, Wichita, Kansas, September 25–27 2006, AIAA 2006-7738.

[38] Kummer, J. D. and Dang, T. Q., "High-Lift Propulsive Airfoil with Integrated Crossflow Fan," *Journal of Aircraft*, Vol. 43, No. 4, July–August 2006, pp. 1059–1068.

[39] Schetz, J. A., Hosder, S., III, V. D., and Walker, J., "Propulsion and aerodynamic performance evaluation of jet-wing distributed propulsion," *Aerospace Science and Technology*, Vol. 14, No. 1, 2010, pp. 1–10.

[40] Felder, J. L., Brown, G. V., DaeKim, H., and Chu, J., "Turboelectric Distributed Propulsion in a Hybrid Wing Body Aircraft," *20th International Society for Airbreathing Engines*, Gothenburg, Sweden, September 12 2011, ISABE-2011-1340.

[41] Fredericks, W. J., Moore, M. D., and Busan, R. C., "Benefits of Hybrid-Electric Propulsion to Achieve 4x Cruise Efficiency for a VTOL UAV," *2013 International Powered Lift Conference*, Los Angeles, CA, August 12–14 2013, AIAA 2013-4324.

[42] Gohardani, A. S., Doulgeris, G., and Singh, R., "Challenges of future aircraft propulsion: A review of distributed propulsion technology and its potential application for the all electric commercial aircraft," *Progress in Aerospace Sciences*, Vol. 47, No. 5, 2011, pp. 369–391.

[43] Moore, M. D., "NASA Puffin Electric Tailsitter VTOL Concept," *10th AIAA Aviation Technology, Integration, and Operations (ATIO) Conference*, Fort Worth, Texas, 13–15 September 2010, AIAA-2010-9345.

[44] Lange, R. H., Cocke, Jr., B. W., and Proterra, A. J., "Langley Full-Scale Tunnel Investigation of a 1/3-Scale Model of the Chance Vought XF5U-1 Airplane," Naca-rm-l6i19, National Advisory Committee for Aeronautics, 1946.

[45] White, R. P., "Free-Spinning-Tunnel Tests of a 1/16-Scale Model of the Chance Vought XF5U-1 Airplane, TED No. NACA 2349," Naca-rm-l7i23, National Advisory Committee for Aeronautics, 1947.

[46] Moore, M. D., "The Forthcoming Era of Distributed Electric Propulsion and What it Means," NASA Langley Colloquium Lecture, 14 July 2015.

[47] Barnstorff, K., "Ten-Engine Electric Plane Completes Successful Flight Test," http://www.nasa.gov/langley/ten-engine-electric-plane-completes-successful-flight-test, April 30 2015.

[48] Warwick, G., "NASA Tests Distributed Electric Propulsion," *Aviation Week & Space Technology*, Aug 25 2014, pp. 31.

[49] Moore, M. D., Goodrich, K., Viken, J., Smith, J., Fredericks, B., Trani, T., Barraclough, J., German, B., and Patterson, M., "High Speed Mobility through On-Demand Aviation," *2013 Aviation Technology, Integration, and Operations Conference*, Los Angeles, CA, August 12–14 2013, AIAA 2013-4373.

[50] Paulson, Jr., J. W., "Wind-Tunnel Investigation of a Fowler Flap and Spoiler for an Advanced General Aviation Wing," Nasa-tn-d-8236, National Aeronautics and Space Administration, 1976.

[51] Holmes, B. J., "Flight Evaluation of an Advanced Technology Light Twin-Engine Airplane (ATLIT)," Contractor Report NASA CR-2832, National Aeronautics and Space Administration, 1977.

[52] Palumbo, D. L., Nark, D. M., Burley, C. L., and Rizzi, S. A., "Aural Effects of Distributed Propulsion (Oral Presentation)," *14th AIAA Aviation Technology, Integration, and Operations Conference*, Atlanta, GA, 16–20 June 2014, http://stabserv.larc.nasa.gov/flyover/ATIO2014/Aural_Effects_of_Distributed_Propulsion.ppsx.

[53] "Stalling speed," *Title 14 Code of Federal Regulations Part 23 Section 49*, 2011.

[54] Kuhn, R. E. and Draper, J. W., "An Investigation of a Wing-Propeller Configuration Employing Large-Chord Plain Flaps and Large-Diameter Propellers for Low-Speed Flight and Vertical Take-Off," Naca-tn-3307, National Advisory Committee for Aeronautics, December 1954.

[55] Kuhn, R. E. and Draper, J. W., "Investigation of Effectiveness of Large-chord Slotted Flaps in Deflecting Propeller Slipstreams Downward for Vertical Take-off and Low-speed Flight," Naca-tn-3364, National Advisory Committee for Aeronautics, 1955.

[56] Kuhn, R. E. and Draper, J. W., "Investigation of the Aerodynamic Characteristics of a Model Wing-Propeller Combination and of the Wing and Propeller Separately at Angles of Attack up to 90 Degrees," Naca-tr-1263, National Advisory Committee for Aeronautics, 1956.

[57] Welstead, J. R. and Felder, J. L., "Conceptual Design of a Single-Aisle Turboelectric Commercial Transport with Fuselage Boundary Layer Ingestion," *54th AIAA Aerospace Sciences Meeting*, San Diego, CA, January 2016.

[58] Snyder, M. and Zumwalt, G., "Effects of Wingtip-Mounted Propellers on Wing Lift and Induced Drag," *Journal of Aircraft*, Vol. 6, No. 5, 1969, pp. 392–397.

[59] Patterson, Jr., J. C. and Bartlett, G., "Effect of a Wing-Tip Mounted Pusher Turboprop on the Aerodynamic Characteristics of a Semi-Span Wing," *21st AIAA, SAE, ASME, and ASEE Joint Propulsion Conference*, Monterey, CA, 8–10 July 1985, AIAA 85-1286.

[60] Patterson, Jr., J. C. and Bartlett, G. R., "Evaluation of Installed Performance of a Wing-tip-Mounted Pusher Turboprop on a Semispan Wing," Nasa-tp-2739, National Aeronautics and Space Administration, 1987.

[61] Miranda, L. R. and Brennan, J. E., "Aerodynamic Effects of Wingtip-Mounted Propellers and Turbines," *4th Applied Aerodynamics Conference*, San Diego, CA, June 9–11 1986, pp. 221–228, AIAA-86-1802.

[62] Abeyounis, W. K., Patterson, James C., J., Stough, H. P., I., Wunschel, A. J., and Curran, P. D., "Wingtip Vortex Turbine Investigation for Vortex Energy Recovery," *SAE Aerospace Technology Conference and Exposition*, SAE Paper 901936, October 1–4 1990.

[63] Moore, M. D., Clarke, S., Stoll, A., Clark, A., MacAfee, S., and Foster, T., "Affordable Flight Testing of LEAPTech Distributed Electric Propulsion," http://nari.arc.nasa.gov/sites/default/files/MooreSeedling.pdf, January 13-15 2015, NASA Aeronautics Research Mission Directorate 2015 LEARN/Seedling Technical Seminar.

[64] Warwick, G., "Electrifying Aviation: Light aircraft are early targets for the efficiency and safety benefits touted for electric propulsion," *Aviation Week & Space Technology*, Jul 7 2014, pp. 18.

[65] National Aeronautics and Space Administration, "Transformative Aeronautics Concepts Program," http://www.aeronautics.nasa.gov/programs-tacp.htm, July 2015, accessed 22 Dec 2015.

[66] Costruzioni Aeronautiche TECNAM S.r.l., "P2006T," http://www.tecnam.com/aircraft/p2006t/, 2012, accessed 22 Dec 2015.

[67] Costruzioni Aeronautiche TECNAM srl, Via Maiorise CAPUA (CE) – Italy, *P2006T - Aircraft Flight Manual*, 3rd ed., May 5 2014, Doc. No. 2006/044.

[68] Borer, N. K., Moore, M. D., and Turnbull, A., "Tradespace Exploration of Distributed Propulsors for Advanced On-Demand Mobility Concepts," *14th AIAA Aviation Technology, Integration, and Operations Conference*, Atlanta, GA, 16–20 June 2014, AIAA 2014-2850.

[69] Borer, N. K. and Moore, M. D., "Integrated Propeller-Wing Design Exploration for Distributed Propulsion Concepts," *53rd AIAA Aerospace Sciences Meeting*, Kissimmee, Florida, 5-9 January 2015, AIAA 2015-1672.

[70] Keen, E. B., *A Conceptual Design Methodology for Predicting the Aerodynamics of Upper Surface Blowing on Airfoils and Wings*, Master's thesis, Virginia Polytechnic Institute & State University, 2004.

[71] Gentry, Garl L., J., Takallu, M. A., and Applin, Z. T., "Aerodynamic Characteristics of a Propeller-Powered High-Lift Semispan Wing," Technical Memorandum 4541, NASA, 1994.

[72] Prandtl, L., "Applications of Modern Hydrodynamics to Aeronautics," Technical Report 116, National Advisory Committee for Aeronautics, 1923.

[73] Weissinger, J., "The Lift Distribution of Swept-Back Wings," Technical Memorandum 1120, National Advisory Committee for Aeronautics, March 1947.

[74] Katz, J. and Plotkin, A., *Low-Speed Aerodynamics: From Wing Theory to Panel Methods*, McGraw-Hill, Inc., 1991.

[75] Miranda, L. R., Elliott, R. D., and Baker, W. M., "A Generalized Vortex Lattice Method for Subsonic and Supersonic Flow Applications," Contractor Report 2865, NASA, 1977.

[76] Rankine, W. J. M., "On the Mechanical Principles of the Action of Propellers," *Transactions of the Institute of Naval Architects*, Vol. 6, 1865, pp. 13–39.

[77] Froude, R. E., "On the Part Played in Propulsion by Differences of Fluid Pressure," *Transactions of the Institute of Naval Architects*, Vol. 30, 1889, pp. 390–405.

[78] McCormick, Jr., B. W., *Aerodynamics of V/STOL Flight*, Dover, Mineola, New York, 1999.

[79] Drzewiecki, S., *Théorie générale de l'hélice*, Gauthier-Villars et cie., Paris, 1920.

[80] Glauert, H., *Aerodynamic Theory*, Vol. IV, Div. L, chap. Airplane Propellers, Julius Springer, Berlin, 1935, pp. 169–269.

[81] Betz, A., "Schraubenpropeller mit Geringstem Energieverlust," *Nachrichten von der Gesellschaft der Wissenschaften zu G´ottingen, Mathematisch-Physikalische Klasse*, 1919, pp. 193–217.

[82] Goldstein, S., "On the Vortex Theory of Screw Propellers," *Proceedings of the Royal Society of London. Series A, Containing Papers of a Mathematical and Physical Character*, Vol. 123, No. 792, 1929, pp. 440–465.

[83] Prandtl, A. and Betz, A., *Vier Abhandlungen zur Hydrodynamik und Aerodynamik*, Gottingen, 1927.

[84] Larrabee, E. E., "Practical Design of Minimum Induced Loss Propellers," SAE Technical Paper 790585, Society of Automotive Engineers, 1979.

[85] Larrabee, E. E. and French, S. E., "Minimum induced loss windmills and propellers," *Journal of Wind Engineering and Industrial Aerodynamics*, Vol. 15, December 1983, pp. 317–327.

[86] Adkins, C. N. and Liebeck, R. H., "Design of Optimum Propellers," *Journal of Propulsion and Power*, Vol. 10, No. 5, Sept.–Oct. 1994, pp. 676–682.

[87] Theodorsen, T., "The Theory of Propellers III: the Slipstream Contraction with Numerical Values for Two-Blade and Four-Blade Propellers," Naca-tr-777, National Advisory Committee for Aeronautics, 1944.

[88] Kroo, I., "Propeller-Wing Integration for Minimum Induced Loss," *Journal of Aircraft*, Vol. 23, No. 7, 1986, pp. 561–565.

[89] Witkowski, D. P., Lee, A. K. H., and Sullivan, J. P., "Aerodynamic Interaction Between Propellers and Wings," *Journal of Aircraft*, Vol. 26, No. 9, 1989, pp. 829–836.

[90] Fratello, G., Favier, D., and Maresca, C., "Experimental and Numerical Study of the Propeller/Fixed Wing Interaction," *Journal of Aircraft*, Vol. 28, No. 6, June 1991, pp. 365–373.

[91] Snyder, Jr., M. H., *Effects of a Wingtip-Mounted Propeller on Wing Lift, Induced Drag, and Shed Vortex Pattern*, Ph.D. thesis, Oklahoma State University, 1967.

[92] Miley, S. J., Howard, R. M., and Holmes, B. J., "Wing Laminar Boundary Layer in the Presence of a Propeller Slipstream," *Journal of Aircraft*, Vol. 25, No. 7, 1988, pp. 606–611.

[93] Koning, C., *Aerodynamic Theory*, Vol. IV, Div. M, chap. Influence of the Propeller on Other Parts of the Airplane Structure, Julius Springer, Berlin, 1935, pp. 361–430.

[94] Franke, A. and Weinig, F., "The Effect of Slipstream on an Airplane Wing," NACA-TM-920, National Advisory Committee for Aeronautics, 1939.

[95] Squire, H. B. and Chester, W., "Calculation of the Effect of Slipstream on Lift and Induced Drag," Reports and Memoranda 2368, British Aeronautical Research Council, 1950.

[96] Mcveigh, M. A., Gray, L., and Kisielowski, E., "Prediction of Span Loading of Straight-Wing/Propeller Combinations Up to Stall," Nasa-cr-2602, National Aeronautics and Space Administration, October 1975.

[97] George, M. and Kisielowski, E., "Investigation of Propeller Slipstream Effects on Wing Performance," USAAVLABS Technical Report 67-67, Dynasciences Corporation, Blue Bell, Pennsylvania, November 1967.

[98] Rethorst, S., "Aerodynamics of Nonuniform Flows as Related to an Airfoil Extending Through a Circular Jet," *Journal of the Aeronautical Sciences*, Vol. 25, No. 1, 1958, pp. 11–28.

[99] Wu, T. Y. and Talmadge, R. B., "A Lifting Surface Theory for Wings Extending Through Multiple Jets," Tech. Rep. 8, Vehicle Research Corp., Pasadena, California, 1961.

[100] Ribner, H. and Ellis, N., "Theory and Computer Study of a Wing in a Slipstream," *4th Aerospace Sciences Meeting*, Los Angeles, CA, June 27-29 1966, AIAA 66-466.

[101] Marretta, R. M. A., "Different Wings Flowfields Interaction on the Wing-Propeller Coupling," *Journal of Aircraft*, Vol. 34, No. 6, 1997, pp. 740–747.

[102] Marretta, R. A., Davia, G., Lombardib, G., and Milazzo, A., "Hybrid numerical technique for evaluating wing aerodynamic loading with propeller interference," *Computers & Fluids*, Vol. 28, No. 8, November 1999, pp. 923–950.

[103] Cole, J., Maughmer, M., and Bramesfeld, G., "Aerodynamic Design Considerations for Tiltrotor Wing Extensions and Winglets," *51st AIAA Aerospace Sciences Meeting including the New Horizons Forum and Aerospace Exposition*, Grapevine, Texas, 07 - 10 January 2013, AIAA 2013-1088.

[104] Dang, T. Q., "Simulations of Propeller/Airframe Interference Effects Using an Euler Correction Method," *Journal of Aircraft*, Vol. 26, No. 11, 1989, pp. 994–1001.

[105] Fu, W., Li, J., and Wang, H., "Numerical Simulation of Propeller Slipstream Effect on A Propeller-driven Unmanned Aerial Vehicle," *Procedia Engineering*, Vol. 31, 2012, pp. 150–155.

[106] Rangwalla, A. and Wilson, L., "Application of a Panel Code to Unsteady Wing-Propeller Interference," *Journal of Aircraft*, Vol. 24, No. 8, 1987, pp. 568–571.

[107] Cho, J. and Williams, M. H., "Propeller-Wing Interaction Using a Frequency Domain Panel Method," *Journal of Aircraft*, Vol. 27, No. 3, 1990, pp. 196–203.

[108] Cho, J. and Cho, J., "Quasi-steady aerodynamic analysis of propeller-wing interaction," *International Journal for Numerical Methods in Fluids*, Vol. 30, No. 8, August 1999, pp. 1027–1042.

[109] Jameson, A., "Preliminary Investigation of the Lift of a Wing in an Elliptic Slipstream," Aerodynamics Report 393-68-6, Grumman, 1968.

[110] Anderson, Jr., J. D., *Introduction to Flight*, McGraw Hill, New York, 6th ed., 2008.

[111] Anderson, Jr., J. D., *Fundamentals of Aerodynamics*, McGraw Hill, 4th ed., 2005.

[112] Ting, L. and Liu, C., "Thin Airfoil in Nonuniform Parallel Streams," *Journal of Aircraft*, Vol. 6, No. 2, 1969, pp. 173–175.

[113] Prabhu, R. K. and Tiwari, S. N., "Linearized Potential Solution for an Airfoil in Nonuniform Parallel Streams," NASA-CR-173047, National Aeronautics and Space Administration, August 1983.

[114] Nichols, R., Tramel, R., and Buning, P., "Solver and Turbulence Model Upgrades to OVERFLOW 2 for Unsteady and High-Speed Applications," *24th AIAA Applied Aerodynamics Conference, Fluid Dynamics and Co-located Conferences*, San Francisco, CA, June 5-8 2006, AIAA 2006-2824.

[115] Nichols, R. and Buning, P., *User's Manual for OVERFLOW 2.2*, NASA Langley Research Center, Hampton, VA, August 2010.

[116] Gentry, Jr., G. L., Booth, Jr., E. R., and Takallu, M. A., "Effect of Pylon Wake with and Without Pylon Blowing on Propeller Thrust," Nasa-tm-4162, National Aeronautics and Space Administration, 1990.

[117] Kleinstein, G. and Liu, C. H., "Application of Airfoil Theory for Nonuniform Streams to Wing Propeller Interaction," *Journal of Aircraft*, Vol. 9, No. 2, 1972, pp. 137–142.

[118] Moriarty, P. and Hansen, A., "AeroDyn Theory Manual," Technical Report NREL/TP-500-36881, National Renewable Energy Laboratory, January 2005.

[119] Drela, M. and Youngren, H., "XROTOR Download Page," http://web.mit.edu/drela/Public/web/xrotor/, accessed 26 May 2014.

[120] Hepperle, M., "MH 114," http://www.mh-aerotools.de/airfoils/mh114koo.htm, 16 Feb 2008, accessed 5 Nov 2015.

[121] ASTM International, "Committee F44 on General Aviation Aircraft," http://www.astm.org/COMMITTEE/F44.htm, 2015, accessed 29 Dec 2015.

[122] "Reference landing approach speed," *Title 14 Code of Federal Regulations Part 23 Section 73*, 2011.

[123] "Landing," *Title 14 Code of Federal Regulations Part 25 Section 125*, 2014.

[124] Stoll, A. M., "Comparison of CFD and Experimental Results of the LEAPTech Distributed Electric Propulsion Blown Wing," *15th AIAA Aviation Technology, Integration, and Operations Conference*, Dallas, TX, 22-26 June 2015, AIAA 2015-3188.

[125] Raymer, D. P., *Aircraft Design: A Conceptual Approach*, American Institute of Aeronautics and Astronautics, 4th ed., 2006.

[126] Kinney, D. and McDonald, R., "VSPAero / OpenVSP Integration," http://www.openvsp.org/wiki/lib/exe/fetch.php?media=workshop15:vspaero_2015.pdf, August 2015, accessed 18 April 2016.

[127] Conway, J., "Analytical Solutions for the Actuator Disk with Variable Radial Distribution of Load," *Journal of Fluid Mechanics*, Vol. 297, August 1995, pp. 327–355.

[128] Johnson, W., *Helicopter Theory*, Dover Publications, Inc, New York, 1980.

[129] Nishizawa, A., "FEATHER Project in JAXA and Toward Future Electric Aircraft," http://www.nianet.org/ODM/ODM2016, accessed 19 April 2016.

[130] "JAXA's Electric Aircraft!: Exploring the technologies that the FEATHER (Flight demonstration of Electric Aircraft Technology for Harmonized Ecological Revolution) project has demonstrated," *Flight Path*, , No. 9/10, 2015, pp. 16–17, http://www.aero.jaxa.jp/eng/publication/magazine/pdf/en_fp_no0910_high.pdf, accessed 17 April 2016.

[131] Bradley, M., Dale, G., and Okai, K., "Grease and Trash Feed Advances in Biofuels," *Aerospace America*, December 2015, pp. 44.

[132] Hepperle, M., "MH 117," http://www.mh-aerotools.de/airfoils/mh117koo.htm, 16 Feb 2008, accessed 6 April 2016.

[133] "Prediction Procedure for Near-Field and Far-Field Propeller Noise," Aerospace Information Report SAE AIR 1407, Society of Automotive Engineers, Inc., 400 Commonwealth Drive, Warrendale, PA 15096, May 1977.

[134] MT-Propeller, "MTV-7 Variable Pitch Propeller Datasheet," March 2005, accessed 5 April 2016.

[135] Joby Motors, "Products," http://www.jobymotors.com/public/views/pages/products.php, 2011, accessed 16 Oct., 2015.

[136] Vidal, R. J., "The Influence of Two-Dimensional Stream Shear on Airfoil Maximum Lift," *Journal of the Aerospace Sciences*, Vol. 29, No. 8, 1962, pp. 889–904.

[137] Borer, N. K., Patterson, M. D., Stoll, A. M., Derlaga, J. M., and Moore, M. D., "Design and Performance of the NASA SCEPTOR Distributed Electric Propulsion Flight Demonstrator," *AIAA Aviation 2016*, Washington, D.C., June 13-17 2016, [upcoming publication].

[138] Hahn, A. S., "Vehicle Sketch Pad: A Parametric Geometry Modeler for Conceptual Aircraft Design," *48th AIAA Aerospace Sciences Meeting Including the New Horizons Forum and Aerospace Exposition*, Orlando, Florida, January 4–7 2010, AIAA-2010-657.

[139] OpenVSP, http://www.openvsp.org/, accessed 28 Aug 2012.

VITA

Michael Patterson was born and raised in Alabama. He earned a Bachelor's Degree in Aerospace Engineering from Auburn University in 2010 before enrolling at the Georgia Institute of Technology for graduate school. He earned a Master's degree in Aerospace Engineering in August of 2012 from Georgia Tech, adding to the long list of his extended family that can call themselves Ramblin' Wrecks from Georgia Tech. He left Atlanta prior to completing his dissertation to join the Aeronautics Systems Analysis Branch at NASA Langley Research Center where he works as an aerospace engineer.